

**EFFECTS OF COROTATING SOLAR WIND
STRUCTURES ON 27-DAY VARIATIONS IN
GALACTIC COSMIC RAYS OBSERVED BY THE
PRINCESS SIRINDHORN NEUTRON MONITOR**

THANA YEERAM

**A THESIS SUBMITTED IN PARTIAL FULFILLMENT
OF THE REQUIREMENTS FOR
THE DEGREE OF DOCTOR OF PHILOSOPHY
(PHYSICS)
FACULTY OF GRADUATE STUDIES
MAHIDOL UNIVERSITY
2014**

COPYRIGHT OF MAHIDOL UNIVERSITY

Thesis
entitled

**EFFECTS OF COROTATING SOLAR WIND
STRUCTURES ON 27-DAY VARIATIONS IN
GALACTIC COSMIC RAYS OBSERVED BY THE
PRINCESS SIRINDHORN NEUTRON MONITOR**

.....
Mr. Thana Yeeram
Candidate

.....
Prof. David Ruffolo,
Ph.D. (Physics)
Major advisor

.....
Lect. Alejandro Sáiz,
Ph.D. (Physics)
Co-advisor

.....
Asst. Prof. Somsak Dangtip,
Ph.D. (Applied Nuclear Physics)
Co-advisor

.....
Prof. Banchong Mahaisavariya,
M.D., Dip Thai Board of Orthopedics
Dean
Faculty of Graduate Studies
Mahidol University

.....
Assoc. Prof. Weerachai Siripunvaraporn,
Ph.D. (Geophysics)
Program Director
Doctor of Philosophy Program
in Physics
Faculty of Science
Mahidol University

Thesis
entitled
**EFFECTS OF COROTATING SOLAR WIND
STRUCTURES ON 27-DAY VARIATIONS IN
GALACTIC COSMIC RAYS OBSERVED BY THE
PRINCESS SIRINDHORN NEUTRON MONITOR**

was submitted to the Faculty of Graduate Studies, Mahidol University
for the degree of Doctor of Philosophy (Physics)

on
March 10, 2014

.....
Mr. Thana Yeeram
Candidate

.....
Lect. Paisan Tooprakai,
Ph.D. (Physics)
Chair

.....
Prof. David Ruffolo,
Ph.D. (Physics)
Member

.....
Asst. Prof. Somsak Dangtip,
Ph.D. (Applied Nuclear Physics)
Member

.....
Lect. Alejandro Sáiz,
Ph.D. (Physics)
Member

.....
Prof. Banchong Mahaisavariya,
M.D., Dip Thai Board of Orthopedics
Dean
Faculty of Graduate Studies
Mahidol University

.....
Prof. Skorn Mongkolsuk,
Ph.D. (Biological Science)
Dean
Faculty of Science
Mahidol University

ACKNOWLEDGEMENTS

I greatly appreciate with the effort from Prof. Dr. David Ruffolo, my advisor, for his valuable advice for the success of this thesis. All crucial aspects of my study and research were supported by his attention and kindness. He always suggested and gave me great chances, encouragement, clear concepts, methods, and visions on the road of studying physics and cosmic ray research.

I would like to sincerely thank my co-advisors. Dr. Alejandro Sáiz provided me valuable suggestions and techniques for data analysis. He always clearly gave and showed me good guidance and discussion on cosmic ray research and my thesis. I also appreciate the good advice for preparing the thesis from Asst. Prof. Somsak Dangtip.

I am grateful to my thesis defense chair, Dr. Paisan Tooprakai, for presiding over the thesis defense, and for suggestions and checking over the thesis.

I would like to thank Mr. Nattapong Kamyam for explaining neutron monitor datasets, including cosmic ray data processing, technical support, and other important techniques. Special thanks are due to to Asst. Prof. Tanin Nutaro for his technical support and good suggestions.

Special thanks go to Mr. Pornsak Sommart, as a fellow students, who shared many valuable activities with me and to Miss Usanee Toternpun, who helped and shared many crucial cosmic ray research documents and discussion.

I am heartily thankful to Dr. Michael Allen for original providing the \LaTeX class file. Thanks to Mr. Nattapong and others for providing a \LaTeX template.

I also appreciate Dr. Achara Seripienlert, who gave me good academic suggestions and effort. Thanks to Dr. Watcharawuth, Mr. Wirin, Dr. Ghilea, Dr. Snodin, Lect. Waraporn, and everyone in the Space Physics and Energetic Particles Lab, for sharing ideas and encouragement.

Special thanks go to my family for their cheerfulness, love, and all support. I heartily recognize my great teacher, Miss Boonsanong Roojak, who inspired me to be a teacher and to Ms. Sumala, who pushed me forward to study in the University.

Finally, I am grateful to the Thai Ministry of Science and Technology, the Thailand Research Fund, and Department of Physics, Mahasarakham University for support and funding.

EFFECTS OF COROTATING SOLAR WIND STRUCTURES ON 27-DAY VARIATIONS IN GALACTIC COSMIC RAYS OBSERVED BY THE PRINCESS SIRINDHORN NEUTRON MONITOR.

THANA YEERAM 5138427 SCPY/D

Ph.D. (PHYSICS)

THESIS ADVISORY COMMITTEE : DAVID RUFFOLO, Ph.D. (PHYSICS), ALEJANDRO SÁIZ, Ph.D. (PHYSICS), SOMSAK DANGTIP, Ph.D. (APPLIED NUCLEAR PHYSICS)

ABSTRACT

Data from the *Princess Sirindhorn Neutron Monitor* at Doi Inthanon, Thailand, with a vertical cutoff rigidity of 16.8 GV, have been utilized to determine the diurnal anisotropy (DA) of Galactic cosmic rays (GCRs) near Earth during solar minimum conditions between 2007 November and 2010 November. We have identified trains of enhanced DA over several days, and find that these trains are often recurrent after a solar rotation period (~ 27 d). By investigating solar coronal holes as identified from synoptic maps and solar wind parameters observed by spacecraft, we found that the intensity and anisotropy of cosmic rays are associated with the high-speed streams (HSSs) in the solar wind, which are in turn related to the structure and evolution of the equatorial and higher-latitude coronal holes. An enhanced DA was observed after the onset of some, but not all, HSSs. During the time periods of recurrent trains, the DA was often enhanced or suppressed according to the sign of the interplanetary magnetic field \mathbf{B} , which suggests a contribution from a mechanism involving a southward gradient in the GCR density, n , and a gradient anisotropy along $\mathbf{B} \times \nabla n$. In one non-recurrent and one recurrent sequence, an HSS from an equatorial coronal hole was merged with that from a trailing mid-latitude extension of a polar coronal hole, and the slanted HSS structure in space, within which the GCR density was depressed, can account for the southward GCR gradient. We conclude that the gradient anisotropy is a source of temporary changes in the GCR diurnal anisotropy under solar minimum conditions. The 27-day modulations of GCRs intensity are well correlated with the magnetic field magnitudes and solar wind speed as predicted by the solar modulation theory of GCRs.

KEYWORDS: SOLAR WIND / NEUTRON MONITOR / SPACE PHYSICS

200 pages

ผลกระทบของโครงสร้างลมสุริยะแบบหมุนร่วมต่อการเปลี่ยนแปลงในรอบ 27 วันของรังสีคอสมิกกาแล็กติกที่สังเกตโดยสถานีตรวจวัดนิวตรอนสิรินธร

EFFECTS OF COROTATING SOLAR WIND STRUCTURES ON 27-DAY VARIATIONS IN GALACTIC COSMIC RAYS OBSERVED BY THE PRINCESS SIRINDHORN NEUTRON MONITOR

ธนา ชีรัมย์ 5138427 SCPY/D

ปร.ค. (ฟิสิกส์)

คณะกรรมการที่ปรึกษาวิทยานิพนธ์: เดวิด รูฟโฟโล, Ph.D. (PHYSICS), อเลสซานโดร ซาอิส, Ph.D. (PHYSICS), สมศักดิ์ แดงดีบ, Ph.D. (APPLIED NUCLEAR PHYSICS)

บทคัดย่อ

จากการศึกษาแอนไอโซโทรปีประจำวันของรังสีคอสมิกกาแล็กติกใกล้โลกที่สังเกตโดยสถานีตรวจวัดนิวตรอนสิรินธร ณ ยอดดอยอินทนนท์ ด้วยค่าเชิงเกร็งทางแม่เหล็กขีดเริ่ม 16.8 กิกะโวลต์ ในช่วงเงื่อนไขที่ดวงอาทิตย์มีกิจกรรมต่ำที่สุดในระหว่างเดือนพฤศจิกายน 2007 ถึง พฤศจิกายน 2010 เราได้จำแนกพบขบวนการแอนไอโซโทรปีที่มีขนาดเพิ่มขึ้นต่อเนื่องเป็นเวลาหลายวัน โดยขบวนการเหล่านี้มักจะเกิดซ้ำตามรอบการหมุนรอบตัวเองของดวงอาทิตย์ในรอบ 27 วัน เมื่อสืบหาหลุมโคโรนาที่ได้จากการชี้เฉพาะจากแผนที่ซินออปติกและตัวแปรลมสุริยะความเร็วสูงที่สังเกตโดยยานอวกาศ พบว่าความเข้มและแอนไอโซโทรปีของรังสีคอสมิกมีความเกี่ยวข้องกับลมสุริยะความเร็วสูงซึ่งมีความสัมพันธ์กับโครงสร้างและวิวัฒนาการของหลุมโคโรนาในบริเวณศูนย์สูตรและละติจูดที่สูงขึ้นของดวงอาทิตย์ การเพิ่มของแอนไอโซโทรปีประจำวันได้เกิดขึ้นภายหลังการเคลื่อนที่ผ่านของลมสุริยะความเร็วสูงในบางครั้ง โดยในคาบเวลาที่เกิดขบวนการ บ่อยครั้งสังเกตเห็นแอนไอโซโทรปีที่เพิ่มหรือลดขึ้นอยู่กับเครื่องหมายของสนามแม่เหล็กระหว่างดาวเคราะห์ ซึ่งบ่งชี้ถึงผลกระทบจากกลไกที่ประกอบด้วยเกรเดียนต์ในรังสีคอสมิกในทิศใต้ของดวงอาทิตย์ และแอนไอโซโทรปีจากเกรเดียนต์ จากกรณีศึกษาของเหตุการณ์ที่เวียนและไม่เวียนซ้ำ พบกระแสลมสุริยะความเร็วสูงที่มาจากหลุมโคโรนาบริเวณศูนย์สูตรประสานกับที่มาจากหลุมโคโรนาเชิงขั้วที่ขยายตัวสู่บริเวณละติจูดตอนกลาง ทำให้เกิดโครงสร้างแบบเอียงของลมสุริยะความเร็วสูงที่มีผลให้รังสีคอสมิกมีความเข้มลดลง แล้วได้เกรเดียนต์ไปทางทิศใต้ จึงสรุปว่าแอนไอโซโทรปีจากเกรเดียนต์เป็นสาเหตุหนึ่งของการเปลี่ยนแปลงชั่วคราวของแอนไอโซโทรปีประจำวันในช่วงกิจกรรมสุริยะต่ำสุด ส่วนการลดลงแบบ 27 วันของความเข้มรังสีคอสมิกกาแล็กติกมีสหสัมพันธ์ที่ดีกับความเข้มสนามแม่เหล็กและความเร็วลมสุริยะ ดังทฤษฎีการ โมดุลชันของรังสีคอสมิกโดยดวงอาทิตย์

200 หน้า

CONTENTS

	Page
ACKNOWLEDGEMENTS	iii
ABSTRACT (ENGLISH)	iv
ABSTRACT (THAI)	v
LIST OF TABLES	x
LIST OF FIGURES	xi
CHAPTER I INTRODUCTION	1
1.1 Overview	1
1.2 Nature of the problem	7
1.3 Approach toward a solution	12
1.3.1 Observational databases	12
1.3.2 Objectives	13
1.4 Outline of the thesis	15
CHAPTER II BACKGROUND KNOWLEDGE	16
2.1 Galactic cosmic rays at Earth	17
2.1.1 General	17
2.1.2 Atmospheric cascades	18
2.1.3 Energy spectra and modulation with the solar cycle	21
2.1.4 Abundances of the elements	23
2.2 Neutron monitor measurements	25
2.2.1 History	25
2.2.2 Designs and principles of neutron monitors	27
2.2.3 Cutoff rigidity	31
2.2.4 Asymptotic direction of measurement	33
2.2.5 Diurnal variation at neutron monitor energies	34
2.3 Plasma and magnetic field from the Sun to the heliosphere	36
2.3.1 solar wind	36
2.3.2 Magnetic fields in the solar photosphere and corona	36

CONTENTS (cont.)

	Page
2.3.3 Interplanetary spiral magnetic field	39
2.3.4 Magnetic field sectors	41
2.3.5 Heliospheric current sheet	42
2.4 Solar modulation and anisotropy of Galactic cosmic rays	45
2.4.1 General	45
2.4.2 Streaming equation and cosmic ray anisotropy expressions	46
2.4.3 Modulation transport equation	52
2.4.4 Spherically symmetric modulation	55
2.4.5 Non-spherically symmetric modulation	56
2.4.6 The solar cycle modulation	57
2.5 Corotating solar wind structures	59
2.5.1 Coronal holes as a source of high speed solar wind streams	59
2.5.2 Corotating interaction regions	61
2.5.3 27-day cosmic ray intensity variations	63
CHAPTER III PRINCESS SIRINDHORN NEUTRON MONITOR	66
3.1 Station information	67
3.1.1 Geographical location	67
3.1.2 Geomagnetic location and cutoff rigidity	68
3.1.3 Configuration of the Princess Sirindhorn Neutron Monitor	69
3.1.4 Neutron monitor detection system	74
3.2 Angular and rigidity response of PSNM	79
3.2.1 Asymptotic directions	79
3.2.2 Geomagnetic corrections	79
3.2.3 The response function of PSNM at Doi Inthanon	81
CHAPTER IV DATA ANALYSIS	84
4.1 PSNM data processing	84
4.1.1 Uncorrected data	84
4.1.2 Pressure correction	86

CONTENTS (cont.)

	Page
4.1.3 PRELIM process	87
4.2 Other data used in this research	95
4.2.1 ACE interplanetary magnetic field and plasma data	95
4.2.2 STEREO-A synoptic maps	95
4.2.3 Wilcox Solar Observatory heliospheric current sheet	96
4.3 Harmonic analysis of count rate data	97
4.4 Time synchronization of PSNM, ACE, and STEREO-A data	99
4.5 Classifying high speed solar wind streams and corotating interaction regions	101
CHAPTER V RESULTS	102
5.1 Statistics of diurnal amplitude and phase at Doi Inthanon	102
5.2 Trains and recurrent trains of enhanced and suppressed diurnal variations	105
5.3 Gradient anisotropy	107
5.4 Case studies	111
5.4.1 Carrington rotations 2070 & 2071	111
5.4.2 Carrington rotation 2093	117
5.4.3 Carrington rotation 2064	117
5.5 27-day cosmic ray intensity modulation	119
5.6 Coronal holes and high speed solar wind streams	130
5.6.1 Evolution of coronal holes during solar minimum from 2007 to 2010	130
5.6.2 Statistics of CIRs and HSSs	131
CHAPTER VI DISCUSSION	140
6.1 Contribution of $\mathbf{B} \times \nabla n$ anisotropy to the recurrent diurnal variations	140
6.1.1 Latitudinal gradient of Galactic cosmic rays	142

CONTENTS (cont.)

	Page
6.1.2 Characteristics of trains and recurrent trains of suppressed and enhanced diurnal variations	145
6.2 Contributing factors of the 27-day modulation of Galactic cosmic ray intensity	153
6.2.1 Effects of convection and adiabatic deceleration	153
6.2.2 Effects of diffusive barriers	155
6.2.3 Effects of drifts	156
6.2.4 The 27-day modulation of Galactic cosmic ray intensity at Doi Inthanon	157
CHAPTER VII CONCLUSIONS	161
REFERENCES	163
APPENDICES	183
Appendix A 27-day variations in GCR intensity as observed by PSNM	184
Appendix B Extreme Ultraviolet Imager and image processing of STEREO/EUVI synoptic maps	188
B.1 Extreme Ultraviolet Imager	188
B.2 Image processing of the synoptic maps	190
Appendix C Gyroradius of cosmic rays and magnetic rigidity	196
BIOGRAPHY	200

LIST OF TABLES

Table		Page
2.1	Average solar wind parameters at 1 AU, for the time around solar activity minimum, compiled by Schwenn (1990).	38
5.1	Trains of enhanced diurnal variation at Doi Inthanon from November, 2007 to November, 2010	105
5.2	The HSS events in this study (2007-2008)	136
5.3	The HSS events in this study (2009-2010)	137
5.4	The CIR events in this study (2007-2008)	138
5.5	The CIR events in this study (2009-2010)	139
B.1	EUVI telescope properties (Wülser et al. 2003)	189

LIST OF FIGURES

Figure	Page
1.1 The aurora is caused by a flood of charged plasma racing away from disturbances on the Sun. (http://www.public.iastate.edu/~sdk/fick2003/october.html)	3
1.2 Archimedean spiral geometry of the interplanetary magnetic field.	5
1.3 Coronal holes appear as darker areas when viewed in this extreme UV wavelength (195 Ångstroms). This large equatorial hole area from April 27, 2008 was one of the largest seen by STEREO (Ahead). Although they are usually located at the poles of the Sun, coronal holes can occur other places as well. The magnetic field lines in a coronal hole extend out into the solar wind rather than coming back down to the Sun's surface as many do in other parts of the Sun. They are often the source of high speed solar wind streams that carry solar plasma into space and possibly impact the Earth. (http://stereo.gsfc.nasa.gov/gallery/)	8
2.1 Schematic representation of the typical development of the secondary cosmic radiation within the atmosphere arising from an incident primary particle (Simpson et al. 1953).	19
2.2 The differential energy spectra of cosmic rays from observations made from above the Earth's atmosphere. The spectra for hydrogen, helium, carbon and iron are shown. The solid line represents the unmodulated spectrum for hydrogen in interstellar space. The flux of helium nuclei below about 60 MeVnucleon ⁻¹ is due to an additional flux of the anomalous ⁴ He component. (From Simpson (1983). The arrows indicate the ranges of kinetic energies for each species corresponding to the vertical cutoff rigidity of 16.8 GV at Doi Inthanon.	22
2.3 Modulation of cosmic ray flux with the solar activity cycles (http://neutronm.bartol.udel.edu). As solar activity rises (top panel), the count rate recorded by a neutron monitor in Thule, Greenland decreases (bottom panel).	23

LIST OF FIGURES (cont.)

Figure	Page	
2.4	(a) The relative abundances of cosmic ray elements measured by University of Chicago instruments during the different phases of the solar cycle: solar maximum (open and closed circle); solar minimum condition (squares). (b) The climax NM intensity of ≥ 3 GeV/nucleon for 1962-1981, which is the corresponded to (a) (From Simpson (1983))	25
2.5	The standard pile extended to 12 counters, the IGY neutron monitor (Simpson et al. (1953) in Stoker (2009)).	28
2.6	The 6NM64 super neutron monitor, shown schematically (Carmichael 1968), was designed for higher count rates and better statistics than the IGY neutron monitor.	28
2.7	Charged particle trajectories of different rigidities (energies) traced out in the vertical direction from the same location. The trajectories are arranged from the highest (labeled 1) to lowest energies (labeled 15). The trajectories labeled 1, 2, and 3 show increasing geomagnetic bending before escape into space. Trajectory 4 develops intermediate loops near the Earth while trajectory 5 near the cutoff rigidity develops complex loops before escaping. The lower energy trajectory 15 in the penumbra escapes after a series of complex loops near the Earth. (From Smart et al. 2000)	32
2.8	Montage of images from 3 different telescopes on SOHO: EIT showing the EUV disk (at 19.5 nm), LASCO-C1 showing the inner corona (at 530.3 nm), and LASCO C2 showing the outer corona (in white light). This shows the two states of solar wind characterized by their brightness and sources. The slow streams are brighter than the fast streams because they are more dense. Note also how well separated from each other they are, both in the low corona as well as in the extended corona. The dark area on the disk near the south pole is a good example of a large coronal hole (from Schwenn 2006).	37

LIST OF FIGURES (cont.)

Figure	Page
<p>2.9 Relationship between the photospheric magnetic field, the source surface field, and the interplanetary magnetic field. The inner circle represents the Sun. The photospheric magnetic field is measured in region 1. Closed field lines (loops) exist in region 2. The dashed circle represents the source surface at which any field lines crossing it are assumed to become radial. Beyond the source surface, the field lines gradually develop a spiral shape. Dashed and solid lines indicate negative and positive magnetic field polarities as observed by spacecraft near 1 AU, respectively (Schatten et al. 1969).</p>	39
<p>2.10 Left: Temporal changes in the inclination (tilt angle) of the solar magnetic field (Gozling and Pizzo 1999, after Hundhausen, 1977), boundaries between closed and open magnetic field lines, and large-scale closed magnetic field lines, around times of solar minimum. Right: Configuration of the HCS in the solar wind for a substantial tilt angle (Jokipii and Thomas 1981). The width of the cone of the HCS is twice the tilt angle.</p>	44
<p>2.11 Diurnal anisotropy as a combination of contributions from convection and diffusion. This can explain the long-term average, but not short-term variations in diurnal anisotropy.</p>	51
<p>2.12 The first continuous observations of coronal holes were made with Skylab in the 1970s in soft X-rays. Coronal holes (dark regions) sometimes take the shape of channels rather than round holes, and may hold their shape through several rotation of the sun. (http://soi.stanford.edu/results/SolPhys200/Hudson/2000)</p>	61
<p>2.13 An idealized view of a corotating interaction region (CIR) and its evolution from a rectangular speed profile at the Sun into a more gradual speed increase at 1 AU (Schwenn 1990).</p>	62

LIST OF FIGURES (cont.)

Figure	Page	
2.14	Schematic model of the tilted dipole. The magnetic axis, M , is tilted with respect to the rotation axis. Slow solar wind emanates from the streamer belt around the heliomagnetic equator. The tilted magnetic equator evolves into a wavy heliospheric current sheet (HCS). CIRs are bounded by forward (F) and reverse (R) shocks. Sizes are not in scale (Kóta and Jokipii 1998).	64
3.1	Cutoff rigidities of PSNM at Doi Inthanon and other neutron monitors around the world. [Courtesy of R. Pyle.]	68
3.2	The building of the PSNM station.	69
3.3	The interior of PSNM at Doi Inthanon. (A) Main data acquisition systems, storage devices, and three bare counters. (B) 18-tube neutron monitor with proportional tube detection systems.	70
3.4	Typical setup for gas-filled neutron detectors.	72
3.5	Sketch of cross-section of the standard 18NM64 neutron monitor at Doi Inthanon.	72
3.6	Cross section of output end of type BP28F stainless steel cathode counter (from Fowler 1963).	74
3.7	The pulse height distribution produced by a neutron source with a BP28 Chalk River neutron counter.	78
3.8	Asymptotic viewing directions for vertically incident Galactic cosmic rays over the central 80% of the rigidity range at Doi Inthanon (Thai) and Yangbajing (Tibet).	80
3.9	Differential response functions of the neutron monitor at Yangbajing (Tibet) and Doi Inthanon (Thailand) during solar minimum using the yield function and spectrum of Nagashima et al. (1989). (T. Kuwabara, private communication, 2010)	83
3.10	Integrated response functions of PSNM and other detectors, using the yield function and spectrum of Nagashima et al. (1989). (K. Munakata, private communication, 2010)	83

LIST OF FIGURES (cont.)

Figure	Page
4.1	Cosray electronics rack diagram. 85
4.2	NM count rate at Doi Inthanon. Notice that the uncorrected count rate has a strong dependence on pressure, which is removed in the corrected count rate. 94
4.3	The Geocentric Solar Ecliptic Coordinates. 96
4.4	Geometry of longitudinal separation between Earth and STEREO-A (not to scale). 99
4.5	The position of STEREO-A with respect to Earth. 100
5.1	Calculated ground-based components of diurnal anisotropy from a harmonic analysis of the neutron count rate at Doi Inthanon for each day from Nov., 2007 to Nov., 2010. These components are not yet corrected for the coupling coefficients. The asterisk indicates the mean diurnal variation. 103
5.2	Asymptotic direction and A_x and A_y directions at Doi Inthanon. The dashed line indicates the mean inflow direction of Galactic cosmic ray flux in free space. 104
5.3	Count rate of the Princess Sirindhorn Neutron Monitor at Doi Inthanon as a function of time, showing recurrent trains of enhanced diurnal anisotropy (DA) in 2008, indicated by arrows, compared with magnetic sectors (toward, T, or away, A) for six successive Carrington rotations, CR2068-2073. Shaded areas represent HSSs with solar wind speed ≥ 450 km s ⁻¹ . Recurrently enhanced DA was often observed in the A sector, while suppressed DA was often observed in the T sector. 106
5.4	Same as Figure 5.3 for CR2092-2098 during 2010. There are three patterns of enhanced diurnal variations: (i) One enhancement mostly in the T sector during CR2092-CR2093. (ii) Repeated enhancement mostly in the A sector, during CR2093-CR2096. (iii) Extended enhancements in both the T and A sectors during CR2097-CR2098. 107

LIST OF FIGURES (cont.)

Figure	Page	
5.5	<p>Illustration of the gradient anisotropy. Darker shading indicates a higher cosmic ray density, n, and the gyration of cosmic rays around the interplanetary magnetic field \mathbf{B} leads to a net anisotropy directed along $\mathbf{B} \times \nabla n$. This can explain some changes in the DA that are associated with changes in the sign of \mathbf{B}, in which case this figure represents a Sunward view of near-Earth space. When superimposing the normal corotational anisotropy toward the right (along Earth's orbit), a southward gradient in the GCR density leads to (a) suppression or (b) enhancement of the diurnal anisotropy in toward (T) and away (A) magnetic sectors, respectively.</p>	108
5.6	<p>Reversed time plots for Carrington rotation (CR) 2070, from 2008 May 15 to June 12. From top: (a) Synoptic map of the solar corona as observed by the STEREO-A/EUVI imager in the Fe XII 195Å bandpass. The position of the HCS from a WSO synoptic chart is shown by a thick light gray line and the projected orbit of the Earth is indicated by gray crosses. Slanted lines show the correspondence with the reversed time axis of the lower plots. (b) Phase (time of maximum) of diurnal variation, in local time. The dashed line indicates the corotational anisotropy (1800 LT). (c) Diurnal anisotropy (DA). The dashed line is the observed average DA. (d) Hourly neutron count rate (thick line) and its running 1-day average (thin line). (e) Solar wind speed. (f) Magnitude of magnetic field. (g) Sunward magnetic field component. Shaded areas represent HSSs with speed $\geq 450 \text{ km s}^{-1}$. Note the enhanced DA lasting for 5 days starting near the onset of the HSS on day of year (DOY) 149, which we attribute to the slanted geometry of the HSS due to the combined effects of CH B and C. The enhanced DA in the HSS is consistent with the $\mathbf{B} \times \nabla n$ anisotropy for a southward cosmic ray gradient associated with the slanted geometry.</p>	112
5.7	<p>Same as Figure 5.6 for CR2071, from 2008 June 12 to July 9. Note the train of enhanced DA, indicated by an arrow, starting near onset of a HSS on day of year (DOY) 177, which we attribute to the slanted geome-</p>	

LIST OF FIGURES (cont.)

Figure	Page
try of the high speed solar wind stream (HSS) due to the combined effects of CHs B and C. The enhanced DA in (c) after the sharp decrease in cosmic ray intensity in (d) is consistent with the $\mathbf{B} \times \nabla n$ anisotropy for a southward gradient associated with the slanted geometry. While the local magnetic field reversed on day 183, the synoptic map (a) indicates that the boundary between toward and away sectors remained near Earth, in comparison with the large gyroradius of cosmic rays observed at Doi Inthanon, so a southward cosmic ray gradient can still contribute to enhanced DA.	113
5.8 Same as Figure 5.6 for CR2093, from 2010 February 4 to March 4. This is an example of a recurrent train of enhanced DA in 2010, in association with the away sector of the interplanetary magnetic field near Earth. A gradient anisotropy could explain this association, although the reason for a southward GCR gradient is not clear.	116
5.9 Same as Figure 5.6 for CR2064, from 2007 December 3 to December 29. An example of a non-recurrent train of enhanced DA in 2007, which is also associated with the away sector of the magnetic field and could also be explained by a gradient anisotropy.	118
5.10 The 27-day variations in GCR intensity and solar wind plasma parameters during late 2007. Vertical lines represent 27-day time periods.	120
5.11 Same as Figure 5.10, for the year 2008.	121
5.12 Same as Figure 5.10, for the year 2009.	122
5.13 Same as Figure 5.10, for the year 2010.	123
5.14 The 27-day variations in moving average of hourly GCR intensity and hourly solar wind speed. The grid lines represent a 27-day period.	124
5.15 Correlation of daily average of GCR intensity with solar wind speed.	125
5.16 The 27-day modulation of daily GCR intensity in this study. The thin line represents a 27-day moving average.	126
5.17 Amplitude of 27-day modulation of GCR intensity.	127

LIST OF FIGURES (cont.)

Figure	Page	
5.18	Synoptic maps of the solar corona from CR2063 to CR2103. The vertical green lines represent the positive polarity coronal holes and the vertical red lines represent the negative polarity coronal holes.	129
5.19	A CIR in 2007 characterized by 5-minute solar wind and magnetic field data. Thick lines represent the forward and the reverse waves of the CIR whereas dashed lines represent the stream interfaces between fast and slow streams.	132
5.20	A CIR in 2008 characterized by 5-minute solar wind and magnetic field data. Thick lines represent the forward and the reverse waves of the CIR whereas the dashed line represents the stream interface between fast and slow streams.	133
5.21	A CIR in 2009 characterized by 5-minute solar wind and magnetic field data. Thick lines represent the forward and the reverse waves of the CIR whereas the dashed line represents the stream interface between fast and slow streams.	134
5.22	A CIR in 2010 characterized by 5-minute solar wind and magnetic field data. Thick lines represent the forward and the reverse waves of the CIR whereas the dashed line represents the stream interface between fast and slow streams.	135
6.1	The radial components of convection and diffusion are usually balanced so the net streaming flux is near the corotational direction, from 1800 LT.	146
6.2	Changes in direction of the streaming flux of cosmic ray particles as produced by (a) enhanced convection or (b) enhanced diffusion. Usually the radial components are balanced so the net streaming flux is corotational.	147
6.3	Contribution to the streaming flux of cosmic ray particles produced by the particle gradient ($\mathbf{B} \times \nabla n$) anisotropy. Together with a steady corotational flux, the resultant flow direction may change in phase to a later hour in the T sector and an earlier hour in the A sector. Here the latitudinal	

LIST OF FIGURES (cont.)

Figure	Page
<p>gradient ∇n is considered to point to the south. Note the resultant anisotropy is enhanced in the A sector.</p>	148
<p>6.4 Contribution to streaming flux of cosmic ray particles produced by particle gradient $\mathbf{B} \times \nabla n$ anisotropy and the combination of convection and enhanced diffusion. The resultant flow direction is observed to be close to 1800 LT (to the right).</p>	150
<p>A.1 Diurnal variations over 27-day periods in 2007.</p>	184
<p>A.2 Diurnal variations over 27-day periods in 2008.</p>	185
<p>A.3 Diurnal variations over 27-day periods in 2009.</p>	186
<p>A.4 Diurnal variations over 27-day periods in 2010.</p>	187
<p>B.1 The Sun Centered Imaging Package (SCIP) of SECCHI includes the EUVI (Wülser et al. 2003).</p>	188
<p>B.2 EUVI telescope cross section (Wülser et al. 2003).</p>	189
<p>B.3 EUVI effective area (Wülser et al. 2003).</p>	190
<p>B.4 Loading of synoptic map image in IGOR Pro.</p>	191
<p>B.5 Loading of synoptic map image in IGOR Pro.</p>	191
<p>B.6 Resultant information and image of the synoptic map.</p>	192
<p>B.7 Changing scale of the synoptic map.</p>	193
<p>B.8 Computed manual ticks.</p>	193
<p>B.9 Image processing in Igor Pro.</p>	194
<p>B.10 Image contrast by User Drawn.</p>	195
<p>B.11 Image filter.</p>	195

CHAPTER I

INTRODUCTION

The purpose of this chapter is to provide descriptions of the thesis for a general reader who is interested in research on cosmic rays. The reader will need a sufficient background knowledge to understand the scientific processes that were carried out in this thesis for seeking answers of a complex nature. First of all, this thesis describes work done to determine the effects of solar wind structures corotating with the Sun on the 27-day variations in cosmic rays having a magnetic rigidity (momentum per unit charge) more than about 16.8 GV. Second, we will overview the current knowledge and understanding of cosmic ray particles as observed from ground- and space-based detectors. Third, we will state the nature of the problem that motivates and stimulates us to do the research, originating from our observations of secondary cosmic rays with a neutron monitor at Doi Inthanon. Solar wind stream structures that corotate with the Sun and their effects on variations in cosmic rays observed by ground-based detectors will be mentioned and reviewed. Then, we will summarize the approach toward a solution: the observational database and objectives of this study, from which the rest of the thesis will follow. The discipline of this study as it fits into the broader and complex world will be mentioned. Finally, an outline of the thesis will be provided for the reader to obtain a perspective view and interlink the ideas in each chapter.

1.1 Overview

In the real world, a type of particles called “cosmic rays” penetrates our body at a rate of several hundreds s^{-1} . What are they? Are they harmful to the human

race? To answer these questions we must know the basic properties of cosmic rays. The great discovery of cosmic rays was in 1912 when Victor Hess successfully made a manned balloon flight to measure ionization of the atmosphere. A rapidly increasing ionization with altitude revealed the first definite evidence that source of the ionizing radiation was in outer space instead of radioactivity on Earth. The radiation was later confirmed and named “cosmic rays” by Millikan in 1925. Therefore, cosmic rays are charged or sub-atomic particles such as protons carrying the momentum and energy along their paths. In addition, cosmic rays can be high energy photons such as x-rays and gamma-rays that individual photons can be measured. From observation and nuclear theory, a “primary cosmic ray” from space can collide with air molecules and produce ionization or “secondary cosmic rays” from nuclear disintegration.

The abundances and energies of cosmic rays have been observed from extensive experimental investigations using balloons and satellites. Cosmic rays consist of about 98% charged atomic nuclei and 2% electrons. For the nuclei, 87% are protons, 12% are helium, and 1% are heavy elements (Simpson 1983). It is customary to express the energy as particle kinetic energy, in units of electron volts (eV) or electron volts per nucleon (eV/n); observed cosmic ray energies range from more than 10^6 to less than 10^{20} eV/n. Since these particles have been accelerated to such high energies, they have been stripped of their orbital electrons to be completely ionized.

Why do we study cosmic rays? Cosmic rays are studied for scientific research and applications. One of the most basic questions about cosmic rays is, “What are their sources?” The primary cosmic rays in space are known to be produced by acceleration of ordinary matter in their source regions. Cosmic rays that originated from the Sun are called “solar energetic particles” (SEPs), while those that originated from extra-solar sources within our own Galaxy are called “Galactic cosmic rays” (GCRs). However, some cosmic rays have extremely high energies, indicating an extragalactic origin since the local galactic magnetic field could not contain particles with such high energies. SEPs are produced during solar storms, which are sudden events that convert



Figure 1.1: The aurora is caused by a flood of charged plasma racing away from disturbances on the Sun. (<http://www.public.iastate.edu/~sdk/fick2003/october.html>).

magnetic energy to other forms of energy. There are two types of solar storms. In solar flares, magnetic energy is converted mainly to heat energy, and in coronal mass ejections (CMEs), magnetic energy is converted mainly to plasma kinetic energy. Most SEP ions emerge from acceleration by CME-driven shock waves traveling through space. Both types of events usually occur during solar maximum when the sunspot number is high. In fact, the maximum energy of SEPs is typically 10-100 MeV/n, which is lower than the energies of GCRs, which have typical energies of 1 GeV/n to 10^{15} eV/n. GCRs are believed to originate from shock-wave acceleration in supernova explosions which are the last stage of evolution of massive stars. The explosion expels much or all of a star's material at a velocity of up to $30,000 \text{ km s}^{-1}$ (10% of the speed of light), driving a shock wave into the surrounding interstellar medium. This shock wave sweeps up an expanding shell of gas and dust called a "supernova remnant," such as the Crab Nebula. They are known to be a source of cosmic rays because of the radio synchrotron radiation emitted by cosmic ray electrons spiraling in the magnetic fields of the remnant and because of gamma rays characteristic of nuclear interactions (Mewaldt 1996).

Solar storms and the solar wind cause variations in cosmic rays and changes

in environmental conditions in near-Earth space called “space weather effects.” Geomagnetic storms are the most powerful space weather effects and are caused by the solar storms that produced SEPs. Space weather affects space systems through radiation damage due to penetration of high energy particles into the electronic components, and spacecraft charging due to discharges (sparks) of accumulated electrostatic charge on a non-conducting material on the spacecraft’s surface. The radiation is also harmful to humans who have worked in space for a long time and during a burst of energetic particles from the Sun. In our atmosphere, space weather causes very wonderful phenomena known as “aurora” as shown in Figure 1.1. The aurora is associated with the solar wind, a flow of ions continuously flowing outward from the Sun. The charged particles are captured by the magnetic field of the Earth, and come speeding in to the upper atmosphere. Collisions between these ions and atmospheric atoms and molecules cause energy releases in the form of auroras appearing in large ovals around the poles. The energy from these particles can cause the gas in the thin upper atmosphere to glow, producing colors that are characteristic of the composition of our atmosphere (mainly nitrogen and oxygen). Furthermore, space weather affects the ground systems such as radio communications and the Global Positioning System (GPS), because of disturbances in the ionosphere. All aircraft flying above 10 km altitude are exposed to a noticeable amount of radiation (Wikipedia). A large geomagnetic storm resulting from a CME at Earth can affect electric power grids at all latitudes (but mainly high latitudes) through a ground-induced current from magnetic induction (see, e.g., Siscoe 2000, Hapgood 2013). From these examples, we thus clearly see that cosmic rays are associated with many activities related to human life.

One of the most effective detectors that observes cosmic rays at Earth is a “neutron monitor.” (Other detectors are described in Section 2.1) A neutron monitor detects atmospheric neutron fluxes, which vary in proportional with the primary cosmic ray fluxes above the atmosphere. Note that the number of secondary neutrons depends on air pressure, which is approximately the weight of air above us per unit area. Since

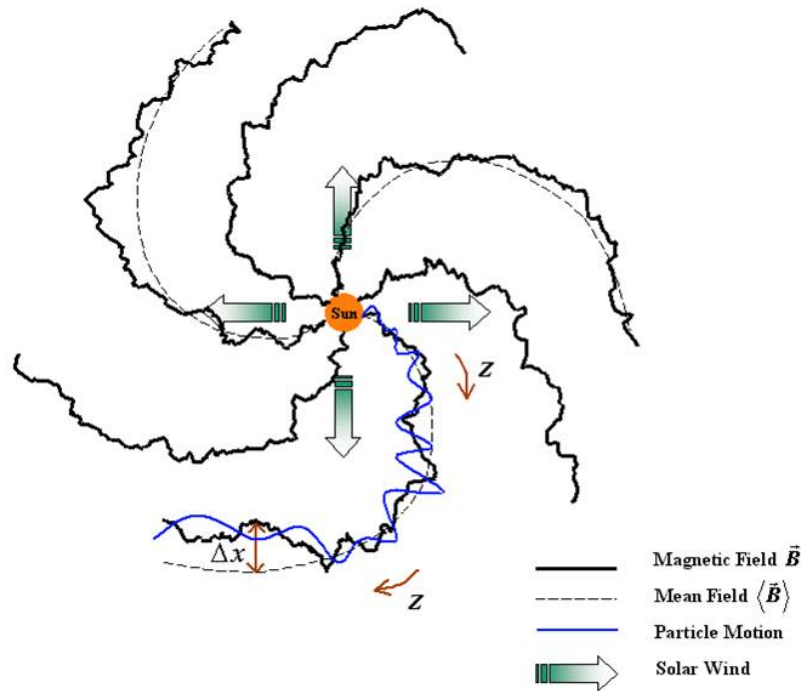


Figure 1.2: Archimedean spiral geometry of the interplanetary magnetic field.

such a detector monitors the flux of cosmic rays continuously, it can provide us with important information about space weather at Earth. In addition, understanding of the following four basic phenomena about cosmic ray fluxes at Earth is a consequence of the invention of neutron monitors (Bieber et al. 2000). First, strong variation (200-400%) of cosmic ray intensity between 0° and 60° geomagnetic latitude. Second, systematic variation of the cosmic ray intensity with the 11-year solar activity cycle and 22-year solar magnetic cycle, which was originally found in ion chamber data from the time period 1937-1952 by Forbush (1954). Third, correlation of recurrent modulation of cosmic ray intensity at Earth with the rotation of the Sun. Finally, from a solar flare event (1956 February 23), a sudden and short burst of relativistic nuclei which escaped only slowly through a continuous barrier region to the interstellar medium. This suggests that space in the solar system is dynamical. Consequently, Parker (1963) developed a quantitative theory for coronal expansion of the solar wind emanates radially from the Sun into interplanetary space. The magnetic field is frozen in the supersonic solar wind because the plasma in the solar wind has high conductivity. The interplanetary magnetic field

has an Archimedean spiral shape because of the solar rotation as shown in Figure 1.2.

In this work, we aim to study time variations in GCR intensity near the Earth as observed by a neutron monitor under the effect of local electromagnetic conditions in the Solar System. Initially, GCRs are nearly isotropically distributed in space since they travel diffusively around the galaxy for $\sim 10^7$ years before entering the solar system. Then GCRs enter the heliosphere which is a bubble of charged particles in the space surrounding the Solar System. The heliosphere distorts the energy spectrum and composition of the incoming cosmic rays through processes of solar modulation. Basically, the solar modulation of GCR intensity is the result of the attempt of GCRs to follow the Archimedean spiral field lines into the Sun when they suffer scattering due to magnetic irregularities in the solar wind. The typical time spent by a GCR in the solar system is rather short, because most of them are swept out of the solar system by the solar wind and its convected interplanetary magnetic field. This leads to the modulation of cosmic ray flux at energies below ~ 100 GeV. However, for those that reach Earth's orbit, the typical lifetime is of the order of a few months to a year (Parker, 1965). They hit the Earth at a rate of ~ 1000 events $\text{cm}^{-2} \text{s}^{-1}$. Given the density gradient, there must be an inward diffusive current in the solar system. This inward current is balanced by an outward convective sweeping as the scattering centers are carried by the solar wind. Moreover, in the solar wind reference frame these scattering centers are receding from each other. Because of that, a particle energy loss is also expected, which depletes the intensity in a differential momentum range (Quenby 1984).

Clear cyclical variations in time are evident in the observed GCR intensities. As will be described in Chapter 2, these GCR intensity variations are linked to the long-term variations such as the Sun's 11 year sunspot cycle and 22 year magnetic cycle. In addition, there are short-term variations in GCR intensity such as 27-day and diurnal (daily) variations which must be investigated in a smaller scale.

1.2 Nature of the problem

During a minimum period of the sunspot cycle (“solar minimum”), the largest structures that persist quasi-periodically in the heliosphere are corotating solar wind structures (CSWSs) that co-rotate with the Sun with a period of 27 days, and are three-dimensional structures in interplanetary space. The CSWSs are mainly composed of expanding “high-speed solar wind streams” (HSSs) with speeds of about $450\text{-}800\text{ km s}^{-1}$ from “coronal holes” (CHs), and the subsequent interaction of the HSSs with the slow-speed streams. First, to understand well about the HSSs their source has to be explained. Slow solar wind is mainly from regions with “streamers” (magnetic loops), which behave as obstacles that slow down the solar wind. In contrast, the CHs as shown in Figure 1.3 are large-scale regions of low-density plasma and open magnetic field lines where a particular CH has a unipolar polarity; the open field lines have a magnetic field pointed toward or away from the Sun. An HSS is usually associated with a CH, and the pattern of coronal magnetic fields is largely extended into interplanetary space as the expanding HSS carries frozen-in magnetic fields. Consequently, the global pattern of CHs and their magnetic polarity is mapped into a spatial structure of the interplanetary field that rotates with the Sun (e.g., Hundhausen et al. 1980) and gives rise to the pattern of alternating magnetic sectors (a sector being a region with a magnetic field mainly “toward” or “away” from the Sun) as observed in the ecliptic plane.

Large polar coronal holes predominate during much of the solar cycle, and they typically have the oppositely directed magnetic fields in different hemispheres. The CHs may migrate to low latitudes or even extend across the equator (Zirker 1977). In fact, even outside the CHs, the Sun can be divided into two regions with a preponderance of outward or inward magnetic field regions. However, the boundary is not exactly along the solar equator; instead, it is a wavy line that is sometimes south and sometimes north of the equator, changing with time. The solar magnetic field weakens with distance from the Sun, and after a few solar radii the solar wind ram pressure dominates

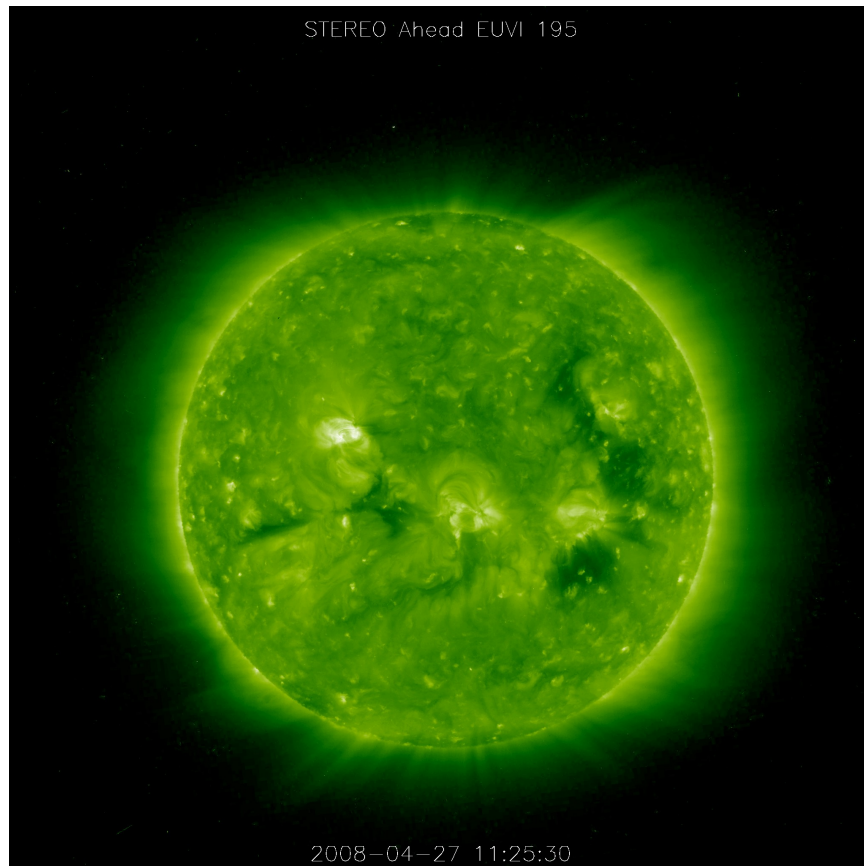


Figure 1.3: Coronal holes appear as darker areas when viewed in this extreme UV wavelength (195 Ångstroms). This large equatorial hole area from April 27, 2008 was one of the largest seen by STEREO (Ahead). Although they are usually located at the poles of the Sun, coronal holes can occur other places as well. The magnetic field lines in a coronal hole extend out into the solar wind rather than coming back down to the Sun's surface as many do in other parts of the Sun. They are often the source of high speed solar wind streams that carry solar plasma into space and possibly impact the Earth. (<http://stereo.gsfc.nasa.gov/gallery/>)

over the magnetic pressure. At this distance, magnetic loops have mostly curved back to the Sun, i.e., neighboring magnetic elements of opposite polarity have canceled out. The remaining magnetic fields bear the predominant polarity of the sector and the field lines are drawn outward with the solar wind. The flow from the northern and southern polarity regions thus divides the hemisphere into two sectors of opposite magnetic polarity, separated by a wavy current (or neutral) sheet. The current sheet continues into interplanetary space as the magnetic field lines are drawn out by the solar wind, and is called the “heliospheric current sheet” (HCS).

The curvature of spiral magnetic field lines (see Figure 1.2) depends mainly on the solar wind speed, with less curvature for a faster solar wind. The interaction between an HSS (with straighter field lines) and upstream slow solar wind ahead of it (normally confined to the vicinity of the HCS) with less than about 400 km s^{-1} and more strongly curved field lines produces a “corotating interaction region” (CIR) at the leading edge of the HSS where the solar wind plasma density and magnetic field are increased by the compressive interaction. Between the two streams there is a stream interface since the magnetic field lines cannot be merged. Magnetic sector boundaries are often found close to the stream interfaces at 1 AU, but they do not physically relate to each other (Schwenn 2006). A CIR appears as a band located around the solar equator in the form of a tilted shell, depending on both heliolatitude and heliolongitude (Gosling and Pizzo 1999). At times near activity minimum CIRs could be observed at latitudes up to 40° as identified in plasma parameters by Ulysses at 4 AU. The current sheet lies in the same sense as the solar magnetic equator but is displaced northward or southward and moves throughout the solar cycle.

When a CIR passes the Earth, an observer can see also a sharp increase in solar wind speed followed by a slow decrease until a new CIR arrives. The CIR appears to be corotating with the Sun since the CH-HSS structure is usually stable for more than one solar rotation. Moreover, with increasing distance from the Sun to 2-5 AU, the compression waves at the CIRs steepen to form corotating shock waves (see Gosling 1976), which sometimes even occurs at 1 AU. Wood et al. (2010) found, from a case study of a CIR event on 2008 January 31, constructing the CIR’s 3-D morphology, that a CIR can be created by HSSs emanating from low latitudes that run into surrounding streamers. The size of the CIR was roughly the same as the duration of the observed density pulse. Since CIRs are inclined relative to the radial direction, the forward and reverse waves bounding the CIRs have both radial and azimuthal components of propagation. The configuration of the HCS and the streamer belt near the Sun thus play a crucial role in the eventual development of CIRs. Since these HSSs and CIRs are predominant and

quasi-periodic, and manifest large-scale structures in interplanetary space, they could contribute significant solar effects to temporal and spatial variations of GCRs in the inner heliosphere.

The 27-day variations of GCRs associated with the CSWSs have been observed and studied for a long time. Most of the studies were based on the long-term variations of GCRs in solar cycles. Some have concentrated on short-term variations of GCRs in a solar rotation (Okazaki et al. 2008). GCRs are affected by the structures since they act as barriers that inhibit the entrance of GCRs from the outer heliosphere. The count rate is reduced temporarily (modulated) followed by a recovery phase in the trailing portion of the HSS. CIRs affect the short-term cosmic ray variations that are driven by CSWSs via the change of particle diffusion properties in local interplanetary space at low and middle latitudes (Chih and Lee 1986, Kóta and Jokipii 1991). GCRs are thus affected by these structures in terms of remarkable quasi-periodic 27-day variations that could be clearly noticed in neutron monitor count rates.

Diurnal anisotropy (DA) is the anisotropy component of GCRs along the equatorial plane. It can be observed by a ground-based detector as a diurnal (daily) variation along with Earth's rotation. If the magnetic field is along the ecliptic plane, an ecliptic-viewing neutron monitor makes a complete measurement of the cosmic ray pitch-angle distribution once every 24 hours, where the pitch angle is defined as the angle between the asymptotic direction of the cosmic ray detector and the interplanetary magnetic field. Cosmic rays of energies up to ~ 100 GeV are affected by the Sun and the interplanetary magnetic field, which introduces an energy-dependent anisotropy (Rao 1972). Then the anisotropic flow of cosmic rays is clearly manifested as a diurnal variation of the counting rates of neutrons or other secondary particles at ground level. The average DA vector has been explained as a consequence of the equilibrium established between the radial convection of the cosmic ray particles by solar wind and the inward diffusion of GCR particles along the interplanetary magnetic fields (see Rao 1972; Forman and Gleeson 1975). In a reference frame corotating with the Sun, convec-

tion and parallel diffusion (i.e., diffusion parallel to the large-scale magnetic field) can nearly cancel and the GCR distribution has almost no net flow. Then in Earth's reference frame, there is a net flow as the corotating GCR distribution impinges on Earth from the dusk sector. The corotating streaming is observed as an average corotational anisotropy along the direction of the Earth's orbit, a flow from the direction of 1800 h local time.

Diurnal variations of GCRs have also been observed to be affected by HSSs and CIRs with the 27-day period of solar rotation. However, the causes of the 27-day variations observed in the DA are not yet completely understood. The 27-day variation is maximal for the component of the solar diurnal vector perpendicular to the interplanetary magnetic field (Parker spiral) rather than that parallel to it (Duggal et al. 1979; Owens et al. 1980). Tolba et al. (1981) suggested that the observed solar rotational periodicity of DA could arise from gradient drifts of particles.

However, there are discrepancies in observations of the secondary cosmic rays when the HSS passed the Earth. According to Iucci et al. (1983), the average amplitudes of diurnal and semi-diurnal anisotropies are found to be larger than normal during the initial phase of the stream but smaller than normal during the decreasing phase of the stream, and the phase is observed to remain almost constant around 1800 LT. However, Munakata et al. (2003) used 17 neutron monitors and 17 components of the Nagoya muon telescope, with median rigidities between ~ 10 GV and ~ 120 GV. They again found amplitudes to be enhanced during the period of the decline of the HSS, which was observed by neutron monitors rather than muon detectors, and considered that this might be associated with the recovery of the cosmic ray intensity variations and that the convection-diffusion model may provide a plausible explanation. Ananth et al. (1995) found that the direction of the DA of enhanced wave trains lies along 1800 LT and the power-law index of the cosmic ray spectrum ("spectral index") is higher than for the suppressed wave trains. Studies of enhanced wave trains associated with the interaction region (Klein and Burlaga 1982) have shown that the diurnal amplitudes

are very large, and the phase shifts towards the earlier hours. Mishra and Mishra (2005) have studied the high-amplitude anisotropic wave train events in 1991-1994 and found that the phase of diurnal variations for the majority of the events shifted towards later hours, whereas it remains in the corotational direction for some events. Mavromichalaki (1989) investigated neutron monitor data of 1970-1977 and found that the phase shifted towards earlier hours and may follow in time the variation of the size of the polar coronal holes. This is in agreement with the drift motions of cosmic ray particles in the IMF. By investigating the differences in the areas of the solar polar coronal holes and their relationship to the cosmic ray intensity as measured by neutron monitors (Thule and McMurdo), the hemisphere having larger areas of CHs inhibits the cosmic ray intensity more than the opposite hemisphere (Agrawal et al. 1978, 1980). The authors attribute this to convective removal of cosmic rays produced by the higher-speed solar wind streams associated with the larger-area CH. According to Singh et al. (2010), HSSs did not play any significant role in causing high- and low-amplitude wave train events and the phase did not shift to earlier hours, but the diurnal amplitudes decreased during the solar activity minima in 2008. In summary, in some events an equilibrium between the radial convection and field-aligned diffusion of cosmic ray particles is found to be inadequate to explain the large amplitude variability of DA and phase observed on a day-to-day basis. Hence, effects of the CSWSs on the 27-day period in diurnal variation still pose an open question and causes of the effects must be clarified.

1.3 Approach toward a solution

1.3.1 Observational databases

Cosmic ray data in this study were obtained from the Princess Sirindhorn Neutron Monitor (PSNM). The PSNM is the first neutron monitor in Thailand, located at the summit of Doi Inthanon, Thailand's highest mountain at an altitude of 2,560 m, 18.59° N, and 98.49° E. With a standard NM-64 design, PSNM should be useful for as

long as a decade with minimal maintenance. The vertical cutoff rigidity (momentum per charge) of 16.8 GV is the highest for any fixed neutron monitor station in the world. Furthermore, the count rate at Doi Inthanon is about 6 times higher than at sea level.

We complementarily utilized the 5-minute and 1-h averaged data of interplanetary plasma from the MAG and SWEPAM instruments of the Advanced Composition Explorer (ACE: see <http://www.srl.caltech.edu/ACE/ASC/level2/index.html>) and from the OMNIWeb site (<http://omniweb.gsfc.nasa.gov/>).

The evolution and features of the CHs are characterized by utilizing Fe XII 195 Å synoptic maps for each Carrington Rotation (CR) from the Extreme Ultraviolet Imager (EUVI) (Howard et al. 2008) of the Sun Earth Connection Coronal and Heliospheric Investigation (SECCHI) (Kaiser et al. 2008) on the Solar TERrestrial RELations Observatory (STEREO) spacecraft.

1.3.2 Objectives

The objectives of this study are

1. To characterize the effect of the corotating solar wind structures on the galactic cosmic ray intensity.
2. To characterize the effect of the corotating solar wind structures on the diurnal variations.
3. To synthesize existing and/or new concepts to explain such effects.

In the present work, the purpose is to characterize effects of CSWSs on the intensity and diurnal variations in GCRs with a 27-day period, the 27-day modulation of GCR intensity, and to explain causes of the effects by reasonable concepts. We will present the neutron count rates observed by the Princess Sirindhorn Neutron Monitor at Doi Inthanon during the recent solar minimum of the 23rd solar cycle. Then we have characterized the plasma and solar wind parameters of CIRs and HSSs, as well as coronal holes that affect these short-term variations in GCR intensity and anisotropy. The neutron count rates have been studied by harmonic analysis for the DA. The DA

exhibits very different behavior from one HSS to another, as will be shown. For short-term variations of GCRs, we are the first to find the cause of the recurrent short-term variations in GCRs as observed as trains of enhanced DA during the recent solar minimum. In the light of the current theory, we present examples in which diurnal variations are enhanced or suppressed according to the $\mathbf{B} \times \nabla n$ anisotropy, especially for a latitudinal gradient associated with a particular type of coronal hole morphology. In addition to the diurnal variations, the 27-day modulations of GCRs intensity are well correlated with the magnetic fields and solar wind speed as predicted by the solar modulation theory of GCRs.

The benefits of this work are understanding the nature of the short-term variation of GCRs in the inner heliosphere by the CIRs and HSSs from the Sun, testing the validity of the transport theory of solar modulation of GCRs, and integrating the results for long-term variation of GCRs in the solar cycles. To study the short-term variations of 27 days in the GCR intensity and anisotropy in the minimum epoch of solar activity is very useful. First, it provides a crucial source of information about how the large-scale corotating solar wind structures from the Sun affect the GCRs throughout the minimum epoch of solar activity, when the disturbances in interplanetary space are minimal and the polarity of the Sun's global magnetic field is well established. Second, CIRs and HSSs in association with the 27-day variations can cause geomagnetic storms near Earth. This space weather can damage satellites and effectively influence the missions of astronauts. For the 27-day solar modulation of GCRs, the depression of GCRs might relate to the variations of physical parameters of the CSWSs in some aspects. Fortunately, the 27-day variations of GCRs in a local scale might correlate to the long-term variation of GCRs through an accumulation effects of the CSWSs.

1.4 Outline of the thesis

This thesis consists of seven chapters and three appendices. Apart from this first chapter of introduction, Chapter 2 gives the fundamental and relevant background knowledge for this study. Chapter 3 describes information, detection and energy response of the Princess Sirindhorn Neutron Monitor at Doi Inthanon. Then, Chapter 4 focuses on data processing and quality control of the nucleonic data obtained from PSNM count rates and data analysis of spacecraft data. Harmonic analysis of neutron count rates for GCR DA will be described. Chapter 5 shows the results of the DA and 27-day variations in GCR intensity from the analysis of PSNM data sets. The corotating solar wind structures characterized by the spacecraft data sets are also shown. Chapter 6 provides a discussion of the objectives of the study in the context of the theory of cosmic ray solar modulation. Chapter 7 describes the conclusions and suggests further work. Finally, three Appendices include the 27-day variations in neutron count rates at Doi Inthanon, the principles of EUVI on STEREO and image processing of STEREO/EUVI synoptic maps, and derivation of rigidity in relativistic form.

CHAPTER II

BACKGROUND KNOWLEDGE

This Chapter deals with basic knowledge that is crucial for understanding this study. Indeed, the study is focused to explain effects of corotating solar wind structures on 27-day variations in Galactic cosmic rays (GCRs) observed by a ground-based neutron monitor. Therefore, we would like to include the history as well as contemporary knowledge and research mainly based on this topic to discuss the original studies, sources, scientific methods, and so on for understanding the subsequent sections. First, we will introduce the history of cosmic ray observations and basic properties of GCRs observed at Earth. We intend to address the lower energy part of GCRs over the energy range from some tens of MeV to some tens or hundreds of GeV. Second, the basic history of the neutron monitor, the main instrument of this study, and measurement principles of cosmic rays will be narrated and reviewed. Next, we will turn back to the Sun to describe the physical parameters and structures of the solar wind and magnetic field from the Sun to interplanetary space. The unsteady conditions in the solar photosphere and corona lead to a dynamical solar wind, which has a frozen-in magnetic field in interplanetary space. However, spatial and temporal variations of the solar wind from the Sun with the solar activity cycle lead to variations in the heliospheric current sheet, that contribute to the long-term variation of GCRs. Then, we will explain how various kinds of physical processes affect the GCR flux in the sense of solar modulation and anisotropy of GCRs conceptually and theoretically. These physical effects can be combined to yield a transport equation. Finally, we will describe the features and effects of corotating solar wind structures on the 27-day cosmic ray intensity variations near Earth. In short, the sequential study of cosmic rays from the past until the present

day is described in order to understand cosmic rays near Earth: the solar modulation of GCRs, the transport of cosmic rays in the heliosphere, and short- and long-term and especially recurrent variations of GCRs.

2.1 Galactic cosmic rays at Earth

2.1.1 General

Observations of Galactic cosmic rays (GCRs) at Earth provide valuable data on the composition, the origin, and the propagation of cosmic rays in space. GCRs are ionized nuclei originating outside the solar system with energies above ~ 100 MeV/nucleon extending up to 10^{18} eV. The sources of GCRs are within the Milky Way Galaxy, and the most effective sources should be supernova remnants (from explosions of massive stars in the last stage of evolution) that accelerate ordinary matter to produce high energy nuclei by a shock acceleration process. As a result, most GCRs are a young sample of matter (within 10 million years or so). Their composition and energy spectrum help us to understand the origins of matter. In addition, GCRs are nearly uniformly and isotropically incident upon the heliosphere. When GCRs reach and then hit Earth, the hitting rate is about $1000 \text{ (m}^{-2}\text{s}^{-1}\text{)}$. In near-Earth space, like solar particles, GCRs travel mostly parallel to the magnetic field and are scattered by the magnetic field irregularities and subject to convection and adiabatic energy loss according to the highly variable solar wind speed and drifts in the large-scale heliospheric magnetic field through interplanetary space. Consequently, the GCR intensity is expected to possess both spatial and temporal dependence. The variability of the solar wind and interplanetary magnetic field is responsible for the temporal variation at fixed positions, whereas spatial gradients in GCR intensity and temporal variations are responsible for differences seen by observers at different positions.

GCRs were discovered in 1912 when Victor Hess flew an ionization detector on a balloon up to an altitude of 5 km. Interestingly, the GCR flux increased with

altitude, implying that they originate outside the Earth (from extraterrestrial sources). At that time he called the penetrating radiation from the outside by the German word “Höhenstrahlung,” which means radiation from above (Bartusiak 2006). In 1927, Clay was the first to report a latitudinal effect; close to the equator, the radiation was less intense than at higher latitudes. When Størmer’s calculations of particle trajectories in the geomagnetic field became available in 1930, the latitudinal effect could be understood as due to shielding by the geomagnetic field. The next cornerstone in cosmic ray research was the discovery of cosmic ray intensity was maximal at an altitude of about 15 km by Pfozter in 1936 (in Kallenrode’s manuscript). This results from the interaction between GCRs and atmospheric atoms that is now called “atmospheric cascade”. In 1937, Forbush observed a world-wide decrease in GCRs during a strong magnetic storm (a Forbush decrease), showing the first evidence for a relation between solar activity and GCRs. Since then, GCR energy spectra, composition and temporal variations have been recorded and studied by ionization chambers, neutron monitors, spacecraft, and so on.

2.1.2 Atmospheric cascades

Since the nucleonic component of the shower exhibits the largest variation with geomagnetic latitude (Simpson 1951), we particularly need to know the properties of this component in the atmosphere. The atmospheric cascade starts with primary particles, which are mostly protons, with rigidity (momentum per charge) more than 1 GV for the atmospheric cutoff to create a shower that reaches ground level. They then collide with air nuclei to yield secondary high energy mesons, nucleons, electrons, and photons. These secondary particles are cascades or chains composed predominantly of nucleons. As the cascade degenerates in total energy the composition of the cascade becomes almost entirely nucleons of $< 1 \text{ GeV nucleon}^{-1}$. The degradation of nucleon energy continues through collision and capture processes, which generate nuclear disintegration at ground level (Figure 2.1). The development of the nucleonic cascade grows and is then attenuated with increasing atmospheric depth x . The atmospheric depth is

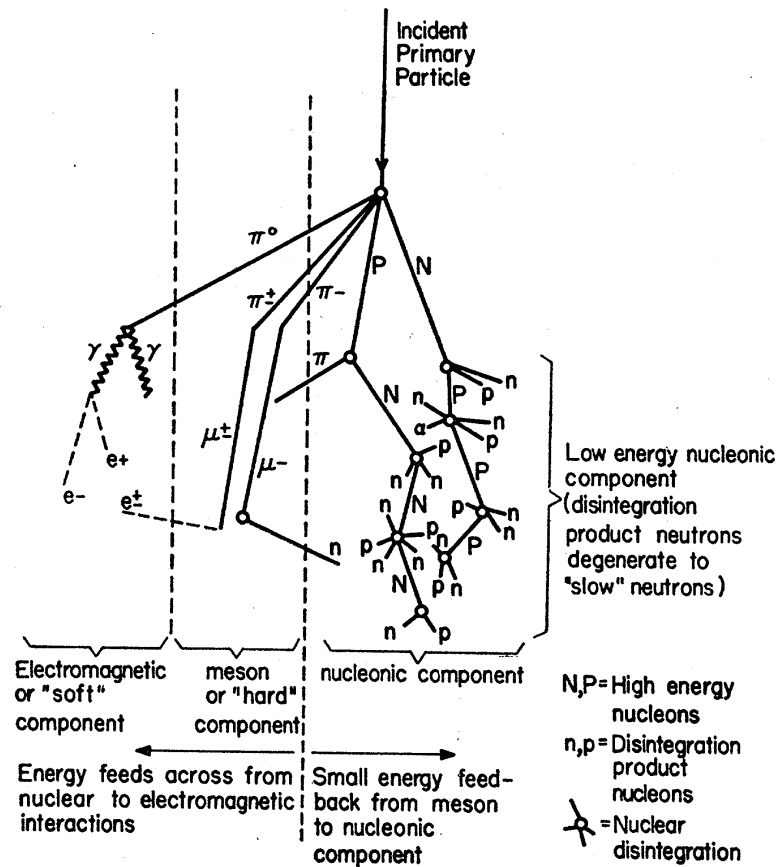


Figure 2.1: Schematic representation of the typical development of the secondary cosmic radiation within the atmosphere arising from an incident primary particle (Simpson et al., 1953).

the mass thickness of the air above a given altitude, measured in g cm^{-2} , approximately proportional to the air pressure at that point, and decreases approximately exponentially as altitude increases. The nucleon flux is simultaneously reduced by the atmospheric absorption. There are atmospheric depths sufficient for the nucleon flux and disintegration production to be in equilibrium at $x > 200 \text{ g cm}^{-2}$, where the nucleon flux varies as the exponential law $I = I_0 e^{-x/L}$ where L is the air absorption mean free path of the nucleon-producing radiation. Each nuclear disintegration yields on average several protons and neutrons having energies in the range $\sim 1 - 20 \text{ MeV}$ which are called "disintegration product nucleons." Meanwhile, the protons rapidly lose energy by ionizing the atmosphere, and the neutrons are reduced in energy by collisions with nitrogen and oxygen of the air to become slow neutrons (Bethe et al. 1940).

According to Simpson (1951), the energy ranges of neutrons in the atmosphere vary according to the kind of nuclear interaction by which they are produced. They may be classified as high energy neutrons, fast neutrons, or slow neutrons. High energy neutrons come from nucleon-nucleon or exchange interactions and may have initial energies extending from primary particle energies (~ 1 GeV or higher) down to the order of 40 MeV. The fast neutrons or disintegration product neutrons with initial energies of the order 2-30 MeV come from nucleon-nucleus collisions and photon, pion, or muon nuclear capture as indicated in Figure 2.1. Most neutrons at about 2 MeV come from the nuclear evaporation process from excited nuclei. After the fast neutrons are moderated in the atmosphere by elastic and inelastic collisions, mainly with nitrogen and oxygen nuclei, to have energies ~ 1 eV or less, they will be called slow neutrons. Many slow neutrons are eventually captured by the $^{14}\text{N}(n,p)^{14}\text{C}$ reaction or by other inelastic events.

When considering the disintegration product nucleons in the atmosphere, most of them are fast and slow neutrons. For example, they are produced from nuclear disintegrations induced by γ , π , or μ particles. However, the nucleon-induced disintegrations have large cross sections thus yield more than one neutron per disintegration. It is more convenient, reliable, and precise to use neutron detectors rather than the ionization from nuclear disintegration to measure the properties and temporal intensity changes of this low energy component (Simpson et al. 1953). In addition, the neutron component most closely fulfills the condition for studying low energy primary intensity variations as well.

The nature of nuclear interactions induced by primary and secondary cosmic rays in the atmosphere is important when designing a ground-based detector for monitoring the primary cosmic ray flux (Stoker et al. 2000). Ionization chambers and muon detectors record the ionizing and hard components of secondary cosmic rays, respectively. However, after the discovery of Simpson (1948) that the latitude variation of the intensity of evaporation neutrons is several times larger than that of either the ionizing

or hard component even at sea level, neutron monitors are preferred for a continuous record of cosmic ray primary intensity, as will be described in Section 2.2.

2.1.3 Energy spectra and modulation with the solar cycle

A fundamental cosmic ray measurement is the energy spectrum at Earth. In fact, the energy spectrum spans a very wide range of energies. Figure 2.2 shows the quiet-time spectra of cosmic ray hydrogen, helium, carbon and iron nuclei as a function of the kinetic energy per nucleon. The energy spectra are well represented by power-law energy distributions at energies more than 1 GeV per nucleon. The power-law spectra can be expressed as

$$N(E)dE = KE^{-\gamma}dE \quad (2.1)$$

The energy E is expressed in terms of the kinetic energy per nucleon. The index γ lies in the range 2.5 to 2.7. The GCRs start at energies of some tens of MeV per nucleon. For GCRs with energies more than that, the spectrum has a positive slope until some hundreds of MeV per nucleon. However, the energy spectra of all species possess a pronounced attenuation relative to the power-law at low energies less than about 10 GeV per nucleon. This feature is known as “solar modulation” associated with the outflow of the solar wind in the opposite direction to cosmic rays diffusing in toward the Earth. These spectra are thus strongly influenced by modulation within the solar system.

Furthermore, the feature shows a strong dependence on solar activity with a maximum intensity of cosmic rays occur during solar minimum and vice versa as seen in Figure 2.3. In other words, the lowest intensity is observed at the highest activity and vice versa. With increasing solar activity, the maximum of the GCR energy spectrum shifts towards higher energies because of stronger adiabatic deceleration. The greater the solar activity, the greater the disturbance in the interplanetary magnetic field preventing the propagation of particles with energies less than about 1 GeV per nucleon to the Earth. We will take up the topic of solar modulation of GCRs in more detail in Section 2.4. The

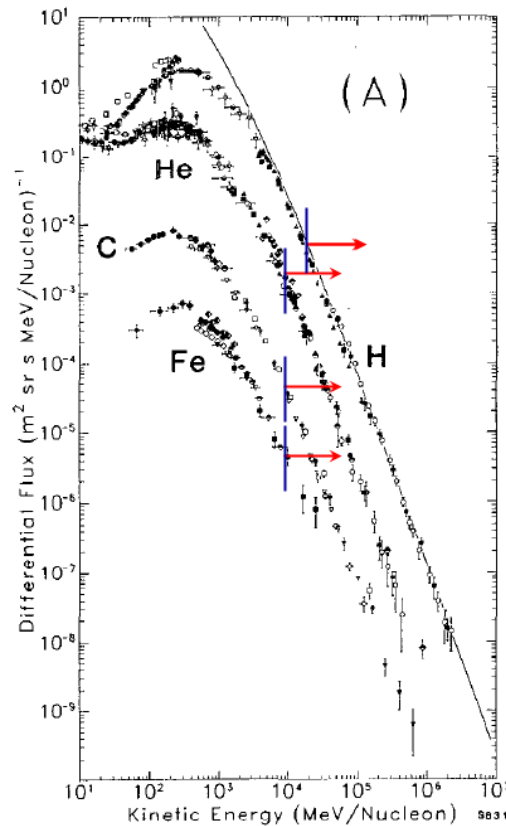


Figure 2.2: The differential energy spectra of cosmic rays from observations made from above the Earth's atmosphere. The spectra for hydrogen, helium, carbon and iron are shown. The solid line represents the unmodulated spectrum for hydrogen in interstellar space. The flux of helium nuclei below about $60 \text{ MeV nucleon}^{-1}$ is due to an additional flux of the anomalous ^4He component. (From Simpson (1983)). The arrows indicate the ranges of kinetic energies for each species corresponding to the vertical cutoff rigidity of 16.8 GV at Doi Inthanon.

energy/rigidity dependence of the solar modulation can also be seen when comparing neutron monitor count rates at different cutoff rigidities. In short, the present picture is that the galactic flux is distorted as it propagates inward through the outer parts of the heliosphere to the Earth.

There are significant differences between the energy spectra of different elements. Some elements have energy spectra similar to iron, for example, nickel and carbon, but others such as boron, titanium, vanadium and potassium show significantly steeper spectra. Consequently, cosmic rays can be divided into two types; primary

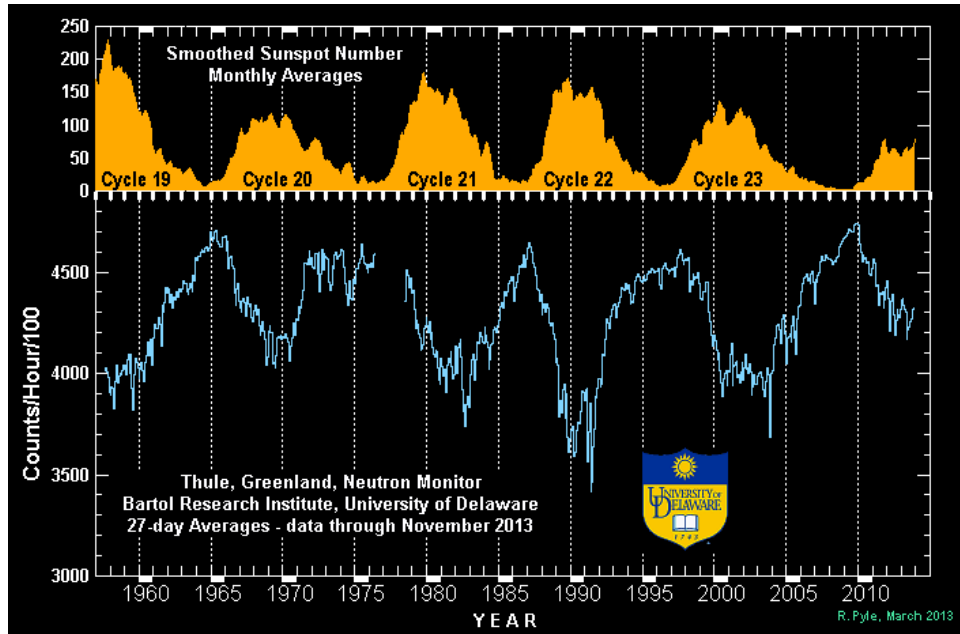


Figure 2.3: Modulation of cosmic ray flux with the solar activity cycles (<http://neutromm.bartol.udel.edu>). As solar activity rises (top panel), the count rate recorded by a neutron monitor in Thule, Greenland decreases (bottom panel).

elements such as iron are accelerated in large abundances in the sources such as supernova, and secondary elements such as boron are created by nuclear interactions of these species with the nuclei of atoms and molecules of the interstellar gas - this process is called “spallation.”

2.1.4 Abundances of the elements

The cosmic ray flux that arriving at the top of the atmosphere has a composition characterized by the numbers of different types. Extensive experimental investigations using balloons and satellites showed that the cosmic ray flux is composed of about 98% protons and nuclei whilst about 2% are electrons (Simpson 1983). Of the protons and nuclei, about 87% are protons, 12% are helium and the remaining 1% are heavier nuclei.

The chemical abundances of the cosmic rays provide important clues to their origin and to the process of propagation from their sources to the Earth. The solar system abundances of the elements are inferred from observations of the photosphere of

the Sun and meteoritic samples. That is, one observes absorption lines due to resonant absorption by ions, atoms and molecules in the Sun's photosphere. Meteorites are useful because they have experienced little fractionation and other geophysical phenomena and are believed to have chemical abundances similar to that of the primitive solar nebula. Alternatively, estimated chemical abundances in the interstellar gas, from the distribution of elemental abundances in the cosmic rays found at the top of Earth's atmosphere, are not so different from those of the solar system. Some of the differences are light elements such as lithium, beryllium, and boron are overabundant in the cosmic rays, as are the elements with atomic numbers between about calcium and iron, which can be accounted for qualitatively as a result of spallation products of the primary elements C, N, and Fe (Longair 1992). Such products should indeed result from spallation because they do not appear as end products of stellar nucleosynthesis. In short, the cosmic ray particles must have been accelerated from material of similar chemical composition to the solar system, which formed from interstellar material. Measurements of the elemental abundances of primary nuclei, He through Ni, at solar maximum and minimum show close agreement as illustrated in Figure 2.4. These measurements were made using satellites at very different modulation levels. Only ^1H and ^4He are found with high abundances in the interstellar medium. They are a result of the Hot Big Bang model in which about 24% helium by mass is synthesized for a wide range of reasonable initial conditions. This corresponds to a hydrogen-to-helium ratio ($^1\text{H}/^4\text{He}$) by number of about $1/0.08=12.5$. However, ^1H and ^4He in cosmic rays are depleted compared with the heavy elements due to the high ionization potential of H and He. Moreover, the ratio is sensitive to the effects of source spectral differences, acceleration, propagation, and solar modulation. A $^1\text{H}/^4\text{He}$ ratio of 21 ± 3 was derived from a power-law spectral fit to data for 50 GeV/nucleon (Simpson 1983).

It may be the case that about 10% of GCR above 1 GV (e.g., causing atmospheric showers) are ^4He because ^4He suffer more modulation at a few GV. However, above 20 GV (e.g., for Doi Inthanon) the ratio of $^1\text{H}/^4\text{He}$ is about 5.3 (where the ^4He

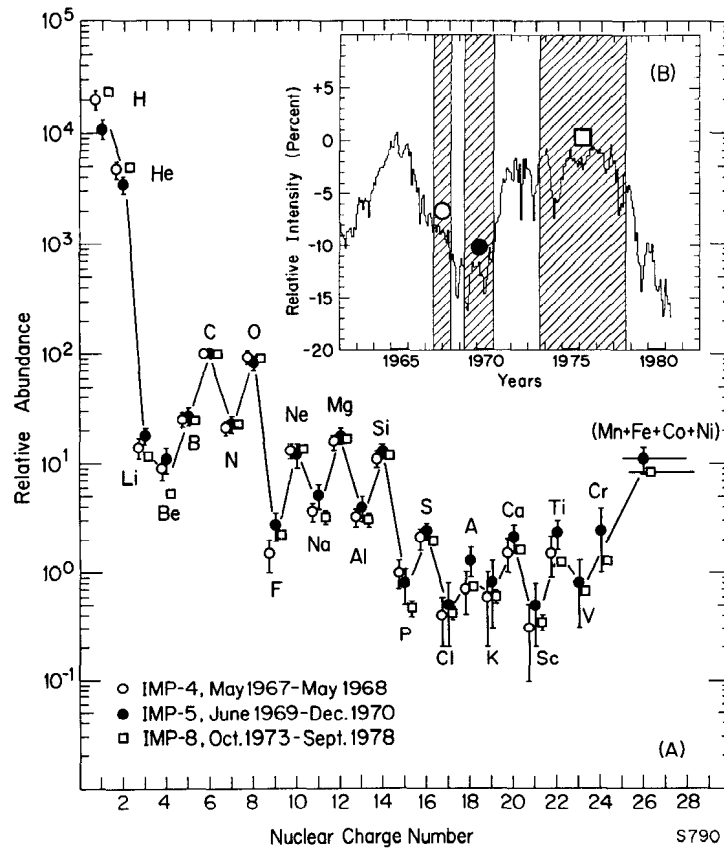


Figure 2.4: (a) The relative abundances of cosmic ray elements measured by University of Chicago instruments during the different phases of the solar cycle: solar maximum (open and closed circle); solar minimum condition (squares). (b) The climax NM intensity of ≥ 3 GeV/nucleon for 1962-1981 which is the corresponded to (a)(From Simpson (1983)).

and ^1H spectra are shifted to match at high rigidity). Neglecting minor ions, this corresponds to ^4He being about 16% of cosmic rays by number or about 43% by mass or by number of nucleons.

2.2 Neutron monitor measurements

2.2.1 History

After discoveries by independent experiments, in the late 1930s and immediately after World War II, that the cosmic ray radiation reaching the top of Earth's atmosphere is produced by nuclear interactions deep in the atmosphere, the knowledge of cosmic rays was developed rapidly. By 1946, it was accepted that energetic nuclear

disintegration product protons and neutrons in the atmosphere can produce further nucleons by successively lower energy nuclear disintegrations. As a result, a nuclear cascade or secondary nucleonic component is formed. In the same year, an investigation of the dependence of the nucleonic cascade on the incident primary cosmic ray energy was performed, but the dependence was not known. Alternatively, in 1948 Simpson used the geomagnetic field cut-off effects as a function of latitude for the analysis and found that the nucleonic component cascade in the atmosphere has a large geomagnetic latitude dependence. Therefore, the neutron monitor was pioneered by John A. Simpson in 1948, opening the chance of measuring intensity variations in the cosmic ray flux down to 1-2 GeV nucleon⁻¹ using the nuclear cascade for the first time. A fully detailed history of the neutron monitor and its development was provided by Simpson (2000).

During the development of the neutron monitor in 1948-1951 the early applications were mainly in two topics: First, to prove that the origin of variations of galactic cosmic rays, the Forbush decreases and the 27-day recurring intensity variations, is solar. The experimental results obtained in 1949-1951 showed that the latitude curves display intensity variations up to ~ 100 GeV so that the origin of the intensity changes was inferred to be beyond the range of the geomagnetic field. As a consequence, since the cosmic ray intensity from the outer heliosphere must be constant over long periods of time, the origin of the Forbush decreases and 27-day recurrent variations is in interplanetary space and controlled by the Sun, a process that was called solar modulation in 1952. Second, to provide the evidence for a dynamical heliosphere. There were balloon flights to measure the absorption of the solar flare particles generating atmospheric cascades in 1956. A solar flare event with proton energies extending beyond ≈ 20 GeV was recorded by a neutron monitor network on 1956 February 23. The transport of relativistic nuclei from the solar event was slow, which was attributed to scattering backward and diffusion through a continuous barrier region of irregular magnetic fields beyond Earth that totally enclosed the solar system (Meyer et al. 1956). The investigation provided the first experimental evidence for a dynamical heliosphere. For these reasons, the neutron

monitor provides us understanding about the cosmic ray variations and the nature of the heliosphere.

With the launch of the IMP 6 spacecraft in 1971, followed by a number of other spacecraft to monitor low and medium energy cosmic rays on a continuous basis, integrated studies have been carried out using both neutron monitor and space observations (Bieber et al. 2000). Nowadays, two means of GCR observation are basically ground-based observations by a world-wide network of neutron monitors, and satellite observations. In this study we focus on neutron monitors that provide information at rather higher energies than spacecraft.

2.2.2 Designs and principles of neutron monitors

A neutron monitor is one of the most effective detectors that provides us information on temporal and spatial variations and processes in interplanetary space. For example, the correlation of recurrent modulation of cosmic ray intensity at Earth with the rotation of the Sun (e.g., Simpson et al. 1953; Simpson 1954; more recently reviewed by Simpson (1998)) is a consequence of the abilities of the neutron monitor.

The neutron monitor is used to continuously detect nucleonic components in the secondary cosmic rays, which are mainly fast neutrons as described in Section 2.1.2. This apparatus is appropriate for observing the primary cosmic ray flux in the energy range between 10^9 and 10^{11} eV, and is useful to detect the cosmic ray particles of energy less than 10^{10} eV such as solar cosmic rays. Even though the high energy disintegration-produced nucleon flux is peaked in the vertical direction (vertical incidence) within the atmosphere, the disintegration product neutrons are emitted almost isotropically from nuclei and scattered nucleons. Therefore, an omni-directional detector such as a neutron monitor measures the neutrons and protons produced within a small volume of the atmosphere surrounding the detector (Simpson et al. 1953).

Initially, the neutron monitor was developed from BF_3 (boron trifluoride) gas proportional counters enriched in the isotope ^{10}B since the counter subsequently

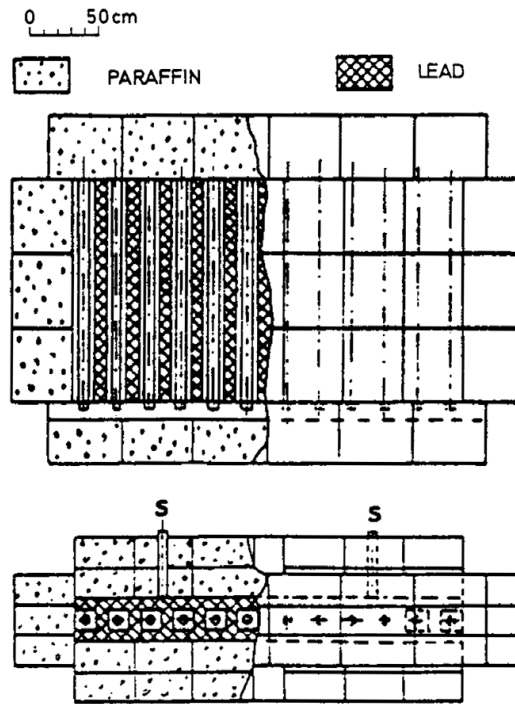


Figure 2.5: The standard pile extended to 12 counters, the IGY neutron monitor (Simpson et al. (1953) in Stoker (2009)).

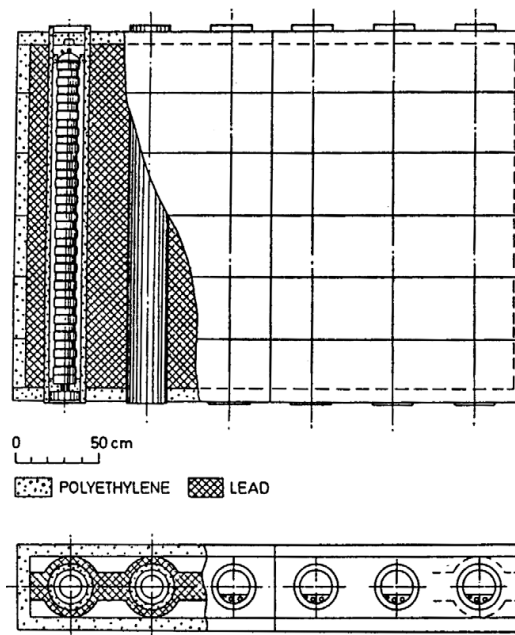


Figure 2.6: The 6NM64 super neutron monitor, shown schematically (Carmichael 1968), was designed for higher count rates and better statistics than the IGY neutron monitor.

allows only the fast neutrons above tens of MeV to be captured (the meson and electron components at all energies are usually not detected). The ^{10}B has a neutron capture cross-section inversely proportional to the neutron velocity. Due to the small ionization loss in the counter gas the electromagnetic and muon components are not recorded. From the first flight above the desert at Inyokern, China Lake, California, the neutron density data displayed a surprisingly large geomagnetic latitude dependence (Simpson 1948). The changes in the primary low energy cosmic ray proton intensity down to 1-5 GeV could be investigated continuously at high latitude and low energy window in the cosmic ray energy spectrum. The development of a practical neutron monitor in 1948-1949 led to a basic standard pile design taking account only of its dependence on barometric pressure (Simpson et al. 1953). Neutron monitors also proved to be superior in short and long-term recording of primary cosmic rays of energies above about 1 GeV because of their long-term stability. Thus, this design could be extended in multiple piles that later become the design adopted for the "International Geophysical Year" (IGY) in 1957, which was implemented at more than 60 sites world-wide to record the cosmic rays.

The physical design of a neutron monitor has been discussed (Stoker et al. 2000) and a brief history of the neutron monitor has been provided (Stoker 2009). From the progression from early experimental designs to the IGY monitor (1957-1958) as shown in Figure 2.5 and to the current standard NM64 (1959) as shown in Figure 2.6, the neutron monitor has been modified for improving the monitor response for measurement purposes. Subsequently, the NM64 super neutron monitor was designed by H. Carmichael for deployment in time for the International Quiet Sun Year 1964. Using unusually large BF_3 proportional counters, Hatton and Carmichael (1964) constructed more efficient neutron counters to record evaporation neutrons produced in the lead, and found that the neutron count rate increased from 1.9% for the IGY to 5.7% for the NM64. The detector used in the neutron monitor is a BF_3 proportional counter, enriched in the 10-boron isotope. Polyethylene was used instead of paraffin wax as moderator

around the big counters and as reflectors and shields encasing a set of at least three counters. Although there are significant differences in dimensions between the IGY and NM64 configurations, the components used are basically the same.

Because of the problem of instrumental sensitivity to external climatic conditions, ambient neutron production, and the low count rate observed with a bare BF_3 detector, the neutron monitor was developed to record more evaporation neutrons produced by interaction in a target or “producer” of high atomic mass inside the monitor. The cosmic-ray neutron monitor system is thus based on measuring the local production of fast neutrons in a high atomic weight target (Simpson 2000). The instrument would be analogous to a nuclear reactor in which lead would substitute for uranium as the producer of neutrons, and hydrogenous materials such as paraffin wax would substitute for the carbon or heavy water moderator. As a consequence, the fragmentation of a lead nucleus by an incident high-energy secondary nucleon in the nucleonic cascade would yield a multiplicity of fast neutrons. The fast neutrons then become thermalized in the surrounding moderator and be detected with high efficiency using a BF_3 proportional counter for slow neutron capture in ^{10}B .

The neutron monitor records predominantly energetic nuclear particles like protons and neutrons, secondary to the primary cosmic ray particles. In a neutron monitor, BF_3 proportional counters surrounded by a lead target detect thermal neutrons produced locally by interacting incident neutrons, protons, pions, and muons. These have relative contributions to the count rate of roughly 85%, 7%, 1%, and 6%, respectively (Hatton 1971). Effects from the ambient atmospheric temperature are thus proved to be very small since only a small fraction of radioactive secondaries like pions and muons that depend on the production height and temperature of the atmosphere is incorporated in the count rate. To a good approximation, the count rate of a neutron monitor depends only on the local atmospheric pressure.

2.2.3 Cutoff rigidity

As high energy particles gyrate about interplanetary magnetic field lines, the dynamics essentially depend on what is known as the rigidity or magnetic rigidity of the particles. The rigidity is defined as

$$P = \frac{pc}{ze} = \frac{m_0\gamma vc}{ze} = \frac{A m_p \gamma vc}{z e}, \quad (2.2)$$

where p is the relativistic three-momentum of the particle, c is speed of light, A is the mass number, and z is the electric charge in units of e . Therefore, particles of different charges and masses but with the same rigidities have the same dynamics in any magnetic field configuration. Normally, the energy of the particles is expressed in terms of their kinetic energy per nucleon and this is a measure of the velocity, or Lorentz factor, $\gamma = (1 - v^2/c^2)^{-1/2}$, of the particles. The rigidity P depends only upon the mass to charge ratio A/z of the particles. Since this number is close to 2 for most elements up to about iron, the different elements should be influenced in the same way (Longair 1992), with the important exception of hydrogen.

The cutoff rigidity P_c is defined as the minimum rigidity with which a charged particle is able to arrive from a given direction at the atmosphere above a given location by crossing the geomagnetic field (McCracken et al. 1962; Smart et al. 2000). The geomagnetic field acts as a spectrometer allowing or forbidding primary cosmic rays to penetrate through the magnetosphere and to arrive from a given direction at given point on Earth. Vertical geomagnetic cutoff rigidities vary from close to zero at the magnetic poles to 17 GV near the geomagnetic equator. As a result, polar neutron monitors detect lower-energy cosmic rays than equatorial neutron monitors. To determine the cutoff rigidity at a given point for a given direction, time-reversed particle trajectories are computed at successively lower rigidities to determine whether the trajectory is “allowed,” i.e., the time reversed trajectory leads to space, or “forbidden,” i.e., the time-reversed trajectory intercepts the Earth. The process is continued to determine a rigidity below which all particles are forbidden at that location. An examination of

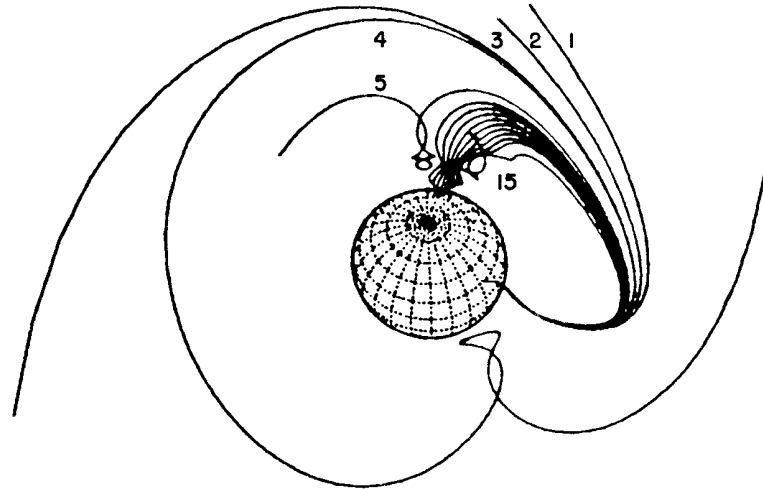


Figure 2.7: Charged particle trajectories of different rigidities (energies) traced out in the vertical direction from the same location. The trajectories are arranged from the highest (labeled 1) to lowest energies (labeled 15). The trajectories labeled 1, 2, and 3 show increasing geomagnetic bending before escape into space. Trajectory 4 develops intermediate loops near the Earth while trajectory 5 near the cutoff rigidity develops complex loops before escaping. The lower energy trajectory 15 in the penumbra escapes after a series of complex loops near the Earth. (From Smart et al. 2000).

the particle trajectories from highest to lowest rigidities shows that there can be an energy range with interspersed allowed and forbidden trajectories called the “cosmic ray penumbra” (Cooke et al. 1991). The actual trajectory calculations are illustrated in Figure 2.7. The trajectories undergo increased geomagnetic bending as the particle rigidity is decreased. Near the cutoff rigidity particle trajectories develop intermediate loops and become complex. In the cosmic ray penumbra, some trajectories are re-entrant, and some are allowed. Taking into account the theorem that the intensity of cosmic rays is always constant along their path in a static magnetic field (Swan 1933) derived from the Liouville theorem, the intensity of the primary cosmic rays incident into the atmosphere is always equal to that in interplanetary space.

To first order, the cutoff for vertically incident particles is sufficient. The vertical cut-off rigidity is a function of latitude and also of the parameters describing the magnetic field (e.g., the Earth’s dipole moment, in the case of a simple dipole field, and additional parameters when perturbing fields are present). The Earth’s magnetic

field affects the penetration of cosmic ray particles in the vicinity of the Earth. For a dipole field, the rigidity for a cosmic ray particle to reach a geomagnetic latitude λ and geocentric radius R is given by (Störmer 1956):

$$P_c = \frac{M}{R^2} \frac{\cos^4 \lambda}{[(1 + \cos \theta \cos^3 \lambda)^{1/2} + 1]^2}, \quad (2.3)$$

where M is the Earth's dipole moment which is approximately 7.5×10^{22} A m², $(M/R_0^2) \approx 60 \times 10^9$ volts, where R_0 is the radius of the Earth, and θ is the angle between the arrival direction of the particle and the tangent of the circle of latitude. Here $\theta = 0$ corresponds to arrival from the west for positive particles or corresponds to arrival from the east for negative particles. The simplified format of the equation (2.3) (in units of GV) for a dipole field centered at Earth's center is

$$P_c = \frac{14.5 \cos^4 \lambda}{R^2}, \quad (2.4)$$

(Smart and Shea 2005) where R in units of Earth radii. However, this formula is grossly in error for Doi Inthanon. For research work, we use the International Geomagnetic Reference Field (IGRF) and trace particle orbits to determine the cutoff rigidity.

2.2.4 Asymptotic direction of measurement

In order to specify the true direction of the incoming primary cosmic rays from space, it is crucial to correct for geomagnetic field bending of the charged particles. The trajectory of the particle can be traced until it reaches the ground as long as the description of geomagnetic field is sufficiently known. Such an approach would require traced particles from all directions to determine the response. However, it is more practical to trace particles of opposite charge but the same rigidity from the detector location back to space through the field. Consequently, for a given cutoff rigidity there may be some trajectories that remain forever within the geomagnetic field or intersect the Earth's surface. The accessible directions of the particles are known as "asymptotic direction of approach" (McCracken et al. 1962) and the set of rigidity-dependent accessible directions defines "the monitor's asymptotic cone of view". The asymptotic

directions are determined by the latitudes and longitudes of the observing stations on the Earth, the incident directions, and the rigidities of the cosmic rays. The asymptotic cone of acceptance of a detector is the solid angle containing all the asymptotic directions of approach which significantly contribute to the count rate of the detector (Rao et al. 1963). The effective width of these asymptotic cones can span from 10° for polar neutron monitors to more than 30° for near-equatorial stations (Moraal et al. 2000).

Besides the internal geomagnetic field that is modeled by a series of spherical harmonic functions with inclusion of secular variation terms, the level of geomagnetic disturbance as characterized by the Kp geomagnetic index also affects the neutron monitor's asymptotic cone of view (Tsyganenko 1989). The geomagnetic field is distorted by interaction of the interplanetary magnetic field with the magnetosphere resulting in a compressed geomagnetic field on the sunward side and an extended tail on the anti-sunward side of the Earth. When accounting for the disturbed conditions with the Kp index, Duldig et al. (1993) found that the most obvious changes can be seen in the direction of view of the polar monitors. It is also apparent that the equatorial viewing instruments have had their views significantly changed.

Although it is necessary to consider the effect of the asymptotic direction for an isotropic cosmic ray distribution in interplanetary space, the effect becomes important when deducing the anisotropic distribution of the cosmic ray intensity observed on Earth. In order to estimate the anisotropy of the cosmic ray intensity in interplanetary space, Nagashima (1971) has derived the cosmic ray anisotropy on the basis of the variations of the cosmic ray intensity in various directions.

2.2.5 Diurnal variation at neutron monitor energies

Neutron monitors provide information of cosmic ray anisotropy in which they determine the flux of particles with a rigidity above their cutoff rigidities corresponding to particles coming from a range of asymptotic directions. The asymptotic directions of cosmic ray particles viewed from a fixed neutron monitor on the Earth rotate once

a day because of the Earth's rotation. Consequently, an anisotropic distribution of the cosmic ray intensity is observed as a daily periodic change called the diurnal variation. The diurnal variation (or diurnal anisotropy) is the percentage deviation from a daily mean of the count rate, which roughly exhibits a sine curve with a 24-hour period. Then the amplitude and phase (time of maximum cosmic ray intensity) are calculated. The diurnal variation with local solar time has been extensively investigated over the years (see, e.g., Thambyahpillai and Elliot 1953; Duggal and Pomerantz 1975; Mori et al. 1981), since this provides information concerning the cosmic ray flow patterns in space.

The diurnal variation arises from a net azimuthal streaming of the cosmic ray particles in interplanetary space (McCracken and Rao 1966). Cosmic ray particles of various energies exhibit significant anisotropies and the magnitude of anisotropy is dependent on the particle energy. Cosmic rays of energy up to ~ 100 GeV are affected by the Sun and the interplanetary magnetic field which completely destroy the galactic near-isotropy (Rao 1972). From extensive analysis of all neutron monitor data during 1954-1965, Rao et al. (1963) and McCracken and Rao (1965) have found that the average diurnal variation of cosmic ray intensity follows

$$\frac{\delta J(E)}{J(E)} = \begin{cases} AE^{-\gamma} \cos(\phi - \phi_0) \cos \Lambda & \text{for } E \leq E_{\max} \\ 0 & \text{for } E > E_{\max}. \end{cases} \quad (2.5)$$

where $A = (0.38 \pm 0.02) \times 10^{-2}$, $\gamma = 0$, $\phi_0 = 89 \pm 1.6^\circ$ East of the Earth-Sun line measured anticlockwise from the noon meridian, ϕ is the asymptotic longitude, Λ is the asymptotic latitude of the station and $E_{\max} \sim 100$ GeV. In other words, the average diurnal anisotropy is (a) energy independent in the energy range 1-100 GeV; (b) varies as cosine of the declination, Λ ; (c) has an average amplitude of about 0.38 ± 0.02 %; and (d) has the maximum flux incident from $\phi_0 = 89 \pm 1.6^\circ$ E of the Sun-Earth line (Rao 1972). It is notable that this equation is obtained after correcting for the width (longitude) of the asymptotic cone of acceptance of each station. Comprehensive reviews of solar diurnal anisotropy are provided (Pomerantz and Duggal 1971; Rao 1972). We will illustrate the calculation of diurnal anisotropy in Section 2.4.2 in the framework of diffusion theory.

2.3 Plasma and magnetic field from the Sun to the heliosphere

2.3.1 Solar wind

The corona of the Sun is unstable because the temperature ($1-4 \times 10^6$ K) is so high that plasma blows away as the solar wind (Parker 1958). Parker's hydrodynamic solar wind model is a valid approximation for the solar wind when the Sun is not disturbed. In fact, the solar wind has high variability in space and time reflecting the underlying coronal structures. The basic features of the solar wind can be described as follows: It is a continuous flow of plasma dominated by electrons and protons. This outflow of fully ionized atoms also carries traces of neutral hydrogen and heavier elements, such as alpha particles, oxygen and iron ions. The solar wind flows with a supersonic speed of about 400 km s^{-1} , which is 40 times the sound speed in the solar wind near the Sun. It carries out the frozen-in magnetic field into the heliosphere and the magnetic field strength is some nanoteslas at Earth's orbit. Subsequently, two distinct types of plasma flow are observed - the fast and the slow wind as shown in Figure 2.8.

The main characteristics of the two basic states are described (Schwenn 1990) from the measurements in the plane of the ecliptic as tabulated in Table 2.1. There are differences in the speed, the proton density, the mass flux, and the helium content, but similarities in the flux densities of energy and momentum.

2.3.2 Magnetic fields in the solar photosphere and corona

The photospheric magnetic field was discovered by Hale in 1902. Spectral line observations of the photosphere reveal a complex magnetic field pattern associated with sunspots, active regions, and other visible features. The splitting of spectral lines due to the Zeeman effect suggests a photospheric field in the order of $10^{-4} \text{ T} = 1 \text{ G}$ outside of sunspots and 3000 G to 4000 G inside them. The photospheric magnetic

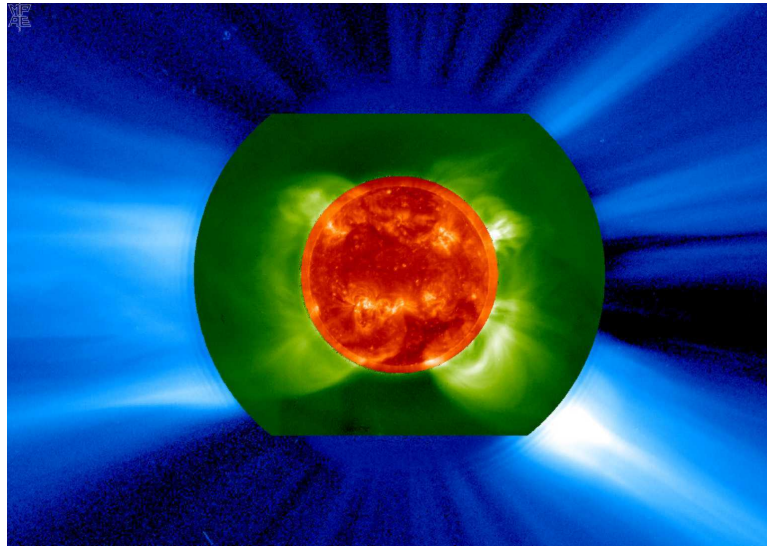


Figure 2.8: Montage of images from 3 different telescopes on SOHO: EIT showing the EUV disk (at 19.5 nm), LASCO-C1 showing the inner corona (at 530.3 nm), and LASCO C2 showing the outer corona (in white light). This shows the two states of solar wind characterized by their brightness and sources. The slow streams are brighter than the fast streams because they are more dense. Note also how well separated from each other they are, both in the low corona as well as in the extended corona. The dark area on the disk near the south pole is a good example of a large coronal hole (from Schwenn 2006).

field is rather complex and highly variable. *In situ* observations in interplanetary space indicate that many of the small-scale photospheric structures form closed loops within less than two solar radii.

Alternatively, the coronal magnetic field can be described by coronal holes and helmet streamers which are dominant features in the solar corona. The coronal holes are regions of open field lines, allowing for a fast electron escape in fast solar wind streams (see Section 2.5.1). They appear as dark features because of a lower density of electrons and low emission in X-rays. The coronal holes are the dominant feature over the poles of the Sun. Sometimes they can migrate down to the solar equator or even into the opposite hemisphere. On the other hand, the helmet streamers develop over active regions, and the legs of the helmet streamer connect regions of opposite magnetic field polarity. Electrons are trapped inside these loops. Then there is Thompson scattering of visible light photons by free electrons, and thus the brightness is proportional to the

Table 2.1: Average solar wind parameters at 1 AU, for the time around solar activity minimum, compiled by Schwenn (1990).

Parameter	Slow speed solar wind	High speed solar wind
Flow speed V_p	250-400 km s ⁻¹	400-800 km s ⁻¹
Proton density n_p	10.7 cm ⁻³	3.0 cm ⁻³
Proton flux density $n_p V_p$	3.7×10^8 cm ⁻² s ⁻¹	2.0×10^8 cm ⁻² s ⁻¹
Proton temperature T_p	3.4×10^4 K	2.3×10^5 K
Electron temperature T_e	1.3×10^5 K	1×10^5 K
Momentum flux density	2.12×10^8 dyne cm ⁻²	2.26×10^8 dyne cm ⁻²
Total energy flux density	1.55 erg cm ⁻² s ⁻¹	1.43 erg cm ⁻² s ⁻¹
Helium content n_{He}/n_p	2.5%, variable	3.6%, stationary

total number density of electrons along the line of sight, hence the helmet streamer is a bright feature in the corona (Figure 2.8). The streamer belt's extension and its inclination relative to the solar equator vary over the solar cycle since the streamer belt is associated with the active regions.

A physical model that can account for the important effects that the magnetic field has upon the inner corona is the source surface model as shown in Figure 2.9. Region 1 represents the photosphere, where the magnetic field motion is governed by the detailed motions of the plasma near the photosphere. In region 2, the magnetic field energy density is greater than the plasma energy density and hence controls the configuration. The force-free condition, $\mathbf{j} \times \mathbf{B} = 0$, is then used. For simplicity, one might make the further assumption $j = 0$. The magnetic field in this region may then be derived from the Laplace equation: $\nabla^2 \phi = 0$, where ϕ is a magnetic potential. This is called a potential field model. In region 3 transverse magnetic fields are transported by the radially flowing plasma. The magnetic field on the surface boundary between regions 2 and 3 serves as a source surface for the interplanetary magnetic field. As described in the photospheric field, the solar source surface can be defined above the closed loops, while the overall field pattern is carried outwards by the solar wind. The source surface lies at a height of about $2.5 R_\odot$ and can be determined from the photospheric field pattern using a potential model (Schatten et al. 1969; Zhao and Hoeksema 1993). Model constraints on the field are as follows: (a) the magnetic field at the source surface

is directed radially and (b) currents either vanish or are horizontal in the corona.

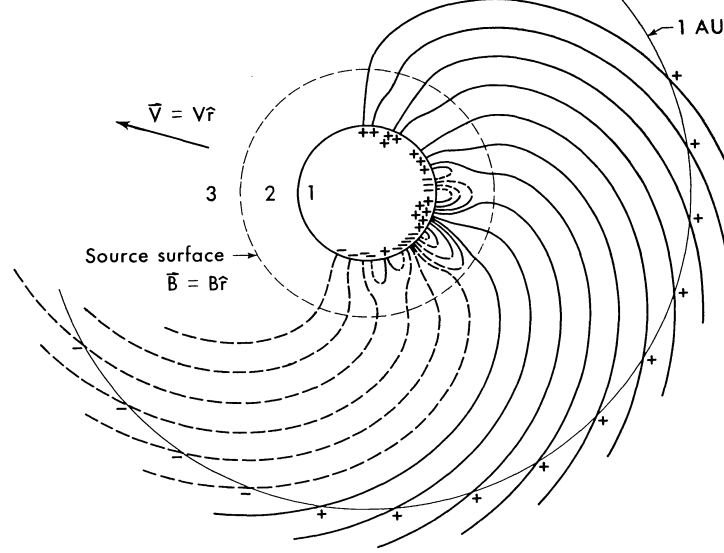


Figure 2.9: Relationship between the photospheric magnetic field, the source surface field, and the interplanetary magnetic field. The inner circle represents the Sun. The photospheric magnetic field is measured in region 1. Closed field lines (loops) exist in region 2. The dashed circle represents the source surface at which any field lines crossing it are assumed to become radial. Beyond the source surface, the field lines gradually develop a spiral shape. Dashed and solid lines indicate negative and positive magnetic field polarities as observed by spacecraft near 1 AU, respectively (Schatten et al. 1969).

2.3.3 Interplanetary spiral magnetic field

According to high conductivity of the solar wind, the radial coronal magnetic field is frozen into it (Alfvén 1950) and carried out into interplanetary space. We now present a simple model of the interplanetary magnetic field (IMF) to illustrate the IMF features observed in space for quiet solar conditions. In spherical coordinates (r, θ, ϕ) centered at the Sun, the radial and angular displacement of the frozen-in field lines when the Sun rotates are

$$\begin{aligned} r &= r_0 + Vt \\ \phi &= \phi_0 + t\Omega_{\odot} \sin \theta, \end{aligned} \quad (2.6)$$

where r is the heliocentric distance, V is the solar wind speed, ϕ_0 is a source longitude, r_0 a source radius, $\Omega_{\odot} = 2.7 \times 10^{-6}$ radians s^{-1} is the sidereal rotational frequency of

the Sun, and θ and ϕ are the solar colatitude and longitude of the observer.

Then equation (2.6) defines an Archimedean spiral which is well ordered on a large scale, as shown in Figure 2.9 and is rewritten in more familiar form:

$$r - r_0 = V \cdot \frac{\phi - \phi_0}{\Omega_{\odot} \sin \theta}, \quad (2.7)$$

The spiral angle between the direction of the field lines and the radius vector at r is given by

$$\tan \psi = \frac{(r - r_0)d\phi}{dr} = \frac{(r - r_0)\Omega_{\odot} \sin \theta}{V}. \quad (2.8)$$

At 1 AU, $r\Omega_{\odot} \approx 400 \text{ km s}^{-1} \sim V$, so streamlines are inclined at $\psi \sim 45^\circ$ to the radial direction.

Since by definition \mathbf{B} is along the field lines, its radial and azimuthal components satisfy

$$\frac{B_{\phi}}{B_r} = -\frac{(r - r_0)d\phi}{dr} = -\frac{\Omega_{\odot} \sin \theta (\phi - \phi_0)}{V}, \quad (2.9)$$

with the colatitude $\theta = \text{constant}$. From the magnetic flux conservation $\nabla \cdot \mathbf{B} = 0$, the radial component of \mathbf{B} can be determined from

$$\frac{1}{r^2} \frac{\partial}{\partial r}(r^2 B_r) + \frac{1}{r \sin \theta} \frac{\partial}{\partial \theta} B_{\theta} \sin \theta + \frac{1}{r \sin \theta} \frac{\partial}{\partial \phi} (B_{\phi}) = 0. \quad (2.10)$$

With the assumption that $B_{\theta} = 0$ and azimuthal symmetry $\partial B_{\phi} / \partial \phi = 0$, the above equation gives

$$B_r = B_0 \left(\frac{r_0}{r} \right)^2, \quad (2.11)$$

where B_0 is the magnetic field from the footpoint. Substituting this expression into equation (2.9) we get B_{ϕ} and then the spiral IMF configuration is given by

$$\mathbf{B}_1 = \mathbf{B}_0 \left(\frac{r_0}{r} \right)^2 (\mathbf{e}_r - \tan \psi \mathbf{e}_{\phi}). \quad (2.12)$$

On average, the large scale IMF is consistent with the Parker spiral field model (e.g., Burlaga et al. 1984).

2.3.4 Magnetic field sectors

It has been found that the interplanetary magnetic field as observed near the Earth (near solar equatorial plane) has a tendency to point away from the Sun (positive polarity) or toward the Sun (negative polarity) for a duration of several days. This pattern has been called the magnetic field sector structure (Wilcox and Ness 1965). The intervals of organized magnetic polarity tend to recur with a 27-day period in association with the solar rotation. Therefore, there exists a large-scale interplanetary magnetic sector structure that corotates with the Sun (Wilcox 1968). Moreover, the structure is well established in all phases of solar cycle.

As the unipolar magnetic field in a sector is frozen in the solar wind, thus the source of the field may be associated with the high speed stream emerging from a coronal hole, which is contained in that sector. Observationally, the sign of the magnetic field within a sector corresponds to the pattern of coronal holes (Burlaga et al. 1978; Sheeley and Harvey 1978). In addition, the azimuthal distribution of the IMF is normally divided into two or four alternating polarity sectors. However, around solar minimum, the patterns are stable over months according to the stability of coronal holes that evolve slowly from one rotation to the next. In conclusion, the sector structure of the IMF near the Earth, which has an orbit that is inclined by 7.3° relative to the solar equatorial plane, matches the large-scale solar and coronal polarity patterns if the solar wind traveling time (4 to 5 days) is taken into account.

Alternatively, it is generally accepted that the sector structure is a result of the projection into interplanetary space of the dominant polarities of the two solar hemispheres (Hundhausen 1977; Bruno et al. 1982; Behannon et al. 1983). The predominant polarity of each hemisphere reverses at, or following, sunspot maximum (Wilcox and Scherrer 1972). The heliosphere is divided into two hemispheres of opposite magnetic polarity by a thin current sheet near the equatorial plane according to the oppositely directed magnetic fields and the flow from the north and south polarities (Newkirk and

Fisk 1985). According to $\mathbf{j} \propto \nabla \times \mathbf{B}$, the reversal of the magnetic field direction near the equatorial plane corresponds to a thin sheet of electric current flowing in this plane. In other words, as the current sheet separates the two magnetic field polarities a current must flow inside it. Because the Sun rotates, the passage of the current sheet at the Earth or spacecraft is observed as a sector boundary crossing that causes a reversal of the magnetic polarity.

2.3.5 Heliospheric current sheet

As described earlier, the current sheet is a vast and thin region lies in between positive and negative polarities of the Sun. The sign of the radial component of the magnetic field is the same as that of the latitude with respect to the current sheet. It is embedded in slow, dense solar wind emerging from the streamer belt (Newkirk 1972). When the current sheet is swept and extended into interplanetary space by the solar wind, it is called the interplanetary current sheet or heliospheric current sheet (HCS) as shown in Figure 2.10).

In addition, the HCS is warped because the solar magnetic field is not dipolar. The excursion in heliomagnetic latitude of the Earth is much larger than that in heliographic latitude which is 7.3° . As a result, the HCS is warped in such a way that a spacecraft at Earth sees it almost periodically since the spacecraft would be in or very near the Ecliptic plane, and the sheet moves around faster than the orbital motion of the Earth, which takes one year to complete one revolution. The base of the sheet at the Sun takes about 27 days to complete one rotation, and the whole sheet almost follows that timing, but it is more like a big wave moving out from the Sun. The current sheet thus has a wavy, “ballerina skirt” structure as it extends into interplanetary space and it recurs every solar rotational period.

The inclination of the HCS defines the width of a cone inside which an observer in space alternately sees different polarities of the coronal/interplanetary magnetic field. The maximum inclination of the neutral line at each time is called the tilt angle

which can be roughly viewed as the inclination of the heliomagnetic equator. During solar minimum the tilt angle is small so the HCS is roughly aligned with the solar equator. However, with increasing solar activity the tilt angle is large so the HCS becomes wavy and extends to higher solar latitudes through the tips of the helmet streamers. For example, in 1992, magnetic dipole was tilted approximately 30° relative to the solar rotation axis (Hoeksema 1995), whereas in 1997, when Ulysses returned to low latitudes, the magnetic dipole was roughly oriented parallel to the rotation axis.

The HCS usually creates a two- or four-sector pattern according to the dipole or quadrupole fields of the Sun during the solar cycle, respectively. The sector structure arises from the fact that the current sheet is warped like baseball stitches since the fields are not symmetric. As the Sun rotates, an observer close to the solar equatorial plane passes through the current sheet an even number of times during every solar rotation (Thomas and Smith 1981). Figure 2.10 also shows the warped current sheet resulting from the wobbling of the HCS with respect to the fixed solar rotation direction together with the radial motion of the solar wind. The latter causes a delay in the appearance of one particular sign of the photospheric magnetic field as observed at a point in space. Good background information about the HCS may be found in Chen (1989).

The magnetic field of the warped HCS can be written mathematically by taking into account the Parker spiral field \mathbf{B}_1 , sector structure, and the tilt angle α as (Quenby 1984)

$$\mathbf{B} = \mathbf{B}_1 S [1 - 2H(X)], \quad (2.13)$$

where $S = 1 (-1)$ for positive (negative) solar magnetic polarity,

$$\begin{aligned} X &= \theta - \left[\frac{\pi}{2} + \sin^{-1} \left[\sin \alpha \sin \left(\phi - \phi_0 + \frac{r\Omega}{V} \right) \right] \right] \\ &\approx \theta - \left[\frac{\pi}{2} + \alpha \sin \left(\phi - \phi_0 + \frac{r\Omega}{V} \right) \right], \text{ for } \alpha \ll 1 \end{aligned} \quad (2.14)$$

(Jokipii and Thomas 1981), and $H(X) = 0 (-1)$ if $X < 0 (> 0)$ is the Heaviside step function. The field direction alternates with the 11-year cycle, so that, for example, from 2000 to the present the magnetic field polarity at the solar north pole was negative

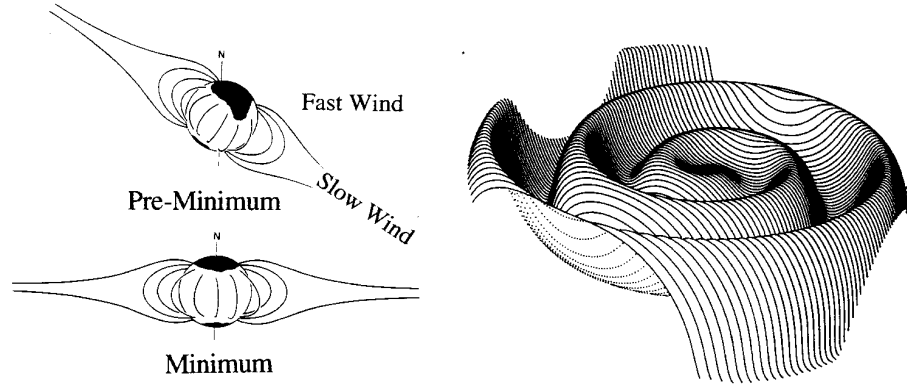


Figure 2.10: Left: Temporal changes in the inclination (tilt angle) of the solar magnetic field (Gozling and Pizzo 1999, after Hundhausen, 1977), boundaries between closed and open magnetic field lines, and large-scale closed magnetic field lines, around times of solar minimum. Right: Configuration of the HCS in the solar wind for a substantial tilt angle (Jokipii and Thomas 1981). The width of the cone of the HCS is twice the tilt angle.

($S = -1$, field directed toward the Sun), while during the next cycle from about 2014 to 2025 it should be positive ($S = 1$, field directed away from the Sun), and so on.

From equation (2.14), we can see that the current sheet represents the boundary between toward and away IMF at $X = 0$. This indicates that the HCS is thin compared with the scale of the particle gyroradius. A spacecraft situated above the current sheet cannot directly detect it. This means that the recurrent magnetic sector structure will disappear far from the HCS.

In conclusion, the HCS is an established major structural feature of the heliosphere, and its source is related to coronal structures. As we will see later, the HCS plays a crucial role in organizing the large-scale solar wind structure that corotates with the Sun.

2.4 Solar modulation and anisotropy of Galactic cosmic rays

2.4.1 General

The interplanetary magnetic field possesses small-scale irregularities. The irregularities appear with dimensions of $10^5 - 10^7$ km, which are comparable to the radius of gyration of typical cosmic ray particles. Parker (1958) pointed out the effect of scattering from irregularities in the interplanetary magnetic field, which causes low energy cosmic rays to convect outwards with the flow. The irregularities scatter, or reflect, the cosmic rays back and forth along the lines of the large-scale field, so that the cosmic ray particles undergo a random walk in the frame of reference of the magnetic irregularities (Parker 1965). Particle diffusion either along or across field lines is important. When the scattering is infrequent, the diffusion along lines of force is much stronger and the particle motion is described by the guiding center approximation between scattering. The diffusion coefficient describing this random walk is a tensor quantity K_{ij} with a larger value parallel than perpendicular to the large-scale field.

Anisotropy of GCRs is primarily determined by local scattering and bulk flow conditions at the point of measurement. Consequently, to determine the anisotropy the streaming equation of cosmic rays is derived. Then the diurnal variations of cosmic rays can be approximated by the azimuthal anisotropy with zero radial anisotropy.

The contribution of the small-scale fluctuations in the field to the diffusion tensor K_{ij} follows from the power spectrum of the small-scale fluctuations at zero wavelength (Jokipii 1966, 1967; Jokipii and Parker 1968, 1969). Scattering (or diffusion) of cosmic rays by turbulent magnetic field irregularities is therefore described by the cosmic-ray diffusion tensor; the diffusion of particles in the i -direction in terms of a diffusion tensor K_{ij} may come from the flow in the j -direction. In a Cartesian coordinate system $(\mathbf{e}_1, \mathbf{e}_2, \mathbf{e}_3)$ with $\mathbf{e}_3 = \mathbf{B}/|\mathbf{B}|$, the diffusion tensor may be written in matrix form

as (Parker, 1965)

$$\begin{aligned}
 K_{ij} &= \frac{v^2}{3(\nu_c^2 + \omega^2)} \begin{pmatrix} \nu_c & \omega & 0 \\ -\omega & \nu_c & 0 \\ 0 & 0 & \frac{\nu_c^2 + \omega^2}{\nu_c} \end{pmatrix} \\
 &= \begin{pmatrix} K_{\perp} & K_A & 0 \\ -K_A & K_{\perp} & 0 \\ 0 & 0 & K_{\parallel} \end{pmatrix}, (i = 1, 2, 3; j = 1, 2, 3). \quad (2.15)
 \end{aligned}$$

Here, the diagonal elements or symmetric part of the diffusion tensor describe diffusion of particles parallel (K_{\parallel}) or perpendicular (K_{\perp}) to the mean magnetic field. The parallel diffusion is determined by scattering by irregularities in the field, whereas the perpendicular diffusion coefficient is determined by both the scattering and the random walk of the field lines (Jokipii 1966). The off-diagonal, antisymmetric terms (K_A) describe effects of gradient and curvature drifts (Jokipii et al. 1977) and sometimes called the pressure drift (Jokipii and Parker 1970) since the flux is proportional to and perpendicular to density gradient of cosmic rays, ∇U . The flux deduced from the pressure drift is the result of the curvature of the average field \mathbf{B} and the gradients in the field and particle densities (Parker 1957). In practice, the cosmic-ray diffusion tensor can be defined by the proportionality between the particle flux and large-scale density gradients. In the high energy limit, the gyroradius R_L of GCRs is larger than a magnetic field correlation length. For cosmic rays near 1 AU, $K_A = vR_L/3$, where v is the particle speed and R_L is the particle Larmor radius, is well justified only for rigidities greater than about 4 GV (Forman et al. 1974; Bieber and Matthaeus 1997). If the particle charge changes sign, the sign of K_A changes. Here K_A is dependent on the direction of unit vector \mathbf{e}_3 , which is dependent on the direction of \mathbf{B} (away from or toward the Sun).

2.4.2 Streaming equation and cosmic ray anisotropy expressions

The net flux of particles with kinetic energy T in the frame locally at rest with respect to the plasma in the solar wind frame follows from the diffusive flux as

$$S_i(x_k, t, T) = -K_{ij} \frac{\partial U}{\partial x_j}. \quad (2.16)$$

To transform equation (2.16) from the solar wind frame to the observer's (Earth) frame, the relative motion of Earth and the solar wind must be included. The particle phase space distribution function should be the same in both frames according to Lorentz invariance. Consequently, the diffusive flux and the convective flux are combined in a streaming equation

$$\mathbf{S} = C\mathbf{V}U - \mathbf{K} \cdot \nabla U, \quad (2.17)$$

where \mathbf{S} is the differential cosmic ray current density (or cosmic ray flux) in a given energy interval and $C\mathbf{V}U$ is the convective differential current density that crosses a unit area normal to \mathbf{S} in unit time. Here

$$C = 1 - \frac{1}{3U} \frac{\partial(\alpha TU)}{\partial T} \quad (2.18)$$

is the Compton-Getting factor and $\alpha = (T + 2E_0)/(T + E_0)$. The term $C\mathbf{V}U$ implicitly includes the electric-field drift velocity $\mathbf{E} \times \mathbf{B}/B^2$, as shown by Forman and Gleeson (1975).

The diffusion tensor in equation (2.15), however, can be split into a symmetric part \mathbf{K}^s and an antisymmetric part \mathbf{K}^a as

$$\begin{aligned} K_{ij} &= \begin{pmatrix} K_{\perp} & 0 & 0 \\ 0 & K_{\perp} & 0 \\ 0 & 0 & K_{\parallel} \end{pmatrix} + \begin{pmatrix} 0 & K_A & 0 \\ -K_A & 0 & 0 \\ 0 & 0 & 0 \end{pmatrix} \\ &= K_{ij}^s + K_{ij}^a, (i = 1, 2, 3; j = 1, 2, 3). \end{aligned}$$

Thus,

$$\begin{aligned} \mathbf{K}^a \cdot \nabla U &= K_A \mathbf{e}_1 \mathbf{e}_2 \cdot \nabla U - K_A \mathbf{e}_2 \mathbf{e}_1 \cdot \nabla U \\ &= K_A \mathbf{e}_1 \frac{\partial U}{\partial r_2} - K_A \mathbf{e}_2 \frac{\partial U}{\partial r_1} \\ &= -K_A \mathbf{e}_3 \times \nabla U \\ &= -K_A \frac{\mathbf{B}}{|\mathbf{B}|} \times \nabla U. \end{aligned} \quad (2.19)$$

Then equation (2.17) is

$$\mathbf{S} = C\mathbf{V}U - \mathbf{K}^s \cdot \nabla U + K_A \frac{\mathbf{B}}{|\mathbf{B}|} \times \nabla U. \quad (2.20)$$

This equation is important in quantifying cosmic ray anisotropy. The cosmic ray anisotropy in free space is defined as

$$\mathbf{A} = \frac{3\mathbf{S}}{vU} \quad (2.21)$$

(Gleeson and Axford 1967) and the scattering mean free path tensor of cosmic rays is

$$\lambda = \frac{3\mathbf{K}}{v}. \quad (2.22)$$

In the weak scattering limit $\nu_c^2 \ll \omega^2$ (see equation (2.15)),

$$K_A = \frac{v^2}{3\omega} = \frac{v\rho}{3}, \quad (2.23)$$

where $\rho = v/\omega$ is the gyroradius in the mean magnetic field. Equation (2.20) then becomes

$$\mathbf{A} = \frac{3C\mathbf{V}}{v} - \lambda^s \cdot \frac{\nabla U}{U} + \rho \frac{\mathbf{B}}{|\mathbf{B}|} \times \frac{\nabla U}{U}. \quad (2.24)$$

This equation can be written in a simpler form (Chen, 1989; Bieber and Chen, 1991)

$$\mathbf{A} = \mathbf{A}_c - \lambda^s \cdot \mathbf{G} + \rho \frac{\mathbf{B}}{|\mathbf{B}|} \times \mathbf{G}, \quad (2.25)$$

where $\mathbf{G} = \nabla U/U$ is the gradient vector of cosmic ray density and $\mathbf{A}_c = 3C\mathbf{V}/v$ is the convective part of the anisotropy.

For convenience, the Cartesian coordinate system $(\mathbf{e}_1, \mathbf{e}_2, \mathbf{e}_3)$ with \mathbf{e}_2 pointing northward and \mathbf{e}_3 parallel to \mathbf{B} away from the Sun is then transformed to a spherical coordinate system $(\mathbf{e}_r, \mathbf{e}_\theta, \mathbf{e}_\phi)$ with \mathbf{e}_r pointing to the Earth and \mathbf{e}_θ pointing southward. The relation between the two systems is

$$\begin{pmatrix} \mathbf{e}_1 \\ \mathbf{e}_2 \\ \mathbf{e}_3 \end{pmatrix} = \begin{pmatrix} \sin \psi & 0 & \cos \psi \\ 0 & -1 & 0 \\ \cos \psi & 0 & -\sin \psi \end{pmatrix} \times \begin{pmatrix} \mathbf{e}_r \\ \mathbf{e}_\theta \\ \mathbf{e}_\phi \end{pmatrix}, \quad (2.26)$$

where ψ is the angle measured counter-clockwise from the mean field direction to the radial direction.

As a result, the radial, latitudinal, and azimuthal components of the anisotropy

vector can be written as:

$$A_r = A_c - \lambda_r G_r + \rho \sin \psi G_\theta + (\lambda_{\parallel} - \lambda_{\perp}) \sin \psi \cos \psi G_\phi, \quad (2.27)$$

$$A_\theta = -\rho \sin \psi G_r - \lambda_{\perp} G_\theta - \rho \cos \psi G_\phi, \quad (2.28)$$

$$A_\phi = (\lambda_{\parallel} - \lambda_{\perp}) \sin \psi \cos \psi G_r + \rho \cos \psi G_\theta - \lambda_\phi G_\phi, \quad (2.29)$$

(Forman and Gleeson 1975), where λ_{\parallel} and λ_{\perp} are the mean free paths parallel and perpendicular with respect to the mean field; $\lambda_r = \lambda_{\parallel} \cos^2 \psi + \lambda_{\perp} \sin^2 \psi$, and $\lambda_\phi = \lambda_{\parallel} \sin^2 \psi + \lambda_{\perp} \cos^2 \psi$; and G_r, G_θ , and G_ϕ are the radial, latitudinal, and azimuthal gradients, respectively.

The anisotropy of cosmic rays can be expressed in a spherically symmetric model where G_θ is absent and G_ϕ is zero in yearly averaged data. That is

$$A_r = \frac{3}{v} (CV - K_{rr} \frac{\partial U}{\partial r}), \quad (2.30)$$

$$A_\theta = \frac{3}{v} (K_A \sin \psi \frac{\partial U}{\partial r}), \quad (2.31)$$

$$A_\phi = \frac{3}{v} (K_{\parallel} - K_{\perp}) \sin \psi \cos \psi \frac{\partial U}{\partial r}, \quad (2.32)$$

where $K_{rr} = K_{\parallel} \cos^2 \psi + K_{\perp} \sin^2 \psi$. The radial and azimuthal components of this anisotropy give the diurnal variation, with magnitude

$$A^2 = A_r^2 + A_\phi^2, \quad (2.33)$$

and phase

$$\phi_{\max} = [180^\circ + \tan^{-1}(A_\phi/A_r)]/15 \text{ hr}, \quad (2.34)$$

where the phase ϕ_{\max} is expressed as the time of maximum intensity in hours.

In the classical interpretation, there are no drifts, and zero radial flow in which there is a balance between radially inward diffusion and outward convection, so that $A_r = 0$ (McCracken and Rao 1965). We thus have

$$A_\phi = \frac{3CV/v(K_{\parallel} - K_{\perp}) \sin \psi \cos \psi}{K_{\parallel} \cos^2 \psi + K_{\perp} \sin^2 \psi}. \quad (2.35)$$

If $K_{\parallel} \gg K_{\perp}$, then $A_{\phi} = 3C(V/v) \tan \psi$. In the Archimedean spiral model of the IMF (Parker 1958), $\tan \psi = \Omega r \sin \theta / V$, where Ω is rotational frequency of the Sun. We thus have $\xi_{\phi} = 3C\Omega r \sin \theta / v$. For $T > 1$ GeV, $C = 1.5$ for a typical power-law intensity spectrum of the form $P^{-2.5}$, with $V = 400 \text{ km s}^{-1}$, $\theta = \pi/2$, and for relativistic particles $v = c = 3 \times 10^8 \text{ m s}^{-1}$. Then we find $A_{\phi} = 0.6\%$ at 1 AU, and $\phi_{\max} = 18 \text{ hr}$. Because of the Ωr term, this is called the “corotational anisotropy” because its value is the same as it would be if particles corotated with the Sun (which they do not) with speed of 400 km s^{-1} . However, the diurnal anisotropy from observations is about 0.2-0.4%, roughly perpendicular to the Earth-Sun line and coming from 1800 Local Time (LT) in the 2-20 GeV proton energy range. This can be explained (e.g., Parker 1964, 1967, Jokipii and Parker 1969) in that the full corotation effect is realizable only if the perpendicular pressure gradient is relieved by scattering (diffusion) in irregularities perpendicular to the line of force. The calculations show that the geometry of the spiral form of the field beyond the orbit of Earth plays an essential role in providing sufficient diffusion across the lines of force. The calculations also show that variation in outer radius R and in K_{\perp}/K_{\parallel} due to changing wind conditions may contribute to some of the observed changes in the amplitude of the diurnal variation. Subramanian (1971) discusses small but cumulative errors that may reduce the value of A_{ϕ} to that observed if the value of the upper energy is less than 200 GeV.

This anisotropy maximum in the direction from 1800 LT may be the result from a mean flow of the isotropic diffusion along the lines of magnetic field, which lies in the direction to 9 h LT (i.e., from 21 h LT) on average. However, there is an additional flow caused by the magnetic fluctuations due to the solar wind flowing outward from the Sun (i.e., from 12 h LT). This flow tends to push cosmic ray particles to the 0-hour direction on average. Since the steady-state is considered in the equilibrium (no net flow in the radial direction), the flow of cosmic rays in the 12-hour direction is balanced and thus the anisotropy flows in the 18-hour direction as shown in Fig 2.11. In addition, the anisotropy is called “co-rotational” since it is in the same direction

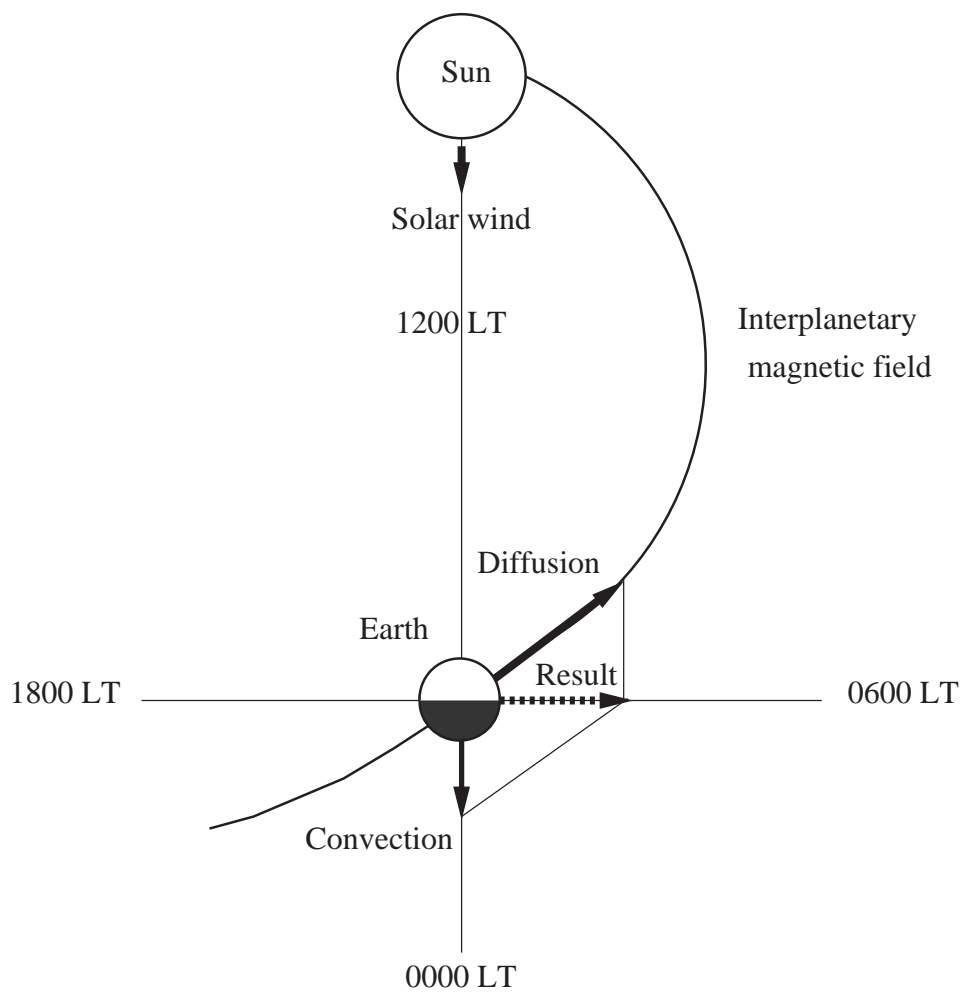


Figure 2.11: Diurnal anisotropy as a combination of contributions from convection and diffusion. This can explain the long-term average, but not short-term variations in diurnal anisotropy.

as the solar rotation. The mechanism as described is called the “convection-diffusion model” (Morrison 1956; Parker 1958; Gleeson and Axford 1967). The model employs the so-called “force field approximation” (Gleeson and Axford 1968). The force field approximation makes the assumption that no net radial streaming flow of cosmic ray flux occurs. This assumption is on the basis that large-scale changes in the IMF occur over time scales much longer than cosmic ray particle and solar wind transit times. Therefore, the radial flow of particles is approximately zero, which implies an isotropic cosmic ray flux in the corotating frame within the heliosphere.

It is notable that this balance exists in a statistical sense only. Departures from equilibrium streaming must occur in response to fluctuations of the relevant parameters of the interplanetary medium. However, the non-equilibrium streaming will eventually lead to a spatial redistribution of particles to the equilibrium condition (Hashim et al. 1972).

2.4.3 Modulation transport equation

To describe the galactic cosmic ray distribution in interplanetary space, the physical processes that govern the cosmic rays there need to be understood. In the zeroth-order approximation the motion of the guiding center of individual cosmic ray particles is along the mean spiral magnetic field direction. The electric field vanishes in the solar wind frame, a correlation length is small compared with the overall scale of the field, and the solar wind velocity V is small compared with the cosmic ray velocity v . The latter leads to a very small anisotropy of the cosmic rays in the frame of the wind, so that the diffusion, or Fokker-Planck, approximation to the particle motion is valid. To describe the random walk of the cosmic ray particles, we introduce the particle distribution $W(x_i, t)$. Then we transform to the fixed frame by using $x_i \rightarrow x_i - V_i t$ where V is the solar wind speed, but still define T as the kinetic energy. The divergence of the total particle flux gives the accumulation at a point, yielding the Fokker-Planck

equation (Parker 1965)

$$\frac{\partial W}{\partial t} + \frac{\partial}{\partial x_i} (WV_i) - \frac{\partial}{\partial x_i} \left(K_{ij} \frac{\partial W}{\partial x_j} \right) = 0. \quad (2.36)$$

If $U(x_i, T, t)$ represents the probability distribution over kinetic energy T , so that

$$W(x_i, t) = \int dTU(x_i, T, t), \quad (2.37)$$

then the Fokker-Planck equation for U is

$$\frac{\partial U}{\partial t} + \frac{\partial}{\partial x_i} (UV_i) + \frac{\partial}{\partial T} \left(U \frac{dT}{dt} \right) - \frac{\partial}{\partial x_i} \left(K_{ij} \frac{\partial U}{\partial x_j} \right) = 0. \quad (2.38)$$

The Fokker-Planck equation is derived from the complete continuity equation for $U(\mathbf{r}, T, t)$ where the net streaming in \mathbf{r} and T space with all quantities measured in the stationary frame (fixed frame) is

$$\frac{\partial U}{\partial t} + \nabla \cdot \mathbf{S} + \frac{\partial}{\partial T} \left(\frac{dT}{dt} \right) U = 0, \quad (2.39)$$

where in the frame fixed with respect to the Sun the observer sees the streaming flux as in equation (2.20). The energy gain that results from the energy change in the fixed frame is

$$\left(\frac{dT}{dt} \right) U = \mathbf{V} \cdot \nabla P \quad (2.40)$$

(e.g. Quenby, 1984). Now

$$\begin{aligned} \gamma m_0 v^2 &= \gamma E_0 \beta^2 = \beta^2 \gamma^2 \frac{E_0}{\gamma} = \frac{(\gamma^2 - 1)E_0}{\gamma} \\ &= \frac{\gamma + 1}{\gamma} (\gamma - 1) E_0 = \alpha T, \end{aligned} \quad (2.41)$$

where

$$\alpha = \frac{\gamma + 1}{\gamma} = \frac{T + 2m_0 c^2}{T + m_0 c^2}, \quad (2.42)$$

where $T = (\gamma - 1)m_0 c^2$ and m_0 is the particle rest mass. Putting $P = (1/3)U\gamma m_0 v^2$ (Quenby 1984) into equation (2.40) gives

$$\left(\frac{dT}{dt} \right) U = \mathbf{V} \cdot \nabla \left(\frac{\alpha T U}{3} \right) \quad (2.43)$$

After substituting equation (2.43) and equation (2.20) into equation (2.39),

$$\frac{\partial U}{\partial t} = -\nabla \cdot (C\mathbf{V}U) + \nabla \cdot (\mathbf{K}^s \cdot \nabla U) - \nabla \cdot \left(K_A \frac{\mathbf{B}}{|\mathbf{B}|} \times \nabla U \right) - \frac{1}{3} \frac{\partial}{\partial T} [\mathbf{V} \cdot \nabla (\alpha T U)]. \quad (2.44)$$

From the derivation, there is energy loss on average for all particles in the solar wind frame and the fixed frame equations arise finally as a result of the transformation of number density. However, an energy loss termed appeared in the final equation via the Compton-Getting transformation.

Alternatively, the third term on the right-hand side of Equation (2.44) can be rewritten to show the drift effect that was first considered by Jokipii and Levy (1977). Note that

$$\begin{aligned} 0 &= \nabla \cdot [\nabla \times (U K_A \mathbf{e}_3)] = \nabla \cdot [(\nabla U) \times (K_A \mathbf{e}_3) + U \nabla \times (K_A \mathbf{e}_3)] \\ &= -\nabla \cdot [(K_A \mathbf{e}_3) \times \nabla U] + \nabla \cdot [U \nabla \times (K_A \mathbf{e}_3)] \end{aligned} \quad (2.45)$$

(Chen 1989) by using the vector identity $\nabla \times (f\mathbf{A}) = f\nabla \times \mathbf{A} + \nabla f \times \mathbf{A}$. By definition, the pitch-angle drift velocity over the near-isotropic particle distribution is

$$\langle \mathbf{v}_d \rangle = \nabla \times \left(K_A \frac{\mathbf{B}}{|\mathbf{B}|} \right) \quad (2.46)$$

(Parker 1957; Jokipii et al. 1977), so we have

$$\nabla \cdot \left(K_A \frac{\mathbf{B}}{|\mathbf{B}|} \times \nabla U \right) = \nabla \cdot (\langle \mathbf{v}_d \rangle). \quad (2.47)$$

Hence, the contribution of drifts in the Fokker-Planck equation is through the divergence of the drift current. Equation (2.46) indicates that the guiding centers of an isotropic distribution of particles will have a net motion parallel to \mathbf{B} if $\mathbf{B} \cdot (\nabla \times \mathbf{B}) \neq 0$, and a net motion perpendicular to \mathbf{B} if the field gradient $\nabla B \neq 0$ or $(\mathbf{B} \cdot \nabla)\mathbf{B} \neq 0$.

The fourth term of equation (2.44) can be further simplified by substitution of equation (2.18) into equation (2.44) to give

$$\frac{\partial U}{\partial t} = -\nabla \cdot (\mathbf{V}U) + \nabla \cdot (\mathbf{K}^s \cdot \nabla U) - \langle \mathbf{v}_d \rangle \cdot \nabla U + \frac{2}{3} (\nabla \cdot \mathbf{V}) \frac{\partial}{\partial T} (\alpha T U). \quad (2.48)$$

In conclusion, there are four physical processes in equation (2.48): convection, diffusion, gradient and curvature drifts, and adiabatic deceleration in the first, second, third, and fourth terms in the right-hand side, respectively.

2.4.4 Spherically symmetric modulation

Spherically symmetric modulation throughout the heliosphere is a reasonable assumption for describing the main features of 11-year modulation (but not 22-year modulation). Then we assume that $U = U(r, T)$ with no latitudinal or longitudinal gradients. In addition, the observations reveal that solar wind speed \mathbf{V} is in the radial direction so the radial component of equation (2.20) can be written in the form:

$$S_r = C\mathbf{V}U - K_{rr} \frac{\partial U}{\partial r}, \quad (2.49)$$

where K_{rr} is the radial diffusion coefficient for cosmic rays with kinetic energy T . At high energies (≥ 1 GeV) the Compton-Getting C is fairly fixed at 1.5 and S_r is observed to be infinitesimal ($S_r = 0$), so equation (2.50) becomes (e.g., Gleeson and Axford 1968)

$$\frac{1}{U} \frac{\partial U}{\partial r} = \frac{C\mathbf{V}}{K_{rr}}. \quad (2.50)$$

Integration of this equation gives the solution (Jokipii 1971)

$$U(r, T) = U_\infty(T) \exp \left[-C \int_r^{D_m} \frac{V}{K_{rr}} dr \right], \quad (2.51)$$

where $U_\infty(T)$ represents the interstellar density of cosmic rays with energy T at the outer boundary of the spherical modulation region, $r = D_m$. This simple picture can qualitatively explain the features of the 11-year variation of cosmic ray intensity which possesses strong modulation during sunspot maximum. As a consequence, the modulation can be caused by an (i) increase in V and/or (ii) increase in D_m and/or (iii) decrease in K_{rr} during this period.

The radial dependence is due to K_{rr} , which may be expressed in terms of K_{\parallel} , K_{\perp} , and the spiral angle ψ by transforming \mathbf{K} from the Cartesian coordinate system with \mathbf{e}_3 in the direction of the IMF into a spherical coordinate system with $\theta = \psi$. Since

$$\mathbf{e}_r = \sin \psi \cos \phi \mathbf{e}_1 + \sin \psi \sin \phi \mathbf{e}_2 + \cos \psi \mathbf{e}_3, \quad (2.52)$$

therefore

$$K_{rr} = \mathbf{e}_r \cdot \mathbf{K} \cdot \mathbf{e}_r = K_{\parallel} \cos^2 \psi + K_{\perp} \sin^2 \psi. \quad (2.53)$$

Then K_{\parallel} and K_{\perp} can be calculated from the IMF power spectrum and solar plasma data.

For spherically symmetric modulation without statistical acceleration, the modulation equation can be expressed as:

$$\frac{\partial U}{\partial t} + \frac{1}{r^2} \frac{\partial}{\partial r} \left(r^2 V U - r^2 K_{rr} \frac{\partial U}{\partial r} \right) = \frac{1}{3r^2} \frac{\partial}{\partial r} (r^2 V) \frac{\partial}{\partial T} (\alpha T U) \quad (2.54)$$

(cf. Parker 1965; Gleeson and Axford 1967).

2.4.5 Non-spherically symmetric modulation

Actually, the three-dimensional dynamical heliosphere the latitudinal effects of cosmic ray modulation must be established. Even though the spherically symmetric modulation can explain the gross cosmic ray modulation during solar maximum qualitatively, the features of the latitudinal and 22-year variation of cosmic ray intensity as observed by the ground-based and space-borne detectors cannot be achieved by this picture. From the observational evidence, Sarabhai and Subramanian (1966) suggest that the marked excess in 5303 Å coronal line activity at northern heliolatitudes might lead to a north to south gradient in cosmic ray intensity. The solar polar coronal holes and the magnetic fields related to the polar regions play a role in the modulation process.

Perpendicular gradients and related anisotropies are direct evidence of a non-spherically symmetric cosmic ray distribution (Hedgecock et al. 1972; Quenby 1984). Hashim and Bercovitch (1972) show that the $\mathbf{B} \times \nabla U$ drift due to a north to south gradient showed up in neutron monitor and meson telescope data as a sector structure-correlated effect in the diurnal variation. In other words, for \mathbf{B} outwards, $\nabla_{\perp} U$ to the south yields a flow 45° E of the Earth-Sun line. They also found relationship between the latitudinal gradient and rigidity as $G_{\theta} = (R/\text{GV})^{-0.65} 5.5\% \text{ AU}^{-1}$. Besides this, direct measurement of the latitudinal gradient by spacecraft (McKibben et al. 1979,

Roelof et al. 1981) indicated a magnitude of 1 to 5% per degree at $P \sim 1$ GV. Use of the Earth's excursion of $\pm 7.25^\circ$ in heliolatitude over a year can give rise to annual and semiannual waves in cosmic ray intensity. Swinson and Kananen (1982) employed sector-structure correlated changes in the ecliptic plane component of the diurnal variation seen by cosmic ray detectors to confirm the direction switch of the antisymmetric gradient seen by Antonucci et al. (1978). Swinson and Kananen emphasized the dominance of this one-way gradient over the symmetric gradient. Alternatively, local control of the position of the current sheet and its variability in the plane of symmetry of the cosmic ray intensity is analyzed (Moussas and Tritakis 1982). They point out that in 1974-1977 there was an influence of the north polar coronal hole at all latitudes, agreeing with the southward displacement of the current sheet predicted by Rosenberg (1970). However, rather less than 50% of the polarity data are in good statistical agreement with the Rosenberg effect model for the dominant sector structure.

The related anisotropies seen in equation (2.29) support that the latitudinal gradient causes the cosmic ray variations. When the cosmic ray intensity is azimuthally symmetric ($\partial/\partial\phi = 0$), this vector has three components in spherical coordinates according to equation (2.29) as:

$$A_r = 3CV/v - \lambda_{rr}G_r + \text{sgn}(B)\rho \sin \psi G_\theta, \quad (2.55)$$

$$A_\theta = -\text{sgn}(B)\rho \sin \psi G_r - \lambda_\perp G_\theta, \quad (2.56)$$

$$A_\phi = (\lambda_\parallel - \lambda_\perp) \sin \psi \cos \psi G_r + \text{sgn}(B)\rho \cos \psi G_\theta, \quad (2.57)$$

where $\text{sgn}(B) = +1(-1)$ in $qA > 0(< 0)$ drift cycles (Bieber and Chen 1991).

2.4.6 The solar cycle modulation

As seen in Figure 2.3, the time variation of neutron monitor counting rates, which correspond to cosmic ray protons at energies of several GeV, has an 11-year cycle associated with the solar sunspot cycle, with pronounced maxima occurring during sunspot minima. The 11-year cosmic ray cycle is qualitatively related to large scale

structures from the Sun. The increased modulation (i.e., cosmic ray decrease) during periods of solar maximum is related to more magnetic turbulence, which decreases the diffusion coefficient in the outer heliosphere. This leads to strong modulation. Furthermore, the accumulation of numerous transient shocks and coronal mass ejections (CMEs) in the distant heliosphere will create magnetic barriers (so-called global merged interaction regions, or GMIRs) which also reduce the transport of cosmic rays into the inner heliosphere (le Roux and Potgieter 1995). In contrast, during solar minimum there is a lower level of magnetic turbulence and fewer magnetic barriers for cosmic rays so that cosmic ray modulation is lower.

There is also a strong trend of a 22-year cycle when the cosmic ray maxima alternate between sharper and more rounded peaks. This can be readily understood to be the result of the alternating direction of the gradient and curvature drifts of the cosmic rays as the solar magnetic field changes sign at successive sunspot maxima (Jokipii and Thomas 1981; Kota and Jokipii 1983). The 22-year cosmic ray cycle is related to the 22-year magnetic polarity cycle. The polarity of the Sun's magnetic field is important for the cosmic ray drift that arises from the anti-symmetric part of the diffusion tensor (K_A) in Parker's transport equation. During the period in which the solar magnetic fields spiral outward in the north and inward in the south ($A > 0$), the GCR protons (with $qA > 0$) drift into the heliosphere from the polar regions of both hemispheres, which are separated by the HCS. Easy access of GCRs over the poles of the Sun is expected because the magnetic field lines there are much less wound up. During the opposite polarity, where the solar fields are inward in the north and outward in the south ($A < 0$), GCR protons drift into the heliosphere along the HCS. As a result, drifts and waviness of the HCS along the solar cycle can explain the alternating flat and peaked cosmic ray intensity (Jokipii and Kota 2000) where the current sheet is relatively flat during the center of the solar cycle minimum. During a $qA > 0$ epoch the cosmic rays come in along the poles of the heliosphere and are insensitive to the structure of the HCS. The full intensity is thus reached much sooner and remains at a high level

throughout solar minimum; the cosmic rays will exhibit a flat time intensity profile. On the other hand, during a $qA < 0$ epoch the cosmic rays come along the HCS to reach Earth's orbit and are sensitive to the waviness of the HCS. Thus, cosmic ray flux is increased when the HCS is nearly flat; the cosmic ray intensity will exhibit a peaked time intensity profile, and decreases when the tilt and the waviness of the HCS increase.

Drift models often assume the same K_{\parallel} and K_{\perp} for alternating 11-year cycles and predict smaller radial gradients for the $qA > 0$ cycle when particles drift inward at the poles. The latter is in accord with the phase shift of the corotational anisotropy to earlier hours that has been observed in the diurnal variations in the 1-100 GV range; the phase shift toward earlier hours is due to smaller inward diffusion than outward convection.

2.5 Corotating solar wind structures

During the solar minimum of activity cycle (sunspot cycle), the largest structures that persist quasi-periodically in the heliosphere are corotating solar wind structures (CSWSs). The CSWSs co-rotate with the Sun with the period of about 27 days, and are three-dimensionally distributed in interplanetary space. The CSWSs mainly comprise expanding high-speed solar wind streams (HSSs) with speeds of about 450-800 km s⁻¹, and the subsequent interaction of the HSSs emerged from coronal holes (CHs) with the slow-speed streams. In the frame work of current theory, these quasi-periodic structures may contribute significant solar effects to 27-day variations in GCR intensity and diurnal anisotropy as observed by neutron monitors at ground level.

2.5.1 Coronal holes as a source of high speed solar wind streams

Coronal holes are regions of low-density plasma, and open unipolar magnetic fields on the Sun. They appear dark in ultraviolet and X-ray wavelengths because of the low emission in these windows compared with surrounding regions at the Sun. Coronal

holes were first recognized in the late 1950s, when M. Waldmeier noticed long-lived regions of tiny intensity in images made with a visible light coronagraph (Murdin 2001). In the 1960s and 1970s, ultraviolet and X-ray images of the Sun taken with rocket-borne and orbiting telescopes confirmed that coronal holes exist as discrete patches of lower brightness on the solar disk.

Primarily, coronal holes are sites of acceleration of HSS (Krieger et al. 1973; Nolte et al. 1976; Hundhausen 1977). The comprehensive Skylab observations in the early 1970s allowed making the connection between rotating coronal holes and transient HSSs at the Earth's orbit. A famous coronal hole observed with Skylab in 1973 is shown in Figure 2.12. Later, the Ulysses spacecraft, which passed over the north and south poles of the Sun in the early 1990s, found that outside a $\pm 20^\circ$ range around the ecliptic plane, the solar wind was exclusively high-speed. In addition, at latitudes higher than 50°S , only the fast solar wind streaming out of the coronal hole is observed (Phillips et al. 1995). Because Ulysses's observations were done during the declining phase of the solar cycle, this large volume of HSS can be thus well correlated with the long-lasting northern and southern polar coronal holes. Coronal holes can migrate to low-latitudes or even extend across the equator (Zirker, 1977) and cause HSS observed near the ecliptic plane. The data from the Pioneer 10/11 and Voyager 1/2 deep space missions (Richardson, 2004 and references therein) and the journey of Ulysses over the region of solar poles have provided great understanding of many effects that were first identified in the neutron monitor data. Therefore, the identification of coronal holes as the source of HSSs is one result of high resolution observations of the Sun that have been critical for interpreting results from neutron monitors.

Coronal holes occur when the Sun's magnetic field is open to interplanetary space. The open configuration of the magnetic field allows solar wind plasma to escape more easily as a HSS. The open magnetic field lines rooted in coronal holes are expected to expand superradially, i.e., into a larger volume than would be expected if the field pointed radially away from the center of the Sun (Figure 2.8). This arises because

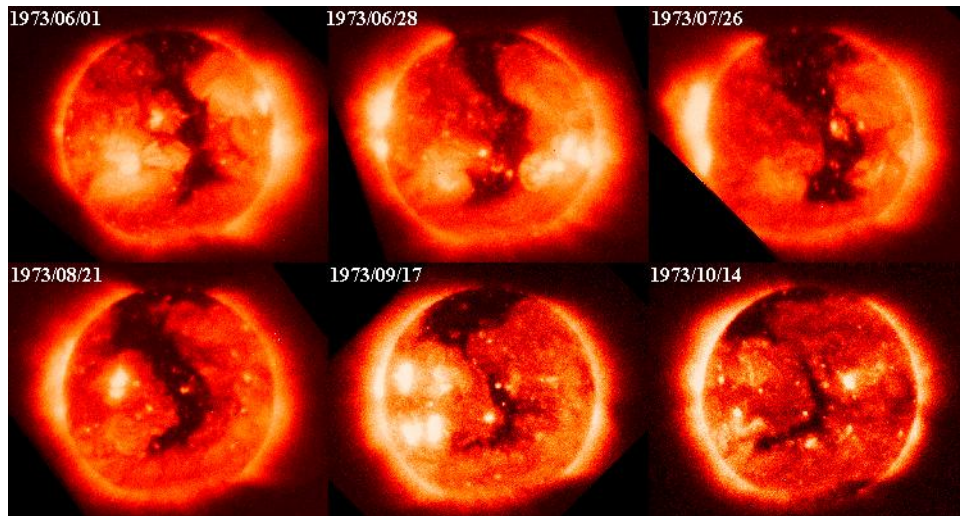


Figure 2.12: The first continuous observations of coronal holes were made with Skylab in the 1970s in soft X-rays. Coronal holes (dark regions) sometimes take the shape of channels rather than round holes, and may hold their shape though several rotation of the sun. (<http://soi.stanford.edu/results/SolPhys200/Hudson/2000/001020/001020.html>).

the solar magnetic field near solar minimum has a strong dipolar component. At large distances from the Sun, the energy in the HSS begins to exceed the magnetic energy, so the solar wind is able to stretch the magnetic field lines nearly radially.

2.5.2 Corotating interaction regions

The interaction of a HSS that has relatively straight field lines (see equation (2.8)) with slow solar wind (normally confined to the vicinity of the HCS) of less than about 400 km s^{-1} that has more strongly curved field lines produces a corotating interaction region (CIR) at the leading edge of the HSS. The solar wind plasma density and magnetic field are increased there by a collision and kinetic steepening to form a compression wave at the leading edge of HSSs. The kinematic steepening is a nonlinear term $(\mathbf{V} \cdot \nabla)\mathbf{V}$ in kinematic equations of plasmas. The compression also extends to high latitudes, but the amplitude of the compression decreases latitudinally (Barouch and Burlaga 1976). A kinematic rarefaction would cause a decrease in the magnetic field strength (Parker 1963) at the trailing edge of HSSs.

Figure 2.13 shows an idealized evolution of a CIR in the inner heliosphere. As

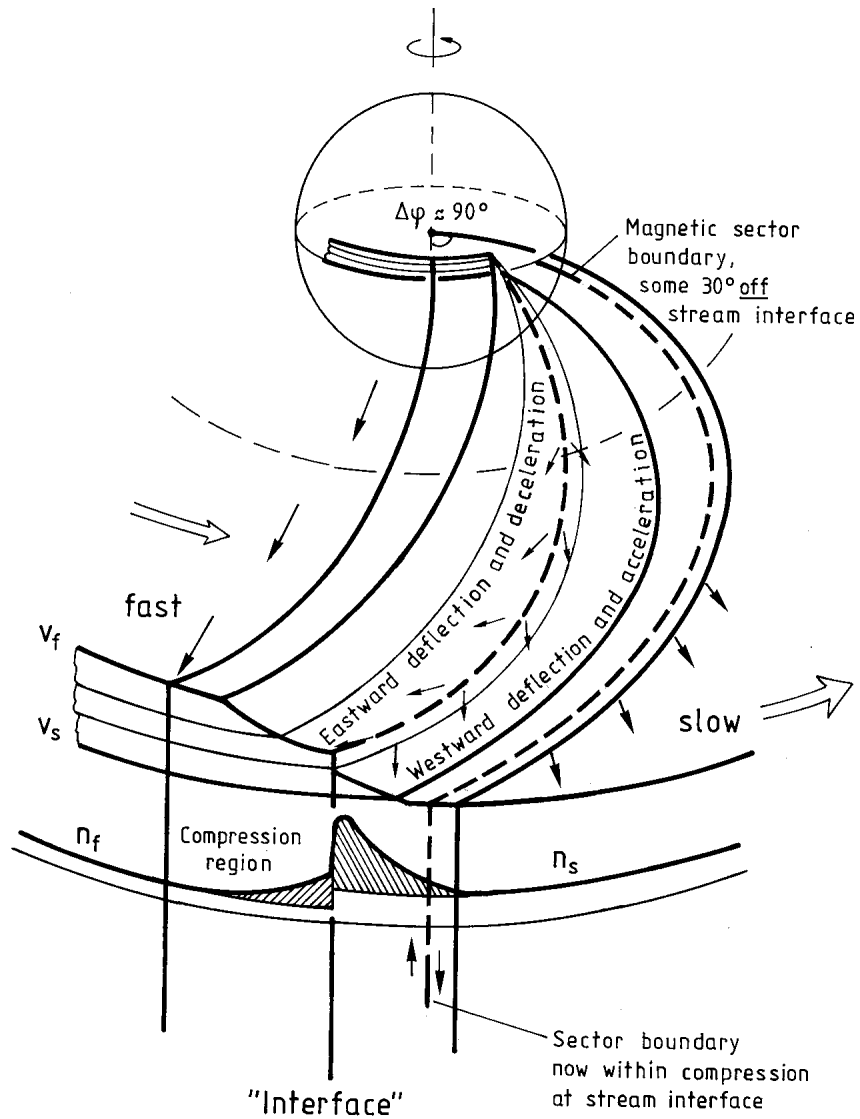


Figure 2.13: An idealized view of a corotating interaction region (CIR) and its evolution from a rectangular speed profile at the Sun into a more gradual speed increase at 1 AU (Schwenn 1990).

fast and slow streams propagate outward, flow compression and deflection on both sides of the interface smooth the abrupt change in the solar wind speed, leading to a continuous increase in solar wind speed as well as temperature and total pressure. The dynamical process is the deflection in the flow direction of the solar wind stream interaction. On the leading edge, the slow wind is deflected westward. The difference in the velocity shear at the front and rear boundaries of the stream is attributed to kinematic steepening of the front boundary and kinematic broadening of the rear boundary (Burlaga 1995). A sector boundary may be present in the slow solar wind preceding a CIR, or may be incorporated into the CIR along with the slow solar wind (e.g., Pizzo and Gosling 1994).

The CIR lies approximately along the Archimedean spiral. Among both streams there is a stream interface (SI) since the magnetic field lines cannot be merged. Magnetic sector boundaries are often found close to the SIs at 1 AU, but they do not physically relate to each other (Schwenn, 2006). The magnetic field is maximal at the SI, because the gradient in speed is greatest there (Pizzo 1982). A CIR appears as a band located around the solar equator in the form of tilted shell, depending on heliolatitudes and heliolongitudes (Gosling and Pizzo, 1999). CIRs are thus dominant structures in the solar wind where high- and low-speed solar wind interact in the heliosphere during solar activity minimum. When persistent coronal holes and their associated HSSs are present at low heliospheric latitudes, a recurrent disturbance pattern of the HCS and alternating magnetic sectors dominates the solar wind. A model of a CIR along the wavy HCS is depicted in Figure 2.14. The forward waves propagate to lower heliographic latitudes and the reverse shocks/waves to higher latitudes with increasing heliocentric distance. Since CIRs are inclined relative to the radial direction, the forward and reverse waves bounding the CIRs have both radial and azimuthal components of propagation.

2.5.3 27-day cosmic ray intensity variations

The 27-day recurrent variations in the fluxes of cosmic rays are generated by solar wind and interplanetary magnetic field structures that recur with the period of

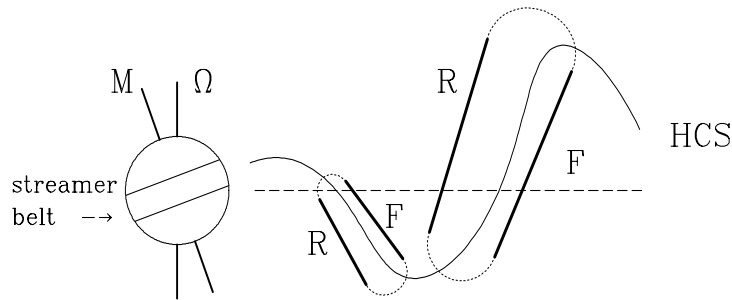


Figure 2.14: Schematic model of the tilted dipole. The magnetic axis, M , is tilted with respect to the rotation axis. Slow solar wind emanates from the streamer belt around the heliomagnetic equator. The tilted magnetic equator evolves into a wavy heliospheric current sheet (HCS). CIRs are bounded by forward (F) and reverse (R) shocks. Sizes are not in scale (Kóta and Jokipii 1998).

solar rotation. The 27-day variations (sometimes called 26-day variations when observed from a spacecraft) are observed from an Earth-orbiting spacecraft or a ground-based instrument in the synodic frame. The state of the interplanetary magnetic field and both the isotropic and anisotropic components of the cosmic ray intensity all more or less vary with the period of about 27 days. In the past, the search for the regions on the Sun responsible for the recurring intensity variations examined correlations with intense recurring coronal green line emission regions (Babcock 1953, Simpson et al. 1955). This led to matching of recurring unipolar magnetic field regions (UM), later are called “coronal holes”, with the 27-day recurring cosmic ray intensity modulation (Simpson et al. 1955). The history of recurrent modulation has been reviewed by Simpson et al. (1998).

The 27-day variations of GCRs associated with the CSWSs have been observed and studied for a long time as described above. GCRs are affected by the structures since they act as barriers that inhibit the inflow of GCRs from the outer heliosphere. The count rate is reduced temporarily (modulated) followed by a recovery phase in the trailing portion of the HSS. McKibben et al. (1999) shows how CIRs produce clearly visible recurrent 27-day modulation in the cosmic ray intensity but are principally responsible for the local phenomenon of modulation. CIRs affect the short-term cosmic

ray variations that are driven by CSWSs via the change of particle diffusion properties in the local interplanetary space in low and middle latitudes (Chih and Lee 1986; Kóta and Jokipii 1991). GCRs are thus affected by these structures in terms of remarkable quasi-periodic 27-day variations that could be clearly noticed in neutron monitor count rates.

However, from the Ulysses investigations of CIRs and the recurring modulation of GCRs, for latitudes more than 40°S where the signature of CIRs is not detected, the 27-day variation is still be observed. This suggests that the observed particle recurring intensity variations are not a local modulation phenomena (McKibben et al. 1995). The same authors found that the amplitudes of recurring modulation of the GCRs are controlled by the modulation mechanism and particle propagation, which are a function of particle magnetic rigidity, rather than energy per nucleon. This is in agreement with the magnetic rigidity dependence for the 27-day variations from Climax (~ 3 GV) to Huancayo (~ 20 GV) as first reported by Fonger (1953) and Simpson (1954). The amplitude of the high-energy cosmic ray intensity variations is the largest in middle-latitude regions and decreases for increasing solar latitude.

The recurrent variations of cosmic ray fluxes are related to CIRs and the HCS, which are recurrent structures in the interplanetary medium in low and middle latitude regions during the solar activity minima. These can provide considerable information on the mechanisms of cosmic ray transport, e.g., diffusion and gradient/curvature drifts, and thereby, indirectly, information on solar modulation in the global heliosphere (Zhang et al. 1999 in Fisk and Jokipii 1999). Although CIRs cannot produce a global or a long term effect on the cosmic rays, studies using magnetic field and cosmic ray measurements from Voyager in the outer heliosphere (Burlaga et al. 1985) have established that the reduced particle diffusion in the enhanced magnetic fields inside the interaction regions is a source for cosmic ray depressions. Therefore, it has been proposed that the 11-year solar cycle cosmic ray variation is the result of accumulated disturbances from global merged interactions (Burlaga et al. 1993).

CHAPTER III

PRINCESS SIRINDHORN NEUTRON MONITOR

HRH Princess Sirindhorn graciously gave her permission for a neutron monitor station at Doi Inthanon, Thailand's highest mountain, to be called the "Princess Sirindhorn Neutron Monitor" (PSNM) on 2003 January 29. PSNM is a joint project between Chulalongkorn University, Mahidol University, and Ubon Ratchathani University. After donation of the neutron monitor detection system from Shinshu University, Japan, and support for transportation of the instruments to Thailand from the US National Science Foundation (US NSF) via the Bartol Research Institute, University of Delaware, construction of PSNM was initiated in October, 2006 and then finished in August, 2007. In addition, groups from the University of Delaware, Shinshu University, and Tasmania University, Australia, provided substantial technical recommendations for setting up PSNM. Additional support for materials and supplies was also provided by Mahidol University, Ubon Ratchathani University, Chulalongkorn University, the Thailand Research Fund (TRF), and so on.

PSNM is one of many ground-level neutron monitor stations in the world for detecting and recording the by-products of nuclear interactions of high energy primary cosmic rays with Earth's atmosphere. However, with the highest geomagnetic cutoff (threshold) rigidity in the world, PSNM has provided unique data on primary cosmic rays and other valuable scientific information since 2007. PSNM is continuously monitoring and recording mainly the flux of the GCRs with a large detector at a high time resolution to overcome the small flux of high-rigidity GCRs at Earth. These high count rate data are sufficient to study and investigate the short- and long-term variations of GCRs, and the time and rigidity dependence of the GCR flux. For short-term variations, the key point

is the directional dependence of the GCR flux, including transient diurnal anisotropy of cosmic rays. Moreover, we may study space weather affected by the solar wind and solar storms, 27-day variations in the GCR flux in association with solar rotation, the cosmic ray spectrum at solar minimum, and the rigidity dependence of Forbush decreases due to solar flares and coronal mass ejections. In conclusion, PSNM serves to provide unique data and information on the highest energy cosmic rays ever recorded by a fixed neutron monitor station, which are important in studying the spatial and temporal variations of GCRs.

The following Sections aim to provide understanding of the physical structures of PSNM, detection of neutrons, the variations of GCRs observed with PSNM, and quantifying the measurements as free space quantities.

3.1 Station information

3.1.1 Geographical location

The PSNM station is located at the summit of Doi Inthanon in Chiang Mai Province at latitude 18.59°N and longitude 98.49°E . Doi Inthanon is the highest mountain in Thailand with altitude 2565 m from sea level. The altitude of the station is very important because the neutron flux decreases exponentially when the pressure increases; the neutrons are absorbed in the atmosphere according to the air mass or pressure over the station. Consequently, with every decrease in altitude of 100 m, neutron counts are reduced by about 8%. For example, if the PSNM were set at altitude 2000 m from sea level the neutron count rates would greatly decrease, by about 40%. Therefore, the neutron monitor should be placed at high altitude to record the neutron count rates with improved statistics. According to these effects, the reduced atmospheric absorption at 2560 m leads to a count rate that is 6 times higher than at sea level. PSNM is therefore one of five neutron monitor stations that record the highest count rates in the world.

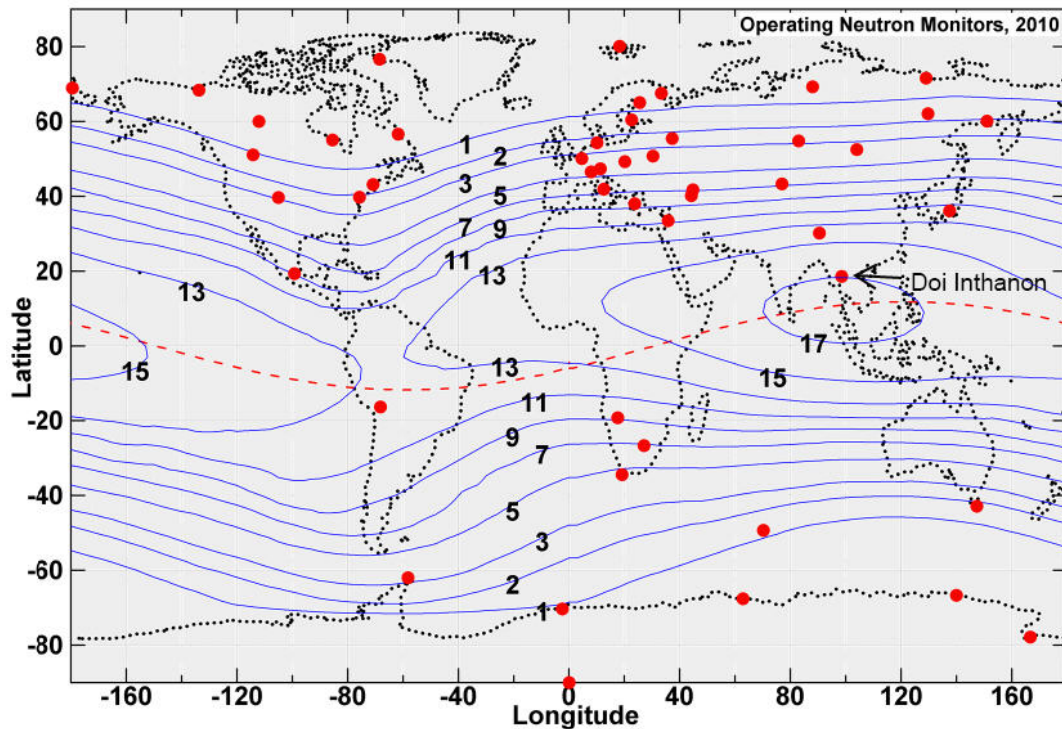


Figure 3.1: Cutoff rigidities of PSNM at Doi Inthanon and other neutron monitors around the world. [Courtesy of R. Pyle.]

3.1.2 Geomagnetic location and cutoff rigidity

Thailand is in a unique location, at the Earth's magnetic equator and close to the offset dipole center. Here the Earth's horizontal magnetic field is strongest, and only relatively high-energy (or high-rigidity) particles can penetrate the field. PSNM is the fixed neutron monitor station located at the world's highest vertical geomagnetic cutoff rigidity (16.8 GV) (see Figure 3.1). This effective cutoff rigidity is obtained as a single value to specify the equivalent total accessible cosmic radiation within the "penumbra" (rigidity range with partial transmission) in a specific arrival direction at a particular location. The values of cutoff rigidities vary from 0 near the geomagnetic poles and around 17 GV in Thailand.

As the count rate decreases with increasing rigidity according to the decreasing cosmic ray energy spectrum, count rates recorded at sea level in Thailand must be the lowest for one tube anywhere in the world. However, with 18 tubes of the neutron

monitor at high altitude, the PSNM count rates are sufficiently high that they can be used for advanced analysis.

3.1.3 Configuration of the Princess Sirindhorn Neutron Monitor

To achieve useful measurements of secondary neutrons from the Earth's atmosphere in the proportional counter and continuously operate the neutron monitor for several decades, the configuration of the neutron monitor must be well designed and isolated from the outer environment. Therefore, the PSNM building was constructed as shown in Figure 3.2 and the interior of PSNM is shown in Figure 3.3. The station includes the following:



Figure 3.2: The building of the PSNM station.

- The building. This configuration protects the overall instrumentation systems inside from some outdoor factors such as sunlight, rain, and wind. The building allows some control of the temperature and relative humidity. The dehumidifier system helps to absorb the water vapor at Doi Inthanon where the humidity is close to 100% much of the time. The dehumidifier is critical to proper operation

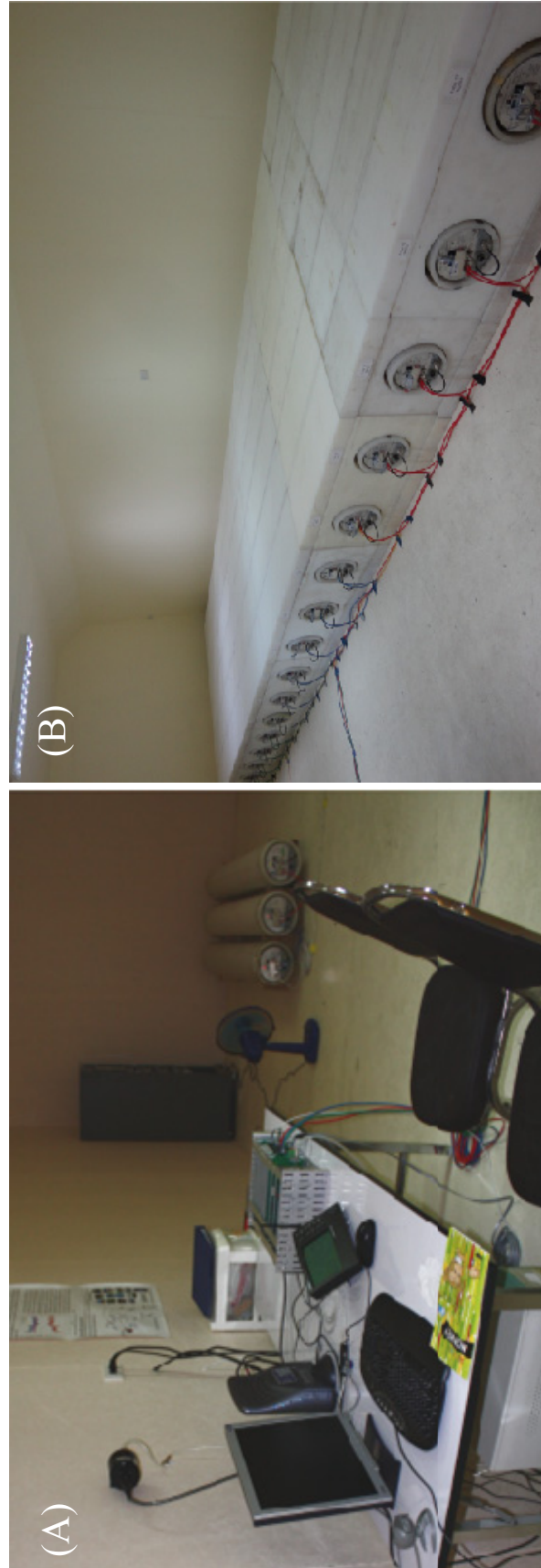


Figure 3.3: The interior of PSNM at Doi Inthanon. (A) Main data acquisition systems, storage devices, and three bare counters. (B) 18-tube neutron monitor with proportional tube detection systems.

in a tropical environment, as the proportional counters are maintained at high voltage and are very sensitive to humidity.

- Proportional tube detection systems. This part includes 18 proportional tubes in a standard NM-64 design as shown in Figure 3.3. The configuration of PSNM, from the outer to the inner parts, includes an outer moderator/reflector made of polyethylene, 29 tons of lead producer, the inner polyethylene moderators, and $^{10}\text{BF}_3$ gas-filled counter tubes. Three bare counters without a reflector or lead producer are also installed. The pre-amplifier is schematically shown in Figure 3.4. This is a crucial part of the detection systems.
- Electronics and data acquisition systems. This part includes an interface for the neutron counters, power supply, real-time clock, 3 barometers, and readout board, which can be seen in Figure 3.3(A).
- The storage devices. A computer system monitors and continuously records the neutron monitor count rates, bare count rates, pulse height and time delay histograms, and other housekeeping information. The data are recorded on hard disks of the computer while a visual basic program kindly provided by Paul Evenson displays the operational details and essential data such as the count rate data and air pressure readings from the barometers.

For more details of the installation, building, and other features of the PSNM, the reader may see in Nutaro (2008) and Kamyan (2011).

Now, we will focus on the proportional tube detection systems since they detect the neutrons. The principles of the NM64 can be described according to its configuration. Two basic types of neutron interactions with matter are involved. First, a neutron can be scattered and slowed down by a light nucleus such as a proton (hydrogen nucleus), transferring some of its kinetic energy to the nucleus. Second, the neutron can induce a nuclear reaction. An incoming atmospheric neutron, typically of sub-GeV

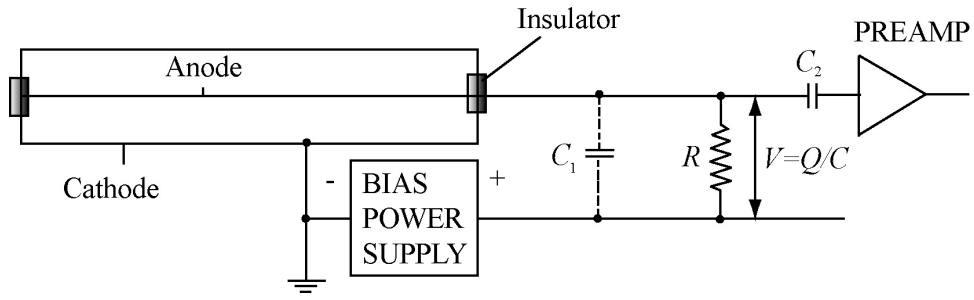


Figure 3.4: Typical setup for gas-filled neutron detectors.

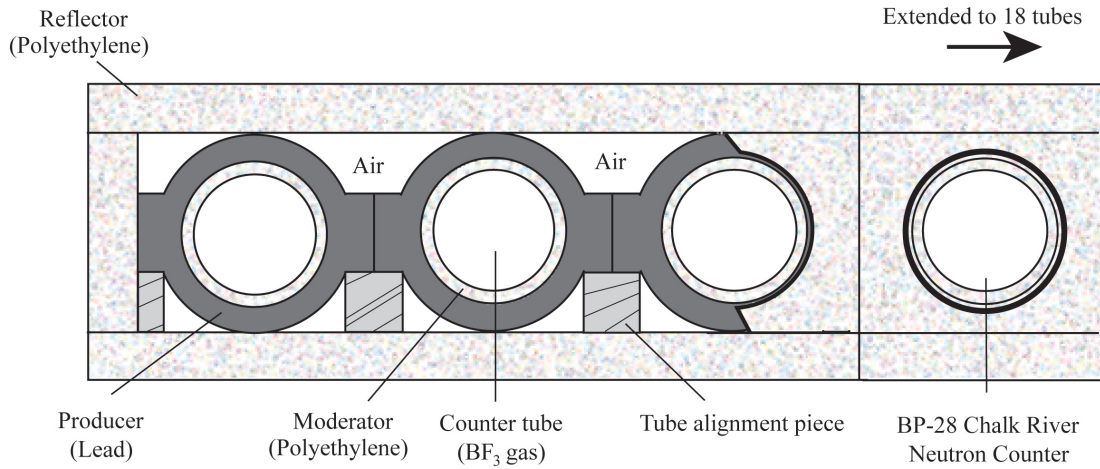


Figure 3.5: Sketch of cross-section of the standard 18NM64 neutron monitor at Doi Inthanon.

energy, can interact with a lead nucleus, causing it to fragment and produce several more neutrons, typically in the MeV range, amplifying on signal. After slowing down in the reflector and/or moderator (which have only light nuclei and a high hydrogen content), a neutron with epithermal or thermal energy finally interacts with a ^{10}B nucleus in the tube according to



emitting the charged particles ${}^7\text{Li}$ and ${}^4\text{He}$ into the gas. The counters are operated in the proportional mode, and the ionization produced by the reaction products initiates the multiplication process and generates a strong electronic signal. The principle components in the NM64 design are shown in Figure 3.5 and summarized as follows.

1. The polyethylene moderator/reflector serves to reject low-energy neutrons produced in atmospheric showers and in the local surroundings from entering the detector. It also serves to contain low-energy neutrons produced in interactions within the lead. The moderator contains a significant fraction of H as the energy loss per neutron elastic collision increases with decreasing atomic mass A (e.g., Clem and Dorman 2000) as

$$\frac{dE}{E} = \frac{4A \cos^2 \Theta_{\text{recoil}}}{(1 + A)^2}. \quad (3.2)$$

2. The lead producer of 99.99% purity provides a thick heavy-nucleus target for inelastic interactions in which secondary neutrons are produced, known as evaporation neutrons. The neutron production rate per unit mass of material is proportional to A^γ with $\gamma \sim 0.7$ in the 100-700 MeV incident energy range, which slowly decreases with increasing energy (at $E \geq 400$ GeV, $\gamma \sim 0.0$; Shen, 1968). The evaporation neutrons have an energy distribution that shows a maximum at about 2 MeV and reaches energies up to about 15 MeV. The following specifications apply to the NM64 type neutron monitor. The probability for a cosmic ray neutron or proton that hits the neutron monitor to interact with a nucleus of the lead target is $\sim 50\%$. The average number of evaporation neutrons produced per nuclear reaction in the lead is 15 and the detection probability for evaporation neutrons by the counter tube is 6%. With these parameters, the average count rate of a high latitude sea level NM64 neutron monitor with 6-BF₃ counter tubes is 70 counts s⁻¹ and for an equatorial sea level neutron monitor it is 50 counts s⁻¹.

3. The inner polyethylene moderator contains a large fraction of H that slows down a secondary neutron from the lead producer. The neutron elastic interaction path-length of H in typical moderator material is ~ 1 cm for $E_n \leq 1$ MeV and each interaction reduces the incident neutron energy by a factor of two on average. Consequently, the neutron is slowed down to thermal energies around 0.025 eV to enhance the probability of detection in the counter.

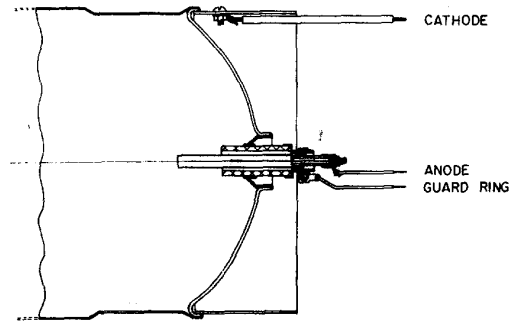


Figure 3.6: Cross section of output end of type BP28F stainless steel cathode counter (from Fowler 1963).

4. The gas-filled counter is the most important assembly in the neutron monitor. The neutron monitor at PSNM uses BP-28 Chalk River neutron counters. The counter assembly weights 40 kg and consists of three parts. First, the amplifier-discriminator possesses a fully transistorized output amplifier and 0.3 volts or more at 30 ohms impedance discriminator. Second, the BP28 neutron counter is made from a stainless steel cylinder 1.90 m long and 15 cm in diameter with an electrical connector at one end. The cross-section of the output end of a stainless steel counter is shown in Figure 3.6. Detector walls are ~ 0.075 cm to 0.084 cm thick stainless steel that absorbs ~ 3 % of the neutrons. The diameter of the anode wire is 0.2 mm and the anode is near ground. The cathode is maintained at high voltage of about -2.8 kV so electrons drift toward the anode in the strong electric field between the cathode and anode. The capacitance in the cylindrical tube is about 20 pF. With $V = Q/C$, a signal of ~ 1.5 mV is produced. The tube is filled to a pressure of 20 cm Hg with 96% enriched $^{10}\text{BF}_3$ at 20°C .

3.1.4 Neutron monitor detection system

As the data we want to receive from the neutron detection systems must be measurable and recordable, electrical signals such as voltage pulses from the detections are used. In the neutron monitor detection systems, however, neutrons are measured indirectly because they produce no direct ionization events. In other words, neutron de-

tectors must be based on detecting the secondary events produced by neutron-induced nuclear reactions. Such reactions occur when very slow neutrons generated by the reflector, producer, moderator, and so forth encounter a nucleus in the counter and cause it to disintegrate. The reaction cross-section is inversely proportional to the neutron speed. The slow thermal neutrons are effectively absorbed by ^{10}B which has the huge cross-section for neutron absorption of 3840 barns with $\sigma \propto 1/v$ up to about 100 keV (Krane 1988). The thermal neutrons are then captured in an exothermic fission reaction that is accompanied by the release of energy and energetic charged particles into the gas as



The amount of the energy deposited in the detector is the energy available from the nuclear reaction. Moreover, the large amount of energy released in the fission process dominates the background signal from any penetrating atmospheric charged particles. The reaction products are the energetic nuclei, ^7Li and ^4He . About 94% of the reactions leave ^7Li in the 480 keV excited state, releasing 2.31 MeV as kinetic energy to the ^4He and ^7Li nuclei. The 480 keV gamma ray is lost from the detector, while only 2.31 MeV is deposited. Then about 6% of the reactions go directly to the ground state, releasing 2.78 MeV as kinetic energy. In fact, the product nuclei from the nuclear fission process can cause ionization events that give rise to electrical signals that are detected by standard electronics to yield the neutron count rate.

It is notable that the interior walls are coated with activated charcoal that serves to absorb electronegative gases that build up during neutron irradiation. In a BF_3 -filled detector, three fluorine atoms are released with each neutron capture. If not absorbed, the fluorine atoms would combine with ionization electrons released in subsequent neutron captures. Initially, this process would reduce the electronic pulse

amplitude and then output pulses would be eliminated altogether (Evans et al., 1976).

According to the neutron capture events in the counter as described above, the lithium and helium ions, with a very short range in the gas, move in opposite directions away from the reaction site. They give up most of their kinetic energy by ionizing the surrounding BF_3 gas along their paths. Consequently, primary electrons are simply removed from valence shells of the gas atoms. Then each electron will create further ion pairs in the tube, where approximately 30 eV is required for each ionization (i.e., to create an ion pair). Most of the kinetic energy appears in the ^4He particle because its velocity is greater than that of ^7Li by conservation of momentum. If ^4He or ^7Li hits the wall of the detector, it does not deposit all of its energy as ionization. This causes the “wall effect.” The disintegrations to produce ^4He and ^7Li can occur anywhere in the counter and give rise to an isotropic distribution of ionized tracks that causes a dispersion of pulse rise time of $\sim 4.5 \mu\text{s}$ (Fowler 1963). As will be explained, if the disintegration products gave up all their energy to ionization of the gas, and if all the produced electrons were collected simultaneously at the anode, only two sizes of pulses would appear. The pulse sizes corresponds to energies of 2.31 and 2.78 MeV.

The ionization electrons will move toward the central wire which is the anode while the positively charged ions will move toward the tube wall which is the cathode. The detector operates in the proportional range, in which the electric field is strong, so that the primary electrons can gain sufficient energy to ionize the gas molecules and create secondary ionization. The subsequent ionizations will be produced rapidly and continuously by the secondary electrons and so on when the field strength is stronger than the threshold and increases further near the anode wire in a cylindrical geometry. Therefore, there is a large multiplication of the number of electrons. This cumulative amplification process is known as avalanche ionization. The signal is amplified in the strong electric field close to the anode wire. When a total of A ion pairs result from a single primary pair, the process has a gas amplification factor of A . For a BF_3 -gas filled counter, in an appropriate voltage range, the amplification is constant and the gain A is

approximately 20 for the tube. In principle, the number of secondary ionization events is proportional to the number of primary ionization events in the counter. Moreover, the output signals come mainly from the avalanche process. Subsequent to a neutron capture, about 2×10^5 free electrons are produced in the counter, leading to a signal of ~ 1.5 mV for 20 pF.

Because the amplification process requires a high electric field strength, an advantage of the cylindrical detector design is the high electric field near the inner wire. In a cylindrical detector, the electric field at radius r from the anode is $(V/r) \ln(b/a)$ where a and b are the anode wire and cathode tube inner radius, respectively. In addition, the total amplification will be proportional to the electric field traversed, not the distance traversed since the mean free path of ionization electrons is very short (about 1 to 2 μm). This means that the avalanche takes place near the anode wire. The electrons drift very fast to the anode wire with a drift velocity three orders of magnitude higher than the drift velocity of positive ions.

Neutron counters operated in the proportional mode could provide an average output current or individual pulses, depending on the associated electronics, but neutron monitors always count individual pulses. The pulse height is measured and one count is stored in system memory. The neutron counters in pulse mode are shown as registers of individual neutron counts. Neutron monitor tubes at Doi Inthanon count with a rate of ~ 34 Hz/tube. A differential pulse height spectrum of counts for a BF_3 proportional counter is displayed in Figure 3.7. There is a minimum collecting energy. If the discriminator is set in the right range, small changes in the tube voltage or amplifier gain will not affect the count rate.

In conclusion, proportional counters are extremely sensitive when the voltage is in the right range. The signal produced by the heavily ionizing Li and He is relatively large and easily distinguished from background signals. All of the electrons are collected within a few tenths of a microsecond. Each pulse corresponds to one neutron interaction. The amount of charge in each pulse is thus proportional to the number

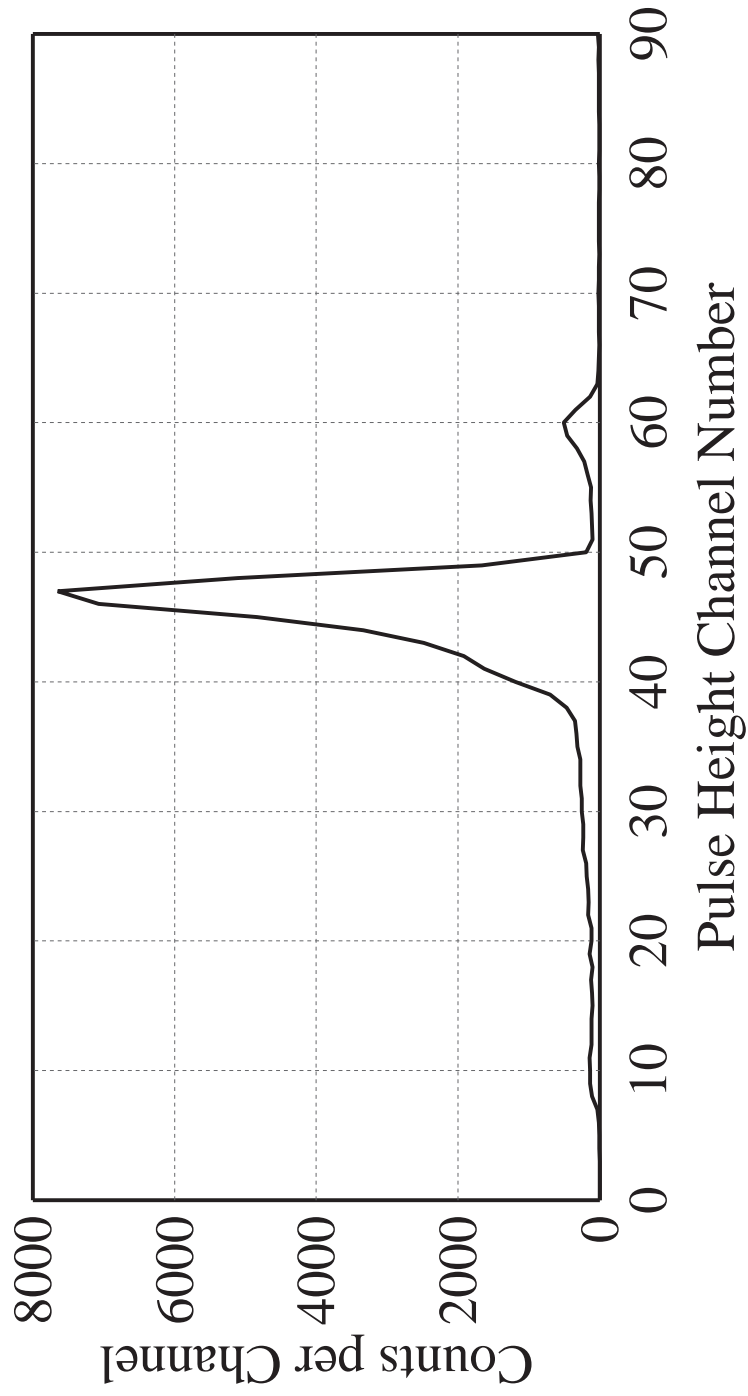


Figure 3.7: The pulse height distribution produced by a neutron source with a BP28 Chalk River neutron counter.

of original electrons produced. The proportionality factor in this case is the gas amplification factor. The number of electrons produced is proportional to the energy deposited by the nuclear interaction products.

3.2 Angular and rigidity response of PSNM

In order to determine the cosmic ray intensity variation in interplanetary space, we have to correct for the factors that contribute to ground-level cosmic ray observations at Earth. For neutron monitor observations, it is necessary to accurately take into account the effects of the atmosphere and (for angular distributions) the magnetosphere. These are usually considered in terms of the asymptotic directions, geomagnetic cutoff rigidity, and coupling coefficients.

3.2.1 Asymptotic directions

As described in Chapter 2, the asymptotic directions of a detector on Earth are the true directions of the incoming primary cosmic rays in space before passing through Earth's magnetic field to that station. Asymptotic directions of vertically incident particles at PSNM at Doi Inthanon are illustrated in Figure 3.8. The vertical asymptotic directions range over about 30° of latitude, but about 120° of longitude. When taking non-vertically incident particles into account, the asymptotic viewing cone covers $\sim 20\%$ of the sky.

3.2.2 Geomagnetic corrections

Geomagnetic corrections have been performed in order to relate the ground-based observations of diurnal anisotropy, i.e., the change in count rate with a 1-day period as Earth's rotation sweeps the asymptotic viewing cone around the sky, to the cosmic ray anisotropy in free space. Because Doi Inthanon has a wide asymptotic viewing cone, for cosmic rays of varying rigidity and different arrival directions at the atmosphere, the diurnal variation observed on the ground is broadened compared with the directional dis-

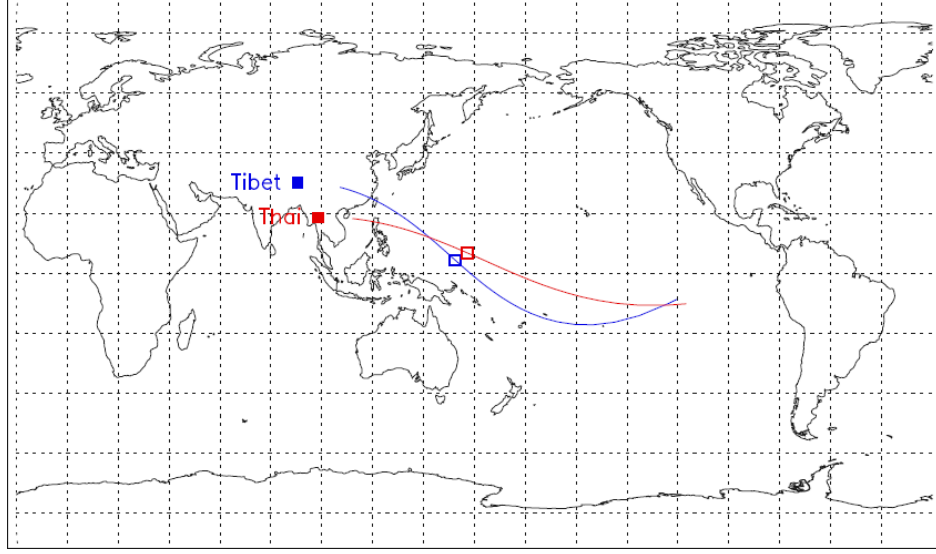


Figure 3.8: Asymptotic viewing directions for vertically incident Galactic cosmic rays over the central 80% of the rigidity range at Doi Inthanon (Thai) and Yangbajing (Tibet).

tribution in free space, i.e., the ground-based diurnal amplitude is typically smaller than variations in the directional distribution. The relations between the diurnal anisotropy in free space and that observed on the ground are (Bieber and Chen 1991)

$$A^{(E)} = A^{(G)}/d, \quad (3.6)$$

$$\phi^{(E)} = \phi^{(G)} + \delta\phi, \quad (3.7)$$

where A is the amplitude of the diurnal anisotropy, ϕ is the phase or time of maximum, and d (<1) and $\delta\phi$ are the coupling coefficients, which depend on the spectrum (rigidity dependence) of the anisotropy. The superscript (G) designates the amplitude and phase measured on the ground and the superscript (E) designates the amplitude and phase in free space in a reference frame fixed with respect to Earth (GSE coordinates). The variational spectrum is assumed to be a power law with an upper limiting rigidity (P_u) of 100 GV.

Based on particle tracing through Earth's magnetic field (Lin et al. 1995), using the response function of Nagashima et al. (1989), and assuming a flat spectrum $G(P) = 1$ for the anisotropy, the coupling coefficients were determined by T. Kuwabara.

The coupling coefficient d for the amplitude, 0.667, indicates that the asymptotic direction of peak DA is close to the Equator, and the coupling coefficient $\delta\phi$ for the amplitude, 4.168 h, indicates that there is a phase shift of 62.5° from the longitude of Doi Inthanon (T. Kuwabara, private communication, 2010).

The true local time of PSNM can be determined by using the longitude of Doi Inthanon, 98.49°E , which for 15° per hour corresponds to a time shift from UT (at 0°E) of 6.566 h instead of 7.00 h, as used for standard time in Thailand. However, the true local time in free space (phase in free space) has to be accounted for because we need to know the inflow direction or phase of cosmic rays in free space. Taking the values of $\delta\phi$ and the true local time of PSNM, the phase in free space is

$$\begin{aligned}\phi^{(E)} &= \phi^{\text{LT}} + 4.168 \text{ h} \\ &= \phi^{\text{UT}} + 6.566 \text{ h} + 4.168 \text{ h} \\ &= \phi^{\text{UT}} + 10.734.\end{aligned}\tag{3.8}$$

3.2.3 The response function of PSNM at Doi Inthanon

To establish a relation between the changes of primary cosmic ray intensity and the count rate recorded by neutron monitor, the response function of the neutron monitor has been determined. As the atmospheric showers of secondary particles are detected by a neutron monitor, a yield function resulting from the propagation of the primary and secondary particles and the detection response of a neutron monitor to these particles such as neutrons, protons, muons, and pions must be incorporated. Therefore, the response function $N(P_c, x, t)$ is count rate of a detector, which is a function of the energy or rigidity of the primary cosmic rays and can be determined by integrating the primary cosmic ray spectrum times the yield function:

$$N(P_c, x, t) = \int_{P_c}^{\infty} \sum_{i=1}^n (Y_i(P, x) j_i(P, t)) dP = \int_{P_c}^{\infty} W_T(P, x, t) dP,\tag{3.9}$$

where P_c is the geomagnetic cutoff, x is the atmospheric depth, t is time, $Y_i(P, x)$ represents the neutron monitor yield function for primaries of particle type i and $j_i(P, t)$ represents the primary particle rigidity spectrum for type i at time t .

The differential response function is the contribution to the count rate per

primary cosmic ray rigidity, and is related to the intensity spectrum j of primary particles on top of the atmosphere by

$$W_T(P, x, t) = - \left. \frac{dN(P_c, x, t)}{dP_c} \right|_{P_c=P} = \sum_{\text{species}} Y(P, x) j(P, t), \quad (3.10)$$

where $Y(P, x)$ is the so-called “atmospheric yield function” of a particular species of primary particles, representing the number of neutron monitor counts per incident primary which is essentially the neutron monitor detection efficiency of primary particles. The yield function incorporates all production and absorption effects that are in a thickness x of the atmosphere, where x should be expressed in terms of the airmass or pressure. After correction to a fixed pressure x_0 , the yield function is approximately time independent, so temporal changes in the differential response function are always in fixed proportion to changes in the primary intensity. The differential response function has a maximum value in the range of 4-7 GV at sea level (depending on the solar modulation epoch) as shown in Figure 3.9. The dominating contribution to the yield function is from secondary neutrons, but protons and μ^- contribute a significant fraction above 5 GV. If the atmospheric yield function for the production of secondaries is known, and using certain assumptions about cosmic ray composition, the cosmic ray primary spectrum at the top of the atmosphere can be deduced from the neutron monitor differential response function. To model the effects of spectral variations, the yield functions are used to calculate changes in the count rate from

$$\delta N(P \geq P_c) = \int_{P_c}^{\infty} Y(P) \delta j(P) dP. \quad (3.11)$$

The integral response function (count rate, N) can be directly measured in units of $(\text{m}^2 \cdot \text{sr} \cdot \text{s})^{-1}$ during a neutron monitor latitude survey. A calculated integral response function for PSNM at Doi Inthanon is shown in Figure 3.10.

Since the intensity must decrease with increasing cutoff rigidity, the neutron monitor at Doi Inthanon, detecting the cosmic rays with the highest cutoff rigidity, should have a minimal response in comparison with other neutron monitor stations.

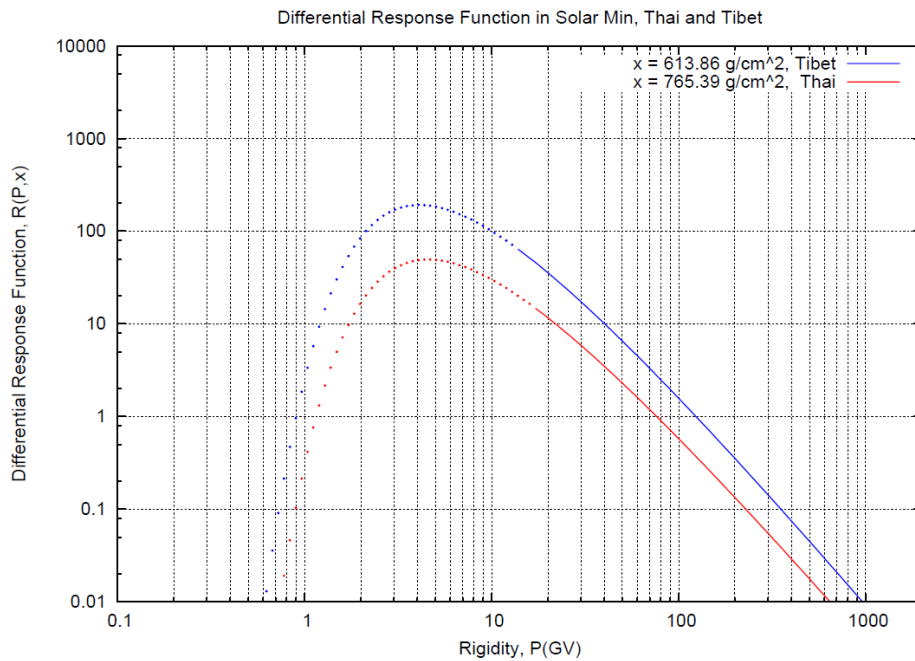


Figure 3.9: Differential response functions of the neutron monitor at Yangbajing (Tibet) and Doi Inthanon (Thailand) during solar minimum using the yield function and spectrum of Nagashima et al. (1989). (T. Kuwabara, private communication, 2010)

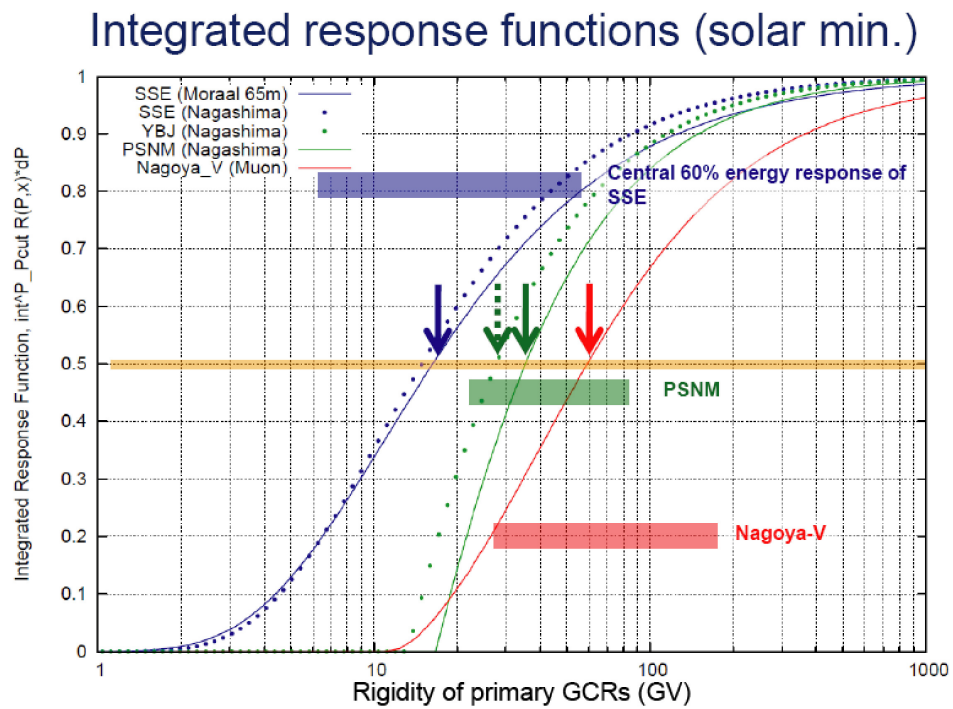


Figure 3.10: Integrated response functions of PSNM and other detectors, using the yield function and spectrum of Nagashima et al. (1989). (K. Munakata, private communication, 2010)

CHAPTER IV

DATA ANALYSIS

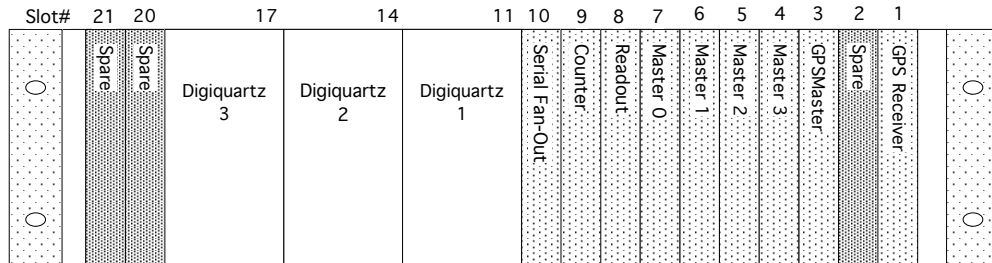
In this thesis work, we have used data from various sources to study 27-day recurrence in diurnal variation in GCRs. The first data source is the hourly pressure-corrected data from PSNM at Doi Inthanon. The second source is ACE interplanetary magnetic field and plasma data. The data provide referent plasma properties of HSSs near Earth as observed by the ACE spacecraft. The last source is Fe XII 195Å synoptic maps from the two STEREO spacecraft for each Carrington Rotation (CR) corresponding to 27.2753 days. The synoptic maps present images of solar coronal holes as sources of HSSs in each solar rotation. The time interval of this study spans November 2007 to November 2010, near and during the solar minimum of activity.

4.1 PSNM data processing

4.1.1 Uncorrected data

The uncorrected count rate of neutrons is recorded in minute, hour, and pulse height formats. The electronics system of each tube was connected to a master electronics rack as shown in Figure 4.1, which then connects to a COM port in the computer. To count the uncorrected neutron count rate, the data acquisition system operates sequentially with the time clock, which can be summarized in the following steps. First of all, the remote units continuously count neutrons, collect a sample of pulse heights, and calculate time delays between events. Second, once per second the GPS system sends a pulse to the master boards. Third, the masters send a “sync” command to the remotes. Fourth, the remotes format data as of the time of the sync and resume

Cosray 2000 Rack, Front View



Notes:

- 1) The 19" rack is a Vector CCA 14S/90 for 4.5" X 9.5" boards with 21 slots at 0.75" centers, and only 15 slots with connectors.
- 2) The spare slots are wired like the GPS and Master slots, and have individual Readout select lines.
- 3) Slots 10, 9 and 8 are designated for the Counter Expansion (or Serial Fan-out), Counter, and Readout boards respectively and exclusively.
- 4) A Counter Expansion Input board would allow access to the 10 counter channels in case the barometers are not mounted in the rack, or other signals need counting. This is slot 10 and is currently used for serial expansion.
- 5) Master boards may be placed in any slot. Master 3 located in Slot 4 is only used at South Pole.
- 6) Up to 3 Digiquartz barometers may occupy 3 slots in locations 11, 14, and 17.
- 8) The slots behind the Digiquartz barometers (12,13,15,16,18,19) do not require connectors or guide rails.

Figure 4.1: Cosray electronics rack diagram.

taking data. Fifth, the masters request and collect data from the remotes. Sixth, the readout board requests and collects data from the masters, the counter board, and the GPS master. Finally, the readout board packages the data locally and also transmits to the computer. The computer can ask for playback of recorded data.

All the information about neutron counts is digitized in this way and processed with the data acquisition software named "LandMonitor" which is written in Visual Basic. The collected data are written to files at the start of every minute and the start of every hour. To compute hourly count rates the accumulated number of counts at each hour is subtracted by the value at the previous hour. Then the hourly neutron counts are stored at the middle of every hour.

Pulse heights at PSNM (as described in Section 3.1.4) are stored at the ftp server at Doi Inthanon, and can be constructed by using data (from neutron monitor to Cosray) from the directory "Histograms." By plotting the number of counts recorded in SPHA columns versus channel number we will get the pulse height spectra of neutron

counts.

4.1.2 Pressure correction

The count rate of neutrons is dependent on the airmass over the neutron monitor since the response of neutron monitor is a function of atmospheric depth. Therefore, the uncorrected count rate of neutrons of each hour must be corrected first by considering the effect of the air overburden. During stable atmospheric conditions, the barometric pressure recorded at the monitor site is a good measure of the air overburden and an approximate correction can be written as

$$dC = -\beta C dp, \quad (4.1)$$

where C is the hourly uncorrected neutron count rate, β is the attenuation or barometric coefficient and is a positive value, dC is change in the count rate C and dp is the change in the barometric pressure. Actually, β is a weighted sum of individual β_i for each secondary component that contributes to the count rate. For a constant absorption rate, integrating this equation

$$\int_{C_0}^C \frac{dC}{C} = -\beta \int_{p_0}^p dp, \quad (4.2)$$

leads to

$$C = C_0 e^{-\beta(p-p_0)}, \quad (4.3)$$

where C_0 is the hourly pressure-corrected neutron count rate, p is the hourly pressure, and p_0 is the average (reference) pressure at a given station; at PSNM we used 563 mm Hg. A more convenient form for calculating the hourly corrected count rate is

$$C_0 = C e^{\beta(p-p_0)}. \quad (4.4)$$

From Kamyani (2011) the barometric coefficient for PSNM was determined as the slope of the graph for linear least square fits of hourly residuals of the uncorrected logarithmic count rate vs. residuals of pressure, where a “residual” represents a difference in a quantity from its running 24-hour average. The reason why we use residuals is

because small deviations of the uncorrected logarithmic count rate and the pressure are correlated but the 24-hour average values may not be. Then the values of β separately determined for each of five months were averaged for the best fit value, which is 0.83% per mm Hg. The equation (4.4) tells us that the higher the pressure, the higher the ratio of corrected to uncorrected count rates. The pressure from Digiquartz1 is used for the correction.

4.1.3 PRELIM process

To prepare the preliminary data files, hereafter called PRELIM files, of hourly neutron count rates for each month, the uncorrected count rate has to be examined for some unusual problems that occurred sometimes, e.g., when an individual tube's rate clearly deviated from the others, or when the power went out during that hour, which are problems that can be corrected for. Then the examined count rate will be corrected for by the pressure effect. The PRELIM file is generated and derived from RAW files as described by Kamyran (2011). Furthermore, to achieve the PRELIM process the various formats of files must be considered.

In this section, we focus on the process of preparing the PRELIM data and correcting for the unusual problems. The process of the PRELIM file format was well documented by Kamyran (2011), starting with automated processing. This system was written in the LINUX operating system on the computer server called "cosmic." There are 10 steps for preparing the PRELIM file. After the automated processing in which all commands are included in the dailytask script file, "`~/dailytask`", all steps are run and sent by email automatically everyday. These steps are Step 1 to 5.

STEP 1. To prepare a Digiquartz pressure and an AIR pressure from Minute files. For example, in April 16, 2009, local time.

The input file is "`~/MinuteData/PRS_09_04_16.DAT`".

The command is "`./Pprepare 04/16/09`" where Pprepare calls "`wPress.c`".

STEP 2. To prepare a count rate (accumulated counts) and GPS times from

HourData files.

The input files are “HHP09_04_15.DAT”, “HHP_09_04_16.DAT”, and “~/HourData/PRS_09_04_16.LOG”.

The output file is “09_04_16.txt” in Universal Time (UT).

The command is “./Hprepare 04/16/09” where “Hprepare” calls “wgetdata.c”.

STEP 3. To calculate the RAW file.

Input files are “09_04_16.txt”, “09_04_17.txt”.

Output file is “raw09_04_16.txt” in UT.

The command is “./calcRaw 04/16/09” where “calcRaw” calls “wRaw.c”.

STEP 4. To calculate the ratio file.

Input file is “raw09_04_16.txt”.

Output file is “ratio09_04_16.txt” in UT.

The command is “./calcRatio 04/16/09” where “calcRatio” calls “wRatio.c”.

STEP 5. To check the data and plot the ratio file.

Input file is “ratio09_04_16.txt”.

Output files are “idloutput” and “plotratio09_04_16.ps”.

The command is “./idlRatio 04/16/09”.

STEP 6. Before going to the next steps of the PRELIM process, the abnormal data and information must be checked first by inspecting the idloutput files. In other words, RATIO files composed of the ratio of NM counts in each tube to the average of NM counts from all tubes for each hour will be checked for irregular data for each tube by “idlplot”. However, we can check these for one time interval by creating an “idlshortterminput” file to run the “IDL” program.

The command is “vi idlshortterminputApr09”.

Key “i” then insert

“plotratioshortterm, ‘ ‘ Apr09", 2009, 4, 1, 2009, 4, 30” and then save this

file, “Esc+:wq.”

Then use “idl <idlshortterminputApr09> ratiocheckApr09.txt”. We will get the file “ratiocheckApr09.txt” that incorporates the information of unusual data for that month.

It is notable that if there are no abnormal data in the ratiocheck of that month, we can skip this step and proceed to Step 9.

Such unusual data, however, should be corrected for as much as possible because a long data gap in the PRELIM data results in a lack of data for that period. This is not appropriate for data analysis, especially when we want to analyze data for an interesting time period. Therefore, the PRELIM files should undergo substantial quality control. Sometimes there are some cases of errors in the corrected counts which are caused by either errors in the NM measurement system or a power outage. First, by using the notation in Kamyran (2011), the errors from the NM measurement system are classified in SPOT, ZERO, BADPRESS, and GLITCH files. Second, the errors from the power outage are DATAGAP and some GLITCH files which are POWEROUT files. These problems can be corrected for separately. In fact, real DATAGAP, GLITCH and BADPRESS are not incorporated for the correction so such hours are discarded from the PRELIM data. The correction for ZERO and POWEROUT can be done manually by the following methods.

- ZERO data. Electronics sometimes output a “0” for the count rate, and the real count rate reappears in the next minute. A ZERO event is such an event at the zeroth minute of the hour, which is a problem for counting an hourly rate. To correct for this we need to replace the average counts calculated from two values of counts at the minute before and after the 0 count. For example, we have a ZERO output for tube 5, 1300 UT, April 16, 2009. Then we will read out the data from the MINUTE file labelled for Local Time (LT)=UT+7, that is, 2000 LT. Therefore, the command is

“`more ~/MINUTEData/PRS_09_04_16.DAT`”. Then search for `/19:59:00` and read out the MCT counts at 19:59:00 and 20:01:00 at Tube 5. Average the MCT counts and replace the value of ZERO in “`09_04_16.txt`”. Save the file and this file will be used as an input of the new RAW file in Step 8.

- POWEROUT data. As described above, the POWEROUT occurs when there are power outages during that time. We can correct for this by counting only good MINUTE data that remained for at least 30 minutes in that hour. Note that the initial time of that hour is the zeroth minute and the final time is the zeroth minute of the next hour. Take the remaining data in each tube, and multiply by $60/x$ where x is the number of good minutes. Next, replace these POWEROUT-corrected count rate data into the RAW files for those hours (the RAW file contains 24 hours from 0 to 23 UT). Then, rearrange them to the right positions. If the pressure data are absent in the file we can find them in `HHP_year_month_day` and put them in the RAW files (the HHP file has 24-hour records in UT between 17 UT of the previous day and 16 UT of today). Finally, those RAW files will be used as inputs of Step 9. It is important to note that we do not calculate a new RAW file in Step 8 for the POWEROUT, because the new RAW file will be reset to the old file.

Besides a POWEROUT caused by a power outage, there are problems with recording counts exceeding the overflow number of $10^{24}=16,777,216$. Consequently, the electronics are restarted to count more neutrons and the “**Ratiocheck**” is reported as GLITCH data. Such problem can be corrected by adding 16,777,216 to the low HCT count to get the neutron counts of that hour.

Furthermore, the hours which are reported as DATAGAPs sometimes are not real DATAGAPs. Therefore, we should first explore the MINUTE data because the DATAGAP may be a POWEROUT.

STEP 7. To insert the information of unusual data in a BADHOUR, SPOT,

GLITCH and ZERO text files. These files are yearly and are important in classifying types of problems (for example, SPOT10.txt lists SPOTs in the year 2010). Because the Ratiocheck of each month reports the monthly SPOT, GLITCH, and ZERO in text files (such as SPOTApr11.txt, GLITCHApr11.txt, and ZEROApr11.txt, respectively in year 2011), it is convenient to put this information into each yearly file above. Therefore, we need not to insert them manually. However, sometimes the SPOTs are not all reported so that we have to carefully check the hourly counts in RAW files.

STEP 8. To calculate a new RAW file. This step is needed only for the days with a ZERO event.

The input files are “09_04_16.txt and 09_04_17.txt”.

The output file is “raw09_04_16.txt” in UT.

The command is “./calcRaw_edit 04/16/09”, where “calcRaw_edit” discards checking the incomplete input file. It is notable that if there are several ZERO events in the month we can calculate new RAW files at one time as

```
“for i in ZERO days (UT), >do ./calcRaw_edit 04/$i/09, >done.”
```

STEP 9. To calculate the total and mean counts for all days of that month.

Input files are all raw files of the month which are

“raw09_04_day.txt”.

The output files are “NMtot09_04_day.txt” and “MEAN09_04_day.txt”.

The commands are “for i in 1 2 3 4 5 6 7...final day of the month”

```
“> do ./calcMean 04/$i/09, done”
```

```
“cat NMtot09_04_*.txt> NMtot09_04.txt”.
```

STEP 10. To calculate the PRELIM file. First, we have to change the date of the preparation and month of the PRELIM data in “wPRELIM.c”.

The command is “vi wPRELIM.c”

Key “i” to change “Date_prepare” (line 41), “mstart” (line 42) and “mstop” (line 43).

For April, “mstart = 4” and “mstop = 4” and then save the file, “Esc+:wq”.

Compile this file and run by commands: “`cc -o wPRELIM wPRELIM.c -lm`”,
then “`./wPRELIM`”.

The input file is “`NMtot09_04.txt`” and the output file is “`PRELIM09_04.txt`”.

The PRELIM data format from the data processing is now as follows:

PRINCESS SIRINDHORN NEUTRON MONITOR AT DOI INTHANON, THAILAND
Latitude 18.59 deg N, Longitude 98.49 deg E, Altitude 2560 m
Reference pressure 563 mmHg, Pressure coefficient 0.83%/mmHg

Operated by Mahidol University, Chulalongkorn University, and Ubon
Rajathanee University

PRELIMINARY DATA:

Start date: 2010 December 1

End date: 2010 December 31

Data prepared: 2011 February 13

CONDITIONS FOR USE OF DATA:

You are welcome to use data from the Princess Sirindhorn Neutron Monitor
at Doi Inthanon, Thailand, under the following conditions:

1. You agree to acknowledge the Princess Sirindhorn Neutron Monitor
Project in any published use of the data. Example: “Neutron monitor data
from Doi Inthanon were provided by courtesy of the Princess Sirindhorn
Neutron Monitor Program.”

2. You agree to send a copy of any publication of thesis using these
data to:

Prof. David Ruffolo
Space Physics and Energetic Particles Group
Department of Physics, Faculty of Science
Mahidol University
Bangkok, 10400, THAILAND
e-mail: ruffolo.physics@gmail.com

Scientific questions about the data may be addressed to Prof. Ruffolo.

3. You may share these data with colleagues, provided you inform them of
these conditions. This is most simply accomplished by including the header
information that came with the file when you got it.

EXPLANATION OF THE DATA AND FORMAT:

While these data are accurate to the best of our knowledge as of the date given above, we reserve the right to correct errors without notifying possible recipients of these data.

Columns in the data are as follows:

1. Year
2. Day of year (1 for January 1, etc.)
3. Center of time interval, in UT
4. Neutron monitor counts per hour, corrected for pressure effect
5. Neutron monitor counts per hour, not corrected for pressure effect
6. Atmospheric pressure, in millimeters of mercury

A zero in any data field denotes a data gap.

A line containing 42 asterisks occurs immediately preceding and following the data, and nowhere else in this file.

Software can use this line to seek past this header material.

YYYY DOY HHMM Corr Uncorr Press

```

2010 335 0030 2212277 2211176 563.06
2010 335 0130 2210680 2199698 563.60
2010 335 0230 2220395 2203505 563.92
2010 335 0330 2216036 2199909 563.88
2010 335 0430 2213250 2202438 563.59
2010 335 0530 2214853 2213383 563.08
2010 335 0630 2217900 2226199 562.55
2010 335 0730 2210770 2225683 562.19
2010 335 0830 2218699 2235706 562.08
2010 335 0930 2212184 2227291 562.18
2010 335 1030 2216114 2226623 562.43
2010 335 1130 2214061 2218292 562.77
2010 335 1230 2214022 2208883 563.28
2010 335 1330 2210403 2200701 563.53
2010 335 1430 2227536 2203813 564.29
2010 335 1530 2206921 2193408 563.74
2010 335 1630 2216868 2204025 563.70
2010 335 1730 2207977 2197191 563.59
2010 335 1830 2202264 2196605 563.31
2010 335 1930 2212744 2213295 562.97
2010 335 2030 2203738 2208316 562.75
2010 335 2130 2211105 2217722 562.64

```

.
.

.

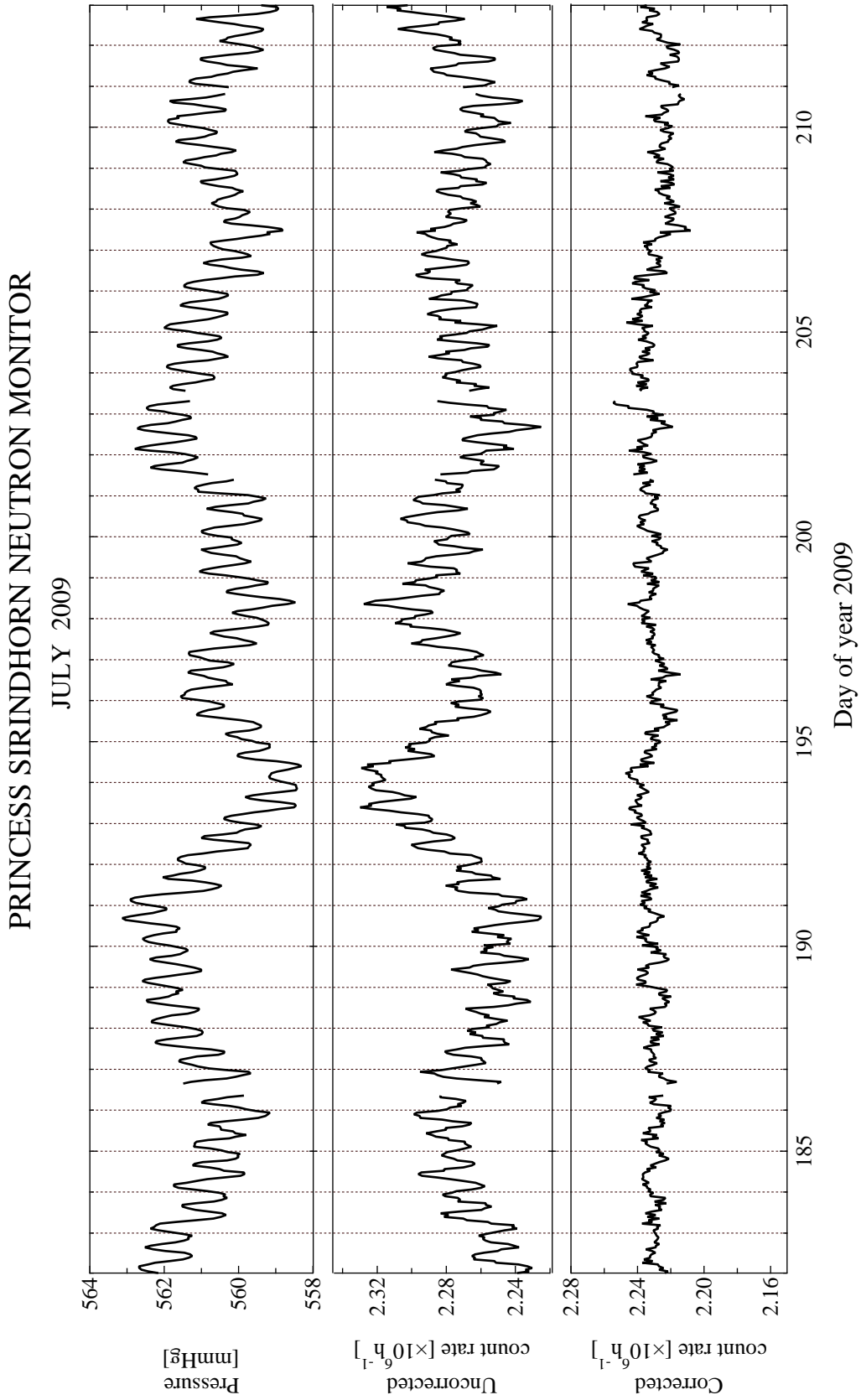


Figure 4.2: NM count rate at Doi Inthanon. Notice that the uncorrected count rate has a strong dependence on pressure, which is removed in the corrected count rate.

From the PRELIM data, we can construct a PRELIM plot, for example in July 2009, as shown in Figure 4.2. The uncorrected neutron count rate varies inversely with pressure, which mainly varies with a 12-hour period, so that two peaks are seen in this rate during each day. The pressure-corrected neutron count rate no longer has a 12-hour variation and clearly possesses a daily (diurnal) variation with an amplitude that varies with time.

4.2 Other data used in this research

4.2.1 ACE interplanetary magnetic field and plasma data

We utilized the 1-h averaged data of interplanetary plasma from the MAG and SWEPAM instruments of the Advanced Composition Explorer (ACE) spacecraft (see <http://www.srl.caltech.edu/ACE/ASC/level2/index.html>) and the OMNIWeb site (<http://omniweb.gsfc.nasa.gov/>). We define the polarity sector of the interplanetary magnetic field (IMF) based on hourly mean IMF components in the Geocentric Solar Ecliptic (GSE) coordinates. The GSE coordinates have their origin at Earth's center, the x_{GSE} -axis points from the Earth to the Sun, the z_{GSE} -axis points north and perpendicular to the ecliptic plane, and the y_{GSE} -axis completes the right-handed system (Figure 4.3). The toward (the Sun) and away (from the Sun) magnetic sectors are defined in terms of the IMF direction relative to a plane normal to the 45° spiral in the ecliptic plane; i.e., the IMF is designated toward (T) if $B_x > B_y$ and away (A) if $B_y > B_x$.

4.2.2 STEREO-A synoptic maps

The evolution and features of the CHs are characterized by utilizing Fe XII 195\AA synoptic maps (<http://secchi.nrl.navy.mil/synomaps/index.php?p=cmnumber.php>) for each 27.28-day Carrington Rotation (CR) from the Extreme Ultraviolet Imager (EUVI) of the Sun Earth Connection Coronal and Heliospheric Investigation (SECCHI) (Howards et al. 2008) on the Solar TERrestrial RELations Observatory (STEREO)

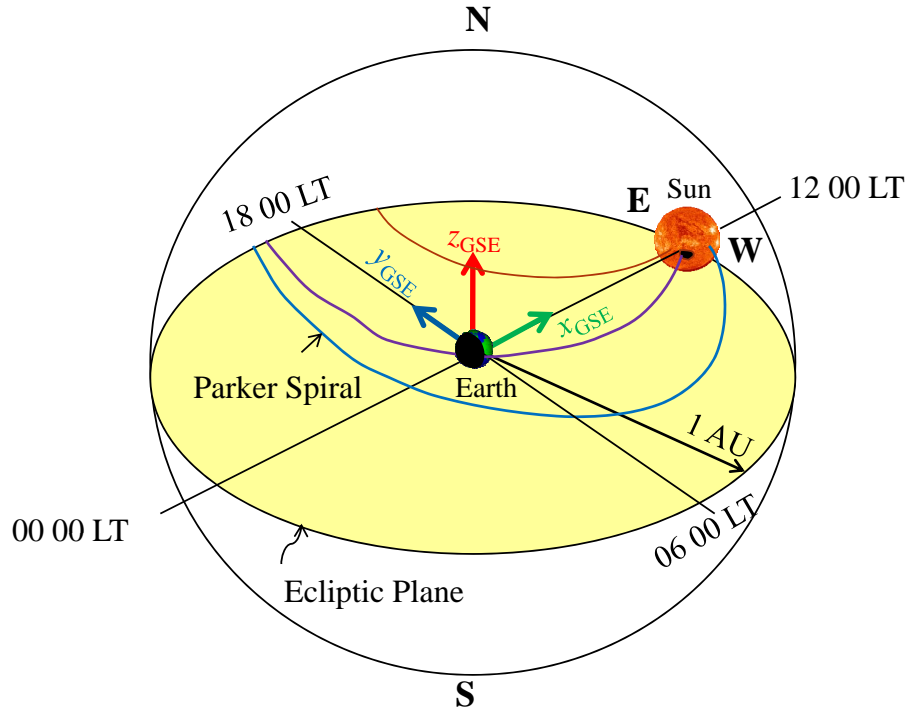


Figure 4.3: The Geocentric Solar Ecliptic Coordinates.

spacecraft (Kaiser et al. 2008). The instruments are described in Appendix B. The synoptic maps are in FITS format with high quality images. They were read in by the useful image processing routines of IgorPro. We have examined data from both STEREO spacecraft, STEREO-A (Ahead) and STEREO-B (Behind), but in this study we show only data from STEREO-A.

4.2.3 Wilcox Solar Observatory heliospheric current sheet

In addition, we plotted the locations of Earth's orbit (crosses) and latitudinal excursions of the heliospheric current sheet (HCS) on the synoptic maps to indicate the source polarity of the IMF. The latitudinal excursions are derived from Potential Field Source Surface (PFSS) analysis of Wilcox Solar Observatory (WSO) magnetograms (<http://wso.stanford.edu/synsource.html>). In PFSS analysis the coronal magnetic field is calculated from photospheric field observations with a potential field model. The field is forced to be radial at a solar wind source surface ($2.5 R_S$) to approximate the effect

of the accelerating solar wind on the field configuration (Schatten et al. 1969).

4.3 Harmonic analysis of count rate data

The hourly pressure corrected data from Doi Inthanon from November 2007 to November 2010, representing solar minimum conditions, have been subjected to harmonic analysis. First, the days with gaps up to 3 hours are filled in by linear interpolation. However, the days with more than three consecutive hours of missing data were discarded in the study. Next, the count rate data have been subjected to removing a 24-h running average for each 27-day data set. Then the fractional excess count rate of neutrons during each day was determined by

$$F(t) = \frac{C(t) - C(t)_{\text{fit}}}{\langle C \rangle}, \quad (4.5)$$

where $C(t)$ is the hourly count rate, $C(t)_{\text{fit}}$ is the 24-h running average count rate, and $\langle C \rangle$ is the daily average count rate.

For each day (in universal time, UT), the fractional excess count rate F as a function of time was fit to a sinusoid of frequency $\omega = 2\pi/(24 \text{ h})$ in the harmonic analysis:

$$\begin{aligned} F(t) &= A_x \cos \omega t + A_y \sin \omega t \\ &= A_0 \cos(\omega t + \phi), \end{aligned} \quad (4.6)$$

where t is the time from the start of the day in UT. Here A_x and A_y represent components of the mean direction of diurnal anisotropy in Cartesian coordinates where

$$A_x(\text{doy}) = \frac{1}{12} \sum_{n=1}^{n=24} A(\text{doy} + \frac{n}{24}) \cos \frac{n\pi}{12}, \quad (4.7)$$

$$A_y(\text{doy}) = \frac{1}{12} \sum_{n=1}^{n=24} A(\text{doy} + \frac{n}{24}) \sin \frac{n\pi}{12}, \quad (4.8)$$

doy is the day of year, and n is the hour of day.

From this method, we have determined the resultant amplitude and time of maximum of the GCR diurnal anisotropy. The diurnal amplitude is

$$A_0 = (A_x^2 + A_y^2)^{1/2}, \quad (4.9)$$

and time of maximum or “phase” is the phase angle of (A_x, A_y) relative to the x axis.

It is notable that in this time period, with solar minimum conditions, there were essentially no effects of large cosmic ray intensity perturbations such as Forbush decreases due to coronal mass ejections.

The calculation can be described as follows:

- Read in PSNM PRELIM data and output anisotropy parameters. Designed to input hourly data and output daily information. Data must be contiguous, starting with the hour centered at 0030 UT. Read file that specifies the desired start doy and a joint count rate at the start of that doy. Lines prior to that doy in the input file are skipped. Missing lines and lines with zeroes are treated in the same way. The input file can contain year boundaries. Gaps up to 3 hours are filled in by interpolation. The data interval is selected to start at the first gap-free doy after the specified doy and end at the last doy before the next gap, or after NMAX days, or at the end of input data, whichever comes first. Perform fit to piecewise linear function in that interval. If the first day of the interval is the same as specified in “oldjoint.txt”, take the first joint count rate value as fixed when fitting, unless it is set to a negative number by the user. The last joint count rate value in the fit is written to “newjoint.txt”, which can be used as “oldjoint.txt” in a following run.
- Need improved linear trend. Cannot use independent linear fit for each day, because that gives a discontinuous line that distorts the diurnal wave. Now use linear least-squares fitting to find optimal piecewise linear fit to data, which “connects the dots” between the optimized “joint” count rate estimates at joint times, set to 0000 UT of each day. However, it is neither practical nor particularly desirable to optimize hundreds of “joint” count rates for a large data set. Therefore, will fit D days at once (solving a $D \times D$ matrix equation, probably using D as 27 to roughly synchronize with solar rotation), and use the final joint count rate as a fixed initial value when fitting the next D days, and so on.

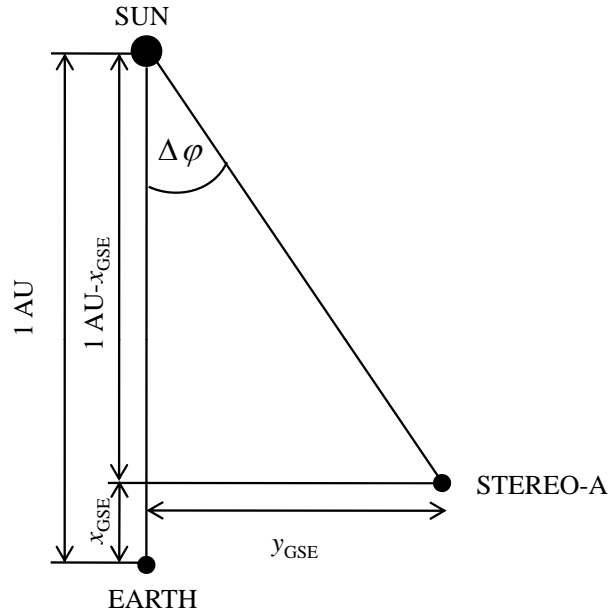


Figure 4.4: Geometry of longitudinal separation between Earth and STEREO-A (not to scale).

- Modification sequence: Remove current daily linear regression and comment out check output and anisotropy calculation. Instead of processing only 2 days at one time, use arrays to store data for up to D days. (More precisely, store until reach edoy (end doy), which is initially EDOY, but thereafter increments by D .) Use linear least squares fitting to determine joint count rates. Produce “check” output and verify that it is reasonable, especially checking at edoy times. Then subtract piecewise linear trend, and determine and output anisotropy parameters, as well as more check output.

Finally, one can determine the components of DA for the count rate data.

4.4 Time synchronization of PSNM, ACE, and STEREO-A data

In order to compare the synoptic maps with the cosmic ray flux and plasma parameters measured at or near Earth we have to correct for the observing angle of

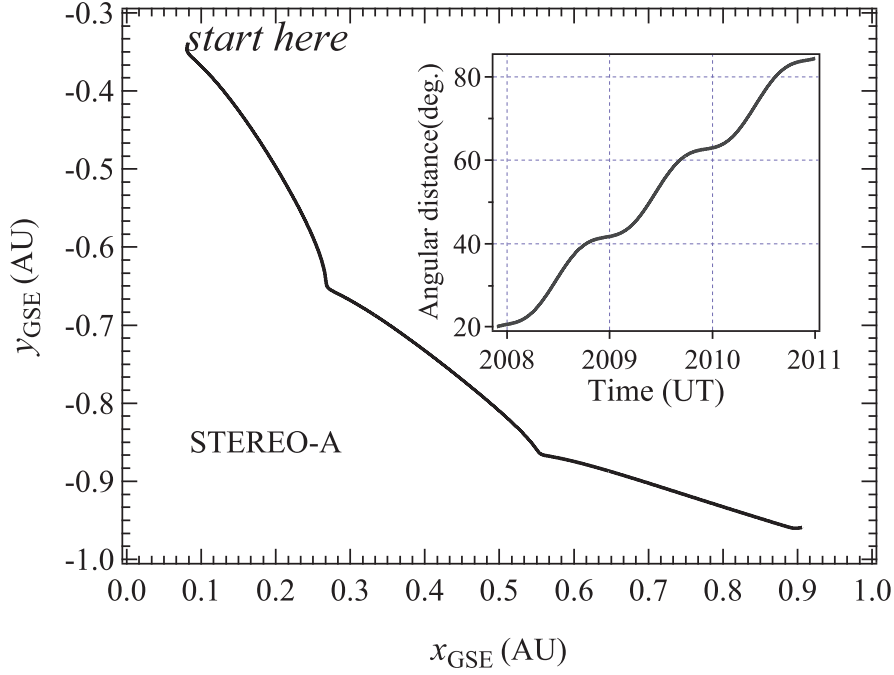


Figure 4.5: The position of STEREO-A with respect to Earth.

(in this case) STEREO-A. First, we assumed that the solar wind speed is constant from the source to the Earth (ballistic mapping back in time). In this study, for the sake of simplicity we neglected the longitudinal separation between the ACE spacecraft and Earth. The position data in GSE coordinates of STEREO-A (taken from <http://www.srl.caltech.edu/STEREO/attorb.html>) were employed to calculate the longitudinal separation ($\Delta\varphi$) between Earth and STEREO-A. The geometry that is used to calculate $\Delta\varphi$ is shown in Figure 4.4. Therefore, $\Delta\varphi$ in each hour can be calculated by

$$\tan \Delta\varphi = \frac{y_{\text{GSE}}}{1\text{AU} - x_{\text{GSE}}}, \quad (4.10)$$

where $1 \text{ AU} = 1.5 \times 10^{11} \text{ m}$. The separation between Earth and STEREO-A monotonically increased during the period of our study, from 20° in November, 2007 to 82° in November, 2010. Orbit of the STEREO-A has been calculated and shown in Figure 4.5. When comparing data from PSNM and ACE with a synoptic chart from, say, STEREO-A, we must shift the latter to account for the solar wind travel time to Earth and the

longitudinal separation, $\Delta\varphi$,

$$\Delta t = \frac{1 \text{ AU}}{V_{\text{ACE}}} - \frac{\Delta\varphi}{\Omega_{\odot}}, \quad (4.11)$$

where V_{ACE} is the solar wind speed as observed by ACE, and for the synodic rotation frequency of the Sun we use $\Omega_{\odot} = 2\pi/26.75$ radians per day, where 26.75 days is the average synodic rotation frequency of solar magnetic features (Bai 1987).

4.5 Classifying high speed solar wind streams and corotating interaction regions

We have used the high-resolution 5-minute interplanetary plasma data from the ACE spacecraft for classifying HSSs and CIRs. An HSS is defined by a higher solar wind speed than the mean value of preceding and following slow solar wind streams by more than 100 km s^{-1} , lasting for at least two days. The peak speed of the HSS is $\gtrsim 450 \text{ km s}^{-1}$ (Mavromichalaki et al. 1988). The basic physical features of the corotating HSSs with respect to interplanetary parameters can be summarized as follows: (1) the proton density rises to high values near the leading edges of the streams, lasting for about one or two days, (2) the interplanetary magnetic field magnitude is proportional to bulk speed with a constant polarity throughout the stream except for some fluctuations lasting a few hours (Iucci et al. 1979), and (3) the proton temperature varies in a pattern similar to that of the flow speed. It increases with speed and shows a slight decrease during the magnetic field descent phase. We characterized CIRs in terms of well known parameters, such as a simultaneous increase in density and magnetic field magnitude at the leading edge of the HSS. For stream interface (SI) identification, across the SI, the solar wind speed and temperature increase whereas the density decreases (in Choi et al. 2009).

CHAPTER V

RESULTS

We will first show statistics of diurnal variations observed by the world's highest rigidity neutron monitor, an 18NM64 at Doi Inthanon, Thailand for the time period of November, 2007 to November, 2010, which included the solar minimum between solar cycles 23 and 24. In near-Earth's space, the average diurnal amplitude was 0.20% and the time of maximum of the diurnal variation was close to 1800 LT, the corotational direction. We found trains and recurrent trains of enhanced and suppressed DA that recurred with about a 27-day period. The DAs had a tendency to be enhanced or suppressed depending on the magnetic polarity of the interplanetary magnetic field. We show that a slanted morphology of coronal holes could contribute to the characteristics of the recurrent diurnal variations observed near Earth. The morphology of coronal holes together with the corotating interplanetary magnetic polarity could affect the diurnal variations by the particle gradient anisotropy $\mathbf{B} \times \nabla n$. We also found that trains of enhanced DA frequently start near the start of a high speed solar wind stream. Then, we will show PSNM 27-day cosmic ray intensity modulation. The HSSs can locally modulate or prevent the diffusion of GCRs, and sometimes produced CIRs in the vicinity of 1 AU. Finally, features and characteristics of coronal holes and plasma parameters were examined. An overview of the evolution and features of CSWSs between CR2063 and CR2103 were described in order to better understand the effects of these CSWSs on variations in GCRs near Earth.

5.1 Statistics of diurnal amplitude and phase at Doi Inthanon

The harmonic analysis using data from the *PSNM* at Doi Inthanon from November, 2007 to November, 2010, according to Equation (4.6), resulted in mean values

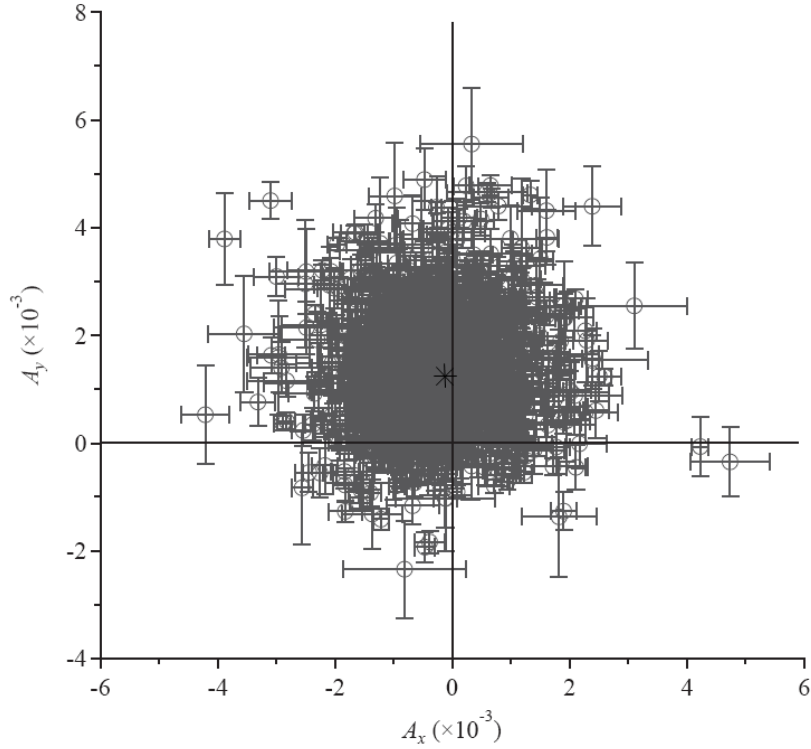


Figure 5.1: Calculated ground-based components of diurnal anisotropy from a harmonic analysis of the neutron count rate at Doi Inthanon for each day from Nov., 2007 to Nov., 2010. These components are not yet corrected for the coupling coefficients. The asterisk indicates the mean diurnal variation.

$\langle A_x \rangle = -0.0002$ (s.d.= 0.0009) and $\langle A_y \rangle = 0.0013$ (s.d.= 0.0011) as shown in Figure 5.1. Interpreting (A_x, A_y) as a harmonic vector, as indicated in Figure 5.2, the mean value has a magnitude $A = 0.0013$ (s.d.= 0.0011) and phase 1.7 radians (s.d.= 0.7). In other words, the mean diurnal variation observed at Doi Inthanon was 0.13%. This phase implies a maximum diurnal enhancement at 6.6 h UT. Doi Inthanon is located at longitude 98.49°E, so the true local time (LT) is UT + 6.57 h, and the diurnal enhancement peaks at 13.1 h LT. The phase shift, calculated as described in Section 3.2.2 and Equation (3.8), implies a peak flux in near-Earth space from the direction of 17.3 h LT, close to the corotational direction, 18 h LT (Rao 1972). Based on the coupling coefficients, the mean value of A implies a mean anisotropy of $A/d = A/0.667 = 0.20\%$ in the near-Earth cosmic ray flux above the cutoff rigidity. All the DA values reported

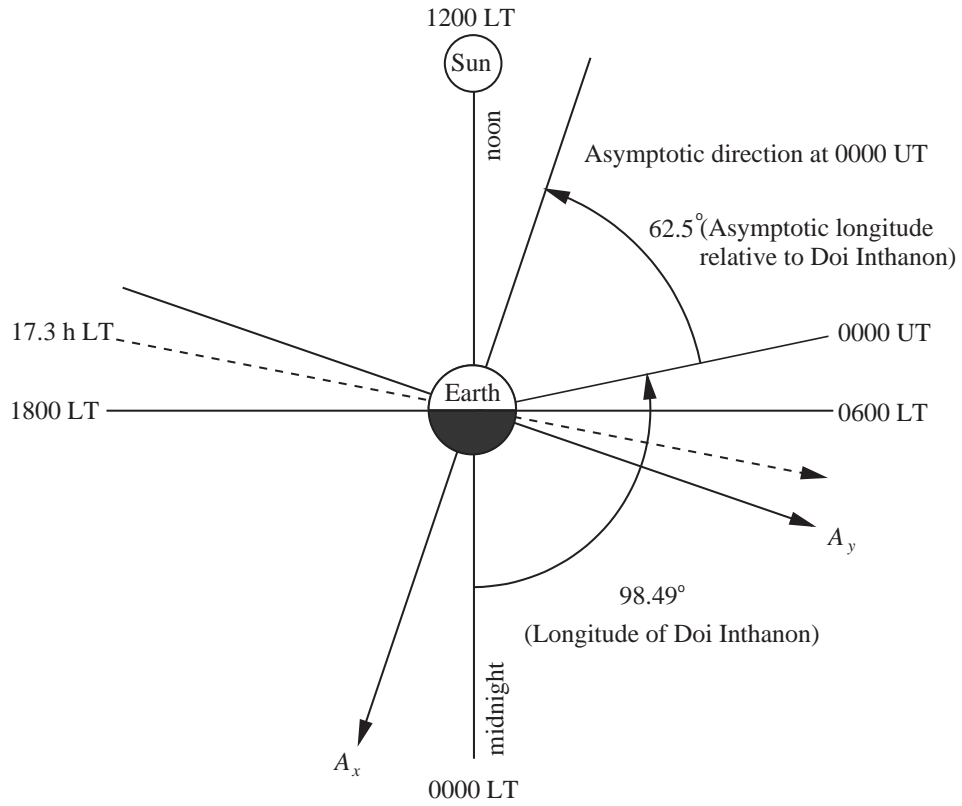


Figure 5.2: Detector orientation and effective asymptotic direction for diurnal variations at Doi Inthanon, and the A_x and A_y directions for diurnal variations. The dashed line indicates the observed mean inflow direction of the Galactic cosmic ray flux in free space. LT: local time. UT: universal time.

in Table 5.1 and Figures 5.3, 5.4, and 5.6-5.13 are already corrected for the coupling coefficient and phase shift.

The coupling coefficients imply that the effective asymptotic direction of cosmic rays (for the purpose of harmonic analysis) is offset by 62.5° from the longitude of Doi Inthanon. The \vec{A}_x -axis indicates a cosmic ray anisotropy component directed *from* the asymptotic direction for 0000 UT, *toward* the opposite direction, and the \vec{A}_y -axis is perpendicular to that as shown in Figure 5.2.

Table 5.1: Trains of Enhanced Diurnal Variation at Doi Inthanon from November, 2007 to November, 2010

Year	Day of Year (DOY)	Duration (d)	Diurnal Variation		Time of Max. Mean \pm s.d. (LT)
			Max (%)	Mean(%)	
2007	309-318	10	0.63	0.40	15.8 \pm 1.8
2007	351-359	9	0.52	0.34	18.5 \pm 2.1
<i>2008</i>	<i>94-103</i>	<i>10</i>	<i>0.40</i>	<i>0.32</i>	<i>17.6 \pm 1.8</i>
<i>2008</i>	<i>125-135</i>	<i>11</i>	<i>0.53</i>	<i>0.37</i>	<i>18.0 \pm 2.2</i>
<i>2008</i>	<i>176-196</i>	<i>21</i>	<i>0.79</i>	<i>0.45</i>	<i>17.8 \pm 1.4</i>
<i>2008</i>	<i>203-209</i>	<i>7</i>	<i>0.46</i>	<i>0.37</i>	<i>17.1 \pm 1.4</i>
<i>2008</i>	<i>219-225</i>	<i>7</i>	<i>0.61</i>	<i>0.40</i>	<i>16.1 \pm 2.5</i>
2009	107-115	9	0.42	0.32	17.5 \pm 0.8
<i>2010</i>	<i>1-11</i>	<i>11</i>	<i>0.38</i>	<i>0.30</i>	<i>15.2 \pm 1.3</i>
<i>2010</i>	<i>34-42</i>	<i>9</i>	<i>0.53</i>	<i>0.39</i>	<i>16.8 \pm 1.6</i>
<i>2010</i>	<i>48-56</i>	<i>9</i>	<i>0.75</i>	<i>0.55</i>	<i>15.9 \pm 1.0</i>
<i>2010</i>	<i>75-88</i>	<i>14</i>	<i>0.54</i>	<i>0.42</i>	<i>17.9 \pm 1.0</i>
<i>2010</i>	<i>112-119</i>	<i>8</i>	<i>0.63</i>	<i>0.55</i>	<i>16.3 \pm 1.3</i>
<i>2010</i>	<i>139-148</i>	<i>10</i>	<i>0.64</i>	<i>0.46</i>	<i>16.8 \pm 1.9</i>
<i>2010</i>	<i>154-172</i>	<i>19</i>	<i>0.74</i>	<i>0.49</i>	<i>17.3 \pm 1.1</i>
<i>2010</i>	<i>186-201</i>	<i>16</i>	<i>0.50</i>	<i>0.40</i>	<i>16.9 \pm 2.1</i>
2010	250-259	10	0.70	0.60	18.1 \pm 2.1

Note: Italicized data refer to recurrent trains.

5.2 Trains and recurrent trains of enhanced and suppressed diurnal variations

Trains of enhanced DA from November, 2007 to November, 2010 are listed in Table 5.1, some of which are recurrent. The trains of enhanced DA were chosen according to a criterion of $DA \geq 0.25\%$ for a duration ≥ 7 days (about one-quarter of a 27-day rotation). We observed two periods of recurrent trains of suppressed and enhanced DAs that roughly repeat after a 27-day Carrington rotation, from CR2068 to CR2073 (Figure 5.3) and from CR2092 to CR2098 (Figure 5.4). The trains of enhanced DA usually start within a few days from the start of an HSS and a depressed GCR flux. Furthermore, the recurrent DAs seem to be magnetic-sector dependent, where the enhanced DAs were mostly in the A sectors and the suppressed ones were mostly in the T sectors.

During the first period of recurrent trains, in Carrington rotations CR2068-

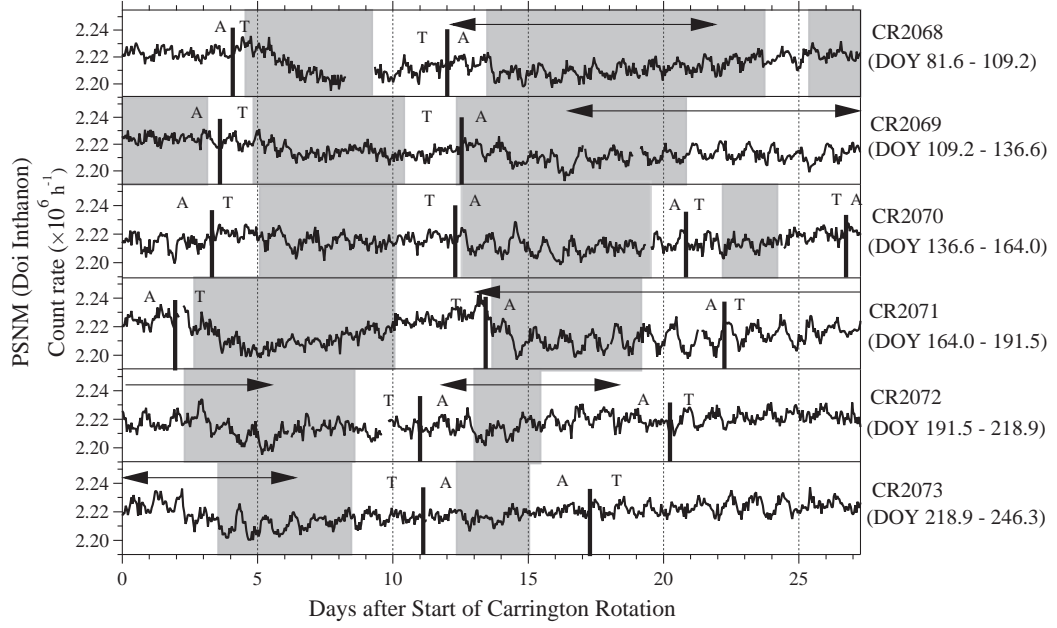


Figure 5.3: Count rate of the *Princess Sirindhorn Neutron Monitor* at Doi Inthanon as a function of time, showing recurrent trains of enhanced diurnal anisotropy (DA) in 2008, indicated by arrows, compared with magnetic sectors (toward, T, or away, A) for six successive Carrington rotations, CR2068-2073. Shaded areas represent HSSs with solar wind speed $\geq 450 \text{ km s}^{-1}$. Recurrently enhanced DA was often observed in the A sector, while suppressed DA was often observed in the T sector.

CR2073 during 2008 (Figure 5.3), the intensity of GCRs usually decreased near the start of an HSS around day 5 of the CR, which was often near the leading edge of a T sector. Note that such recurrent GCR decreases during HSSs represent the well known 27-day variations (Fonger 1953; Simpson 1998). The intensity then recovered completely or partially, mostly before the trailing edge of the stream. This recurrent HSS in the T sector exhibited recurrent trains of enhanced DA only during CR2072-CR2073. Another HSS came on day 12 or 13 of every CR, during the A sector, causing another temporary decrease in GCRs and usually exhibiting a recurrent train of enhanced DA. These trains of enhanced DA were always in the A sector, except during DOY 186-196 and 219-224, when the HCS was close to the heliolatitude of Earth, as we shall discuss in Section 5.4.1.

The other time period of recurrent trains of enhanced and suppressed DA, CR2092-CR2098, exhibited more variability in terms of HSSs and DA. There were three

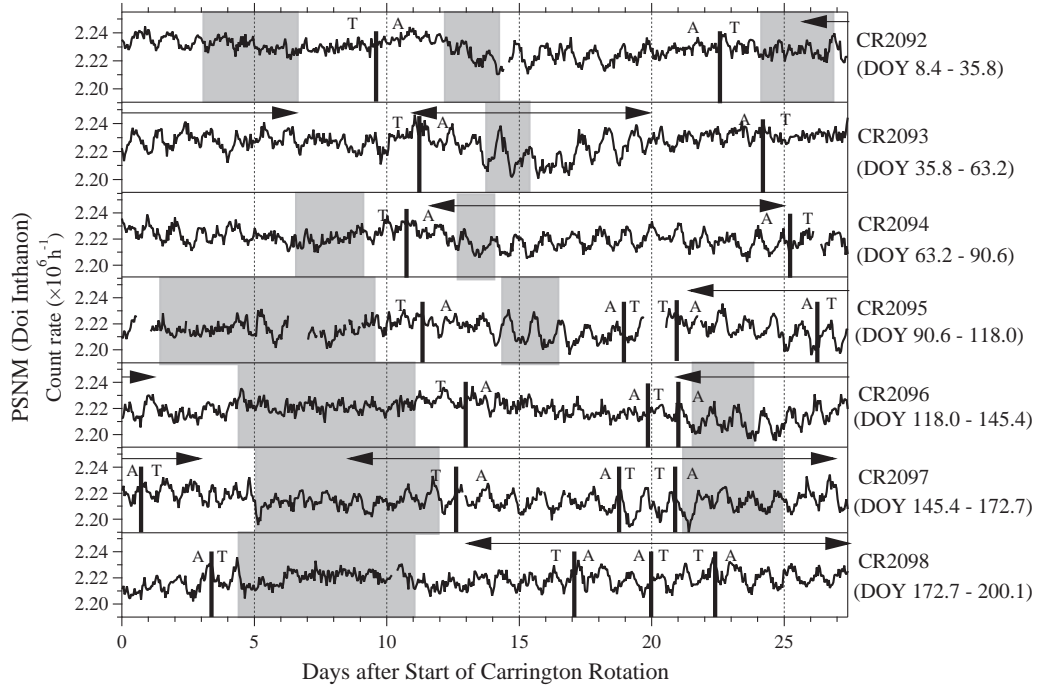


Figure 5.4: Same as Figure 5.3 for CR2092-2098 during 2010. There are three patterns of enhanced diurnal variations: (i) One enhancement mostly in the T sector during CR2092-CR2093. (ii) Repeated enhancement mostly in the A sector, during CR2093-CR2096. (iii) Extended enhancements in both the T and A sectors during CR2097-CR2098.

types of enhanced diurnal variations, as follows: (1) A single train of enhancement mostly in the T sector during CR2092-CR2093, (2) a repeated train of enhancement mostly in the A sector, during CR2093-CR2096, and (3) extended repeated enhancements in both the T and A sectors during CR2097-CR2098.

In summary, during both of these periods of recurrent trains, Figures 5.3 and 5.4 show that there were multiple consecutive Carrington rotations during which the DA was mostly enhanced in the A sectors and suppressed in the T sectors (CR2068-CR2071 and CR2092-CR2095).

5.3 Gradient anisotropy

As found in the previous section, the DA during the recurrent trains tends to be enhanced or suppressed depending on the sign of the magnetic field \mathbf{B} , and was most

commonly enhanced during A sectors and suppressed during T sectors. While effects of convection and diffusion do not depend on the sign of \mathbf{B} , there is a sign dependence for the gradient anisotropy along $\mathbf{B} \times \nabla n$, which could therefore describe this behavior.

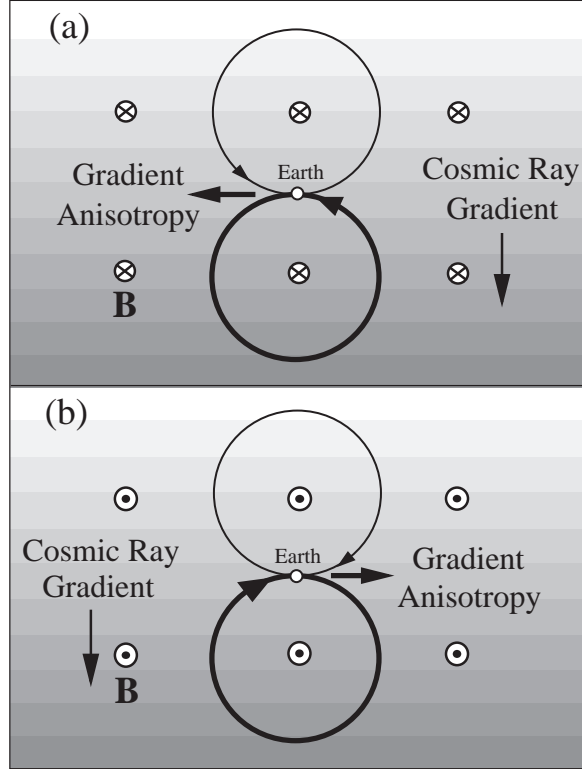


Figure 5.5: Illustration of the gradient anisotropy. Darker shading indicates a higher cosmic ray density, n , and the gyration of cosmic rays around the interplanetary magnetic field \mathbf{B} leads to a net anisotropy directed along $\mathbf{B} \times \nabla n$. This can explain some changes in the DA that are associated with changes in the sign of \mathbf{B} , in which case this figure represents a Sunward view of near-Earth space. When superimposing the normal corotational anisotropy toward the right (along Earth’s orbit), a southward gradient in the GCR density leads to (a) suppression or (b) enhancement of the diurnal anisotropy in toward (T) and away (A) magnetic sectors, respectively.

The well-known gradient anisotropy of GCRs along $\mathbf{B} \times \nabla n$ is illustrated by Figure 5.5. For example, when the cosmic ray density is higher in the southern hemisphere, this provides a southward gradient in the GCR density. The gyration of cosmic rays around the IMF causes an observer to see a net anisotropy along the $\mathbf{B} \times \nabla n$ direction, which is in turn related to the sign of \mathbf{B} . As a result, the anisotropy then enhances or suppresses the usual corotational DA in A and T sectors, respectively.

According to Jokipii et al. (1977), the streaming flux is given by $F_i =$

$-\kappa_{ij}\partial n/\partial x_j$, where κ_{ij} is the diffusion-drift tensor and n is the cosmic ray density. This includes a term for the streaming flux due to the gradient (drift) anisotropy, $\mathbf{F}_A = \kappa_A \mathbf{e}_B \times \nabla n$, where $\mathbf{e}_B = \mathbf{B}/B$. Here κ_A describes the antisymmetric part of the diffusion coefficient, including effects of gradient and curvature drifts. For a positive charge and a scattering mean free path much greater than the gyroradius r_g , both of which are true for GCR ions, we have $\kappa_A = vr_g/3$ (Jokipii et al. 1977), where $r_g = \gamma mv/qB = P/cB$, v is the cosmic ray velocity, γ is the Lorentz factor, m is the rest mass, P is the rigidity, and c is the speed of light. The flux \mathbf{F}_A reverses when the particle charge changes sign. An anisotropy is related to the streaming flux as $\mathbf{A} = 3\mathbf{F}/(vn)$ so the anisotropy is $\mathbf{A} = (r_g/n)\mathbf{e}_B \times \nabla n$. If \mathbf{B} is in the ecliptic plane along the x and y directions of GSE coordinates the gradient anisotropy may be expressed as

$$\begin{aligned}
 \mathbf{A} &= \frac{P}{cB^2n} \mathbf{B} \times \nabla n \\
 &= \frac{P}{cB^2n} \left[\left(B_x \frac{\partial n}{\partial y} - B_y \frac{\partial n}{\partial x} \right) \mathbf{z} + (B_y \mathbf{x} - B_x \mathbf{y}) \frac{\partial n}{\partial z} \right].
 \end{aligned} \tag{5.1}$$

This expression contains two components of anisotropy. The first term of the right-hand side is the North-South anisotropy (in the \hat{z} direction) arising from a gradient in the ecliptic plane. This component would make little contribution to the DA. However, the second term is in the ecliptic plane and arises from a latitudinal gradient in GCRs:

$$A_e = r_g \frac{B_e}{B} |G_z|, \tag{5.2}$$

where the subscript e refers to the magnitude in ecliptic (x, y) plane, and $G_z = (\partial n/\partial z)/n$ is the fractional latitudinal gradient. A density gradient should cause anisotropy even in a homogeneous magnetic field (Spitzer 1952).

It is interesting to note the huge size of the gyroradius for GCRs observed at Doi Inthanon. The angular diameter θ of the gyro-orbit is related to the rigidity by the expression (Subramanian & Sarabhai 1967)

$$\theta \approx \tan^{-1} \frac{2P \sin \alpha}{45B}, \tag{5.3}$$

where the rigidity P is in GV, the interplanetary field B is in nT, and the look direction α is the direction of motion with respect to the magnetic field (the pitch angle of cosmic rays). The median rigidity P of GCRs observed at Doi Inthanon is about 35 GV (K. Munakata 2010, private communication). On DOY 184 of 2008, a 2 nT field was observed by the *ACE* spacecraft, so for $\alpha = 90^\circ$, at Doi Inthanon a median-rigidity ion had an angular gyro-diameter of $\approx 40^\circ$. Thus the GCR gradient anisotropy at Doi Inthanon can provide information about the gradient over a great distance from the ecliptic plane.

For one particularly strong sequence of DA enhancement at Doi Inthanon, we can provide a qualitative explanation for a southward GCR gradient. Data for CR2070 and CR2071 are shown in Figures 5.6 and 5.7, respectively. The most enhanced DA, on DOY 184 of 2008 during CR2071, coincided with a compound HSS from two positive polarity-CHs. In the synoptic map, these are at the Equator (B) and a mid-latitude extension of the south polar CH (C). Their corresponding solar wind streams are evidently merged to become a compound stream, and in Figure 5.7 one can see two distinct peaks in the solar wind speed corresponding to the two CHs. The HSS should therefore be slanted with respect to the solar equator, which should lead to a density gradient perpendicular to its boundary, with fewer particles in the HSS (see Chapter 1). Consequently, the compound HSS from the positive polarity CHs should have a strong latitudinal component of the cosmic ray gradient toward the south. As a result, when the magnetic field was in the A sector ($B_x < 0$) in combination with the southward GCR gradient, Equation (5.1) implies a $\mathbf{B} \times \nabla n$ anisotropy component along $-\hat{y}$, thus enhancing the usual corotational anisotropy.

It is notable that DA values in the trains of enhanced DA were different during the passage of the CIR and HSS (Figure 5.7 and 5.9), especially in the trailing part of the HSSs. In CR2064 around DOY 356-358 and in CR2071 around DOY 184-186, the DAs were higher than they were near the CIR. The greatest enhancement occurred at times when the corresponding CHs were located at heliolatitudes of about 40° - 50° . As the CIR structure extended to high latitudes because of the slanted morphology of

CHs, the latitudinal gradient of GCRs also extended to those high latitudes. In the context of $\mathbf{B} \times \nabla n$ anisotropy, we are able to explain some features of enhanced and suppressed DA in association with a latitudinal gradient of GCRs over a domain that has the dimensions of the gyroradius of the cosmic ray particles.

5.4 Case studies

To study trains of enhanced (or suppressed) DA in more detail, we selected one time period, including the time of maximum DA, from each of the two periods of recurrent trains of enhanced DA, as well as one time period with a non-recurrent train. DAs and phases were also studied in comparison with synoptic maps and interplanetary plasma parameters in order to clarify the mechanism of DA enhancement and suppression.

5.4.1 Carrington rotations 2070 & 2071

We first examine CR2070 and CR2071 (2008 May 15 to July 9), which had recurrent trains of enhanced and suppressed DA, and included the strongest DA found in this study (0.79%). Figures 5.6 and 5.7 show reversed-time plots of GCR data from the *Princess Sirindhorn Neutron Monitor*, together with synoptic maps of the solar corona constructed from Fe XII λ 195 Å images from *STEREO-A/EUVI*, and solar wind plasma parameters from the *ACE* spacecraft. Slanted lines between panels (a) and (b) of each Figure show the correspondence between the solar longitude in the synoptic map and the reversed time axis of the lower plots. There is a direct correspondence between magnetic polarity at the Sun (as determined from the location of Earth's orbit relative to the HCS) and predominant polarities of the HSSs (as determined from the magnetic field components B_x, B_y near Earth). The isolated CH (A) of negative (toward) polarity was located near the solar equator above the HCS, whereas the positive (away) polarity CHs (B and C) were located below the HCS, at the solar equator and southern hemisphere,

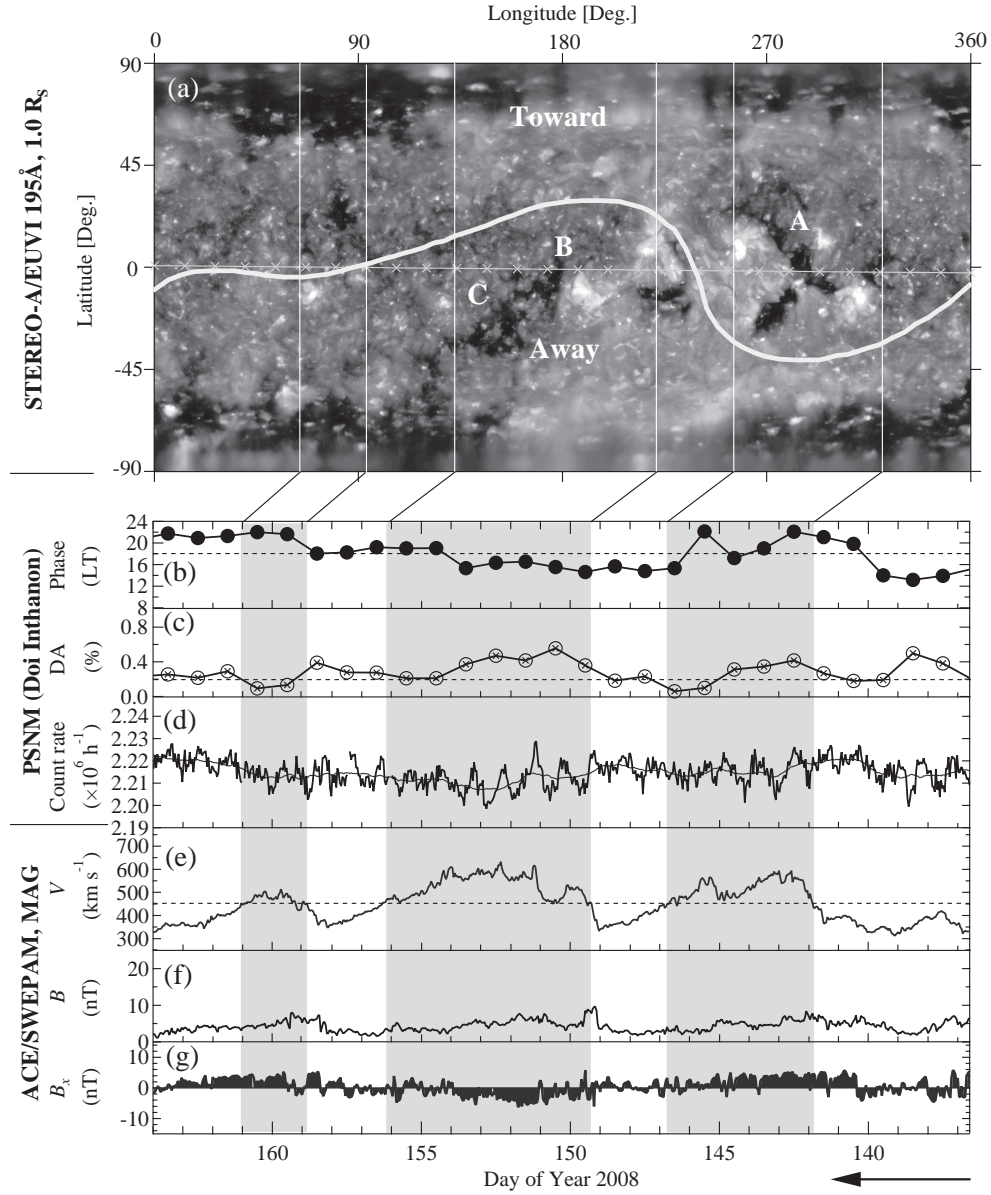


Figure 5.6: Reversed time plots for Carrington rotation (CR) 2070, from 2008 May 15 to June 12. From top: (a) Synoptic map of the solar corona as observed by the *STEREO-A/EUVI* imager in the Fe XII 195Å bandpass. The position of the HCS from a WSO synoptic chart is shown by a thick light-gray line and the projected orbit of the Earth is indicated by gray crosses. Slanted lines show the correspondence with the reversed time axis of the lower plots. (b) Phase (time of maximum) of diurnal variation, in local time. The dashed line indicates the corotational anisotropy (1800 LT). (c) Diurnal anisotropy (DA). The dashed line is the observed average DA. (d) Hourly neutron count rate (thick line) and its running 1-day average (thin line). (e) Solar wind speed. (f) Magnitude of magnetic field. (g) Sunward magnetic field component. Shaded areas represent HSSs with speed $\geq 450 \text{ km s}^{-1}$. Note the enhanced DA lasting for 5 days starting near the onset of the HSS on day of year (DOY) 149, which we attribute to the slanted geometry of the HSS due to the combined effects of CH B and C. The enhanced DA in the HSS is consistent with the $\mathbf{B} \times \nabla n$ anisotropy for a southward cosmic ray gradient associated with the slanted geometry.

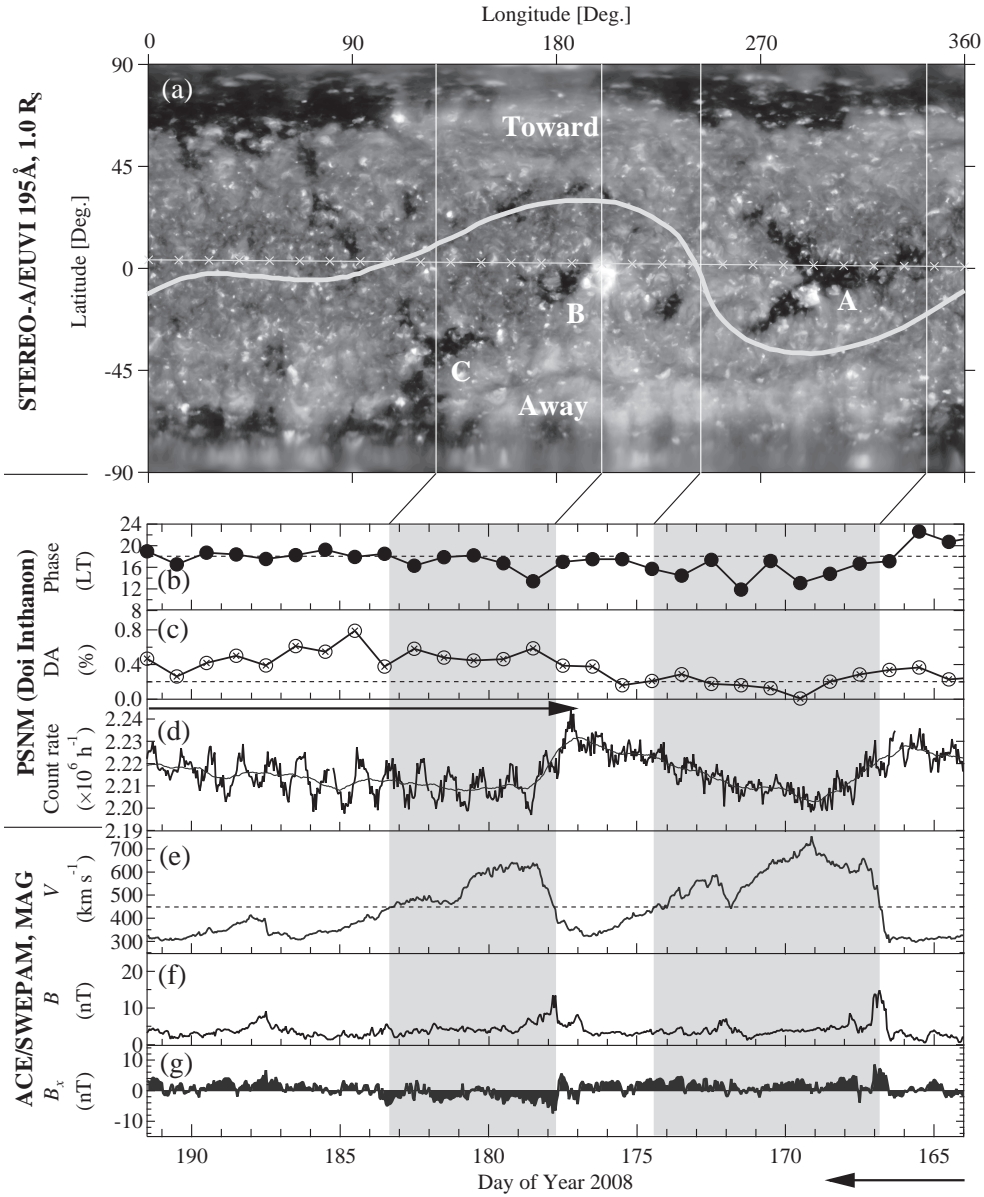


Figure 5.7: Same as Figure 5.6 for CR2071, from 2008 June 12 to July 9. Note the train of enhanced DA, indicated by an arrow, starting near onset of a HSS on day of year (DOY) 177, which we attribute to the slanted geometry of the high speed solar wind stream (HSS) due to the combined effects of CHs B and C. The enhanced DA in (c) after the sharp decrease in cosmic ray intensity in (d) is consistent with the $\mathbf{B} \times \nabla n$ anisotropy for a southward gradient associated with the slanted geometry. While the local magnetic field reversed on day 183, the synoptic map (a) indicates that the boundary between toward and away sectors remained near Earth, in comparison with the large gyroradius of cosmic rays observed at Doi Inthanon, so a southward cosmic ray gradient can still contribute to enhanced DA.

respectively. During the times of recurrent solar wind streams, there was downward modulation of GCR intensity, heralded by compressions in the magnetic field (B) near Earth at their leading edges.

The longest-lasting train of enhanced DA was observed for 21 days from DOY 176 (2008 June 24) to DOY 196 (2008 July 14). This time period included the passage of a CIR and HSS with a lower GCR flux during the HSS. The HSS was associated with two positive polarity CHs (see Figure 5.7; “B” is at the equator and “C” is a mid-latitude extension of the south polar CH). Based on the solar wind speed data, the HSSs are evidently merged to be a compound stream. Indeed, during the preceding Carrington rotation, CR2070, “B” and “C” formed a merged CH (Figure 5.6). The compound HSS should therefore be slanted with respect to the solar equator, which should lead to a GCR density gradient perpendicular to its boundary. Consequently, the compound HSS from the positive polarity CHs in CR2071 should have a component of latitudinal gradient of cosmic rays toward the south. This should cause an additional anisotropy in the ecliptic plane via the $\mathbf{B} \times \nabla n$ gradient drift flux.

To estimate the latitudinal gradient of GCR density, we examined the slope of the decline in the running 24-h average of the *PSNM* count rate during DOY 177-178 to infer a cosmic ray density gradient of $-0.74\% \text{ day}^{-1}$. Assuming that the structure moves past the Earth with the synodic period of 26.75 days (Bai 1987), this corresponds to a longitudinal gradient of $3.2\% \text{ AU}^{-1}$. Assuming for simplicity that the HSS leading edge is slanted by roughly 30° counter-clockwise from the equatorial plane, like the CH complex (see Figure 5.6(a)), we infer a latitudinal gradient of $-5.5\% \text{ AU}^{-1}$. According to Equation (5.2), if the magnetic field is nearly in the ecliptic plane then $B_e \approx B$ and $A_e \approx r_g |G_z|$ (Datter & Venkatesan 1959). For median rigidity protons detected by *PSNM*, at 35 GV, the Larmor radius was about 0.1 AU for the average magnetic field, 7 nT, near the leading edge of the HSS during DOY 177-178, and from $G_z = -5.5\% \text{ AU}^{-1}$ the gradient anisotropy should be about 0.55%, which is in good agreement with the observed enhancement in the DA with amplitude about 0.5%.

In the A sector, the average DA and phase were $0.50 \pm 0.10\%$ and 17.5 ± 1.4 h LT. In the T sector, they were $0.19 \pm 0.09\%$ and 15.6 ± 2.0 h LT in the first half of the Carrington rotation. From these values we see that the DAs are different, but the average phases are consistent with the corotational direction of 18 h LT (although in the T sector there was a larger spread). This is in contrast with the results reported by Mavromichalaki (1989) and Mishra & Mishra (2005) for GCR at lower energy.

In Section 5.2, we discussed that the recurrent trains during CR2068-CR2073 included two types of trains, starting in the A sector (CR2068, CR2069, CR2071, and CR2072) or the T sector (CR2072 and CR2073), as seen from Figure 5.3. The earlier portion, CR2068-CR2071, exhibits mainly enhanced DA during A sectors and suppressed DA during T sectors, which is well explained by a gradient anisotropy associated with a general southward gradient in the GCR density. In contrast, CR2072 and CR2073 contain T-sector trains of enhanced DA that are not explained by the effect of a southward GCR gradient. These two T-sector trains, associated with CH “A”, could have had a northward GCR gradient in CR2072 and CR2073, or could have had an enhanced DA due to other processes such as a combination of convection and diffusion.

CR2071 presents an interesting case where the two types of trains merge into a 21-day train over DOY 176-196. This is the only train in our survey that lasted more than 14 days. After the very strong DA in the A sector during DOY 176-185, which we attribute to a slanted compound HSS due to CH “B” and “C” and the resulting strong southward GCR gradient south of the HCS that leads to a strong gradient anisotropy, it is notable that the DA was still high in the T sector during the recovery of the GCR flux on DOY 186-191. That is still consistent with a southward GCR gradient because the HCS was close to the solar equator. Recalling that the gyro-orbits of GCRs are very large in this rigidity range (see Section 5.3), the gradient anisotropy can result from gradients over a large distance. Indeed, when the HCS is close to Earth in comparison with the particle gyroradius, with an A sector to the south and a T sector to the north, both a southward gradient south of the HCS (due to the CH “B” and “C”) and a northward

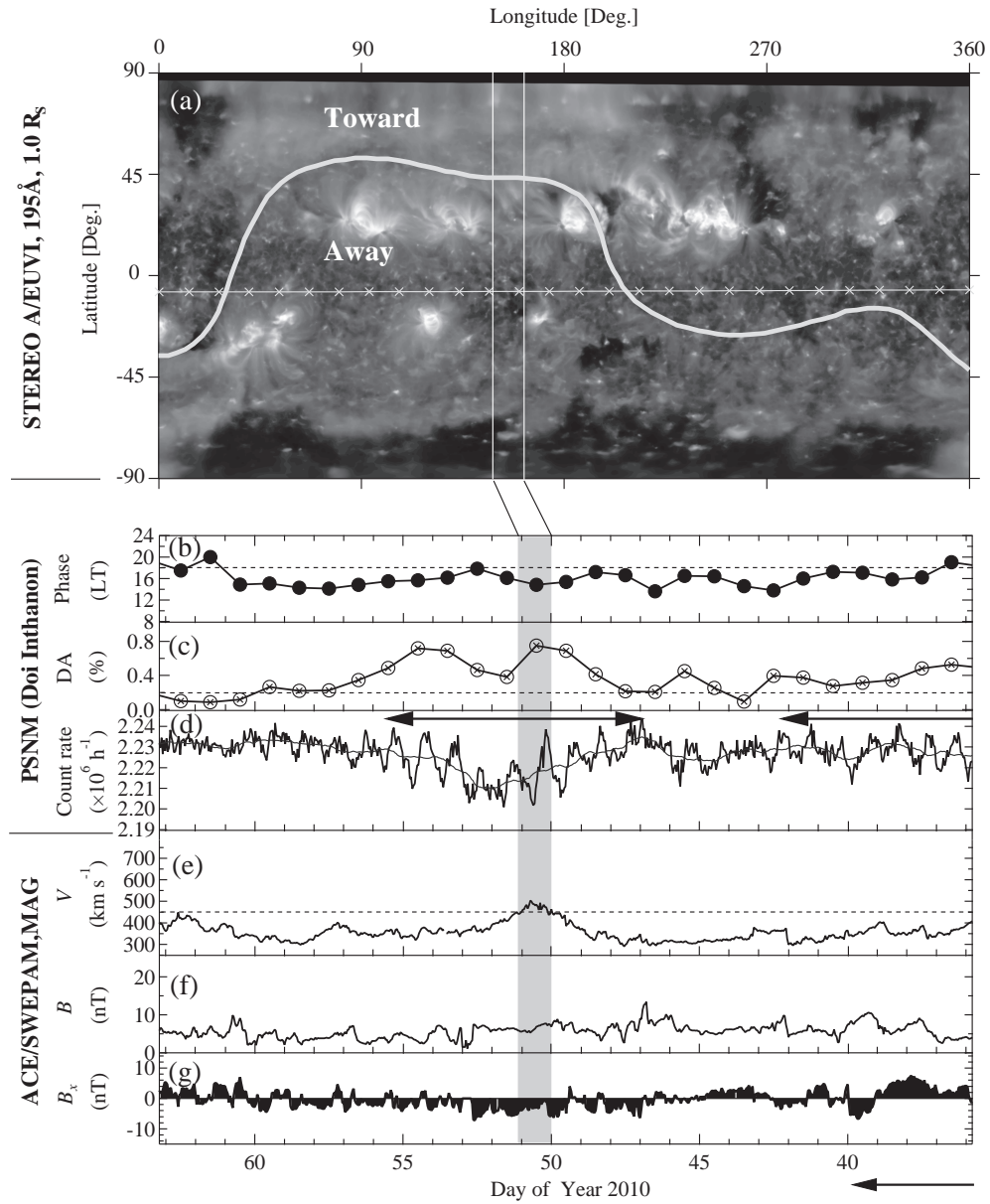


Figure 5.8: Same as Figure 5.6 for CR2093, from 2010 February 4 to March 4. This is an example of a recurrent train of enhanced DA in 2010, in association with the away sector of the interplanetary magnetic field near Earth. A gradient anisotropy could explain this association, although the reason for a southward GCR gradient is not clear.

gradient north of the HCS (due to CH “A”) can contribute to enhanced DA. We suggest that the effects of the two sets of CHs overlapped in solar longitude while the HCS was close to Earth, leading to this continuous train of enhanced DA.

5.4.2 Carrington rotation 2093

Now we turn to the other period of recurrent trains of enhanced DA, in 2010. As shown in Figure 5.8, CR2093 (2010 February 4 to March 4) exhibited two trains, a non-recurrent train that started during an HSS in the T sector during DOY 34-42, and a train during DOY 48-56 that recurred in subsequent Carrington rotations in association with the A sector of the interplanetary magnetic field near Earth. The strongest DA was 0.75%, which was the greatest value observed in 2010. Throughout CR2092-CR2095, the DA was mostly enhanced in the A sectors and suppressed in the T sectors. A gradient anisotropy could explain this association with the sign of \mathbf{B} , which would again require a southward GCR gradient.

We also found a correspondence between polarities of the CHs and the HSSs. A complex CH structure of negative polarity was located far above the solar equator and the HCS, whereas a large stripe of positive polarity CHs was located in the southern hemisphere. Around DOY 48-53, the GCR intensity was clearly reduced during the passage of a HSS that emerged from an isolated positive equatorial CH at longitude about 160° . It is notable that the greatest reduction in GCR intensity and the highest levels of the DA were close to the region of the HSS. Note also that the DA was enhanced during the passage of the moderate HSS in the A sector, but tended to diminish close to the boundaries with the T sector.

In the A sector, the average DA was $0.47 \pm 0.20\%$ and the phase was 15.6 ± 1.1 h LT. In the T sector, the average DA was $0.29 \pm 0.15\%$, mainly in association with the non-recurrent T-sector DA enhancement, and the phase was 16.6 ± 1.8 h LT. Interestingly, the phase of the diurnal variation was generally low during this CR.

5.4.3 Carrington rotation 2064

Now we consider an example of a non-recurrent train of enhanced DA in CR2064 (2007 December 3 to December 29) for which we again found a correspondence between polarities of the CHs and the HSSs (Figure 5.9). An isolated CH of negative

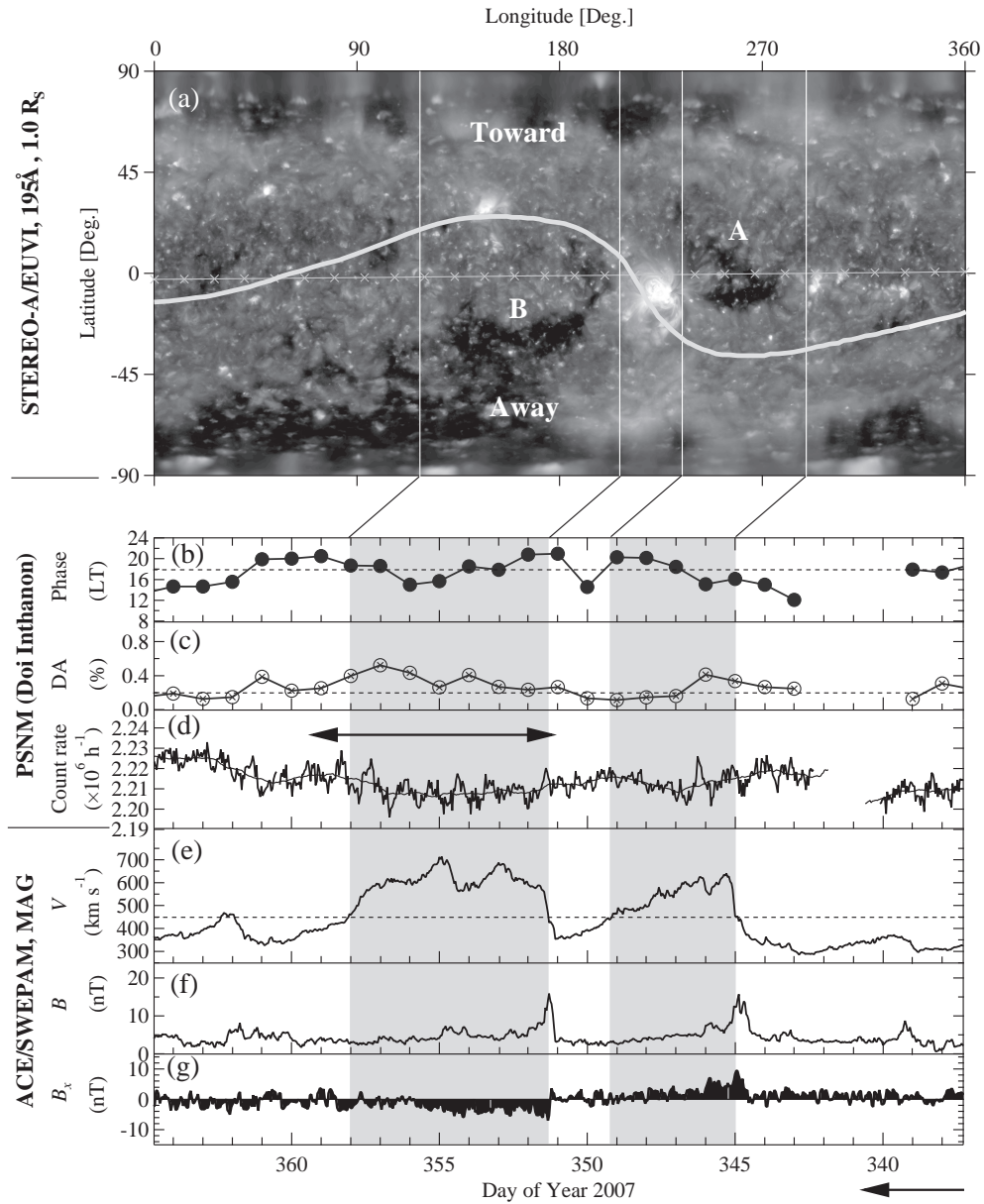


Figure 5.9: Same as Figure 5.6 for CR2064, from 2007 December 3 to December 29. An example of a non-recurrent train of enhanced DA in 2007, which is also associated with the away sector of the magnetic field and could also be explained by a gradient anisotropy.

polarity (“A”) was located at the solar equator and near the HCS, whereas a largely slanted positive polarity CH structure (“B”) was located in the southern hemisphere. Observationally, the larger CH “B” provided a broader HSS region in interplanetary space than the CH “A”.

Around DOY 345-358, the GCR intensity was clearly reduced during the passages of the two HSSs from CH “A” and “B”. As usual, the higher solar wind speed can inhibit the GCR flux. The two CHs were close to each other, so the GCR intensity could not effectively recover around DOY 349 to the previously level as on DOY 343-344. The GCR intensity did clearly recover around DOY 362 behind the passage of the HSS from CH “B”.

Of the two HSSs, only the latter was associated with a train of enhanced DA. This started during the passage of the large HSS with a complex velocity profile associated with CH “B” in the A sector and lasted for 9 days, DOY 351-359. As described before for CR2071, the slanted structure of the CH (“B”) can provide a latitudinal gradient of GCRs toward the south that should cause an enhanced DA by the $\mathbf{B} \times \nabla n$ gradient anisotropy in the A sector. The lower value of the average enhanced DA during this CR should be related to the much lower GCR gradient seen in the *PSNM* count rate. In the A sector of CR2064, the average DA was $0.34 \pm 0.13\%$ and the average phase was 16.7 ± 2.1 h LT, whereas in the T sector, the DA was $0.24 \pm 0.09\%$, which is consistent with the average value during our 3-year survey, and the phase was 17.8 ± 2.7 h LT. We can see that the average phases were close to the corotational direction in both magnetic sectors.

5.5 27-day cosmic ray intensity modulation

Solar modulation of GCRs by the CSWSs that recurs after about 27 days was remarkably clear in this solar minimum. To illustrate the 27-day variations of GCR intensity in association with the variations of the solar wind plasma parameters and interplanetary magnetic field of HSSs and CIRs, we showed yearly plots of the data from late 2007 to late 2010 in Figures 5.10-5.13. Most of the dips of 27-day variations in GCR intensity were observed close to the peak of solar wind speed. In addition, the initial reduction of GCR intensity was close to the peaks of solar wind proton density and magnetic field intensity, which indicate compression of the solar wind plasma.

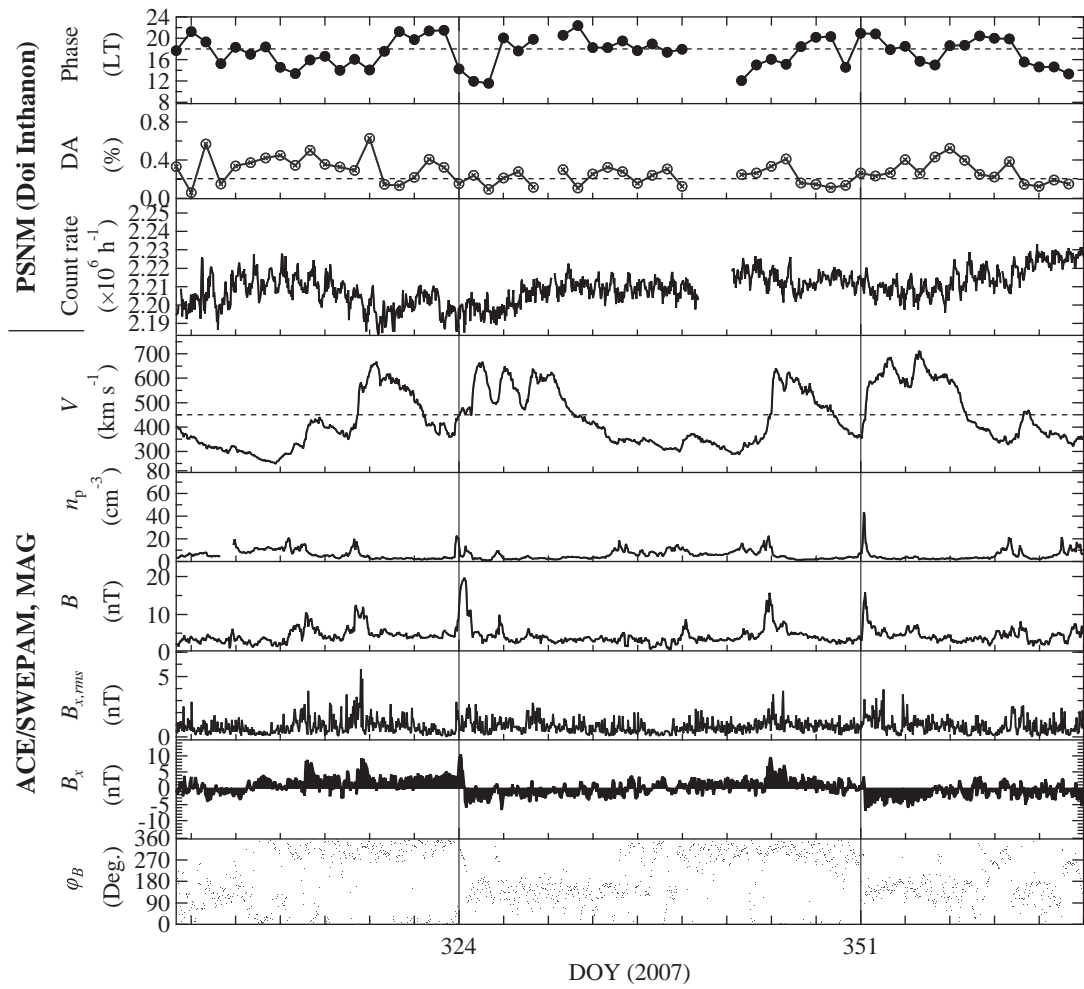


Figure 5.10: The 27-day variations in GCR intensity and solar wind plasma parameters during late 2007. Vertical lines represent 27-day time periods.

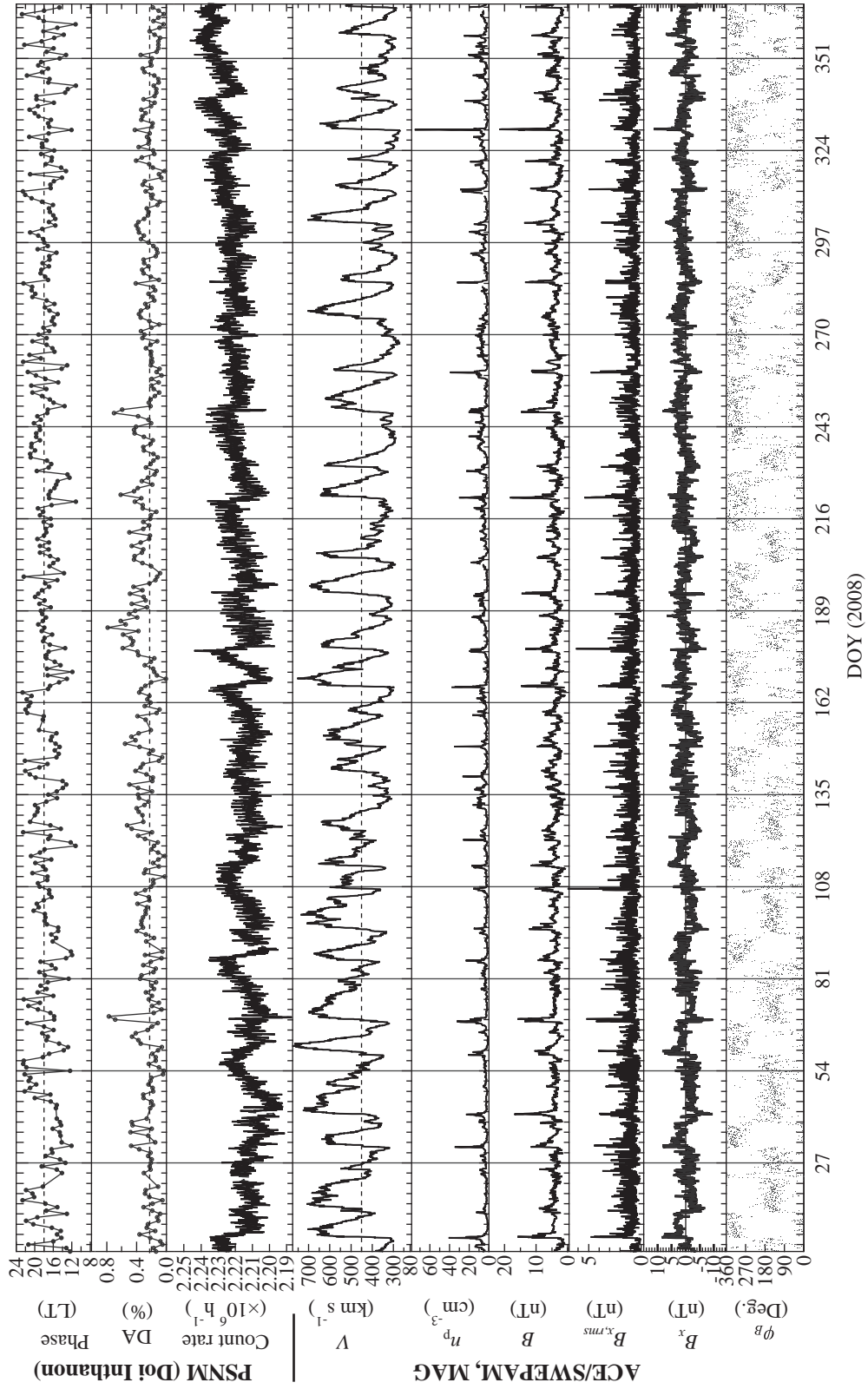


Figure 5.11: Same as Figure 5.10, for the year 2008.

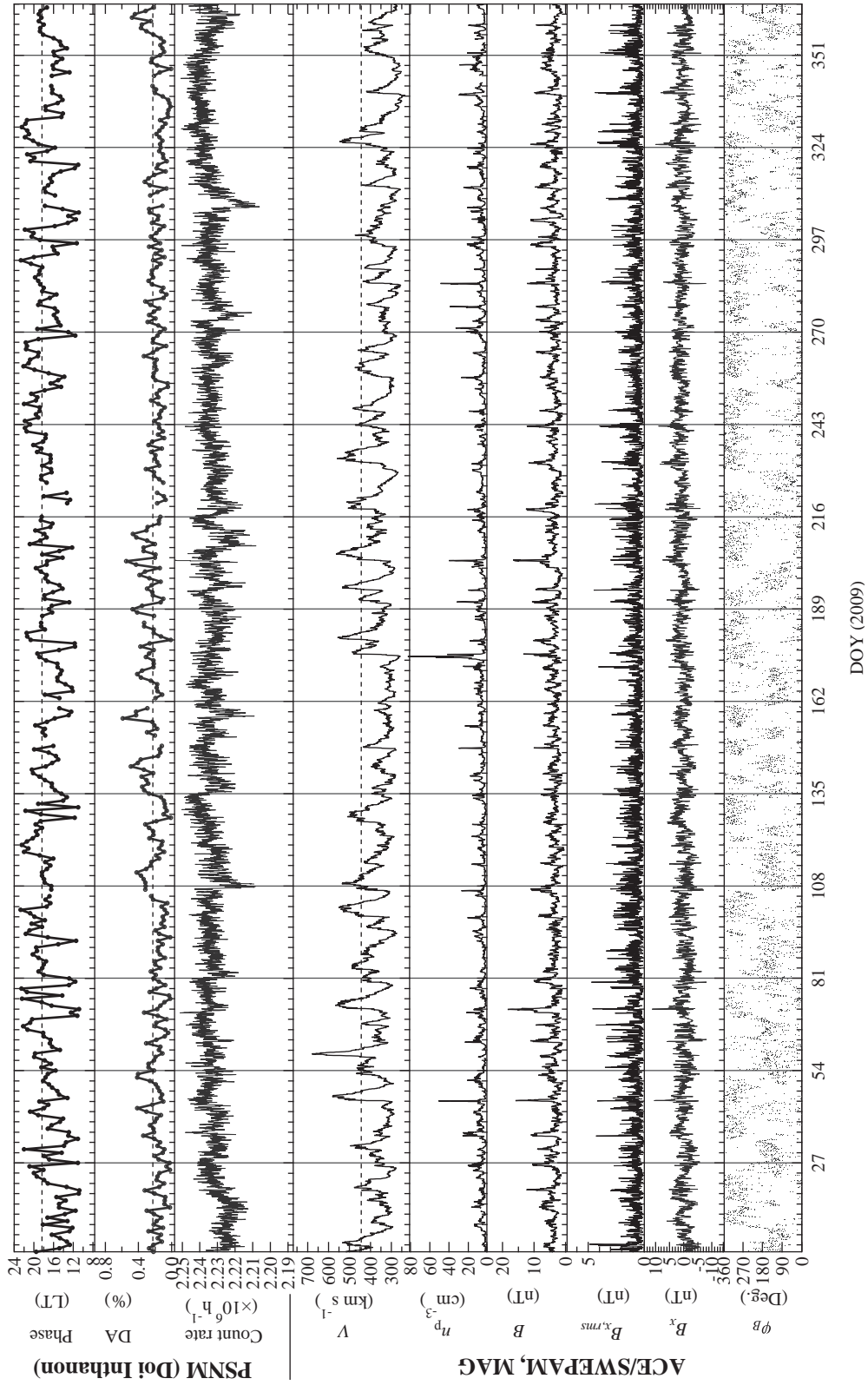


Figure 5.12: Same as Figure 5.10, for the year 2009.

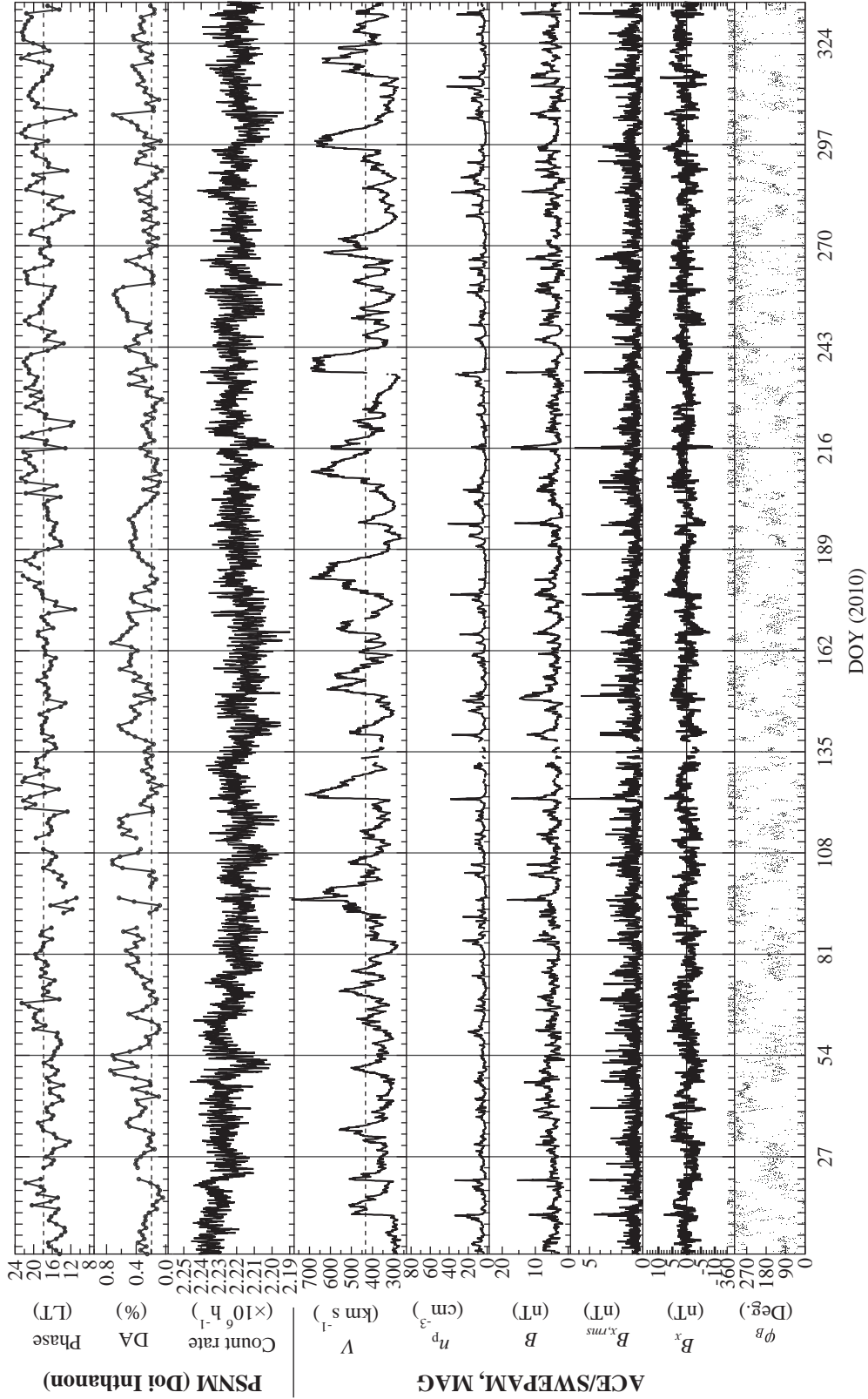


Figure 5.13: Same as Figure 5.10, for the year 2010.

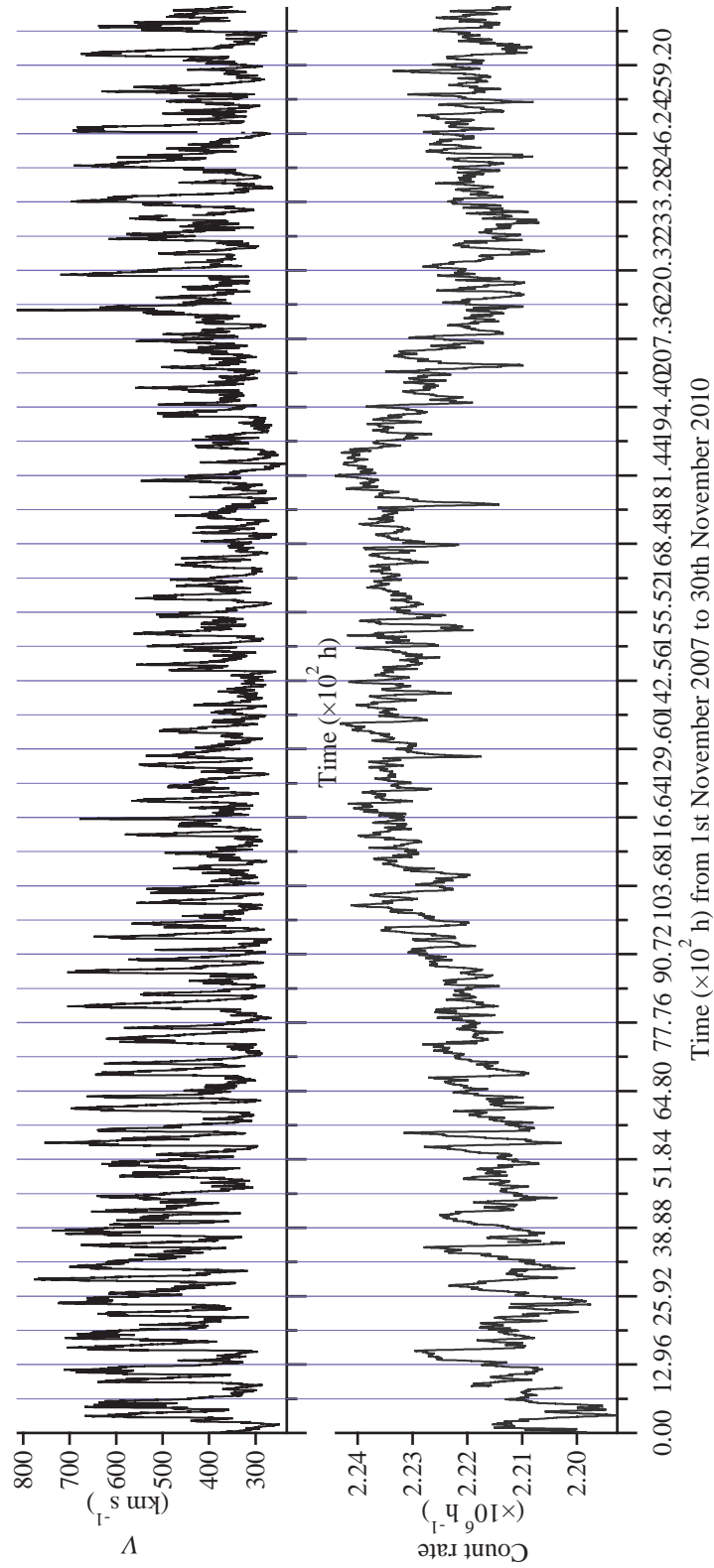


Figure 5.14: The 27-day variations in moving average of hourly GCR intensity and hourly solar wind speed. The grid lines represent a 27-day period.

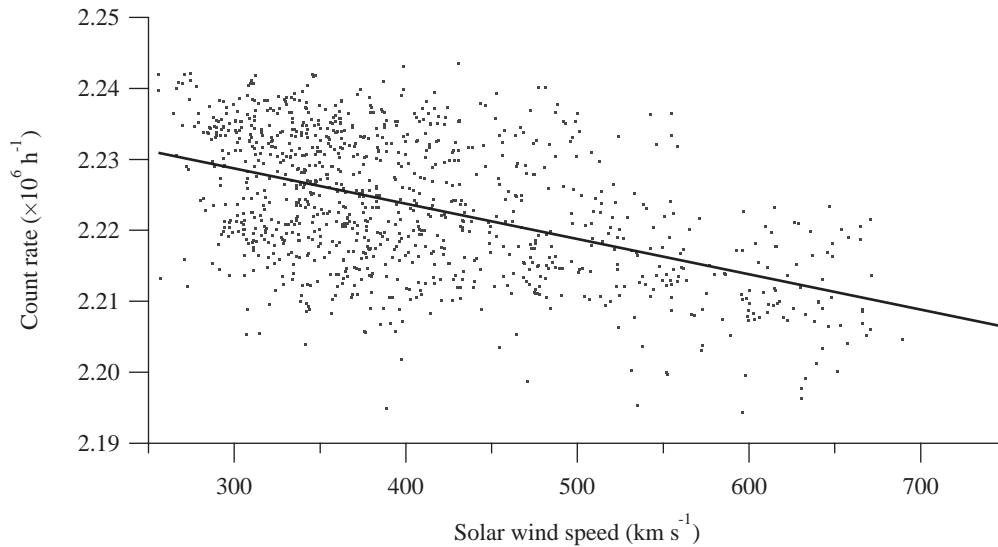


Figure 5.15: Correlation of daily average of GCR intensity with solar wind speed.

Specifically, the overall plot of hourly GCR intensity and solar wind speed is shown in Figure 5.14. The GCR intensity tends to be temporally reduced when the solar wind speed increases and vice versa. In addition, one can see typical patterns of the 27-day modulation of GCR intensity in association with the solar wind speed. It is thus interesting to provide a quantitative basis to assess the effect of the solar wind speed on the GCR flux. We did linear regression analysis between the hourly PSNM count rate, indicating GCR intensity, and solar wind speed to obtain a linear correlation between them as shown in Figure 5.15. We found a linear correlation coefficient of -0.49 . This coefficient implies an anti-correlation between GCR flux and solar wind speed for high rigidity GCRs at Doi Inthanon.

The neutron count rate was frequently suppressed in coincidence with the passages of CIRs and HSSs and then started to recover in the trailing edge of the HSSs. The HSSs from the coronal holes, subsequently, were simple streams if there was only one stream and compound streams if more than two streams are merged. We observed that the 27-day modulation can be phenomenologically categorized into symmetric and asymmetric types following the characteristics of HSSs; symmetric modulation (V-shape) corresponded to a simple stream whereas asymmetric modulation corresponded to a

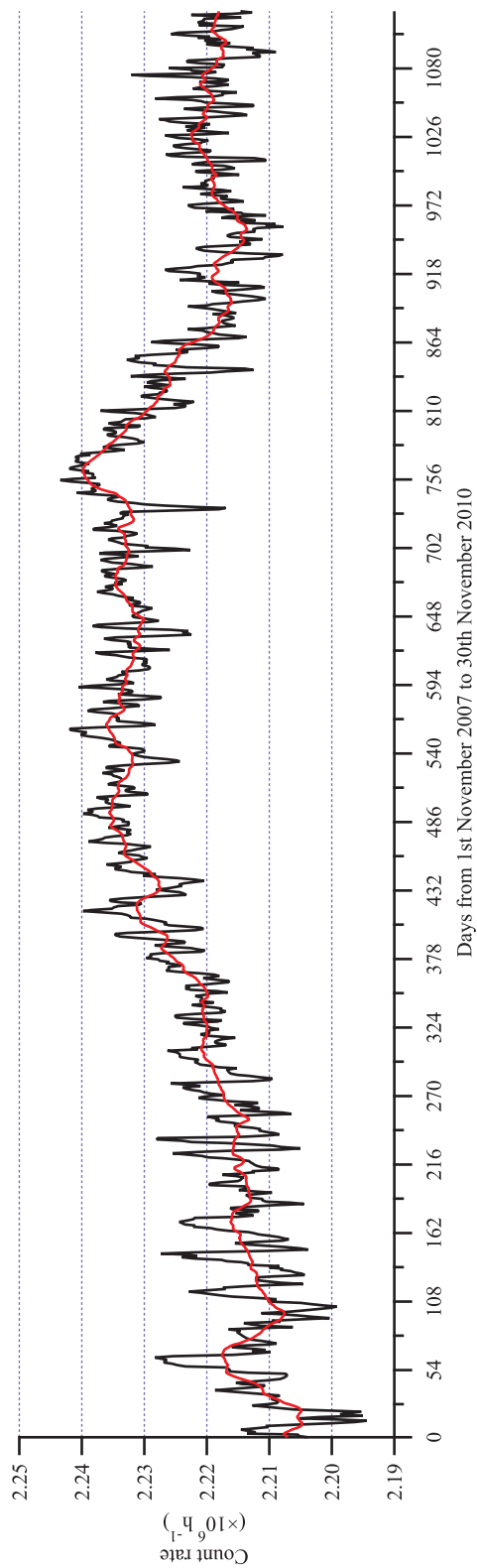


Figure 5.16: The 27-day modulation of daily GCR intensity in this study. The thin line represents a 27-day moving average.

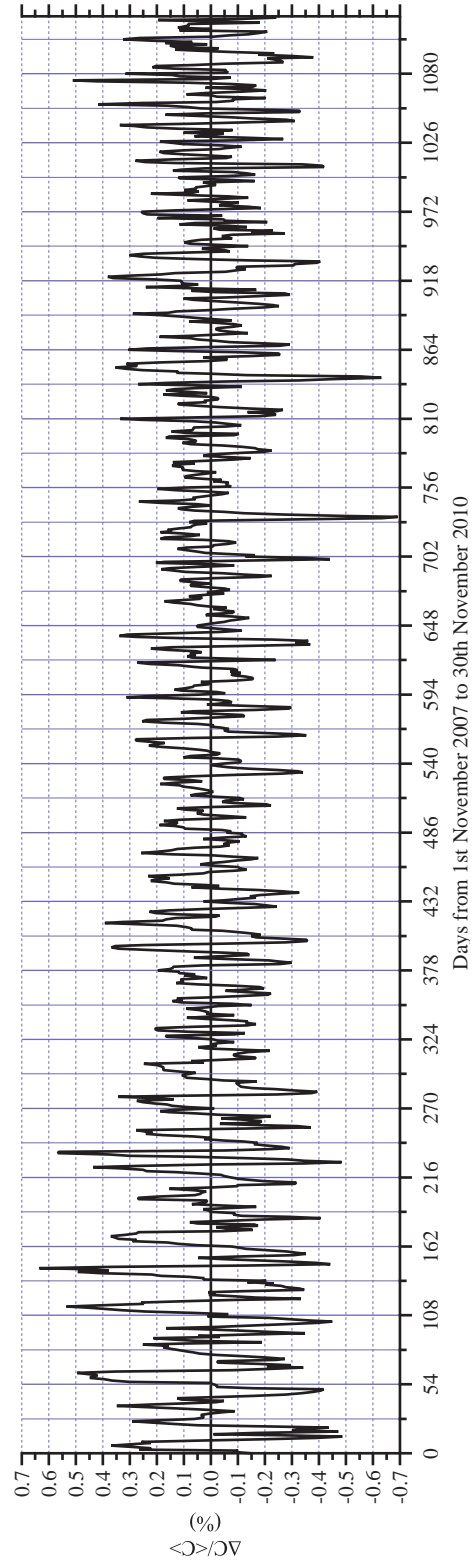


Figure 5.17: Amplitude of 27-day modulation of GCR intensity.

compound stream. This is consistent with a standard explanation of modulation in terms of the force-field model, in which the GCR flux decreases due to a combination of adiabatic deceleration, convection, and diffusion, where the first two of these have a stronger effect for a higher wind speed. Both types of the modulation were characterized for the effects of modulation of GCRs by the Sun in each solar rotational period. From the classification of the CSWSs and the 27-day intensity variations we found that the dip of the 27-day modulation mostly occurred close to the peak of the solar wind speed, for 37 events out of 61 events. For a symmetric shape there were 22 events and for an asymmetric shape there were 15 events. However, in 24 other events the dip of intensity of cosmic rays was not close to the solar wind peak, and for some of these it was in the trailing edge of the HSS.

In addition to the symmetric and asymmetric modulations of GCR intensity, the size or amplitude of the 27-day modulation varied as well. The 27-day modulation of daily GCR intensity at Doi Inthanon is shown in Figure 5.16. The amplitude of the modulation can be represented by the percentage deviation from a 27-day moving average, as shown for daily data in Figure 5.17. The percentages were calculated as $(C(t) - \langle C \rangle_{27}) \times 100 / \langle C \rangle_{27}$, where $C(t)$ is daily average of the hourly neutron count rate and $\langle C \rangle_{27}$ is the 27-day moving average of the neutron count rate. The amplitude of 27-day modulation of GCRs was higher during the years 2007-2008 (amplitude of about 0.5%) than during the years 2009-2010 (amplitude of about 0.2%). It is interesting to note that during the years 2007-2008 there were more HSSs than during the years 2009-2010.

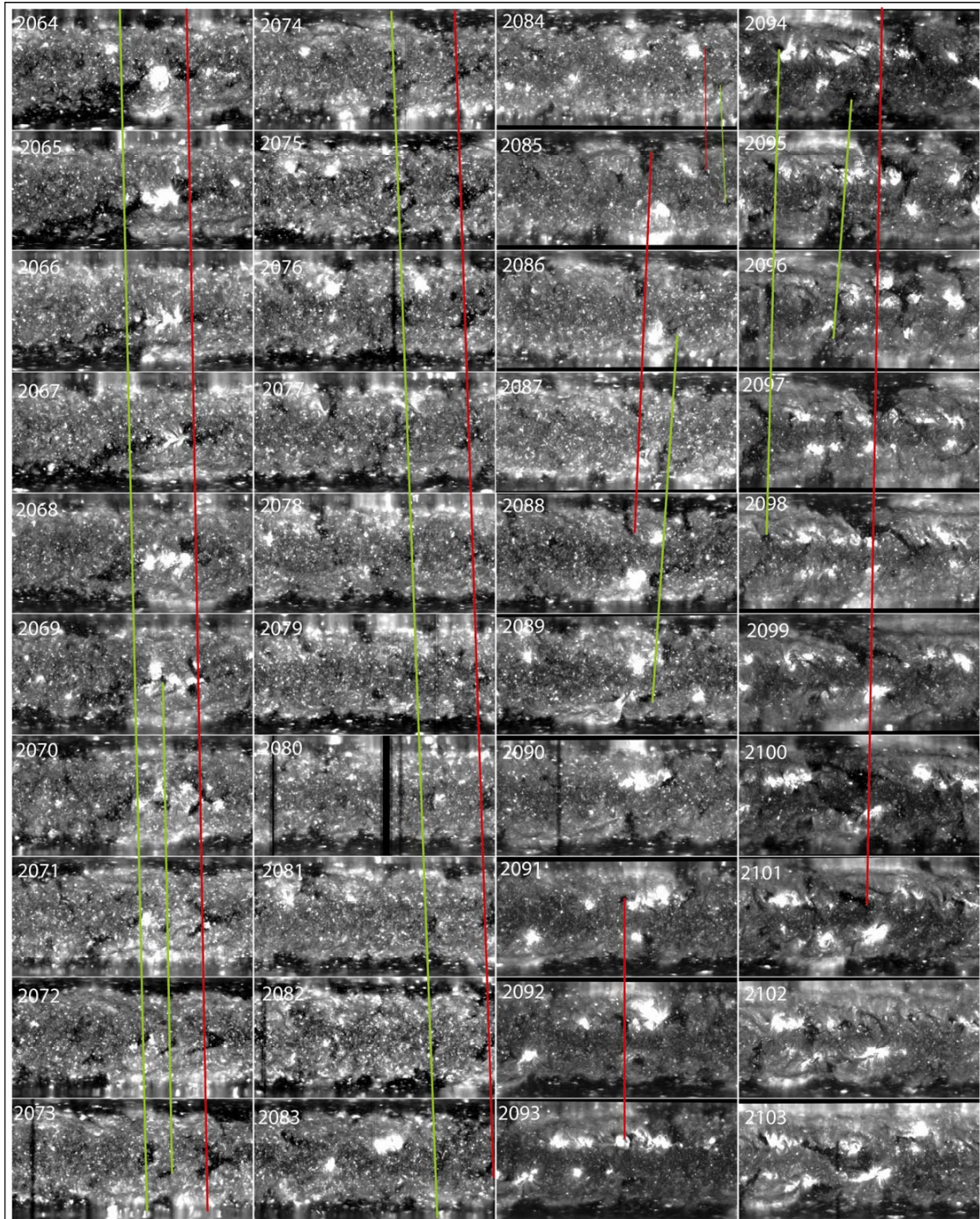


Figure 5.18: Synoptic maps of the solar corona from CR2063 to CR2103. The vertical green lines represent the positive polarity coronal holes and the vertical red lines represent the negative polarity coronal holes.

5.6 Coronal holes and high speed solar wind streams

5.6.1 Evolution of coronal holes during solar minimum from 2007 to 2010

In the minimum phase after the 23rd solar cycle, the features and evolution of CSWSs were closely related to their sources and environments, which changed with time. The synoptic maps of the Sun for 41 Carrington Rotations from CR2063 (November 11, 2007 to December 3, 2007) to CR2103 (November 5, 2010 to December 3, 2010) were examined as shown in Figure 5.18. In overview, two CHs were sources of two typical HSSs which might form CIRs at 1 AU: equatorial and near-equatorial southern CHs with speeds in the range of 600-700 km s⁻¹ as seen in CR2064 (December 3, 2007 to December 30, 2007) to CR2078 (December 20, 2008 to January 17, 2009). This interval is quite long so it included quasi-periodic 27-day solar rotational recurrences of the CSWSs. After that, this feature was less clear but there were still some HSSs with occasional interplay by the northern CHs.

The distribution of CHs is not uniform, and is sometimes it is clumpy; the CHs are densely longitudinally distributed like a strip in the southern and northern hemispheres of the Sun through the solar equatorial regions. CHs were found at all southern heliolatitudes. The southern CHs had positive (away) polarity, whereas the infrequent equatorial CHs on the right of the synoptic maps and the northern CHs typically had negative (toward) polarity. The positive-polarity and negative-polarity equatorial CHs were long-lasting, persisting for about 20 CRs in the time of low solar activity from CR2063 to CR2083. However, after the increase in solar activity (in the year 2010), new CHs were seen only for 2-8 Carrington rotations and they rotated with a period that depended on their latitude. From CR2079 (January 17, 2009 to February 13, 2009) to CR2094 (March 4, 2010 to March 31, 2010) the average solar wind peak speed decreased down to about 450 km s⁻¹ since the equatorial CHs nearly vanished and HSSs from southern and northern CHs in high-latitude (i.e., polar) regions caused

only a slight enhancement in solar wind speed. Some northern CHs moved down to a certain extent starting in CR2076 (October 27, 2008 to November 23, 2008) and were obviously seen in CR2085 (June 30, 2009 to July 28, 2009) and CR2097 (May 25, 2010 to June 21, 2010). The “elephant trunk CHs” were clearly seen in CR2098 (June 21, 2010 to July 19, 2010) surrounded by large numbers of active regions which apparently originated in CR2083. After the elephant trunk CH, the CHs completely moved down to the middle latitudes (about 15° - 60°) until the end of our study period, CR2103.

The shapes of CHs were irregular in general. Some CHs were connected like a chain of islands with an overall slanted shape or horizontal/vertical rectangular-like shape. We saw earlier how these CH shapes played a major role of controlling GCR fluxes as measured by the neutron monitor. From this overview we could see that features and time evolution of CHs were the major parameters which centrally stipulated the temporal and spatial evolution of the CSWSs as observed in 27-day solar rotational recurrences.

The HSSs were released from both the polar and equatorial CHs. Variations of solar wind speed are thus connected to the evolution and distribution of the CHs. The HSSs were spread in angular coordinates, “overexpanding” in angular size with respect to the CHs. There were simple streams that lasted for a few days, but most were compound streams lasting for a maximum of 12 days in a CR (in CR2067 and CR2068) and frequently observed around the southern groups of CHs. The compound streams produced by the groups of CHs near the solar equator exhibited a shorter expansion time of around 3-5 days.

5.6.2 Statistics of CIRs and HSSs

In the time interval in this study, as expected, there were more HSSs than CIRs which were characterized by the plasma and magnetic field data. HSSs were in a total of 61 events in which 34 long lasting-HSS events (\geq five days) were found, comprising about 56% of all HSSs. Therefore, most of HSSs were compound streams,

implying that the long-duration HSSs originated from stable, large compound structures of CHs. In addition, the recurrent and periodic HSSs in 2007-2008 gradually disappeared in 2009-2010. Based on CIR identification, 53 events had CIRs and 8 events did not have CIRs. The CIRs were thus found for more than 86% of the HSSs. In some cases, the HSS could not induce a CIR, with no increase in proton density or magnetic field magnitude. Subsequently, there were stream interfaces (SIs) in 42 CIR events. This means that an SI is crucial in forming a CIR. Lists of HSS and CIR events are shown in Tables 5.3 and 5.4, respectively. We have also selected some examples of CIRs to show some of their characteristics near Earth's orbit (Figures 5.19-5.22) in different years.

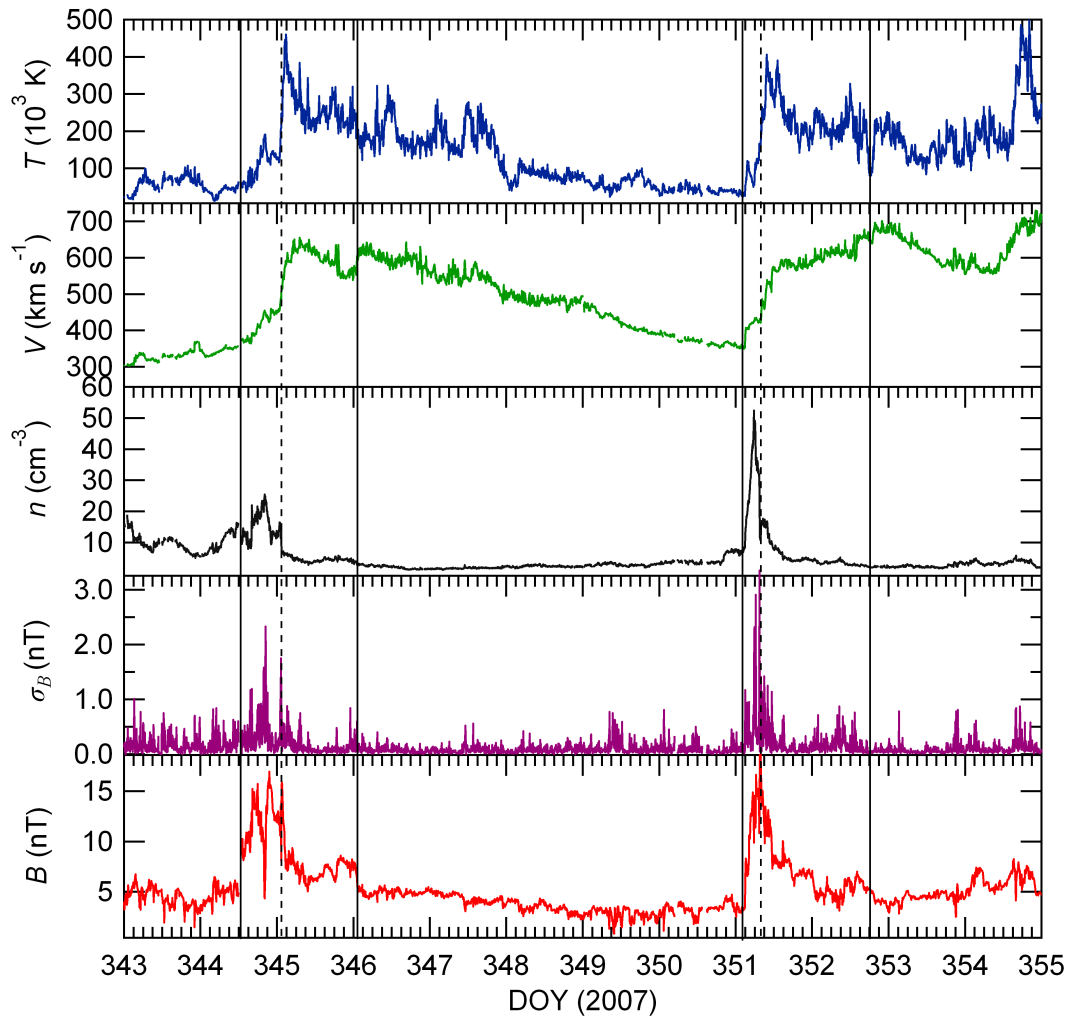


Figure 5.19: A CIR in 2007 characterized by 5-minute solar wind and magnetic field data. Thick lines represent the forward and the reverse waves of the CIR whereas dashed lines represent the stream interfaces between fast and slow streams.

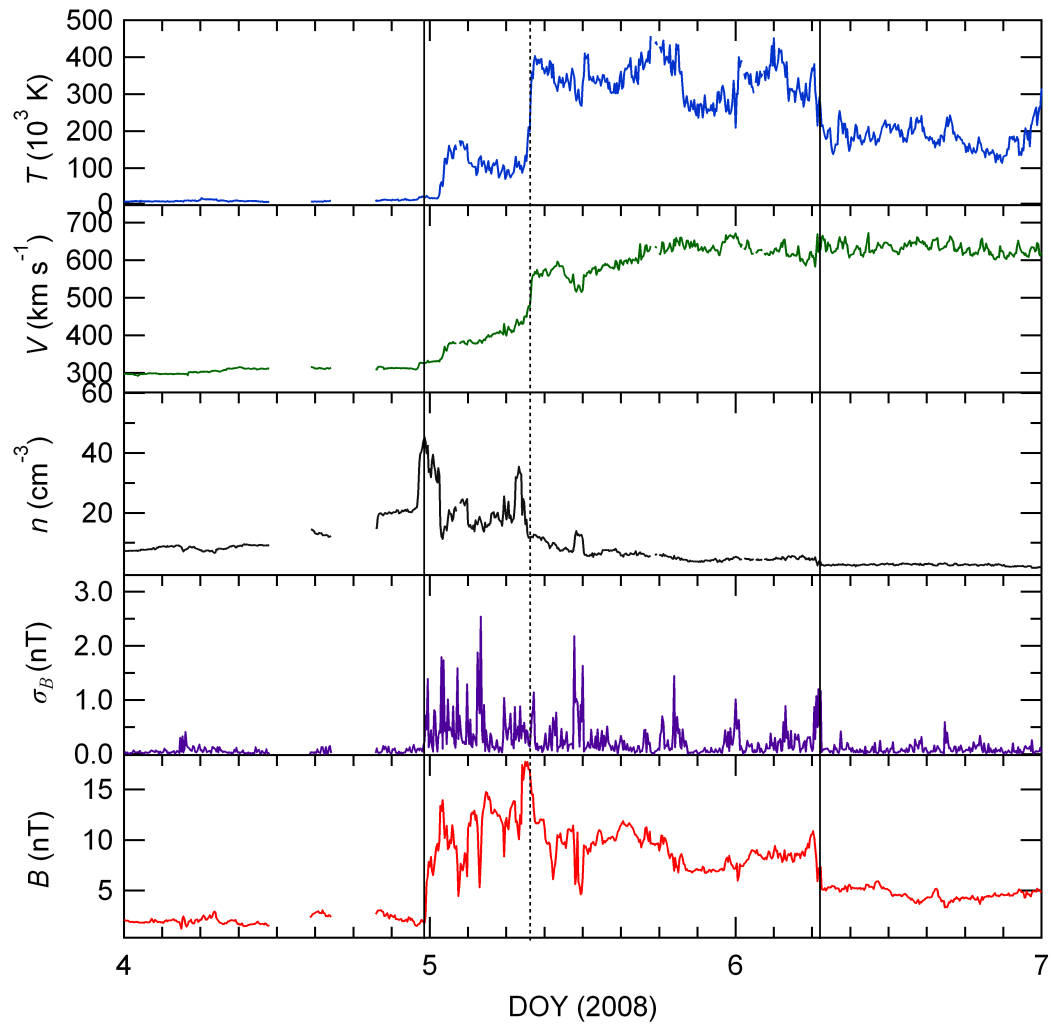


Figure 5.20: A CIR in 2008 characterized by 5-minute solar wind and magnetic field data. Thick lines represent the forward and the reverse waves of the CIR whereas the dashed line represents the stream interface between fast and slow streams.

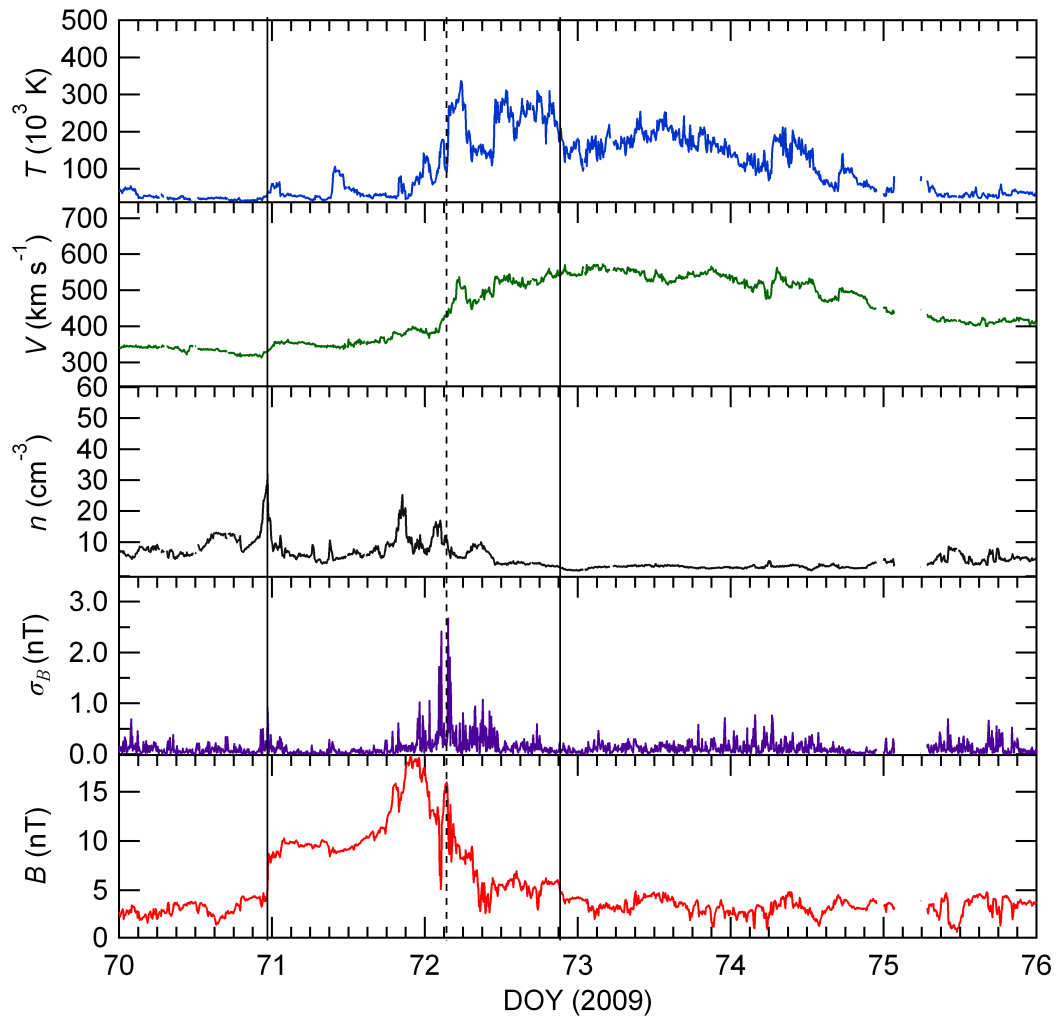


Figure 5.21: A CIR in 2009 characterized by 5-minute solar wind and magnetic field data. Thick lines represent the forward and the reverse waves of the CIR whereas the dashed line represents the stream interface between fast and slow streams.

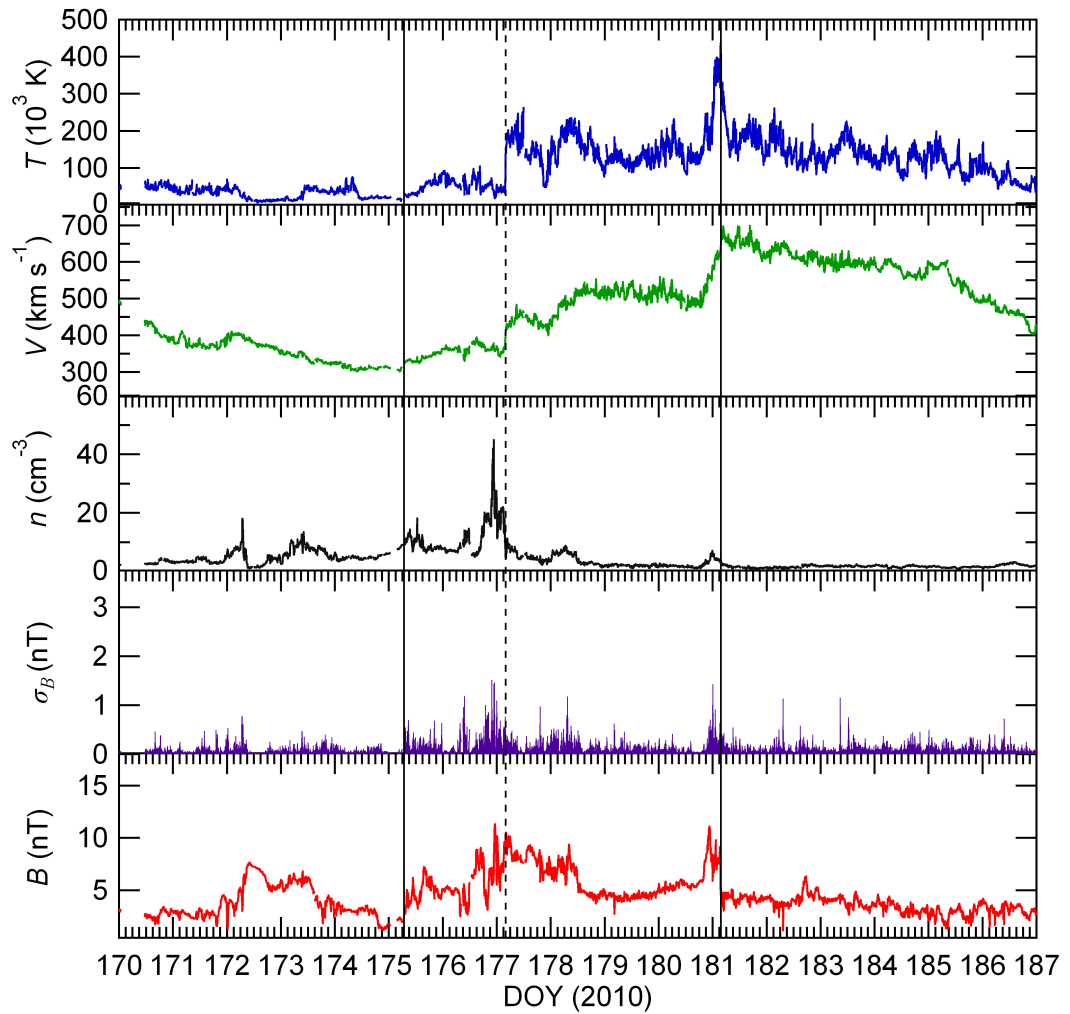


Figure 5.22: A CIR in 2010 characterized by 5-minute solar wind and magnetic field data. Thick lines represent the forward and the reverse waves of the CIR whereas the dashed line represents the stream interface between fast and slow streams.

Table 5.2: The HSS events in this study (2007-2008)

Event	Start Day (Yr/DOY)	Magnetic sector	Day of V_{max}	V_{max} (km s ⁻¹)	Duration (Days)	CR dip close to V_{max} ?
1	07/316	Toward	318.46	667	5	Yes/Symmetric
2	07/323	Away	325.58	668	9	Yes/Asymmetric
3	07/344	Toward	345.29	640	4	Yes/Symmetric
4	07/351	Away	354.92	713	8	Yes/Symmetric
5	08/5	Toward	7.54	706	6	Yes/Asymmetric
6	08/12	Away	14.96	710	10	Yes/Asymmetric
7	08/31	Toward	35.12	619	6	Yes/Symmetric
8	08/41	Away	42.40	725	8	Yes/Symmetric
9	08/49	Away	50.33	611	2	Yes/Symmetric
10	08/58	Toward	61.95	768	6	Yes/Symmetric
11	08/68	Away	71.08	701	12	Yes/Asymmetric
12	08/86	Toward	88.38	676	5	Yes/Symmetric
13	08/95	Away	97.25	709	12	Yes/Asymmetric
14	08/107	Away	107.92	600	6	No
15	08/114	Toward	114.75	654	7	Yes/Asymmetric
16	08/121	Away	126.25	631	9	Yes/Symmetric
17	08/140	Toward	143.00	593	7	No
18	08/149	Away	152.33	632	8	Yes/Symmetric
19	08/166	Toward	169.12	754	8	Yes/Asymmetric
20	08/177	Away	178.50	639	7	Yes/Asymmetric
21	08/193	Toward	196.25	697	8	Yes/Symmetric
22	08/203	Away	205.88	663	3	No
23	08/222	Toward	222.92	645	5	Yes/Asymmetric
24	08/230	Away	231.58	626	2	No
25	08/247	Toward	248.83	622	4	Yes/Asymmetric
26	08/258	Away	259.88	583	2	No
27	08/274	Toward	276.92	705	4	Yes/Symmetric
28	08/285	Away	286.21	548	3	No
29	08/302	Toward	303.62	705	6	No
30	08/312	Away	313.83	573	2	No
31	08/330	Toward	331.92	648	3	Yes/Symmetric
32	08/341	Away	342.25	648	3	Yes/Asymmetric
33	08/358	Toward	358.54	567	2	Yes/Symmetric
34	08/365	Away	366.50	526	5	Yes/Asymmetric

Table 5.3: The HSS events in this study (2009-2010)

Event	Start Day (Yr/DOY)	Magnetic sector	Day of V_{max}	V_{max} (km s^{-1})	Duration (Days)	CR dip close to V_{max} ?
35	09/45	Toward	46.42	581	3	No
36	09/72	Toward	73.08	567	3	Yes/Symmetric
37	09/83	Away	83.88	489	3	Yes/Asymmetric
38	09/98	Toward	101.75	551	4	No
39	09/106	Away	108.67	536	6	Yes/Asymmetric
40	09/126	Toward	128.29	508	4	No
41	09/175	Toward	176.42	487	2	No
42	09/179	Toward	180.67	557	2	Yes/Symmetric
43	09/203	Toward	205.08	563	4	No
44	09/230	Toward	232.96	559	5	No
45	09/257	Toward	259.58	473	4	Yes/Symmetric
46	09/325	Toward	325.71	547	2	No
47	10/11	Toward	11.62	500	5	No
48	10/20	Away	21.00	509	2	Yes/Symmetric
49	10/30	Toward	34.12	559	2	No
50	10/47	Away	50.71	503	2	Yes/Symmetric
51	10/68	Toward	71.08	558	2	Yes/Symmetric
52	10/92	Toward	95.58	814	6	No
53	10/122	Toward	123.58	720	6	No
54	10/139	Away	140.42	510	2	Yes/Symmetric
55	10/150	Toward	152.00	599	7	No
56	10/166	Away	167.96	568	3	No
57	10/175	Toward	182.33	655	10	No
58	10/208	Toward	209.71	691	5	No
59	10/236	Toward	237.38	693	6	No
60	10/267	Toward	268.25	631	7	Yes/Asymmetric
61	10/295	Toward	297.96	676	6	Yes/Symmetric
62	10/315	Toward	319.96	639	7	No

Table 5.4: The CIR events in this study (2007-2008)

Event	Starting Day (Yr/DOY)	Ending Day (Yr/DOY)	Stream Interface?
1	07/316	07/318	Yes
2	07/324	07/325	No
3	07/343	07/346	Yes
4	07/351	07/352	Yes
5	08/4	08/6	Yes
6	08/31	08/32	Yes
7	08/40	08/42	Yes
8	08/58	08/60	Yes
9	08/68	08/69	Yes
10	08/85	08/87	Yes
11	08/94	08/97	Yes
12	08/106	08/108	No
13	08/113	08/115	Yes
14	08/148	08/149	Yes
15	08/166	08/167	Yes
16	08/176	08/178	Yes
17	08/193	08/194	Yes
18	08/221	08/223	Yes
19	08/229	08/232	No
20	08/246	08/248	Yes
21	08/257	08/259	Yes
22	08/284	08/286	Yes
23	08/311	08/313	Yes
24	08/329	08/330	Yes
25	08/337	08/338	Yes
26	08/357	08/358	Yes
27	08/364	08/365	Yes

Table 5.5: The CIR events in this study (2009-2010)

Event	Starting Day (Yr/DOY)	Ending Day (Yr/DOY)	Stream Interface?
28	09/44	09/45	Yes
29	09/70	09/72	Yes
30	09/98	09/99	Yes
31	09/105	09/107	Yes
32	09/174	09/176	Yes
33	09/190	09/192	Yes
34	09/194	09/195	Yes
35	09/202	09/203	Yes
36	09/207	09/209	Yes
37	09/229	09/232	Yes
38	09/322	09/324	No
39	10/9	10/11	No
40	10/90	10/91	No
41	10/101	10/103	Yes
42	10/121	10/123	Yes
43	10/138	10/140	No
44	10/148	10/151	Yes
45	10/166	10/167	No
46	10/175	10/178	Yes
47	10/204	10/206	Yes
48	10/215	10/217	Yes
49	10/235	10/236	Yes
50	10/266	10/268	No
51	10/286	10/289	No
52	10/314	10/315	No
53	10/346	10/347	Yes

CHAPTER VI

DISCUSSION

From the results presented in Chapter 5, we will now discuss the effects of corotating solar wind structures on trains and recurrent trains of enhanced DA and 27-day variations in GCRs in light of current theories and observations. How and why did the intensity and DA of GCRs vary on a day-to-day basis, and a 27-day basis? It is convenient to organize the discussion from diurnal variations to 27-day variations: from the smaller to larger time scale. First of all, we will discuss why $\mathbf{B} \times \nabla n$ anisotropy is a good candidate for explanation of the trains and recurrent trains of enhanced DA that occurred in many consecutive Carrington rotations. Then, we will explain characteristics of the DA and phase of the trains and recurrent trains. Next, we will consider the context of the latitudinal gradient of GCRs observationally and theoretically. Finally, we will search for contributing factors of the 27-day modulation of GCR intensity and discuss their effects on the GCR intensity modulation in detail.

6.1 Contribution of $\mathbf{B} \times \nabla n$ anisotropy to the recurrent diurnal variations

Previous work has remarked on the importance of $\mathbf{B} \times \nabla n$ gradient anisotropy and the latitudinal density gradient of GCRs in the inner heliosphere. The effect of $\mathbf{B} \times \nabla n$ streaming due to a cosmic ray density gradient perpendicular to the ecliptic plane, which introduces a component into the diurnal variation that is perpendicular to and depends on the sense and direction of the magnetic field, is realized to exist at neutron monitor energies in quiet periods (Hashim and Bercovitch 1972). They assume

that the perpendicular gradient anisotropy has a power law dependence on rigidity. In the weak-scattering limit (when the collision frequency ν is negligible), the fluxes driven by perpendicular diffusion are small compared with those driven by $\mathbf{B} \times \nabla n$ (Forman et al. 1974). For long-term averaged equatorial DAs (Owens et al. 1980), the three-dimensional structure of GCR anisotropies at ~ 10 GV as associated with solar rotation was determined for 27-day spectral peaks in long-term data sets. The corotating azimuthal and latitudinal gradients were found to be about twice the steady-state radial gradient ($\sim 3\% \text{ AU}^{-1}$). This was inferred by using the cosmic ray $\mathbf{B} \times \nabla n$ drift in which the component of the corotating gradient perpendicular to the ecliptic gives rise to the 27-day periodicity in the diurnal variation. Therefore, we expect that the enhancement or suppression in magnitude of the diurnal variations is dependent on the latitudinal gradient of the GCRs as affected by the HSSs near Earth.

The long-lasting enhanced DA during typical trains and recurrent trains, such as those in CR2064, CR2071, and CR2093, was closely related to the passage of HSSs that emerged from CHs. For example, an equatorial CH, which merged with that from a trailing mid-latitude extension of a polar CH, produced a slanted HSS structure in space in CR2064 and CR2071, within which the cosmic ray density was depressed. This led to a local latitudinal gradient as the GCR intensity behind the passage of HSS was lower than before the passage. Such a gradient can account for noticeable events of temporary enhancement or suppression (depending on the magnetic field direction) of the DA.

The slanted geometry of CHs plays a role in enhancing the DA in the A sectors when the latitudinal gradient points to the south. The slanted structure was quite flat in CR2067, but more slanted in the subsequent recurrences in CR2068-CR2073 (see Figure 5.7). In addition, the slanted geometry of CHs disappeared in CR2073 which immediately followed the last recurrent trains of enhanced DA in the A sector (Figure 5.3). These observations confirm that the slanted geometry of CHs can enhance the latitudinal gradient and the gradient anisotropy contribution to the DA. Our results are

in agreement with the latitudinal effect of CIRs on the large-scale density gradient of GCRs as investigated by Rouillard and Lockwood (2007). The occurrence of CHs in the low-latitude regions as observed could change the topological distribution of open field lines. More low-latitude open field lines gathering around active regions increase the chance that fast and slow flow coexist at adjacent longitudes, thereby leading to CIRs.

Furthermore, the slanted HSS clearly affected the GCR density in the train of CR2071. GCRs scattered by the compressed IMF cannot refill the depleted regions easily as they are forced to propagate around the slanted structure at which the larger and higher-latitude CH (C) has a larger effect on the diurnal variations. In addition, the presence of kinematic steepening (Parker 1963) and CIR formation may prevent GCRs from recovering as could be seen from the train of roughly constant GCR intensity within the structure.

6.1.1 Latitudinal gradient of Galactic cosmic rays

The latitudinal gradient of GCRs is one of the most important factors in solar modulation of cosmic rays, and it provides a basis for understanding the DA of GCRs. Excellent reviews of the latitudinal gradient have been provided (Venkatesan et al., 1990; Hall et al., 1996). In connection with the CHs, Agrawal et al. (1978) proposed a hypothesis that the larger CH over one polar cap would inhibit the entry of GCRs to the solar system in 1973 to 1974. The cosmic ray intensities taken from neutron monitors at polar stations (Thule and McMurdo) were adjusted for changes in Earth's ecliptic latitude. However, it is difficult to uniquely interpret the cosmic ray intensity differences when equatorial CHs resulting from extension of polar CHs to lower heliolatitudes are very prominent as in this study. Therefore, locally large latitudinal gradients from the equatorial extension of polar CHs plays a role in short-term variations in GCRs. Agrawal et al. (1980) pointed out that out-of-ecliptic gradients produced by CH structures are important for the radial gradient, magnetic curvature drift and gradient drift that contribute to a north-south asymmetry in cosmic ray intensity. In

addition, the stream configuration of multiple, interacting streams may also play a role in large recurrent depressions of GCRs (Richardson 2004).

It is reasonable to assume that in the long term the latitudinal gradient of GCRs is steady in both hemispheres of the heliosphere. One discovery from the fast pole-to-pole passage of Ulysses through the heliosphere is a mismatch between the GCR distribution in the south and north (Simpson et al., 1996; Heber et al., 1996b). The latitudinal gradients were the same in both hemispheres, $\sim 0.3\% \text{ deg}^{-1}$, but the plane of the symmetry was offset southward by $\sim 10^\circ$ of latitude in 1995. There are some explanations to account for the asymmetry of GCR intensity. A possible one is a southward displacement of the HCS with respect to the solar equatorial plane (Smith et al., 2000). Second is overwinding of the Parker spiral in the southern heliosphere (Forsyth et al. 1996). In addition, it might relate to the effect of a GCR radial gradient (Swinson 1970; Agrawal et al. 1980), or the asymmetry may be a result from asymmetry in latitudinal transport based on the Fisk magnetic field model (Hattingh, 1998). During the fast latitude scan of Ulysses in 2007-2008; the KET instrument found that there was zero $\% \text{ deg}^{-1}$ latitudinal gradient for 2.5 GV protons (Heber et al. 2008).

In this study, during CR2064, CR2071, CR2093 and subsequent trains we could estimate the latitudinal gradient by considering that the regions inside an HSS or CIR have fewer particles than the outside. When the HSS collides with the slow stream to the south an interaction region is formed with a size comparable to that of the pulse of density. An interaction region of limited size will move past the observer each solar rotation until this structure vanishes. There are more particles in front of the interaction region but fewer particles behind it (in the rarefaction region or void) so the particle gradients were in the southern direction for the limited duration when the HSS/CIR passed the Earth.

Alternatively, the latitudinal density gradient of GCRs could be organized by the HCS. However, at solar minimum, the HCS becomes nearly flat, in close alignment with the solar equator and the dipole tends to be aligned with the rotation axis. CIRs

tend to be tilted in the same sense as in the HCS. In CR2093, the CIR seemed to depend on the configuration of the HCS with a large tilt and the latitudinal gradient of GCRs could be organized according to the HCS.

During the $A < 0$ IMF polarity, as in our study, the net effect of drifts is that particles travel along the HCS and may exit the heliosphere via the polar regions. This results in a larger radial gradient of cosmic rays and the density of particles might have a local maximum at the HCS. The latter is symmetric about the solar equatorial plane and is known as the bi-directional latitudinal gradient (e.g., Bieber and Chen 1991, Okazaki et al. 2008) in which a negative latitudinal gradient for protons is predicted by the drift model. This drift current is perpendicular to the mean field. On the other hand, from the neutron monitor data, a difference in GCR latitudinal gradients obtained separately in T and A sectors of the interplanetary magnetic field from 1953-1988 was found (Chen et al. 1991). As a result, there should be a unidirectional density gradient (asymmetric about the solar equator) caused by N-S asymmetry in the solar modulation. For a long-term steady state, $\mathbf{B} \times \mathbf{G}$ provides the direction of streaming due to drifts. The combination of the asymmetric and symmetric latitudinal gradients produces a larger gradient on one side of the HCS. This might imply that there exists a south pointing (unidirectional) latitudinal gradient in CR2064, 2071, 2093, and subsequent trains from the local latitudinal gradient provided by the slanted structure of CHs in a short-term period.

It is also possible that adiabatic deceleration can cause a latitudinal gradient of GCRs. In the HSS region, there is a lower density of GCRs where the expansion of solar wind is faster. This behavior is seen in the 27-day modulation of GCR intensity where the GCR intensity is reduced in the HSS region. The cosmic ray particles inside the HSS lose their energy faster than in the slow solar wind streams since in a certain time the plasma volume expansion (the rate of outward convection) is faster. At a CIR where the fast stream (low density of cosmic rays) collides with the slow stream (high density cosmic rays), a cosmic ray gradient can be produced.

6.1.2 Characteristics of trains and recurrent trains of suppressed and enhanced diurnal variations

Here, the association of the $\mathbf{B} \times \nabla n$ gradient drift with the transport of GCRs and characteristics of amplitudes and phases of the trains and recurrent trains is discussed in more detail. According to the theory of cosmic-ray modulation the streaming flux of cosmic rays, \mathbf{S} , is composed of convection and diffusion terms. The convection is dependent on the solar wind velocity V according to the convective part of the radial anisotropy, $A_c = 3CV/v$, where C is the Compton-Getting factor and v is velocity of cosmic rays. The convection is stronger in the fast solar wind than in slow wind so at the leading edge of an HSS the convective anisotropy must be higher than at the trailing edge. Diffusion contains parallel and perpendicular terms which can be characterized by their coefficients in the symmetric part of the diffusion tensor. Since the symmetric part of the diffusion tensor is inversely proportional to magnetic field strength ($K \propto 1/B$), at the CIR diffusion will be reduced. In addition, the anti-symmetric part of the diffusion tensor is associated with gradient and curvature drifts.

Diffusion and drifts are believed to play a role in the recovery phase. GCRs tend to recover between two successive CIRs, in particular in the rarefied fast-flow regions behind the turbulent leading edge where diffusion is dominant. In addition, drifts will be faster in the weak field between CIRs. The large-scale pattern of GCR flows regulated by gradient and curvature drift motions should be relevant to the recovery phase. This implies that at the trailing portion of an HSS the variation of GCR intensity is mainly contributed by adiabatic deceleration, diffusion, and drifts.

Recurrent trains of enhanced DA in 2008

As discussed above, the DA apparently tended to depend on the magnetic sectors of HSSs. Physically, $\mathbf{B} \times \nabla n$ anisotropy thus corresponded to this behavior. However, there were subsequent deviations of DA and phase associated with other processes in the time interval.

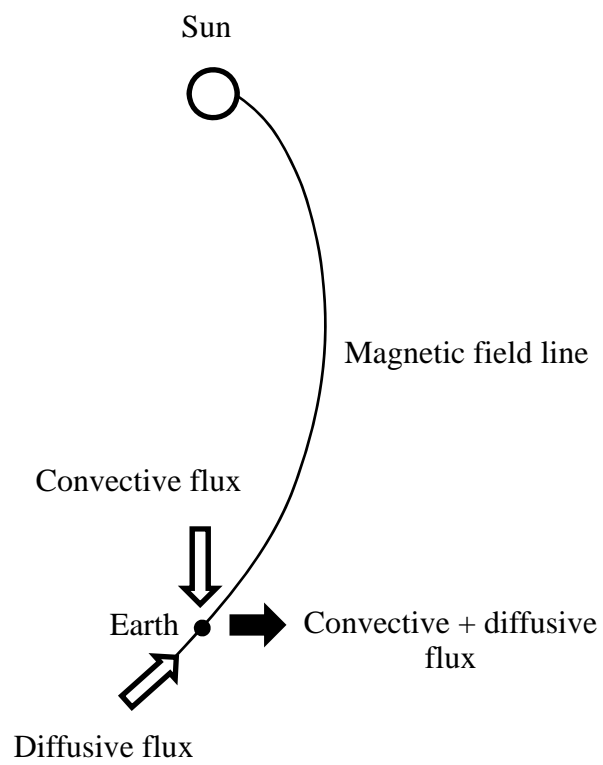


Figure 6.1: The radial components of convection and diffusion are usually balanced so the net streaming flux is near the corotational direction, from 1800 LT.

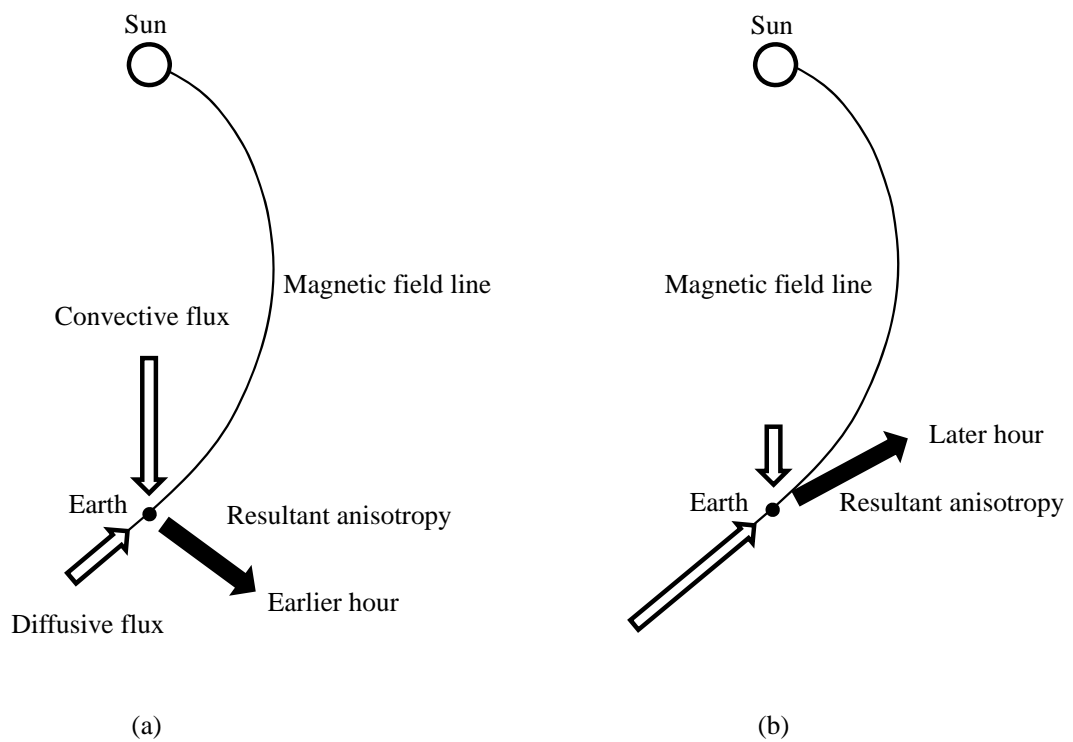


Figure 6.2: Changes in direction of the streaming flux of cosmic ray particles as produced by (a) enhanced convection or (b) enhanced diffusion. Usually the radial components are balanced so the net streaming flux is corotational.

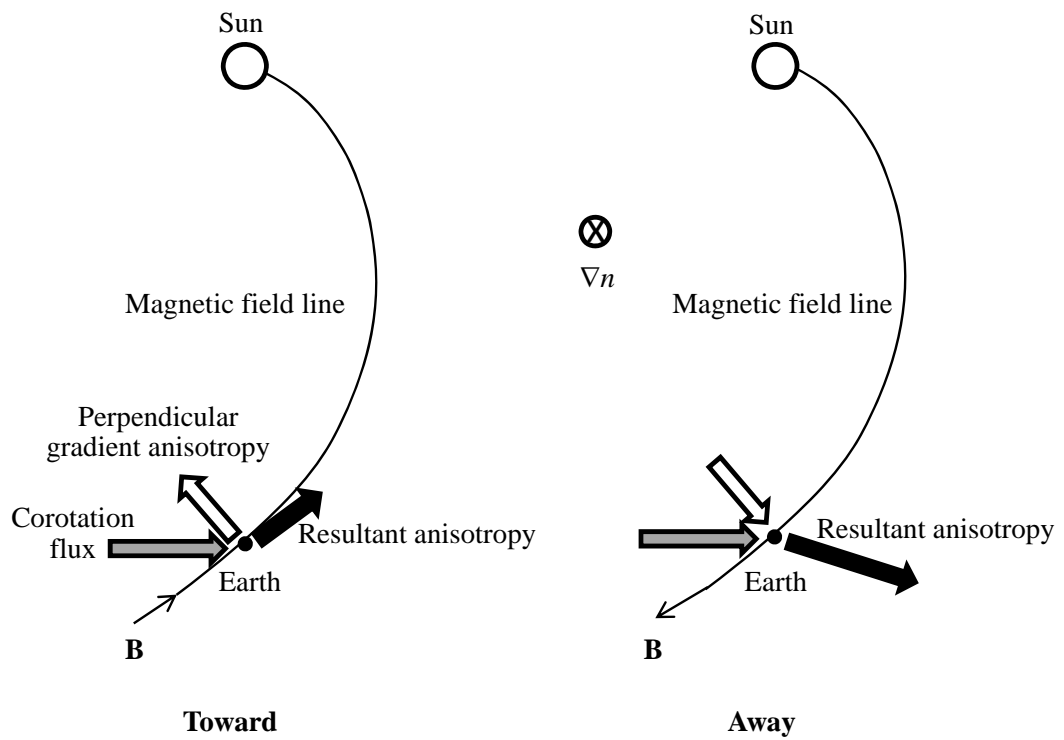


Figure 6.3: Contribution to the streaming flux of cosmic ray particles produced by the particle gradient ($\mathbf{B} \times \nabla n$) anisotropy. Together with a steady corotational flux, the resultant flow direction may change in phase to a later hour in the T sector and an earlier hour in the A sector. Here the latitudinal gradient ∇n is considered to point to the south. Note the resultant anisotropy is enhanced in the A sector.

Specifically, CR2071 as shown in Figure 5.7 can be considered as a typical event of these trains. As in an equilibrium state, there is a corotational flux of GCRs along 1800 LT because the radial components of convection and diffusion are usually balanced (Figure 6.1). Some authors who do not take the gradient anisotropy into account attribute a change in phase to earlier hours to either an enhancement in the convective or a decrease in the diffusive vector (Agrawal and Singh 1975) during the period of the leading-portion of the HSS as demonstrated in Figure 6.2(a). Their view is that during the period of the decline of the HSS, diffusion may be predominate (unless a new equilibrium is reached) and the phase might shift to later hours as shown in Figure 6.2(b). However, that proposed pattern is not evident in data from Doi Inthanon. In fact, the phase could also be affected by the $\mathbf{B} \times \nabla n$ anisotropy, as illustrated in Figure 6.3. Note, however, that during an HSS the IMF is nearly radial (because of the high solar wind speed), which weakens the effect on the phase.

During the train of enhanced DA in CR2071, the phase of the enhanced amplitudes was close to 1800 LT (only in DOY 178 the phase was earlier, which might be an artifact when subtracting the moving average of the rapidly changing GCR flux). Perhaps due to the $\mathbf{B} \times \nabla n$ anisotropy when the slanted latitudinal gradient of GCRs (due to the slanted HSS) pointed to the south in the A sector, and perhaps with unbalanced (enhanced) diffusion in the recovery phase, the resultant phase was close to around 18 h LT as shown in Figure 6.4. When the streaming flux of cosmic ray particles produced by the particle gradient anisotropy with a southward gradient contributes to the steady corotational flux, the resultant flow direction in the A and T sectors can be as shown in Figure 6.3. For example, after DOY 150 in CR2070, when the DA was higher, the phase was in earlier hours in the A sector.

In the case of suppressed DA in the T sector from DOY 166 to DOY 176, the DA decreased to 0.19%, close to the 3-year average value. The phase tended to be near the corotational direction, perhaps because in the normal equilibrium there is no radial anisotropy component and thus the steady diffusion and convection in the

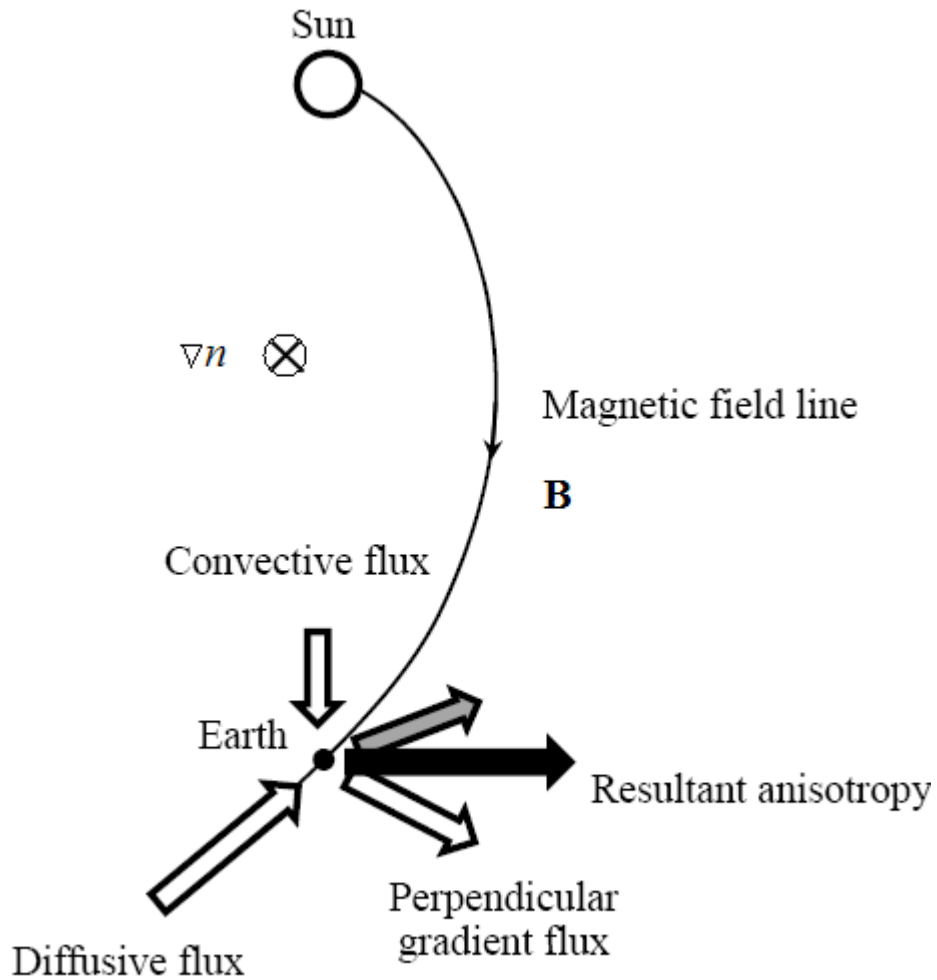


Figure 6.4: Contribution to streaming flux of cosmic ray particles produced by particle gradient $\mathbf{B} \times \nabla n$ anisotropy and the combination of convection and enhanced diffusion. The resultant flow direction is observed to be close to 1800 LT (to the right).

high-speed stream region cause the flow to be near the 1800 h LT as depicted in Figure 6.1. However, the large deviation of the phase in the T sectors might result from the harmonic analysis in which the low amplitude of suppressed DA was difficult to fit.

Recurrent train of enhanced DA in 2010

The recurrent trains in Figure 5.4 were also apparently dependent on the magnetic sector, often starting at a sector boundary. It is notable that diurnal variations sometimes gradually increased and reached the maximum level around the middle of the A sector, or in one case, the T sector.

In CR2093 (Figure 5.8) the suppression of DA could come from a large latitudinal gradient from the northern latitude CHs that gave rise to a stream drifting to low latitudes. The latitudinal gradient should point to the south and DA was suppressed in the T sector (Figure 6.3). The latitudinal transport of HSSs to the lower latitudes is possible and would cause modulation of GCRs as observed. Agrawal et al. (1978) proposed that convection from the larger CHs over one polar hemisphere would inhibit the entry of GCRs to the solar system, and that as a result, the cosmic ray flux would be suppressed from the direction perpendicular to the ecliptic plane that corresponds to the larger solar polar CH. Instead, the enhancements of DA were around DOY 48-55 in the A sector and in the regions of low GCR intensity. The $\mathbf{B} \times \nabla n$ anisotropy should play an important role in the enhanced DA in which the latitudinal gradient should point to the south and magnetic field was away from the Sun.

The interpretation of the enhanced DA in terms of $\mathbf{B} \times \nabla n$ anisotropy might correspond to a phase shift to earlier hour than the corotation hour because of a large latitudinal gradient of GCRs pointed to the south, when the magnetic field was in the A sector. This behavior is illustrated in Figure 6.3 and was clearly seen in CR2070. However, the phase shift to the earlier hours in the T sectors might not correspond to this picture. The large deviation of phase to earlier hours in T sectors might result from the harmonic analysis in which the low amplitude of suppressed DA was difficult to fit. The other possibility that could explain the suppressed DAs in the T sector is a convection-diffusion process, though the normal equilibrium results in no radial anisotropy component, hence a phase angle of 1800 h LT.

The modulation or reduction of GCR intensity during CR2093-CR2096 was not strong so the recovery phase of GCR intensity could occur. However, from the synoptic maps we found that a group of southern polar CHs was the source of the HSSs. The HSSs from mid-latitude or polar CHs can modulate the GCR intensity near the equatorial plane. Measurements from the Ulysses spacecraft have demonstrated that uniformly fast solar wind is present at the poles of the Sun during the declining phase

of the solar activity cycle and at solar minimum, while a mixture of fast and slow streams is observed dominantly near the ecliptic plane (Phillips et al. 1995). Therefore, the HSSs from high-latitude CHs could contribute the recurrent variations of GCRs through the latitudinal expansion from high- to low-latitudes. In other words, HSSs from high-latitudes expand and reach low latitudes. Enhanced perpendicular diffusion in the latitudinal directions could be a mechanism of recurrent 27-day cosmic ray depressions (Jokipii 1973). Recurrent 27-day variations are most prominent at middle latitudes, where CIRs are present and cause recurrent depressions in cosmic ray flux. Below 50° , the recurrent variations of GCRs are in coincidence with the passage of CIRs (Dröge et al. 1996).

Train of enhanced DA in 2007

In CR2064, as shown in Figure 5.9, the characteristics of the enhanced DA during the passage of an HSS in the A sector imply that the influence of the $\mathbf{B} \times \nabla n$ gradient drift is similar to that for enhanced DA during CR2071 in 2008. The slanted HSS could contribute some excess flux to the corotational direction.

In the A sector, around DOY 353-354 DAs were higher than 0.25% and the phase was close to 1800 h LT. This was the result of the $\mathbf{B} \times \nabla n$ gradient drift. When the perpendicular gradient anisotropy was enhanced, one might expect the phase to shift to earlier hours, as in Figure 6.3. However, the solar wind speed was very high, so the field line in Figure 6.3 should be much more radial, with only a small phase shift. In fact, the stronger $\mathbf{B} \times \nabla n$ anisotropy can explain both the enhanced DAs and the shifting of phase to earlier hours in DOY 355-356. The phases shifted to later hours, about 20 h LT around DOY 359-361, corresponding to the weaker DA, and perhaps was not exactly at 18 h LT because of an imbalance with increased diffusion and decreased convection (Figure 6.2(b)).

Before and after CR2064 these features were different in some cases; at the leading portion of the HSS there was no increase of DAs, and the rest possessed lower

DA, and after examining CHs in the synoptic maps we found no slanted structure that caused a local latitudinal gradient for the particle gradient anisotropy.

6.2 Contributing factors of the 27-day modulation of Galactic cosmic ray intensity

The 27-day modulation of cosmic rays is significantly associated with the CSWSs. However, their contribution to the modulation is not fully understood. In general, the amplitude of the high-energy cosmic ray intensity variations is the largest in middle-latitude regions (33° - 35°) and decreases with increasing solar latitude (McKibben et al. 1995). There are some main factors that are thought to be important for the 27-day modulation or corotating decrease of GCRs. Changes in solar wind speed cause variations in convection (Iucci et al. 1979; Newkirk and Fisk 1985; Richardson et al. 1996) and adiabatic cooling (Zhang 1997). The diffusion coefficient may change due to variations in the turbulence level in enhanced/compressed magnetic field regions (Burlaga et al. 1984; Kóta and Jokipii 1991). Variation in magnetic field strength and direction may lead to variations in particle drifts and diffusion coefficients (Kóta and Jokipii 1991, 2001; Burger and Hitge 2004). Alternatively, it is possible to integrate the different processes to explain the corotating decreases (Richardson 2004; Simnett et al. 1998). In sum, the corotating decreases in GCR intensity could be accounted for by different processes since there are simultaneous variations in a number of parameters within a stream: enhanced solar wind speed, corotating barriers, local structures within the CIR, and the direction of the large-scale magnetic field during the passage of a CIR and HSS.

6.2.1 Effects of convection and adiabatic deceleration

When the HSSs pass the Earth they reduce the cosmic ray flux. Effects of CIRs on GCR shielding have been demonstrated observationally (Heber and Berger 1999, Ahluwalia 2003). The appearance of a CIR structure in interplanetary space can

reduce the flux of energetic particles (Richardson 2004).

Generally, convection and adiabatic deceleration from the solar wind modulate the GCR intensity at the Earth. In an extremely simplified theory, the cosmic ray density in the inner solar system is reduced to $N_0 \exp[RV/\kappa]$ by the outward motion of the wind (Parker 1965). Here κ represents the cosmic ray diffusion coefficient which is assumed to be isotropic and uniform out to a distance $r = R$, around 5-40 AU. The particle diffusion into the solar system is against the outward sweeping of the solar wind. Nevertheless, without adiabatic deceleration, cosmic rays would fill the heliosphere to a nearly constant density. The GCR density is lower in the inner heliosphere because of adiabatic deceleration, to be discussed shortly, and diffusion inward to fill the “hole” is counteracted by solar wind convection. A higher solar wind speed resulted in greater convection so an HSS must cause a greater reduction of GCR intensity than a slow stream. It is readily seen that for RV/κ of the order of one, the time the average particle spends in the inner solar prior to observation is of the order of days (Parker 1965). Both the particle energy loss and the depression of the particle density contribute to the observed particle reduced particle intensity. Therefore, convection of the solar wind plays important role for modulation of GCRs at Earth. Since RV/κ at the orbit of Earth is small, on the order of 10^{-1} , the energy reduction at Earth is thus small.

Convection and adiabatic deceleration can simultaneously suppress the GCR intensity and energy during the passage of an HSS (see Ruffolo 1995). GCRs are cooled adiabatically due the expanding magnetic irregularities fields carried in the solar wind. The particle energy loss behind a blast wave from the Sun has been discussed (Parker 1963). Zhang (1997) suggested that adiabatic deceleration of GCRs by the expanding solar wind should be the common aspect of this effect. The reduction of energy results in reduction of intensity of GCR particles because of the steeply falling spectrum of cosmic rays. The stronger decreases in flux inside the compressed magnetic fields of CIRs are the combined effect of enhanced adiabatic deceleration in the fast solar wind and the stronger magnetic fields and reduced diffusion at the CIR, so “the hole” in density is

not filled to the usual level (Thomas and Gall, 1984). From the observations at Doi Inthanon, behind the CIRs and HSSs, there exists intensity suppression, presumably by this mechanism where the modulation amplitude might be related to the expansion rate of the solar wind (the volume expansion is faster in the fast solar wind than in the slow one). The intensity of GCRs is thus low in HSS regions, but high in slow-speed regions. This means that the adiabatic deceleration is also important factor contributing to corotating decreases of GCRs.

6.2.2 Effect of diffusive barriers

At large distances from the Sun, near 11 AU, interactions among streams and shocks may be extensive, and the cosmic ray intensity is more closely related to the magnetic field strength and magnetic turbulence than to stream profiles (Burlaga et al. 1985). The solar wind there can be partitioned into two types of regions: interaction regions where $B/B_P > 1$ and B_P is the magnetic field in the standard Parker spiral configuration; and rarefaction regions where $B/B_P < 1$. When the measured field magnitude is less than B_P , the intensity recovers at a constant rate. This empirical model is usually called the “CR-B” relation where diffusion in the magnetic field is responsible for corotating decreases (Burlaga et al. 1985).

Burlaga et al. (1986) studied the intensity of > 200 MeV cosmic ray protons and a system of corotating flows during 1977-1980 at 0.3-1.0 AU. They suggested that field lines in high speed streams are more irregular than those in slow speed regions adjacent to streams so that GCRs diffusing inward along the spiral lines find it more difficult to enter within the streams than the interstream regions. Reduction of diffusion in CIRs has been modeled (Kóta and Jokipii 1991); a smaller diffusion coefficient in regions of stronger magnetic field, such as CIRs, can explain the rapid local decreases of the cosmic ray flux (Jokipii and Davila 1981). In the inner heliosphere, the magnetic field is nearly aligned with the radial direction in which radial diffusion is determined primarily by the parallel diffusion coefficient $K_{\parallel} = V^2/3$. Moreover, the source of GCR decrease was

a large IMF compression occurring at higher latitudes where the Earth only partially intersected (Rouillard and Lockwood 2007). The models with compressed magnetic field in CIRs may explain the onset of the corotating depressions due to enhanced particle scattering at low latitudes.

6.2.3 Effect of drifts

Since the global solar magnetic fields consist of hemispheres of opposite magnetic polarity separated by a wavy HCS, the gradient and curvature drifts could play a role in guiding the GCRs (Jokipii et al. 1977). The drift models predict a stronger dependence on the HCS tilt angle in the $A < 0$ epoch when positively charged GCRs enter the heliosphere along the HCS (e.g., Jokipii and Thomas 1981). Therefore, the inclination of the HCS acts as a key parameter for the GCR modulation (Kóta and Jokipii 1983). There are strong inverse correlations between GCR intensity and the tilt of HCS during the $qA < 0$ epoch in the minimum phase of solar cycles (e.g., Aslam and Badruddin 2012). However, there are some discrepancies between observations and the drift models. Observations reveal that the corotating modulation is stronger in the $A > 0$ epoch than in the $A < 0$ epoch (see Newkirk and Fisk 1985). Hence, the effects of the HCS on the corotating modulation are not fully understood.

Alternatively, from ground- and space-based observation, corotating modulation is a function of magnetic rigidity. It appears that the maximum amplitude of the 27-day modulation is near 0.6-1.0 GV.

The recurrent cosmic ray intensity modulation near the ecliptic can arise from latitudinal cosmic ray density gradients arranged about a tilted HCS (Badruddin et al., 1985; Newkirk and Lockwood 1981; Newkirk and Fisk 1985; Badruddin and Ananth 2003). Enhanced drifts of particles out of the region of enhanced magnetic field associated with a CIR may cause the cosmic ray decrease (Barouch and Burlaga 1975). From the study of CIRs between 2001 and 2004, Da Silva et al. (2007) found that CIRs reduce the GCR intensity at neutron monitor and muon detector energies by

about 1.9% and 1.3%, respectively. They suggest that the stronger modulation at lower energies implies a smaller spatial scale of modulation.

Alternatively, Burger and Hitge (2004) developed a divergence free Fisk-Parker hybrid heliospheric magnetic field to study its effect on GCRs and found that drifts may be important for corotational modulation. The simulation results a linear relationship between the magnitude of the latitudinal gradient and the modulation amplitude of recurrent variations in the fluxes of GCRs in agreement with observational studies (Zhang 1997). To this point, the HCS could primarily have an effect on the global heliospheric cosmic ray distribution, as well as on recurrent modulation, since it can control both global latitudinal and longitudinal cosmic ray flux distributions. However, Simpson (1998) pointed out that the recurrent amplitude at the same heliocentric latitude did not change significantly even though the tilt angle of the HCS changed from 30° to 15° .

For more discussion of the long term recurrent modulation see Singh and Badruddin (2007).

6.2.4 The 27-day modulation of Galactic cosmic ray intensity at Doi Inthanon

From our observations, the solar wind speed has a major influence on the 27-day modulation. Most of the cosmic ray dips were close to peaks in the solar wind speed. However, the initial depression of GCRs seems to be related to the compression in proton density and magnetic field as embedded in the CIR, not the HSS, as seen in Figures 5.19-5.22. This implies that the magnetic field compression in the CIR is associated with the modulation of GCRs at the beginning and then the high solar wind speed continued the modulation to a maximum value after the passage of the CIR. The structure of the CIR might impede GCRs locally near the ecliptic plane since in the $A < 0$ epoch under consideration, according to the drift model GCRs should have drifted inward along the heliospheric equator to the Sun. They should be relatively sensitive to the structure

of the current sheet and the cosmic ray flux should increase toward the equator (Kóta and Jokipii 1983). When a CIR is present it acts as a barrier to prevent the entry of GCRs from the outside. The cosmic ray flux could thus be suppressed and then deceleration and convection by the solar wind and the diffusive barrier are major parts of the modulation. However, our results as shown in Figures 5.19-5.22 contradict Singh and Badruddin (2007) who find that the interplanetary magnetic field and its variance do not show any significant relationship with cosmic ray intensity change through the passage of CIRs and HSSs.

The characteristics of the 27-day intensity variations and symmetric and asymmetric modulation can be explained by the characteristics of HSSs. For symmetric modulation, the GCR intensity should continually decrease before and after the passage of a simple HSS. The duration of the corotational decrease in GCR intensity was not the same as the duration of increasing speed of the HSS because of the smoothing process (diffusion) from scattering off the magnetic irregularities and flow compression and deflection. As slow and fast streams propagate outward, flow compression and deflection on both sides of interface smooth an abrupt change in solar wind speed, leading to a continuous increase in plasma speed (Burlaga 1995). GCRs could recover if they have time in the slow speed region behind the HSSs. On the other hand, the asymmetric modulation effects mostly coincided with the compound HSSs. The compound streams are effective at preventing the GCRs from entering from outside since the smoothing process and the convection was high for a longer time. Therefore, GCRs had no time to recover to a normal level.

The GCR intensity at Doi Inthanon exhibited a clear anti-correlation with the solar wind speed as seen in Figures 5.14 and 5.15. The higher the solar wind speed, the lower the GCR intensity. The solar wind speeds were typically higher in 2007 and 2008 than in 2009 (solar minimum was shifted to 2009). The solar wind speeds gradually decreased during 2009 and increased again in 2010. Therefore, the GCR intensity increased in 2007 to 2008, and had the highest level in 2009, the time of solar

minimum, and started to decrease in 2010. This suggests that the solar wind speed in the HSSs is an important factor that controls the incoming flux of GCRs. The solar wind has clearly affected the amplitude of corotating decreases of protons above 16.8 GV as observed at Doi Inthanon.

The short-term intensity variations of GCRs are caused by HSSs and CIRs in that they exclude cosmic rays from the inner solar system along with changes in the structure of the solar wind and interplanetary magnetic field that depend on the level of solar activity. As seen in Figures 5.16 and 5.17, the 27-day modulation is correlated with the speed of recurrent HSSs emerging from CHs. The enhanced amplitudes of 27-day modulation were observed, especially in 2007 and 2008, when numerous HSSs with high speeds of 700-800 km s⁻¹ recurred in many CRs. In 2009 when the solar activity was minimal, however, the patterns of HSSs were not recurrent. In 2010, recurrent HSSs were again present when the effect of the active regions on the profile of the HSSs was more dominant. Moreover, as the solar wind speed gradually decreased in 2009 the 27-day modulation was also small. However, when the solar wind speed increased again in 2010 the 27-day modulation increased, though the profiles were less recurrent. This suggests that recurrent HSSs from CHs before solar minimum in 2007 and 2008 are the most important factor that increased the amplitude of 27-day modulation of GCR intensity. However, during 2009 to 2010 the 27-day variation in GCR intensity was not significant. This short-term effect primarily reflects local conditions in the inner heliosphere. Therefore, it is reconfirmed that the incoming GCRs were varied by the local effects of the solar wind in the inner heliosphere near solar minimum.

It is also noteworthy that the long-term variation of the GCR intensity as observed at Doi Inthanon was associated with the tilt of the HCS. As shown in Figure 5.16, the peak of GCR intensity was near the end of 2009, corresponding to the solar minimum conditions when the tilt angle of the HCS was minimal (refer to <http://wso.stanford.edu/>).

In order to illustrate the effects of the HSSs on GCR intensities we considered

the variation in CR2064, CR2071, and CR2093 during the passages of HSSs with high solar wind speeds. In CR2064 (Figure 5.9), around DOY 345 to 358, the intensity variation was clearly reduced because of the passages of two HSSs in rapid succession. The GCR intensity could not effectively recover around DOY 349 to the previous recovery level on DOY 343-344. On the other hand, the GCR intensity recovered clearly around DOY 359 after the passage of an HSS. Then in CR2071, as discussed above, the GCR intensity variations could effectively recover around DOY 166 and 177 except for behind the passage of the compound slanted HSS. The intensity there was not high, perhaps because the convection impeded the entry of GCRs from the outside. However, the diurnal variations were relatively high for many days such that the intensity in the recovery phase of the HSS was varied and there was a $\mathbf{B} \times \nabla n$ flux. Diffusion to refill GCRs into the region behind the CIR plays an important role in the recovery phase in which the convection is decreasing. However, this picture could not be satisfied if the intensity of GCR does not recover to a normal level because of CIR formation and drift streaming around the CIR. The deviation from the convection-diffusion model can be incorporated with the $\mathbf{B} \times \nabla n$ anisotropy (Figure 6.3). Finally, in CR2093 we found that the GCR intensity variations corresponded well with convective removal by the HSSs in which the intensities were low in the HSS regions, but high in the slow wind regions throughout the Carrington Rotation.

CHAPTER VII

CONCLUSIONS

In this work we have characterized, analyzed, and synthesized understanding of the effects of CHs and HSSs on enhanced diurnal variation of GCRs as observed by a neutron monitor at Doi Inthanon, Thailand with a cutoff rigidity of 16.8 GV during a 3-year period near the recent solar minimum. We observed numerous consecutive trains of enhanced DA that lasted more than 7 days, and found that these trains often recurred after a solar rotation period. The suppression and enhancement of DA were mainly in the T and A sectors of the IMF, respectively.

The long-lasting trains of enhanced DA were observed after the passage of some but not all CIRs. After a CIR and within an HSS, there is usually a lower density of GCRs. Such decreases lead to the well-known 27-day variations in which CHs rotate with the Sun and the associated HSSs return with the rotation period of ~ 27 days, leading to recurrent decreases in the GCR flux. The GCR decreases have been attributed to either shielding by the CIR or changes in the cosmic ray diffusion tensor.

During most time periods of recurrent trains of enhanced DA (i.e., CR2068-CR2071 and CR2092-CR2095), the DA was enhanced during the A magnetic sector and suppressed during the T magnetic sector. We propose that the most natural explanation for this is a $\mathbf{B} \times \nabla n$ gradient anisotropy, associated with a southward GCR gradient, that either enhanced or suppressed the usual corotational anisotropy when the magnetic field was outward or inward, respectively. The gradient anisotropy also contributes to the observed phase of the recurrent enhanced and suppressed diurnal variation.

In our data, the very strongest enhancement was associated with a slanted HSS, which can account for a particularly strong GCR gradient and the particularly

strong DA. For detailed case studies, we have selected one time period, including the time of maximum DA, from each of the two recurrent trains of enhanced DA (CR2070-CR2071 and CR2093), and one time period with a non-recurrent train (CR2064). We find that in CR2071 (and subsequent events) and CR2064, the HSS from an equatorial CH merged with that from a trailing mid-latitude extension of the south polar CH to produce a slanted HSS structure in space, within which the cosmic ray density was depressed. This can lead to a particularly strong local latitudinal gradient as the GCR intensity was reduced in the HSS region. The latitudinal gradient of GCRs can be estimated from the angle of the slanted structure and the rate of decrease in the GCR flux at Doi Inthanon. The inferred gradient anisotropy is consistent with magnitude of the temporary enhancement of the DA.

The 27-day modulations of GCRs intensity are well correlated with the magnitudes of magnetic field and solar wind speed as predicted by the solar modulation theory of GCRs. The dominant processes that affect the reduction of GCR intensity are convection, adiabatic deceleration, and diffusive barriers of magnetic fields. Effects of drifts and diffusion are also discussed.

Further work that would be related to this thesis is investigation of the effect of $\mathbf{B} \times \nabla n$ gradient anisotropy on GCRs in more data sets and studying the long-term 27-day variations of GCRs near solar minimum and maximum.

REFERENCES

- Agrawal, S. P., Lanzerotti, L. J., & Venkatesan, D. (1978). Solar-polar coronal holes and the north-south cosmic ray gradient. *Geophysical Research Letters* 5 589-591.
- Agrawal, S. P., Lanzerotti, L. J., Venkatesan, D., & Hansen, R. T. (1980). Solar polar coronal holes and galactic cosmic ray intensities. *Journal of Geophysical Research* 85 6845-6852.
- Agrawal, S. P. & Singh, R. L. (1975). *Time Variation of the Characteristics of the Diurnal Anisotropy of Cosmic Radiation*. International Cosmic Ray Conference, 4, 1193-1198.
- Ahluwalia, H. S. (2003). Solar wind modulation of galactic cosmic rays. *Geophysical Research Letter*, 30(3), 030000-1
- Alfvén, H. (1950). On the Solar Origin of Cosmic Radiation. II, *Physical Review* 77, 375-379.
- Ananth, A. G., Kudela, K., & Venkatesan, D. (1995). Characteristics of Enhanced and Low-Amplitude Cosmic-Ray Diurnal Variation. *Solar Physics* 159 191-202.
- Antonucci, E., Marocchi, D., & Perona, G. E. (1978). Phase reversals in the polar magnetic fields of the sun and in the annual and semiannual variations in cosmic ray intensity. *The Astrophysical Journal* 220 712-718.
- Badruddin, & Ananth, A. G. (2003). Variation of Cosmic Ray Intensity with Angular Distance from Earth to the Current Sheet. International Cosmic Ray Conference 7 3909.

- Badruddin, Yadav, R. S., & Yadav, N. R. (1985). Intensity variation of cosmic rays near the heliospheric current sheet. *Planetary Space Science* *33* 191-201.
- Bai, T. (1987). Periodicities of the flare occurrence rate in solar cycle 19. *The Astrophysical Journal* *318* L85-L91.
- Barouch, E., & Burlaga, L. F. (1975). Causes of Forbush decreases and other cosmic ray variations. *Journal of Geophysical Research* *80* 449-456.
- Barouch, E., & Burlaga, L. F. (1976). Three-dimensional interplanetary stream magnetism and energetic particle motion. *Journal of Geophysical Research* *81* 2103-2110.
- Bartusiak, M. (2006). *Archives of the Universe: 100 Discoveries That Transformed Our Understanding of the Cosmos*. (Random House Digital).
- Behannon, K. W., Burlaga, L. F., & Hundhausen, A.J. (1983). A comparison of coronal and interplanetary current sheet inclinations. *Journal of Geophysical Research* *88* 7837-7842.
- Bethe, H. A., Korff, S. A., & Placzek, G. (1940). On the Interpretation of Neutron Measurements in Cosmic Radiation. *The Physical Review*, *57*(7), 573-587.
- Bieber, J. W., & Chen, J. (1991). Cosmic-ray diurnal anisotropy, 1936-1988 - Implications for drift and modulation theories. *The Astrophysical Journal* *372* 301-313.
- Bieber, J. W., Eroshenko, E., Evenson, P., Flückiger, E.O., & Kallenbach, R. (2000). Cosmic Rays and Earth A Summary. *Space Science Review* *93* 1-9.
- Bieber, J. W., & Evenson, P. (1998). CME geometry in relation to cosmic ray anisotropy. *Geophysical Research Letters* *25* 2955-2958.

- Bieber, J. W., & Matthaeus, W. H. (1997). Perpendicular Diffusion and Drift at Intermediate Cosmic-Ray Energies. *The Astrophysical Journal* 485 655-664.
- Bruno, R., Burlaga, L. F., & Hundhausen, A. J. (1982). Quadrupole distortions of the heliospheric current sheet in 1976 and 1977. *Journal of Geophysical Research* 87 10339-10346.
- Burger, R. A., & Hitge, M. (2004). The Effect of a Fisk-Type Heliospheric Magnetic Field on Cosmic-Ray Modulation. *The Astrophysical Journal Letters* 617 L73-L76.
- Burlaga, L. F. (1974). Interplanetary stream interfaces. *Journal of Geophysical Research* 79 3717-3725.
- Burlaga, L. F. (1995). *Interplanetary Magnetohydrodynamics* (Vol.3). International Series in Astronomy and Astrophysics.
- Burlaga, L. F., Goldstein, M. L., McDonald, F. B., & Lazarus, A. J. (1985). Cosmic ray modulation and turbulent interaction regions near 11 AU. *Journal of Geophysical Research* 90 12027-12032.
- Burlaga, L. F., Goldstein, M. L., McDonald, F. B., Lazarus, A. J., & Mariani, F. (1986). Cosmic ray variations and turbulent flow systems - 0.3-1.0 AU; 1977-1980. *Journal of Geophysical Research* 91 2917-2927.
- Burlaga, L. F., Lepping, R. P., Behannon, K. W., & Klein, L. W. (1984). Large-scale interplanetary magnetic fields - Voyager 1 and 2 observations between 1 AU and 9.5 AU. *Journal of Geophysical Research* 89 10659-10668.
- Burlaga, L. F., McDonald, F. B., Ness, N. F., Schwenn, R., Lazarus, A. J., & Mariani, F. (1984). Interplanetary flow systems associated with cosmic ray modulation in 1977-1980. *Journal of Geophysical Research* 89 6579-6587.

- Burlaga, L. F., Ness, N. F., Mariani, F., Bavassano, B., Villante, U., Rosenbauer, H., et al. (1978). Magnetic fields and flows between 1 and 0.3 AU during the primary mission of HELIOS 1. *Journal of Geophysical Research* 83 5167-5174.
- Burlaga, L. F., Perko, J., & Pirraglia, J. (1993). Cosmic-ray modulation, merged interaction regions, and multifractals. *The Astrophysical Journal* 407 347-358.
- Burlaga, L. F., Schwenn, R., & Rosenbauer, H. (1983). Dynamical evolution of interplanetary magnetic fields and flows between 0.3 AU and 8.5 AU - Entrainment. *Geophysical Research Letters* 10 413-416.
- Carmichael, H., Bercovitch, M., Shea, M. A., Magidin, M., Peterson, R. W. (1968). Attenuation of neutron monitor radiation in the atmosphere. *Canadian Journal of Physics* 46 1006.
- Chen, J. (1989). Long-term modulation of cosmic rays in interplanetary magnetic turbulence. Ph.D. Thesis: Delaware Univ., Newark.
- Chen, J., Bieber, J. W., & Pomerantz, M. A. (1991). Cosmic ray unidirectional latitude gradient - Evidence for north-south asymmetric solar modulation. *Journal of Geophysical Research* 96 11569-11576.
- Chih, P. P., & Lee, M. A. (1986). A perturbation approach to cosmic ray transients in interplanetary space. *Journal of Geophysical Research* 91 2903-2913.
- Choi, Y., Moon, Y. J., Choi, S., Baek, J. H., Kim, S. S., Cho, K. S., et al. (2009). Statistical analysis of the Relationships among Coronal Holes, Corotating Interaction Regions, and Geomagnetic Storms. *Solar Physics* 254 311-323.
- Crooker, N. U., Gosling, J. T., Bothmer, V., Forsyth, R. J., Gazis, P. R., Hewish, A., et al. (1999). CIR Morphology, Turbulence, Discontinuities, and Energetic Particles. *Space Science Reviews* 89 179-220.

- da Silva, M. R., Dal Lago, A., Echer, E., de Lucas, A., Gonzalez, W. D., Schuch, N. J., et al. (2007). Muon and neutron observations in connection with the corotating interaction regions. *Advances in Space Research* 40 348-352.
- Dattner, A., & Venkatesan, D. (1959). Anisotropies in Cosmic Radiation. *Tellus*, 11(2), 239-248.
- Dröge, W., Kunow, H., Heber, B., Müller-Mellin, R., Sierks, H., Wibberenz, G., et al. (1996). Effects of corotating interaction regions on Ulysses high energy particles. American Institute of Physics Conference Series, 382, 515-518.
- Duggal, S. P., & Pomerantz, M. A. (1975). *Long Term Changes in the Solar Diurnal Anisotropy*. International Cosmic Ray Conference, 4, 1209-1215.
- Duggal, S. P., Pomerantz, M. A., Owens, A. J., & Tolba, M. F. (1979). New insights into the variability of the cosmic ray diurnal anisotropy. *Journal of Geophysical Research* 84 6653-6657.
- Duldig, M. L., Cramp, J. L., Humble, J. E., Smart, D. F., Shea, M. A., Bieber, J. W., et al. (1993). *The Ground Level Enhancements of 1989SEP29 and 1989OCT22*. Proceedings of the Astronomical Society of Australia, 10, 211-222.
- Duldig, M. L., & Humble, J. E. (1990). *Enhanced cosmic ray diurnal variations in Mawson and Hobart neutron monitor and underground data records*. Proceedings of the Astronomical Society of Australia, 8, 268-273.
- Firor, J. W., Fonger, W. H., & Simpson, J. A. (1954). Cosmic Radiation Intensity-Time Variations and Their Origin. V. The Daily Variation of Intensity. *Physical Reviews*, 94(4), 1031-1036.

- Fisk, L. A., Jokipii, J. R. (1999). Mechanisms for Latitudinal Transport of Energetic Particles in the Heliosphere. *Space Science Reviews* 89 115-124.
- Fonger, W. H. (1953). Cosmic Radiation Intensity-Time Variations and Their Origin. II. Energy Dependence of 27-Day Variations. *Physical Reviews*, 91(2), 351-361.
- Forbush, S. E. (1954). World-Wide Cosmic-Ray Variations, 1937-1952. *Journal of Geophysical Research* 59 535-542.
- Forman, M. A., & Gleeson, L. J. (1975). Cosmic-ray streaming and anisotropies. *Astrophysics and Space Science* 32 77-94.
- Forman, M. A., Jokipii, J. R., & Owens, A. J. (1974). Cosmic-Ray Streaming Perpendicular to the Mean Magnetic Field. *The Astrophysical Journal* 192 535-540.
- Forsyth, R. J., Balogh, A., Horbury, T. S., Erdoes, G., Smith, E. J., & Burton, M. E. (1996). The heliospheric magnetic field at solar minimum: ULYSSES observations from pole to pole. *Astronomy and Astrophysics* 316 287-295.
- Gleeson, L. J., & Axford, W. I. (1967). Cosmic Rays in the Interplanetary Medium. *The Astrophysical Journal, Letters* 149 L115-L120.
- Gleeson, L. J., & Axford, W. I. (1968). Solar Modulation of Galactic Cosmic Rays. *The Astrophysical Journal* 154 1011-1020.
- Gosling, J. T., Hundhausen, A. J., & Bame, S. J. (1976). Solar wind stream evolution at large heliocentric distances - Experimental demonstration and the test of a model. *Journal of Geophysical Research* 81 2111-2122.
- Gosling, J. T., & Pizzo, V. J. (1999). Formation and Evolution of Corotating Interaction Regions and their Three Dimensional Structure. *Space Science Reviews* 89 21-52.

- Hall, D. L., Duldig, M. L., & Humble, J. E. (1996). Analyses of Sidereal and Solar Anisotropies in Cosmic Rays. *Space Science Reviews* 78 401-442.
- Hapgood, M. *Space Weather: Its impact on Earth and implications for business. Lloyd's 360 Risk Insight*. Lloyd's of London. Retrieved 24 June 2013.
- Hashim, A, & Bercovitch, M. (1972). A cosmic ray density gradient perpendicular to the ecliptic plane. *Planetary Space Science* 20 791-802.
- Hashim, A., Bercovitch, M., & Steljes, J.F. (1972). Streaming of Galactic Cosmic Rays in the Interplanetary Magnetic Field. *Solar Physics* 22 220-234.
- Hattingh, M. (1998). Potchefstroom University, Ph.D. thesis
- Hatton, C. J. (1971). Neutron monitor, Progress in elementary particle and cosmic ray physics. editor Wilson, J.G. and Wouthuysen, S.A. North - Holland.
- Hatton, C. J., & Carmichael, H. (1964). Experimental Investigation of the NM-64 Neutron Monitor. *Canadian Journal of Physics*, 42(12), 2443-2472.
- Heber, B., & Burger, R. A. (1999). Modulation of Galactic Cosmic Rays at Solar Minimum. *Space Science Reviews* 89 125-138.
- Heber, B., Dröge, W., Kunow, H., Müller-Mellin, R., Wibberenz, G. Ferrando, P., et al. (1996). Spatial variation of ~106 MeV proton fluxes observed during the Ulysses rapid latitude scan: Ulysses COSPIN/KET results. *Journal of Geophysical Research* 23 1513-1516
- Heber, B., Gieseler, J., Dunzlaff, P., Gómez-Herrero, R., Klassen, A., Müller-Mellin, R., et al. (2008). Latitudinal Gradients of Galactic Cosmic Rays during the 2007 Solar Minimum. *The Astrophysical Journal* 689 1443-1447.

- Heber, B., Potgieter, M. S., & Ferrando, P. (1997). Solar modulation of galactic cosmic rays: the 3D heliosphere. *Advances in Space Research* 19 795-804.
- Hedgecock, P. C., Quenby, J. J., & Webb, S. (1972). Off-Ecliptic Control of Cosmic Ray Modulation. *Nature Physical Science* 240 173-175
- Hoeksema, J. T. (1995). The Large-Scale Structure of the Heliospheric Current Sheet During the ULYSSES Epoch. *Space Science Reviews* 72 137-148.
- Howard, R. A., Moses, J. D., Vourlidas, A., Newmark, J. S., Socker, D. G., Plunkett, S.P., et al. (2008). Sun Earth Connection Coronal and Heliospheric Investigation (SECCHI). *Space Science Reviews* 136 67-115.
- Hundhausen, A. J. (1977). An interplanetary view of coronal holes. Proceeding in Coronal Holes and High Speed Wind Streams, 225-329.
- Hundhausen, A. J., & Gosling, J. T. (1976). Solar wind structure at large heliocentric distances - an interpretation of Pioneer 10 observations. *Journal of Geophysical Research* 81 1436-1440.
- Hundhausen, A. J., Sime, D.G., Hansen, R.T., & Hansen, S.F. (1980). Polar coronal holes and cosmic-ray modulation. *Science* 207 761-763.
- Iucci, N., Parisi, M., Storini, M., & Villoresi, G. (1979). High-speed solar-wind streams and galactic cosmic-ray modulation. *Nuovo Cimento C Geophysics Space Physics C* 2 421-438.
- Iucci, N., Parisi, M., Storini, M., & Villoresi, G. (1983). The behavior of the cosmic-ray equatorial anisotropy inside fast solar-wind streams ejected by coronal holes. *Nuovo Cimento C Geophysics Space Physics C* 6 145-158.
- Jokipii, J. R. (1966). Cosmic-Ray Propagation. I. Charged Particles in a Random Magnetic Field. *The Astrophysical Journal* 146 480-487.

- Jokipii, J. R. (1967). Cosmic-Ray Propagation. II. Diffusion in the Inter-planetary Magnetic Field. *The Astrophysical Journal* 149 405-415.
- Jokipii, J. R. (1971). Propagation of cosmic rays in the solar wind. *Reviews of Geophysics and Space Physics* 9 27-87.
- Jokipii, J. R. (1973). The Rate of Separation of Magnetic Lines of Force in a Random Magnetic Field. *The Astrophysical Journal* 183 1029-1036.
- Jokipii, J. R., & Davila, J. M. (1981). Effects of particle drift on the transport of cosmic rays. IV - More realistic diffusion coefficients. *Astrophysical Journal* 248 1156-1161.
- Jokipii, J. R., & Kóta, J. (2000). Galactic and Anomalous Cosmic Rays in the Heliosphere. *Astrophysics and Space Science* 274 77-96.
- Jokipii, J. R., & Levy, E. H. (1977). Effects of particle drifts on the solar modulation of galactic cosmic rays. *The Astrophysical Journal, Letters* 213 L85-L88.
- Jokipii, J. R., Levy, E. H., & Hubbard, W. B. (1977). Effects of particle drift on cosmic-ray transport. I - General properties, application to solar modulation. *The Astrophysical Journal* 213 861-868.
- Jokipii, J. R., & Parker, E. N. (1968). Random Walk of Magnetic Lines of Force in Astrophysics. *Physical Review Letters* 21 44-47.
- Jokipii, J. R., & Parker, E. N. (1969). Stochastic Aspects of Magnetic Lines of Force with Application to Cosmic-Ray Propagation. *The Astrophysical Journal* 155 777-798.
- Jokipii, J. R., & Parker, E. N. (1970). On the Convection, Diffusion, and Adiabatic Deceleration of Cosmic Rays in the Solar Wind. *The Astrophysical Journal* 160 735-744.

- Jokipii, J. R., & Thomas, B. (1981). Effects of drift on the transport of cosmic rays. IV - Modulation by a wavy interplanetary current sheet. *The Astrophysical Journal* *243* 1115-1122.
- Kaiser, M. L., Kucera, T. A., Davila, J. M., St. Cyr, O. C., Guhathakurta, M., Christian, E. (2008). The STEREO Mission: An Introduction. *Space Science Reviews* *136* 5-16.
- Kallenrode, M. -B. Galactic cosmic rays. Summer school 'outer heliosphere'. <http://www.sotere.uni-osnabrueck.de/pubs/paper/summerschool-gaks.pdf>. Retrieve 07/03/2014.
- Kamyran, N. (2011). Mahidol University, M.Sc. thesis.
- Klein, L. W., & Burlaga, L. F. (1982). Interplanetary magnetic clouds at 1 AU. *Journal of Geophysical Research* *87* 613-624.
- Kóta, J. and Jokipii, J. R. (1983). Effects of drift on the transport of cosmic rays. VI - A three-dimensional model including diffusion. *The Astrophysical Journal* *265* 573-581.
- Kóta, J., & Jokipii, J. R. (1991). The role of corotating interaction regions in cosmic-ray modulation. *Geophysical Research Letters* 1797-1800.
- Kóta, J., & Jokipii, J. R. (1998). Modeling of 3-D Corotating Cosmic-Ray Structures in the Heliosphere. *Space Science Review* *83* 137-145.
- Kóta, J., & Jokipii, J. R. (2001). The anisotropies of galactic cosmic rays: 3-dimensional modeling. *Advances in Space Research*, 27(3), 607-612.
- Krieger, A. S., Timothy, A. F., & Roelof, E. C. (1973). A Coronal Hole and Its Identification as the Source of a High Velocity Solar Wind Stream. *Solar Physics* *29* 505-525.
- Kunow, H., Lee, M. A., Fisk, L. A., Forsyth, R. J., Heber, B., Horbury, T. S., et al. (1999). Corotating Interaction Regions at High Latitudes. *Space Science Reviews* *89* 221-268.

- Le Roux, J. A., & Potgieter, M. S. (1995). The simulation of complete 11 and 12 year modulation cycles for cosmic rays in the heliosphere using a drift model with global merged interaction regions. *The Astro-physical Journal* 442 847-851.
- Lin, Z., Bieber, J. W., & Evenson, P. (1995). Electron trajectories in a model magnetosphere: Simulation and observation under active conditions. *Journal of Geophysical Research* 100 23543-23550.
- Longair, S. (1992). High Energy Astrophysics: Particles, photons and their detection. Cambridge University Press .
- Mavromichalaki, H. (1989). Application of diffusion-convection model to diurnal anisotropy data. *Earth Moon and Planets* 47 61-72.
- Mavromichalaki, H., Vassilaki, A., & Marmatsouri, E. (1988). A catalogue of high-speed solar-wind streams - Further evidence of their relationship to Ap-index. *Solar Physics* 115 345-365.
- McCracken, K. G., & Rao, U. R. (1965). A survey of the diurnal anisotropy. *International Cosmic Ray Conference*, 1, 213-225.
- McCracken, K. G., & Rao, U. R. (1966). The temporal independence of the occurrence of small scale irregularities in the interplanetary magnetic field. *Planetary Space Science* 14 649-651.
- McCracken, K. G., Rao, U. R., & Shea, A. (1962). *The Trajectories of Cosmic Rays in a High Degree Simulation of the Geomagnetic Field*. Massachusetts Institute of Technology, Laboratory for Nuclear Science.
- McKibben, R. B., Jokipii, J. R., Burger, R. A., Heber, B., Kóta, J., McDonald, F.B., et al. (1999). Modulation of Cosmic Rays and Anomalous Components by CIRs. *Space Science Reviews* 89 307-326.

- McKibben, R. B., Pyle, K. R., & Simpson, J. A. (1979). The solar latitude and radial dependence of the anomalous cosmic-ray helium component. *The Astrophysical Journal, Letters* 227 L147-L152
- McKibben, R. B., Simpson, J. A., Zhang, M., Bame, S., & Balogh, A. (1995). ULYSSES Out-of-Ecliptic Observations of "27-day" Variations in High Energy Cosmic Ray Intensity. *Space Science Reviews* 72 403-408.
- Mewaldt, R. A. (1996). *The Macmillan Encyclopedia of Physics*. John S Rigden (Editor) New York: Simon & Schuster Macmillan Publisher.
- Meyer, P., Parker, E. N., & Simpson, J. A. (1956). Solar Cosmic Rays of February, 1956 and Their Propagation through Interplanetary Space. *Physical Review*, 104(3), 768-783.
- Mishra, R. K., Mishra, R. A. (2005). Harmonics of high-amplitude wave trains in cosmic ray intensity. *Planetary Space Science* 53 739-747.
- Moraal, H., Belov, A., Clem, J. M. (2000). Design and co-Ordination of Multi-Station International Neutron Monitor Networks. *Space Science Reviews* 93 285-303.
- Mori, S., Swinson, D. B., Fujimoto, K., & Nagashima, K. (1981). 22-year variation in the solar diurnal anisotropy of cosmic rays. International Cosmic Ray Conference, 10, 218-221.
- Morrison, P. (1956). Solar Origin of Cosmic-Ray Time Variations. *Physical Review* 101 1397-1404.
- Moussas, X., & Tritakis, B. (1982). Latitudinal and solar-cycle dependence of the interplanetary magnetic field predominant polarity. *Solar Physics* 75 361-375.
- Munakata, Y., Mori, S., Ryu, J. Y., Agrawal, S. P., & Venkatesan, D. (1987). *High-Speed Solar Wind Stream and Modulation of Cosmic Ray Anisotropy*. International Cosmic Ray Conference, 4, 39-42.

- Munakata, Y., Darwish, A., Fujii, Z., Kato, C., & Mori, S. (2003). *High-Speed Solar-Wind Streams from Coronal Holes and Modulation of Cosmic Ray Diurnal Anisotropy*. 28th International Cosmic Ray Conference, 7, 3925-3938.
- Murdin, P. M. (2001). *Encyclopedia of Astronomy and Astrophysics*. C R C Press LLC.
- Nagashima, K., Sakakibara, S., Murakami, K., & Morishita, I. (1989). Response and yield functions of neutron monitor, Galactic cosmic ray spectrum and its solar modulation, derived from all the available world-wide surveys. *Nuovo Cimento C Geophysics Space Physics C 12* 173-209.
- Newkirk, Jr., G. (1972). Coronal Magnetic Fields and the Solar Wind. *NASA Special Publication 308* 11-22.
- Newkirk, Jr., G., & Fisk, L. A. (1985). Variation of cosmic rays and solar wind properties with respect to the heliospheric current sheet. I - Five-GeV protons and solar wind speed. *Journal of Geophysical Research 90* 3391-3414.
- Newkirk, Jr., G., & Lockwood, J. A. (1981). Cosmic ray gradients in the heliosphere and particle drifts. *Geophysical Research Letters 8* 619-622.
- Nolte, J. T., Krieger, A. S., Timothy, A. F., Gold, R. E., Roelof, E. C., Vaiana, G., et al. (1976). Coronal holes as sources of solar wind. *Solar Physics 46* 303-322.
- Nutaro, T. (2008). Construction of the Princess Sirindhorn Neutron Monitor at Doi Inthanaon, Thailand. Report of the project. Ubonratchathani University.
- Okazaki, Y., Fushishita, A., Narumi, T., Kato, C., Yasue, S., Kuwabara, T., et al. (2008). Drift Effects and the Cosmic Ray Density Gradient in a Solar Rotation Period: First Observation with the Global Muon Detector Network (GMDN). *The Astrophysical Journal 681* 693-707.

- Owens, A. J., Duggal, S. P., Pomerantz, M. A., & Tolba, M. F. (1980). The three-dimensional structure of relativistic galactic cosmic ray anisotropies associated with solar rotation. *The Astrophysical Journal* *236* 1012-1016.
- Paizis, C., Heber, B., Raviart, A., Ducros, R., Ferrando, P., Rastoin, C., et al. (1995). *Latitudinal Effects of Galactic Cosmic Rays Observed Onboard the Ulysses Spacecraft*. International Cosmic Ray Conference, 4, 756-759.
- Parker, E. N. (1957). Newtonian Development of the Dynamical Properties of Ionized Gases of Low Density. *Physical Review* *4* 924-933.
- Parker, E. N. (1958). Cosmic-Ray Modulation by Solar Wind. *Physical Review* *110* 1445-1449.
- Parker, E. N. (1963). *Interplanetary Dynamical Processes*. Interscience monographs and texts in physics and astronomy. Interscience Publishers.
- Parker, E. N. (1964). Theory of streaming of cosmic rays and the diurnal variation. *Planetary Space Science* *12* 735-749.
- Parker, E. N. (1965). The passage of energetic charged particles through interplanetary space. *Planetary Space Science* *13* 9-49.
- Parker, E. N. (1967). Cosmic ray diffusion, energy loss, and the diurnal variation. *Planetary Space Science* *15* 1723-1746.
- Phillips, J. L., Bame, S. J., Feldman, W. C., Goldstein, B. E., Gosling, J. T., Hammond, C. M., et al. (1995). Ulysses Solar Wind Plasma Observations at High Southerly Latitudes. *Science* *268* 1030-1033.
- Pizzo, V. J. (1982). A three-dimensional model of corotating streams in the solar wind. III - Magnetohydrodynamic streams. *Journal of Geophysical Research* *87* 4374-4394.

- Pizzo, V. J., & Gosling, J. T. (1994). 3-D simulation of high-latitude inter-action regions: Comparison with ULYSSES results. *Geophysical Research Letters* 21 2063-2066.
- Pomerantz, M. A., & Duggal, S. P. (1971). The Cosmic Ray Solar Diurnal Anisotropy. *Space Science Reviews* 12 75-130.
- Quenby, J. J. (1984). The theory of cosmic-ray modulation. *Space Science Reviews* 37 201-267.
- Rao, U. R. (1972). Solar Modulation of Galactic Cosmic Radiation. *Space Science Reviews* 12 719-809.
- Rao, U. R., McCracken, K.G., & Venkatesan, D. (1963). Asymptotic Cones of Acceptance and Their Use in the Study of the Daily Variation of Cosmic Radiation. *Journal of Geophysical research* 68 345-369.
- Richardson, I. G. (2004). Energetic Particles and Corotating Interaction Regions in the Solar Wind. *Space Science Reviews* 111 267-376.
- Richardson, I. G., Wibberenz, G., & Cane, H. V. (1996). The relationship between recurring cosmic ray depressions and corotating solar wind streams at =1 AU: IMP 8 and Helios 1 and 2 anticoincidence guard rate observations. *Journal of Geophysical research* 101 13483-13496.
- Rosenberg, R. L. (1970). Unified Theory of the Interplanetary Magnetic Field. *Solar Physics* 15 72-78.
- Rouillard, A. P., & Lockwood, M. (2007). The Latitudinal Effect of Corotating Interaction Regions on Galactic Cosmic Rays. *Solar Physics* 245 191-206.
- Ruffolo, D. (1995). Effect of adiabatic deceleration on the focused transport of solar cosmic rays. *The Astrophysical Journal* 442 861-874.
- Sarabhai, V., Subramanian, G. (1966). Galactic Cosmic Rays in the Solar System. *The Astrophysical Journal* 145 206-213.

- Schatten, K. H., Wilcox, J.M., & Ness, N.F. (1969). A model of interplanetary and coronal magnetic fields. *Solar Physics* 6 442-455.
- Schwenn, R. (1990). Large-Scale Structure of the Interplanetary Medium. *Physics of the Inner Heliosphere I*, 99.
- Schwenn, R. (2006). Space Weather: The Solar Perspective. *Living Reviews in Solar Physics* 3 2-36.
- Schulz, M. (1973). Interplanetary sector structure and the heliomagnetic equator. *Astrophysics and Space Science* 24 371-383.
- Sheeley, Jr., N. R., & Harvey, J. W. (1978). Coronal holes, solar wind streams, and geomagnetic activity during the new sunspot cycle. *Solar Physics* 59 159-173.
- Simnett, G. M., Kunow, H., Flückiger, E., Heber, B., Horbury, T., Kóta, J., et al. (1998). Corotating Particle Events. *Space Science Reviews* 83 215-258.
- Simpson, J. A. (1948). The Latitude Dependence of Neutron Densities in the Atmosphere as a Function of Altitude. *Physical Review* 73 1389-1391.
- Simpson, J. A. (1951). Neutrons Produced in the Atmosphere by the Cosmic Radiations. *Physical Review* 6 1175-1188.
- Simpson, J. A. (1954). Cosmic-Radiation Intensity-Time Variations and Their Origin. III. The Origin of 27-Day Variations. *Physical Review* 2 426-440.
- Simpson, J. A. (1983). Elemental and Isotopic Composition of the Galactic Cosmic Rays. *Annual Review of Nuclear and Particle Science* 33 323-382.
- Simpson, J. A. (1998). A Brief History of Recurrent Solar Modulation of the Galactic Cosmic Rays (1937-1990). *Space Science Reviews* 83 169-176.

- Simpson, J. A. (2000). The Cosmic Ray Nucleonic Component: The Invention and Scientific Uses of the Neutron Monitor - (Keynote Lecture). *Space Science Reviews* 93 11-32.
- Simpson, J. A., Babcock, H. W., & Babcock, H. D. (1955). Association of a "Unipolar" Magnetic Region on the Sun with Changes of Primary Cosmic-Ray Intensity. *Physical Review* 98 (5) 1402--1406.
- Simpson, J. A., Fonger, W., & Treiman, S. B. (1953). Cosmic Radiation Intensity-Time Variations and Their Origin. I. Neutron Intensity Variation Method and Meteorological Factors. *Physical Review* 90 934-950.
- Simpson, J. A., Zhang, M., & Bame, S. (1996). A Solar Polar North-South Asymmetry for Cosmic-Ray Propagation in the Heliosphere: The ULYSSES Pole-to-Pole Rapid Transit. *The Astrophysical Journal, Letters* 465 L69.
- Singh, Y. P.; Badruddin. (2007). Corotating high-speed solar-wind streams and recurrent cosmic ray modulation. *Journal of Geophysical Research: Space Physics*, 112 (A5) 101-110.
- Singh, A., Tiwari, A. K., & Agrawal, S. P. (2010). Study of high and low amplitude wave trains of cosmic ray diurnal variation during solar cycle 23. *Journal of Astrophysics and Astronomy* 31 89-96.
- Siscoe, G. (2000). The space-weather enterprise: past, present, and future. *Journal of Atmospheric and Solar-Terrestrial Physics* 62 1223-1232.
- Smart, D. F., & Shea, M. A. (2005). A review of geomagnetic cutoff rigidities for earth-orbiting spacecraft. *Advances in Space Research* 36 2012-2020.
- Smart, D. F., Shea, M. A., & Flückiger, E. O. (2000). Magnetospheric Models and Trajectory Computations. *Space Science Reviews* 93 305-333.
- Smith, E. J., Jokipii, J. R., Kóta, J., Lepping, R.P., & Szabo, A. (2000). Evidence of a North-South Asymmetry in the Heliosphere Associated with a

- Southward Displacement of the Heliospheric Current Sheet. *The Astrophysical Journal* 553 1084-1089.
- Spitzer, Jr., L. (1952). Equations of Motion for an Ideal Plasma. *The Astrophysical Journal* 116 299.
- Stoker, P. H. (2009). The IGY and beyond: A brief history of ground-based cosmic-ray detectors. *Advances in Space Research* 44 1081-1095.
- Stoker, P. H., Dorman, L. I., & Clem, J. M. (2000). Neutron Monitor Design Improvements. *Space Science Reviews* 93 361-380.
- Störmer, C. (1956). The polar aurora. *Quarterly Journal of the Royal Meteorological Society* 82 (351), 115-115.
- Subramanian, G. (1971). Amplitude of Diurnal Anisotropy of Cosmic Ray Intensity, *Journal of Geophysical Research*, 76(4), 1093-1096.
- Subramanian, G., & Sarabhai, V. (1967). Consequences of the Distribution of Galactic Cosmic-Ray Density in the Solar System. *The Astrophysical Journal* 149 417.
- Swann, W. F. G. (1933). Application of Liouville's Theorem to Electron Orbits in the Earth's Magnetic Field. *Physical Review*, 44(3), 224-227.
- Swinson, D. B. (1970). Cosmic ray density gradient perpendicular to the ecliptic plane. *Journal of Geophysical Research* 75 7303-7306.
- Swinson, D. B., & Kananen, H. (1982). Reversal of the cosmic ray density gradient perpendicular to the ecliptic plane. *Journal of Geophysical Research* 87 1685-1687.
- Thambyahpillai, T., & Elliot, H. (1953). World-Wide Changes in the Phase of the Cosmic-Ray Solar Daily Variation. *Nature* 171 918-920.
- Thomas, B. T., & Gall, R. (1984). Solar-flare-induced Forbush decreases - Dependence on shock wave geometry. *Journal of Geophysical Research* 89 2991-2996.

- Thomas, B. T., & Smith, E. J. (1981). The structure and dynamics of the heliospheric current sheet. *Journal of Geophysical Research* 86 11105-11110.
- Tolba, M. F., Pomerantz, M. A., Duggal, S. P., & Owens, A. J. (1981). *27-day variations in the IMF components and the cosmic ray anisotropies*. 17th International Cosmic Ray Conference, 4, 52-55.
- Tsyganenko, N. A. (1989). A magnetospheric magnetic field model with a warped tail current sheet. *Planetary Space Science* 37 5-20.
- Venkatesan, D., & Badruddin. (1990). Cosmic-ray intensity variations in the 3-dimensional heliosphere. *Space Science Reviews* 52 121-194.
- Wang, Y.-M., Sheeley, Jr., N. R., Phillips, J. L., & Goldstein, B. E. (1997). Solar Wind Stream Interactions and the Wind Speed-Expansion Factor Relationship. *The Astrophysical Journal, Letters* 488 L51.
- Wilcox, J. M. (1968). The Interplanetary Magnetic Field. Solar Origin and Terrestrial Effects. *Space Science Reviews* 8 258-328.
- Wilcox, J. M., & Ness, N. F., (1965). Quasi-Stationary Corotating Structure in the Interplanetary Medium. *Journal of Geophysical Research* 70 5793-5805.
- Wilcox, J. M., & Scherrer, P. H. (1972). Annual and solar-magnetic-cycle variations in the interplanetary magnetic field, 1926-1971. *Journal of Geophysical Research* 77 5385-5396.
- Wood, B. E., Howard, R. A., Thernisien, A., & Socker, D. G. (2010). The Three-Dimensional Morphology of a Corotating Interaction Region in the Inner Heliosphere. *The Astrophysical Journal, Letters* 708 L89-L94.
- Wülser, J. P., Lemen, J. R., Tarbell, T. D. C., Wolfson, C. J., Cannon J. Carpenter, B. A, et al. (2003). *EUVI: the STEREO-SECCHI extreme ultraviolet imager*. Proceedings of SPIE Vol. 5171.

- Zhang, M. (1997). A Linear Relationship between the Latitude Gradient and 26 Day Recurrent Variation in the Fluxes of Galactic Cosmic Rays and Anomalous Nuclear Components. I. Observations. *The Astrophysical Journal* 488 841-851.
- Zhang, M. (1999). A Path Integral Approach to the Theory of Heliospheric Cosmic-Ray Modulation. *The Astrophysical Journal* 510 715-725.
- Zhao, X., & Hoeksema, J. T. (1993). Unique determination of model coronal magnetic fields using photospheric observations. *Solar Physics* 143 41-48.
- Zirker, J. B. (1977). Coronal holes and high-speed wind streams. *Reviews of Geophysics and Space Physics* 15 257-269.

APPENDICES

APPENDIX A

27-DAY VARIATIONS IN GCR INTENSITY AS OBSERVED BY PSNM

Data of neutron count rate at Doi Inthanon between 2007 November and 2010 November have been displayed as 27-day variations in GCR intensity for each year (Figures A.1-A.4).

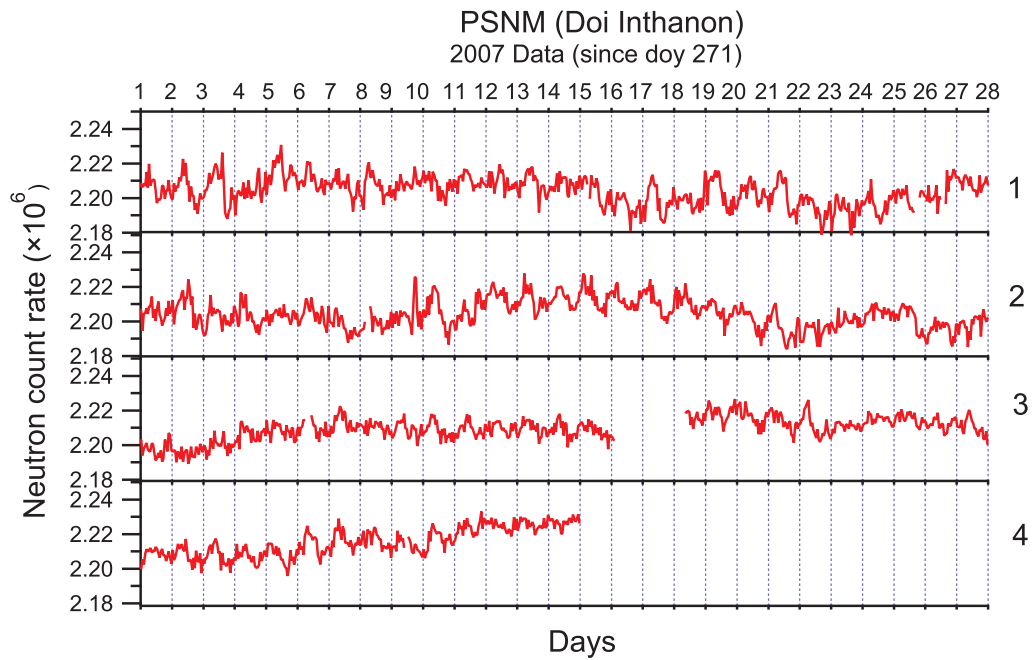


Figure A.1: Diurnal variations over 27-day periods in 2007.

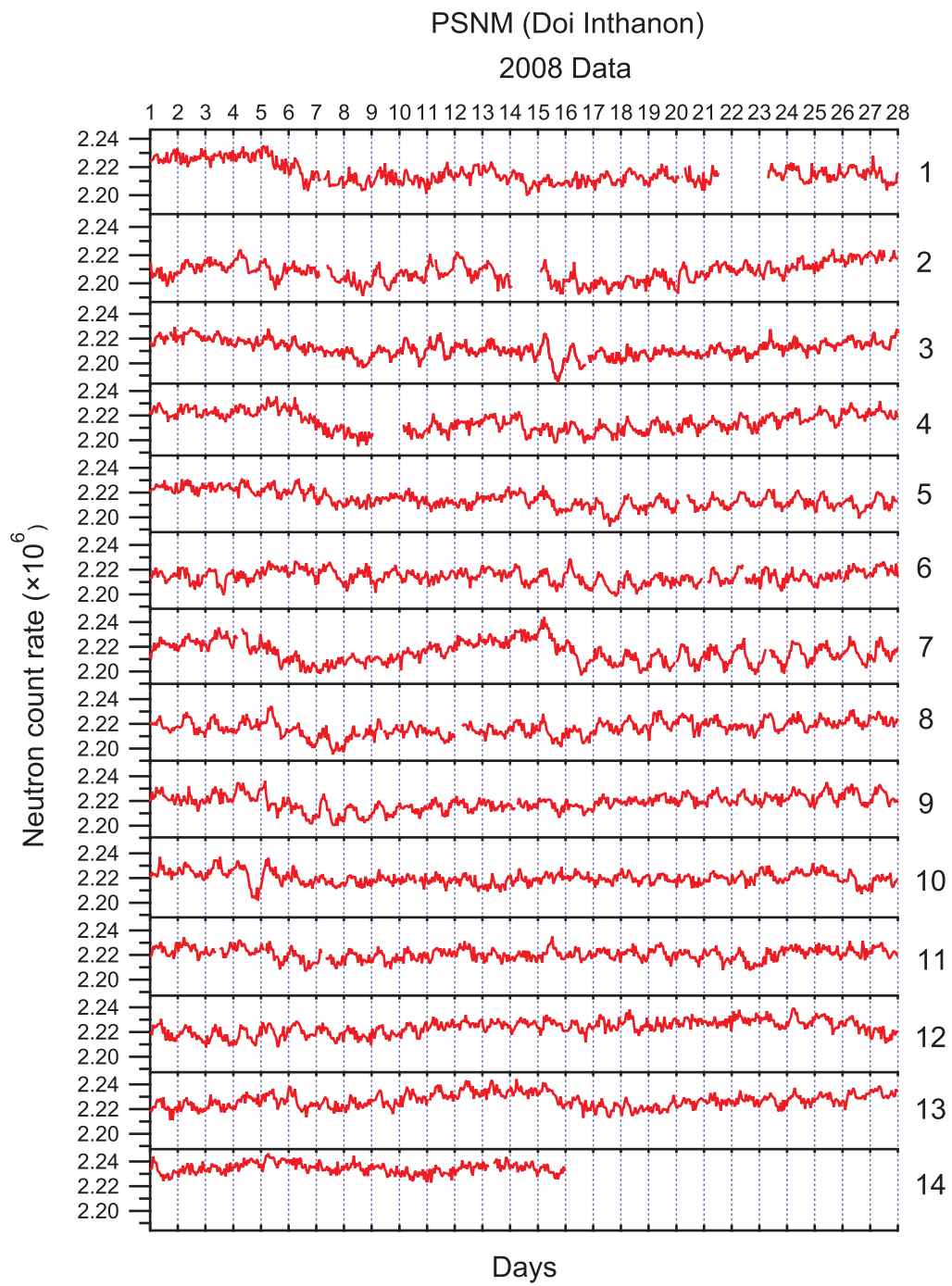


Figure A.2: Diurnal variations over 27-day periods in 2008.

PSNM (Doi Inthanon)
2009 Data

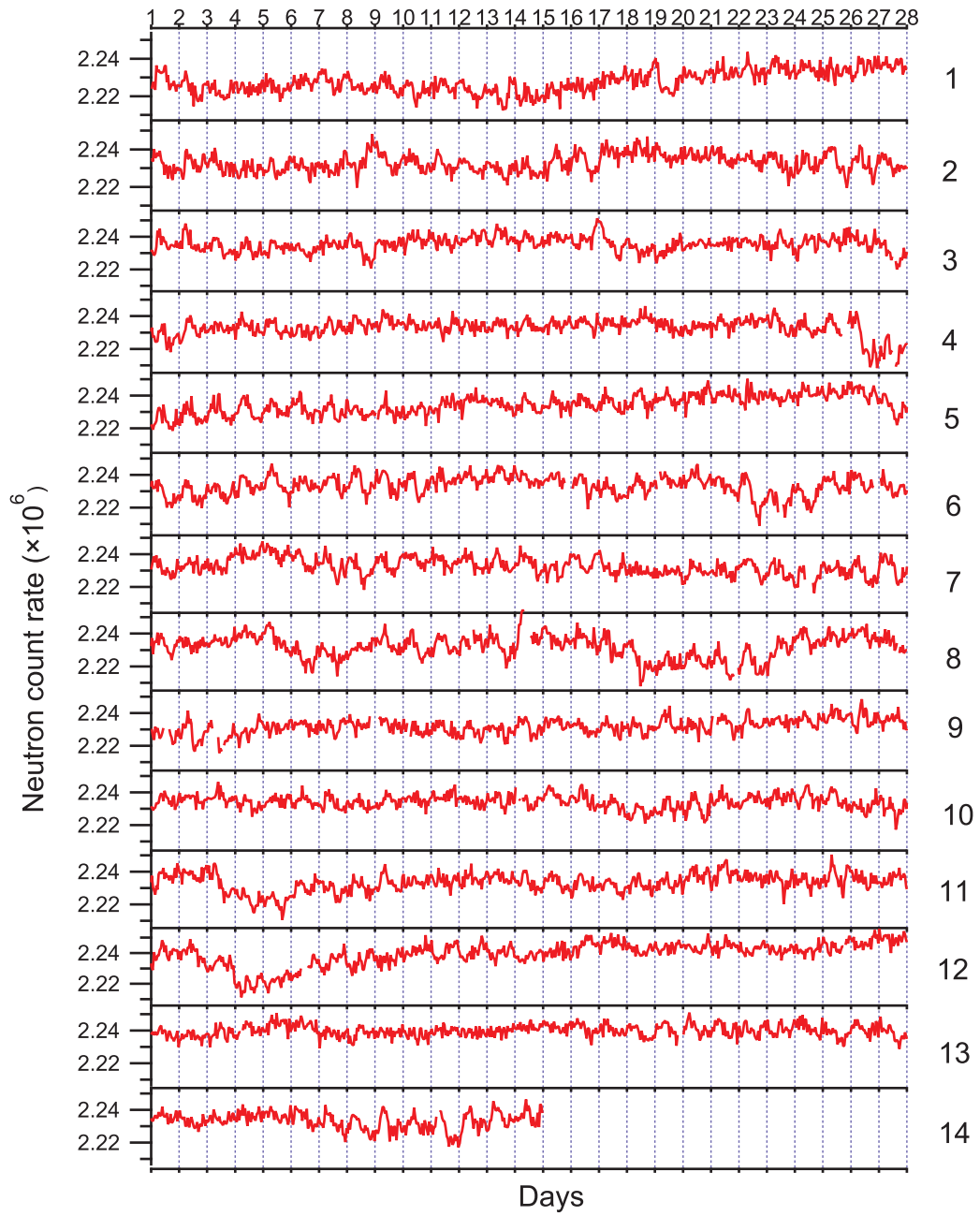


Figure A.3: Diurnal variations over 27-day periods in 2009.

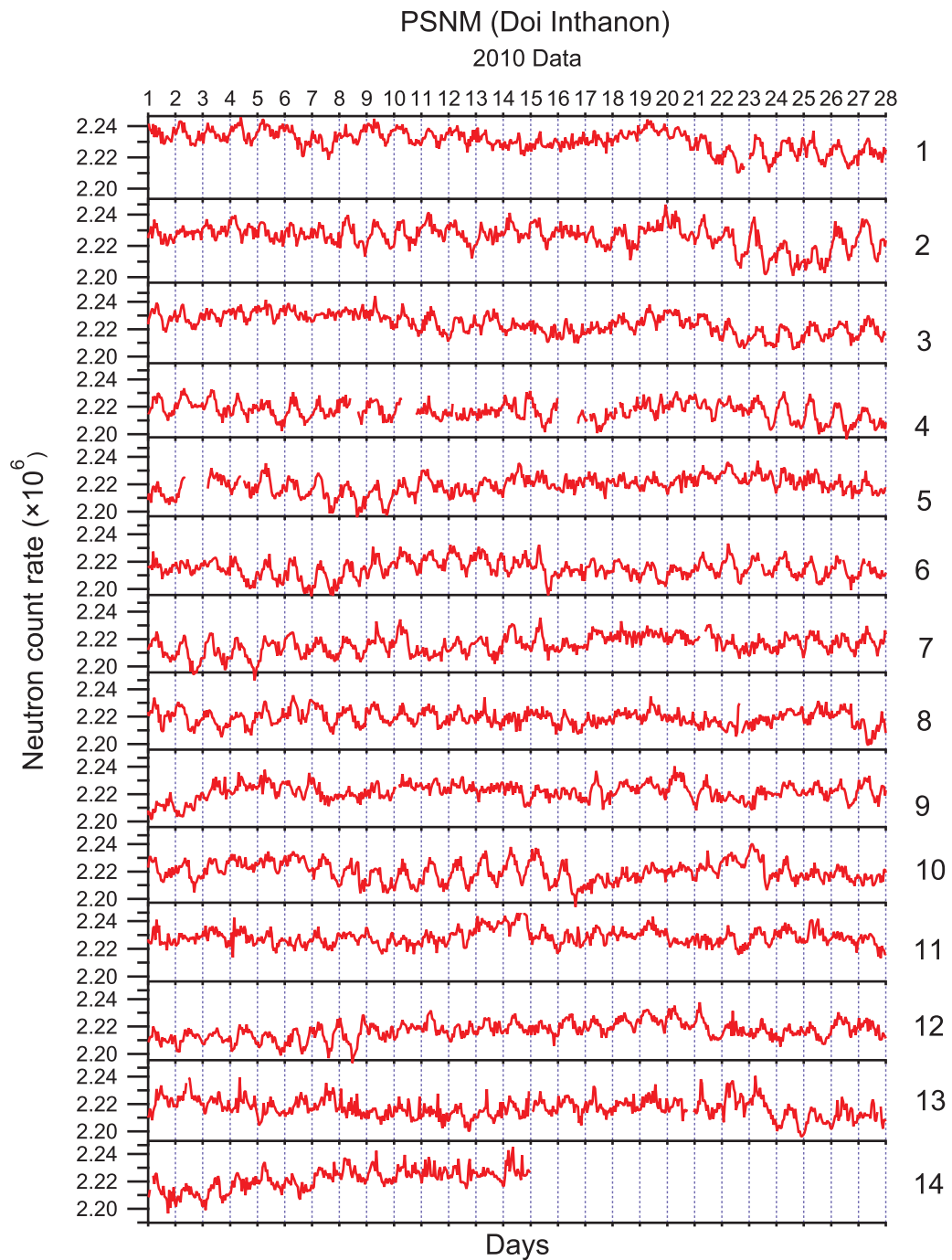


Figure A.4: Diurnal variations over 27-day periods in 2010.

APPENDIX B

EXTREME ULTRAVIOLET IMAGER AND IMAGE PROCESSING OF STEREO/EUVI SYNOPTIC MAPS

B.1 Extreme Ultraviolet Imager

Synoptic maps of the solar corona as used in this study were taken from the Extreme Ultraviolet Imager (EUVI), which is one of five telescopes in the Sun Earth Connection Coronal and Heliospheric Investigation (SECCHI) on the Solar TERrestrial RElation Observatory (STEREO) mission. The five telescopes together image the solar corona from the solar disk to beyond 1 AU. These telescopes are: an extreme ultraviolet imager (EUVI: $11.7R_S$), two traditional Lyot coronagraphs (COR1: $1.5 - 4R_S$ and COR2: $2.5 - 15R_S$) and two new designs of heliospheric imagers (HI-1: $15 - 84R_S$ and HI-2: $66 - 318R_S$). All the instruments use 2048×2048 pixel CCD arrays in a backside-in mode. The EUVI backside surface has been specially processed for EUV sensitivity, while the others have an anti-reflection coating applied.

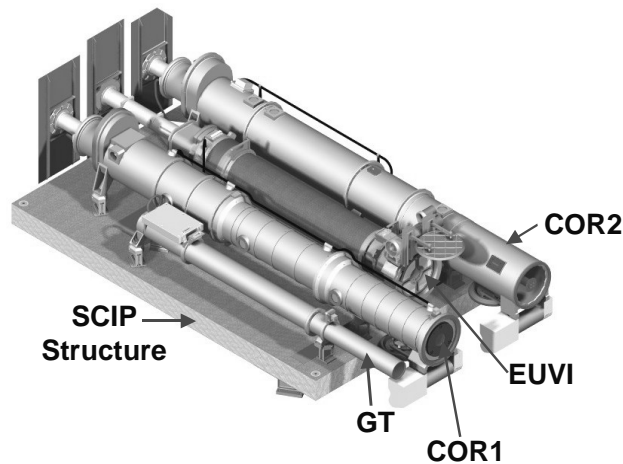


Figure B.1: The Sun Centered Imaging Package (SCIP) of SECCHI includes the EUVI (Wülser et al. 2003).

The EUVI (see Wülser et al. 2003) observes the chromosphere and low corona in four different EUV emission lines between 17.1 and 30.4 nm. It is a small,

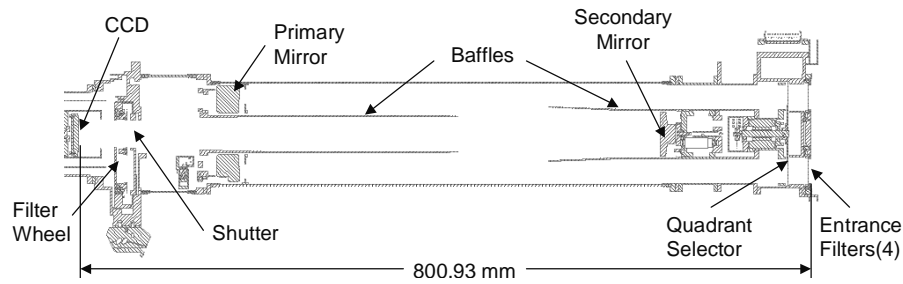


Figure B.2: EUVI telescope cross section (Wülser et al. 2003).

Table B.1: EUVI telescope properties (Wülser et al. 2003)

Instrument type	Normal incidence EUV telescope (Ritchey-Chrétien)
Wavelengths	He II 30.4 nm, Fe IX 17.1 nm, Fe XII 19.5 nm, Fe XV 28.4 nm
IR/visible/UV rejection	$> 10^{13}$ using thin metal film filters
Aperture	98 mm at primary mirror
Effective focal length	1750 mm
Field of view	Circular full sun field of view to ± 1.7 solar radii
Spatial scale	1.6 inch pixels
Detector	Backside illuminated CCD (e2v CCD42-40), 2048 \times 2048 pixels
Mechanisms	Aperture door, Quadrant selector, Filter wheel, Focal plane shutter
Image Stabilization	Active secondary mirror (tip/tilt) Range: ± 7 inch, jitter attenuation: factor 3 at 10 Hz

normal-incidence telescope with thin metal filters, multilayer coated mirrors, and a back-thinned CCD detector. Figure B.1 shows the EUVI on the SCIP platform and Figure B.2 is a cross section through the telescope.

According to an official description (Wülser et al. 2003):

“EUV radiation enters the telescope through a thin metal film filter of 150 nm of aluminum. This filter suppresses most of the UV, visible, and IR radiation and keeps the solar heat out of the telescope. During launch, the filter is protected by the front door. The radiation then passes through the quadrant selector to one of the four quadrants of the optics. Each quadrant of the primary and secondary mirror is coated with a narrow-band, multilayer reflective coating, optimized for one of four EUV lines. After bouncing off the primary and secondary mirror, the radiation continues through

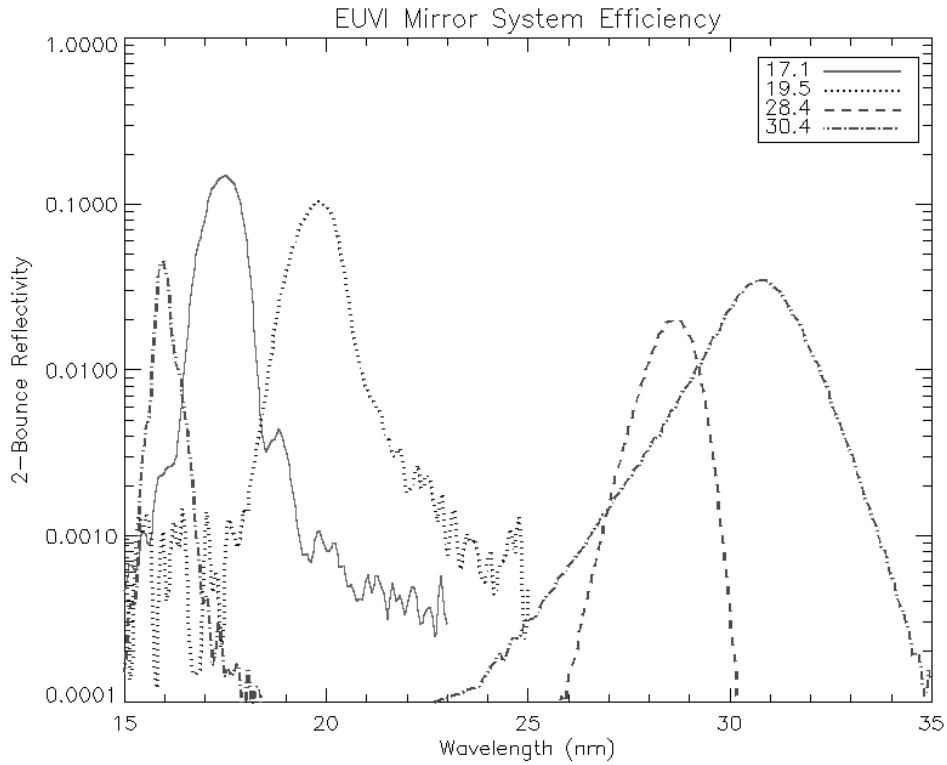


Figure B.3: EUVI effective area (Wülser et al. 2003).

a filter wheel that has redundant thin-film aluminum filters to remove the remainder of the visible and IR radiation. A rotating blade shutter controls the exposure time. The image is formed on a CCD detector. The main parameters for the EUVI telescope are summarized in Table” B.1.

“CCDs were calibrated on the NRL beamline at Brookhaven synchrotron and at the LMSAL XUV calibration facility. The entrance and focal plane filters were also calibrated at the LMSAL XUV calibration facility” (Windt and Catura 1988). “The results of those measurements were used to fit CCD and filter response models. The calibration curves of the individual components were combined to obtain the EUVI effective area as a function of wavelength. The results are shown in Figure” B.3. “The two telescopes (EUVI-A and EUVI-B) have very similar responses.”

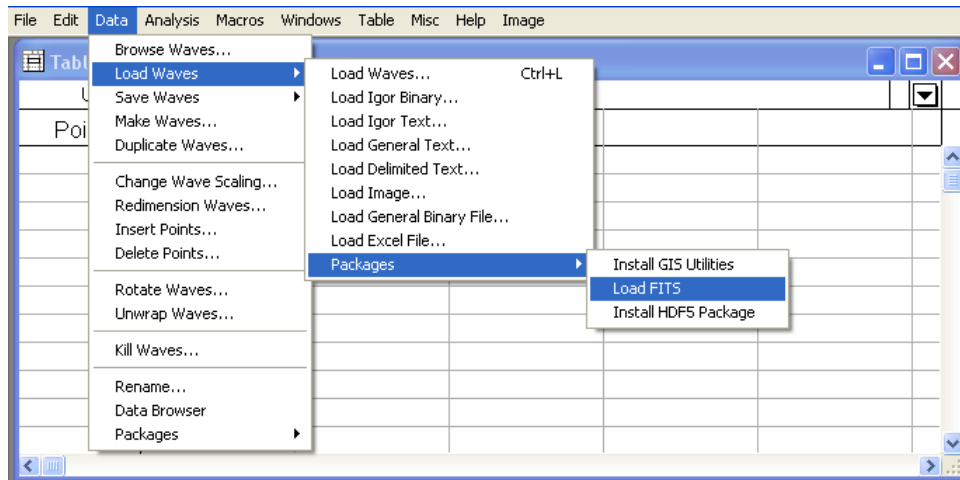


Figure B.4: Loading of synoptic map image in IGOR Pro.

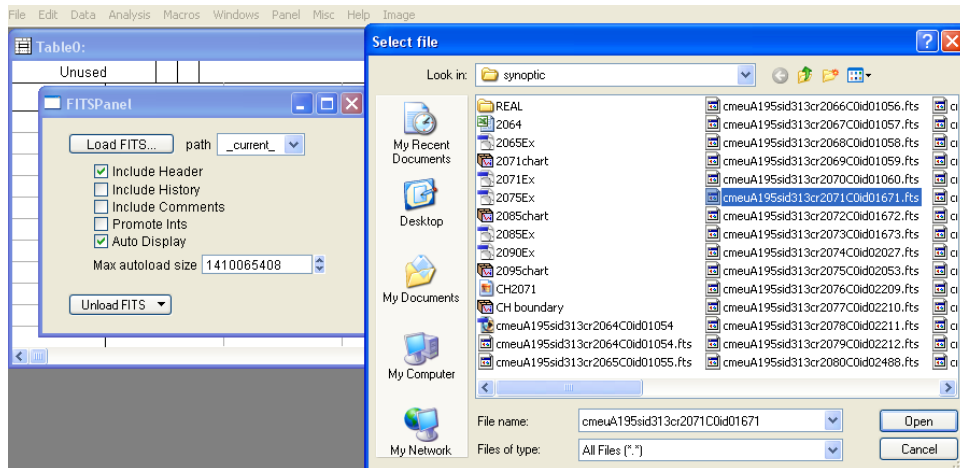


Figure B.5: Loading of synoptic map image in IGOR Pro.

B.2 Image processing of the synoptic maps

Image processing of the synoptic maps of the solar corona used in this study was performed in the Igor Pro program. The synoptic maps are in “Flexible Image Transport System” or FITS format that is the standard astronomical data format endorsed by both NASA and the International Astronomical Union (IAU). There are several steps to load and process the FITS files as follows.

1. Load image of synoptic map in FITS format as shown in Figure B.4, Figure B.5, and Figure B.6.
2. Change scale of the synoptic map both x and y axes: Choose Primary

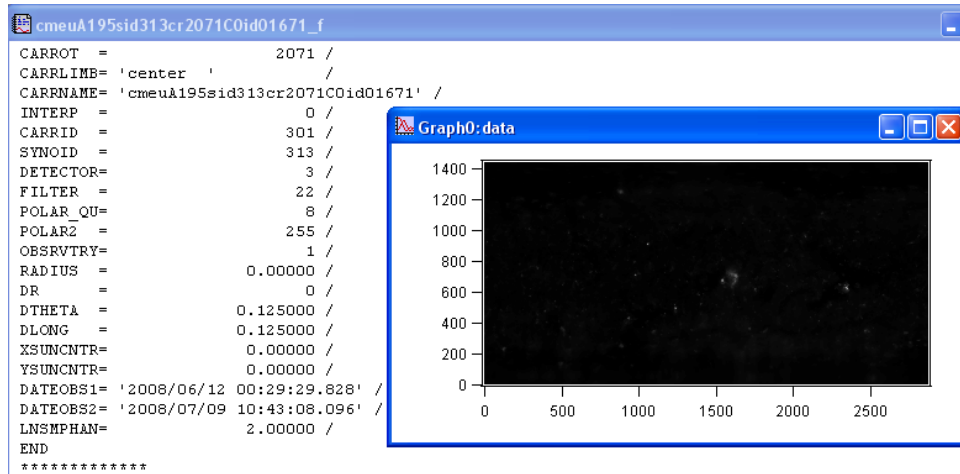


Figure B.6: Resultant information and image of the synoptic map.

wave and Data→Change Wave Scaling→press More Options→SetScale Mode→Start and End→change value (0 to 360 in X and -90 to 90 in Y) and then press Do It as shown in Figure B.7.

3. Manually tick by double click on axis→choose Auto/Man Ticks→Computed Manual Ticks→Tick increment = 45 for x and 90 for y axis as shown in Figure B.8.

4. Image processing of synoptic map image: load Image processing as in Figure B.9→choose Image→Image Contrast and select User Drawn then press Apply as in Figure B.10. Filter image by select Convolution Filtering and press Do It only in $N \times N$ filter as shown in Figure B.11.

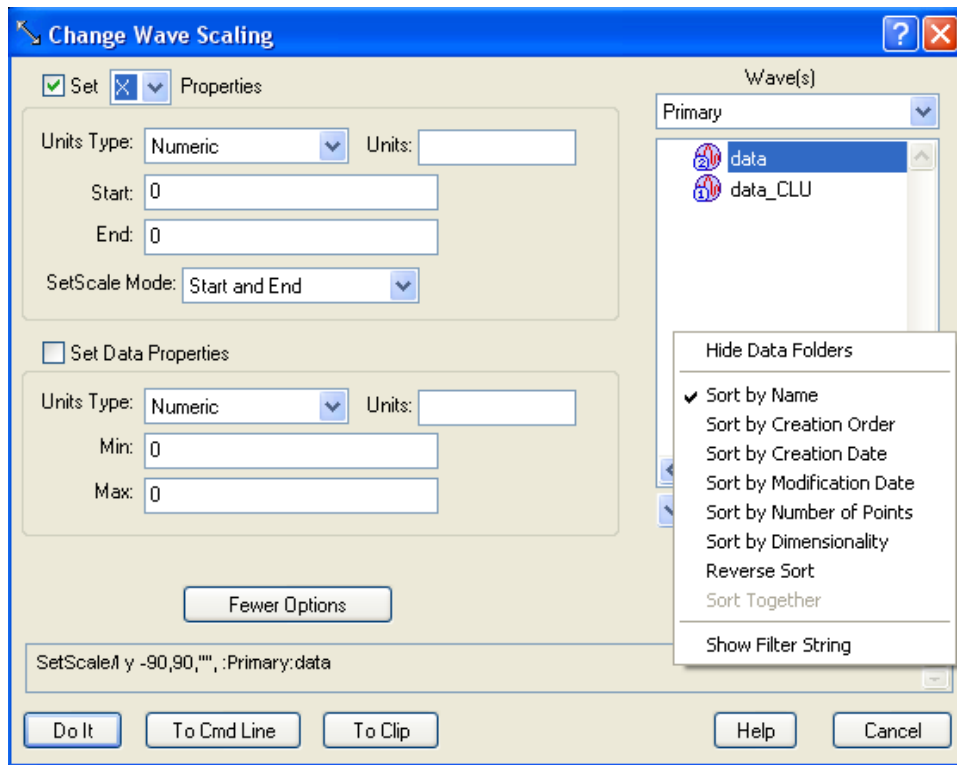


Figure B.7: Changing scale of the synoptic map.

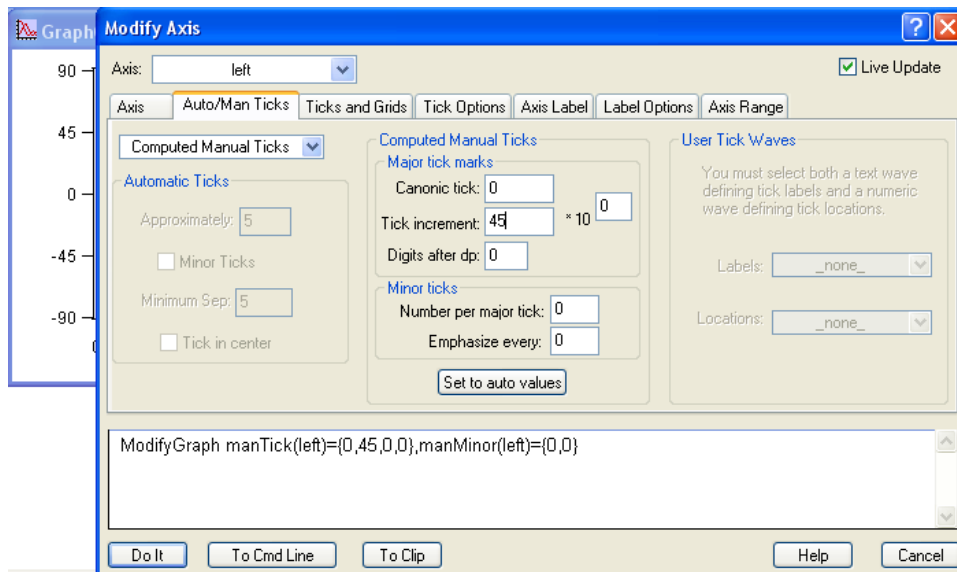


Figure B.8: Computed manual ticks.

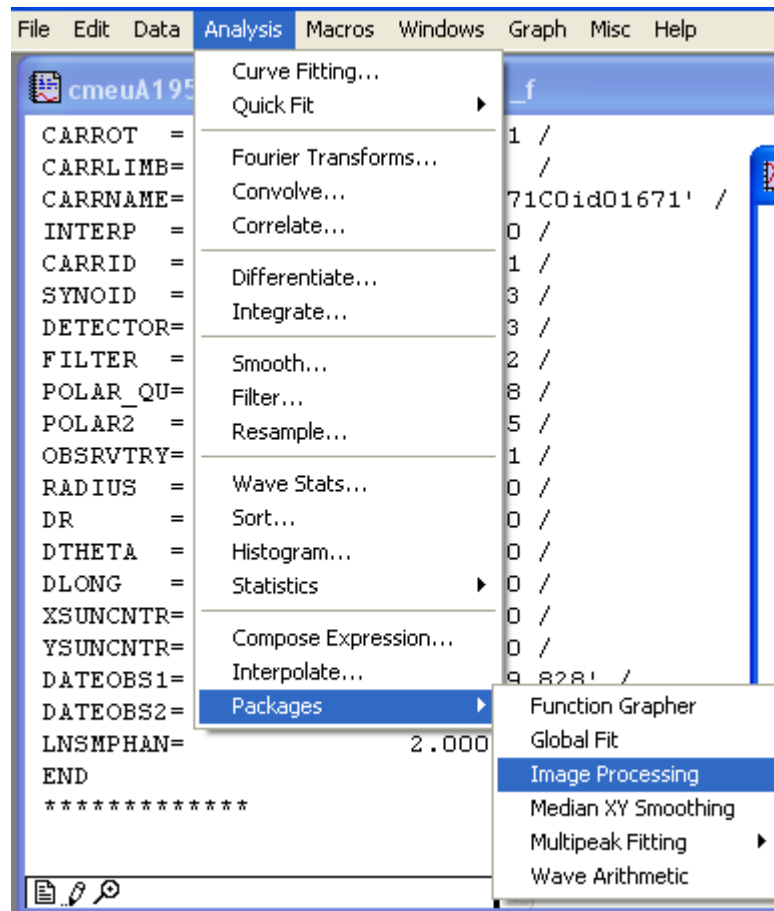


Figure B.9: Image processing in Igor Pro.

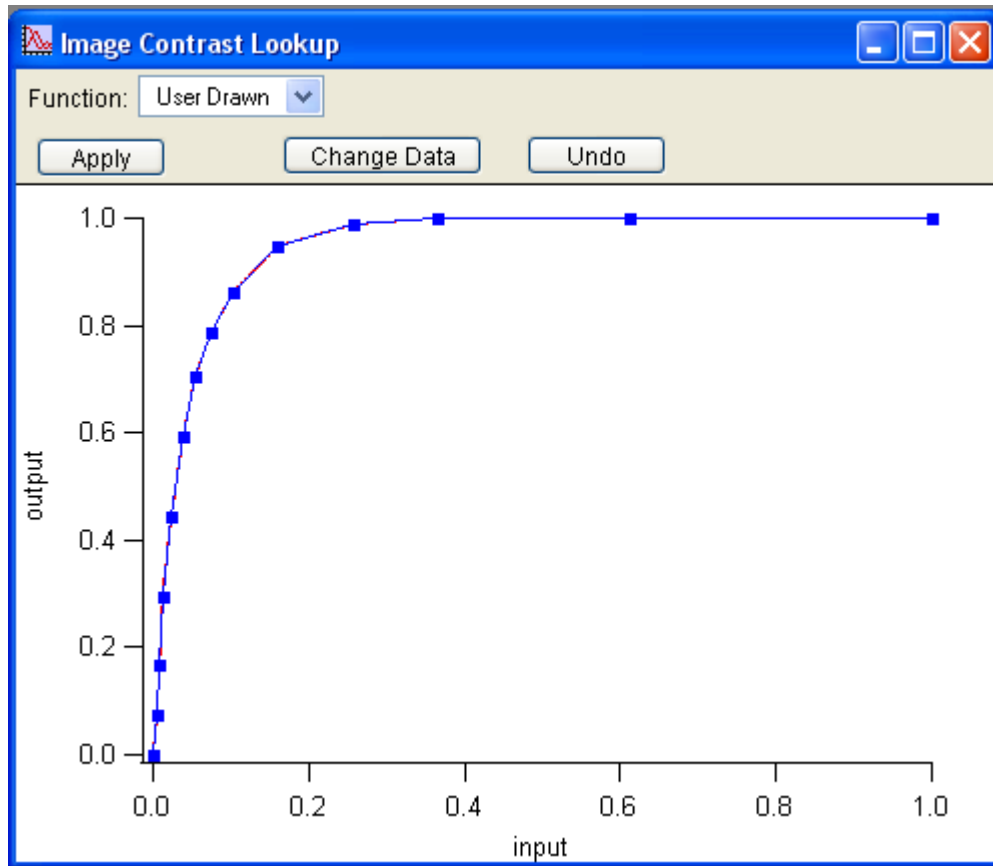


Figure B.10: Image contrast by User Drawn.

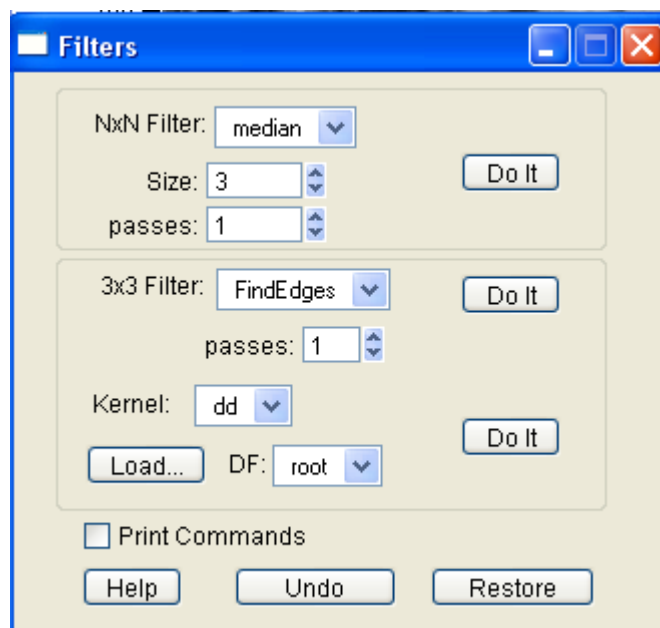


Figure B.11: Image filter.

APPENDIX C GYRORADIUS OF COSMIC RAYS AND MAGNETIC RIGIDITY

In a homogeneous magnetic field and the absence of electric field, the Lorentz force exerted by the magnetic field \mathbf{B} on a charged particle with charge q , mass m and velocity \mathbf{v} is

$$\frac{d\mathbf{v}}{dt} = \frac{q}{\gamma m} \mathbf{v} \times \mathbf{B} \quad (\text{C.1})$$

where $\gamma = (1 - v^2/c^2)^{-1/2}$ is the Lorentz factor, which is the ratio of the energy to the rest energy mc^2 :

$$E = \gamma mc^2. \quad (\text{C.2})$$

Multiply equation (C.1) by the particle velocity \mathbf{v} :

$$\mathbf{v} \cdot \frac{d\mathbf{v}}{dt} = \frac{q}{\gamma m} \mathbf{v} \cdot (\mathbf{v} \times \mathbf{B}). \quad (\text{C.3})$$

Since

$$\frac{d\mathbf{v} \cdot \mathbf{v}}{dt} = \mathbf{v} \cdot \frac{d\mathbf{v}}{dt} + \mathbf{v} \cdot \frac{d\mathbf{v}}{dt} = 2\mathbf{v} \cdot \frac{d\mathbf{v}}{dt}. \quad (\text{C.4})$$

We thus have

$$\mathbf{v} \cdot \frac{d\mathbf{v}}{dt} = \frac{1}{2} \frac{dv^2}{dt}. \quad (\text{C.5})$$

Then equation (C.3) becomes

$$\frac{1}{2} \frac{dv^2}{dt} = \frac{dE_k}{dt} = \frac{q}{\gamma m} \mathbf{v} \cdot (\mathbf{v} \times \mathbf{B}) = \frac{q}{\gamma m} (\mathbf{v} \times \mathbf{v}) \cdot \mathbf{B} = 0. \quad (\text{C.6})$$

It states that in a pure magnetic field, the kinetic energy E_k of a particle is constant along the motion.

In a homogeneous magnetic field along the z axis, $\mathbf{B} = B \cdot \hat{e}_z$, it is convenient to separate \mathbf{v} into components parallel (\mathbf{v}_{\parallel}) and perpendicular (\mathbf{v}_{\perp}) to the magnetic field,

$$\mathbf{v} = \mathbf{v}_{\parallel} + \mathbf{v}_{\perp}. \quad (\text{C.7})$$

Substituting equation (C.7) into equation (C.1) and noting that $\mathbf{v}_{\parallel} \times \mathbf{B} = 0$ we obtain

$$\frac{d\mathbf{v}_{\parallel}}{dt} + \frac{d\mathbf{v}_{\perp}}{dt} = \frac{q}{\gamma m}(\mathbf{v}_{\perp} \times \mathbf{B}). \quad (\text{C.8})$$

The parallel component equation can be written as

$$\frac{d\mathbf{v}_{\parallel}}{dt} = 0 \quad (\text{C.9})$$

and the perpendicular component equation as

$$\frac{d\mathbf{v}_{\perp}}{dt} = \frac{q}{\gamma m}(\mathbf{v}_{\perp} \times \mathbf{B}). \quad (\text{C.10})$$

Equation (C.9) shows that the particle velocity along \mathbf{B} is constant. For motion in the plane perpendicular to \mathbf{B} , we can write equation (C.10) in the form

$$\frac{d\mathbf{v}_{\perp}}{dt} = \boldsymbol{\Omega}_c \times \mathbf{v}_{\perp} \quad (\text{C.11})$$

where $\boldsymbol{\Omega}_c$ is the angular velocity defined by

$$\boldsymbol{\Omega}_c = -\frac{q\mathbf{B}}{\gamma m} = \frac{|q|B}{\gamma m}\hat{\boldsymbol{\Omega}}_c = \Omega_c\hat{\boldsymbol{\Omega}}_c. \quad (\text{C.12})$$

Thus, $\hat{\boldsymbol{\Omega}}_c$ is a unit vector that points in the direction of \mathbf{B} for a *negatively* charged particle ($q < 0$) and in the opposite direction for a *positively* charged particle ($q > 0$). Since $\boldsymbol{\Omega}_c$ is constant and, from conservation of kinetic energy, v_{\perp} is also constant, equation (C.11) shows that the particle acceleration is constant in magnitude and its direction is perpendicular to both \mathbf{v}_{\perp} and \mathbf{B} .

The trajectory of the particle is given by the superposition of a uniform motion along \mathbf{B} (with the constant velocity \mathbf{v}_{\parallel}) and a circular motion in the plane normal to \mathbf{B} (with the constant speed v_{\perp}). Therefore, the particle path is a *helix*. The angle between \mathbf{B} and the direction of motion of the particle is called the *pitch angle* and is given by

$$\alpha = \tan^{-1} \left(\frac{v_{\perp}}{v_{\parallel}} \right) \quad (\text{C.13})$$

where v is the total speed of the particle ($v^2 = v_{\parallel}^2 + v_{\perp}^2$).

The magnitude of the angular velocity Ω_c is known as the *gyro-frequency*, *cyclotron frequency*, or *Larmor frequency*.

The radius of the circular orbit is called *gyroradius*, *cyclotron radius*, or *Larmor radius* and is given by

$$r_c = \frac{v_{\perp}}{\Omega_c} = \frac{\gamma m v_{\perp}}{|q| |\mathbf{B}|} = \frac{\beta \gamma m c}{|q| |\mathbf{B}|} \quad (\text{C.14})$$

when $\beta = v/c$ and so $\gamma = (1 - \beta^2)^{-1/2}$, hence

$$\beta = \frac{\sqrt{\gamma^2 - 1}}{\gamma}. \quad (\text{C.15})$$

Consequently, equation (C.14) is then

$$r_c = \sqrt{\gamma^2 - 1} \frac{\gamma m c}{|q| |\mathbf{B}|} = \frac{\beta \gamma m c}{|q| |\mathbf{B}|}. \quad (\text{C.16})$$

The cyclotron radius can also be expressed by introducing the *magnetic rigidity* P . As the momentum of particle is $p = \gamma m v_{\perp}$, therefore

$$r_c = \frac{\gamma m v_{\perp}}{|q| |\mathbf{B}|} = \frac{p}{|q| |\mathbf{B}|} = \frac{p c}{q c B} = \frac{P}{c B} \quad (\text{C.17})$$

where

$$P = \frac{p c}{q} \quad (\text{C.18})$$

is the magnetic rigidity and $q = ze$. The lower its magnetic rigidity, the more strongly a particle trajectory is curved by the magnetic field. From the above expressions, determination of the cyclotron radius can be made in two cases. First, when we know only the energy of the particle, equation (C.16) will be used. Second, if we know only the rigidity of the particle equation (C.17) will be used.

To calculate the kinetic energy from the magnetic rigidity, we can employ equation (C.18) and the relativistic formula for energy

$$E = (p^2 c^2 + m^2 c^4)^{1/2} \quad (\text{C.19})$$

and

$$E = T + m c^2 \quad (\text{C.20})$$

where T is kinetic energy of the particle and m is its rest mass.

To determine γ we use the relation

$$\gamma = \frac{E}{mc^2}. \quad (\text{C.21})$$

BIOGRAPHY

NAME	Mr. Thana Yeeram
DATE OF BIRTH	28 May 1979
PLACE OF BIRTH	Kampaengphet, Thailand
INSTITUTIONS ATTENDED	Naresuan University, 1998-2002 Bachelor of Science (Physics) Chiang Mai University, 2002-2005 Master of Science (Physics) Mahidol University, 2008-2014 Doctor of Philosophy (Physics)
SCHOLARSHIP RECEIVED	Ministry of Science and Technology
RESEARCH GRANTS	Research assistant, Thailand Center of Excellence in Physics
POSITION	Lecturer, 2005-Present Department of Physics, Science faculty, Mahasarakham University, Thailand 44150. Tel. 084-512-8205 E-mail: thana.thana@hotmail.com
PUBLICATION	Yeeram, T., Ruffolo, D., Sáiz, A., et al. 2014, <i>Astrophys. J.</i> , 784 , 136-146